On the Length Dynamics of Active Polar Filaments

Dissertation zur Erlangung des Grades
des Doktors der Naturwissenschaften der
Naturwissenschaftlichen Fakultät II
– Physik und Mechatronik –
der Universität des Saarlandes

von

Christoph Erlenkämper

Saarbrücken
2012

Tag des Kolloquiums	28.8.2013
Dekan	Prof. Dr. Christian Wagner
Mitglieder des Prüfungsausschusses	Prof. Dr. Albrecht Ott (Vorsitzender)
	Prof. Dr. Dr. Karsten Kruse
	Prof. Dr. Heiko Rieger
	Prof. Dr. Reinhard Lipowsky
	PD Dr. Michael Koblischka

Abstract

The cytoskeleton is the ensemble of linear protein chains and a number of regulatory molecules in living cells. Together, they form a highly active physical network that provides mechanical stability to the cell and is involved in a number of vital processes such as cell locomotion, intracellular transport, and cell division. The length of the filaments is a key parameter for the proper functioning of the cytoskeleton and must therefore be tightly regulated by the cell.

In this work, different models for the length dynamics of active polar filaments are investigated and quantified. Such filaments are able to treadmill, that is, to accumulate subunits at one end and loose them at the other. It is shown that the same properties that lead to treadmilling provide a means to regulate filament length. Length regulation becomes much more efficient when the action of filament destabilizing molecular motors is considered. The analysis of a driven lattice gas model predicts robust length control in a large range of parameters. Finally, the turnover dynamics of the actin cortex, a thin polymer shell underneath the eukaryotic cell membrane, is investigated theoretically and results are compared to experimental findings.

The presented analysis shows that filament length control is possible under diverse biological conditions. The underlying mechanisms provide insights into the turnover dynamics of the cell's actin cortex.

Zusammenfassung

Das Zytoskelett lebender Zellen besteht aus linearen Proteinketten und einer Vielzahl an regulierenden Molekülen. Zusammen bilden sie ein äußerst dynamisches Netzwerk, das der Zelle mechanische Stabilität verleiht und an vielen vitalen Prozessen wie der Zellbewegung, dem intrazellulären Transport und der Zellteilung beteiligt ist. Um das Funktionieren des Zytoskeletts sicher zu stellen, muss die Zelle insbesondere die Länge der Filamente regulieren.

In dieser Arbeit werden verschiedene Modelle für die Längendynamik aktiver polarer Filamente untersucht und quantifiziert. Solche Filamente können eine Laufbanddynamik zeigen, d.h. Untereinheiten an einem Ende anlagern und am anderen verlieren. Es wird gezeigt, dass die gleichen Eigenschaften, die zur Laufbanddynamik führen, zur Regulation der Filamentlänge genutzt werden können. Längenregulation wird effizienter, wenn destabilisierende molekulare Motoren hinzu treten. Die Analyse eines angetriebenen Gittergasmodells zeigt eine robuste Längenregulation für einen breiten Parameterbereich. Anschließend wird die Dynamik im Aktinkortex, einer dünnen Polymerschicht unter der eukaryotischen Zellmembran, untersucht und die Ergebnisse mit experimentellen Befunden verglichen.

Die vorliegende Studie zeigt, dass die Kontrolle der Filamentlänge unter unterschiedlichen biologischen Bedingungen zu finden ist. Die zugrunde liegenden Vorgänge erlauben Einblicke in die Dynamik des Aktinkortex der Zelle.

Contents

Contents

1 Introduction

It is to a large extent unknown what determines the size of biological structures. This statement holds for structures on all length scales from population sizes or the size of individual organisms down to the size of cellular structures or of single molecules. While singular historic events might play an important role for determining, for example, the length of a genome, physics can help to understand the size of other structures, for example, the maximal size of a tree or the necessary size of wings for flying. In this work, possible physical mechanism of size regulation of microtubules and actin filaments are studied, which are important biopolymers present in almost all eukaryotic cells [1].

The cytoskeleton mainly consists of two types of biopolymers, microtubules and actin filaments. This network of filamentous proteins is involved in numerous vital processes and forms important structures [1]: During cell division it builds the mitotic spindle, a microtubule-based structure which segregates the two copies of the genetic material onto the future daughter cell. In later stages of cell division, actin filaments form a ring that cleaves the mother cell upon constriction. Microtubules and actin filaments also form cellular protrusions notably involved in cell locomotion. The sizes of these structures and/or their mechanical properties are often determined by the lengths of the cytoskeletal filaments [2].

Microtubules and actin filaments are linear assemblies of non-covalently linked protein subunits. The two ends of these cytoskeletal filaments are structurally different, which endows them with a structural polarity that is exploited by cells in various ways. As one consequence of this polarity, the kinetics of subunit addition and removal is in general distinct at both ends. Furthermore, in contrast to conventional polymers, the assembly of cytoskeletal filaments is a dissipative process as it depends on the hydrolysis of nucleotide-tri-phosphates. Together, these properties can lead to the so-called treadmilling dynamics [3–5]. In such situations, filaments show net grow at one end, the "plus end" of microtubules or the "barbed end" of actin filaments, and net shrinkage at the opposite end, the "minus end" or "pointed end". In other circumstances, filaments can show a "dynamic instability" [6], where one end is inert and the other switches stochastically between phases of growth and shrinkage.

One important determinant of the filament length distribution is the subunit concentration. Its influence on filament assembly has been studied in great detail both for passive

polymers [7], where assembly is not driven by a ligand associated with the subunits, and for active polymers like microtubules and actin filaments [8–11]. For the latter, it was in particular studied how accessory molecules like capping proteins that inhibit addition of further subunits or severing proteins that cut filaments affect the length distribution [12–15]. More recently, also molecular motors have been considered in this context [16–21].

In this introductory chapter, the molecules involved in the assembly of actin and microtubules are presented and the theoretical concepts that are applied in the subsequent analysis are introduced. In Chapter 2, the dynamics of active polymerization is investigated theoretically. The results of these considerations are then applied to the polymerization of actin filaments, modeling the *in vitro* situation. Chapter 3 treats filament length control by the action of directionally moving molecular motors. The effect of this second active process is an increase in regulation effectivity. In Chapter 4, the situation of a finite ensemble of filaments and accessory proteins is studied. Experiments probing the dynamics of the actin cortex are discussed and results are explained with analytical considerations and stochastic simulations. Different models are presented that can equally account for particular properties of the cortex. A brief summary concludes the work and points to emerging questions for future research.

The individual chapters are mostly self-contained and can be read independently of one another. Each chapter starts with a short introduction to the discussed topics and closes with a summary of the main results. Chapter 4 relies in parts on the results of Chapter 2 since the models for filament polymerization are identical but considered in different contexts. For briefness, I refrained from repeating the model definition in Chapter 4.

Parts of this work were already published [14, 20, 22, 23], or are in preparation for publication.

1.1 Biopolymers

Polymers are aggregates of identical or similar subunits that cluster into regular structures, typically linear chains. Plastics and rubbers such as Polyethylen (PE) or PDMS are widely known examples for technically relevant polymers. The subunits or monomers can be very small (Ethylen) or complex molecules (biopolymers). Polymers usually grow by spontaneous monomer addition to a preformed nucleus until the monomer pool is exhausted [24].

The structures of polymers can differ widely. They can consist of identical (homopolymers) or different types of monomers (heteropolymers) which then might be arranged randomly

(statistic copolymers) or in blocks (block- copolymers) with side-chains of differing length or cross-links to adjacent polymers. The physical properties like the viscosity or the elastic modulus of polymer melts depends critically on the structure and typical length of the constituent polymers [25]. Interactions between the polymers are dominated by entanglement and reptation [26]. In this context, "entanglement" describes the mutual restriction of movement of densely packed and interwoven polymers while "reptation" denotes the thermal one-dimensional movement of polymers in a tube along their long axis.

In biological systems, a large variety of polymers can be found. The subunits of these biopolymers can be linked covalently or by weaker hydrogen bonds or Van-der-Vaals interactions [27]. DNA, for example, is a heteropolymer of four different nucleotides that are covalently connected. Every subunit consists of a sugar molecule, a phosphate group and one out of the four nucleobases guanine, adenine, thymine, and cytosine. The sequence of these subunits stores the genetic information of all known living cells. Proteins are also covalent polymers that are built from 26 different amino acids by covalent peptide bonds. Their sequence determines the protein's shape and function.

Some proteins are able to form polymeric supramolecular structures themselves. Identical or similar proteins aggregate by non-covalent interactions into larger structures, forming long linear chains or tubes. Examples for such proteins are actin, tubulin, vimentin, myosin, or flagellin [2, 7, 27]. Also viral capsides can be viewed as protein polymers but form areal structures from a limited number of subunits. Due to the small binding energies between individual subunits, the protein polymers can be highly dynamic. In living cells, they perform a number of vital tasks such as shape control, cargo transport, or locomotion. Their aggregation and structure is controlled by a large number of regulatory binding partners [1, 27].

This study is focused on active polar biopolymers, such as actin filaments and microtubules. They form linear aggregates with chemically distinct properties at both ends. Their ability to dissipate chemical energy during polymerization makes them examples for out-of-equilibrium systems which are of particular interest in physics. Their complex dynamics are used by living cells in various ways. To differentiate them from polymeric structures such as DNA and proteins, they are called linear filaments in the following. Both filament types and their most important binding molecules are now discussed in turn.

1.1.1 Actin

Actin is a $42kDa$ heavy protein that is roughly globular with an average diameter of $5.4nm$ formed by a single peptide chain. Monomeric actin proteins (G-actin) can polymerize into filamentous aggregates (F-actin) that are often referred to as microfilaments. Monomers
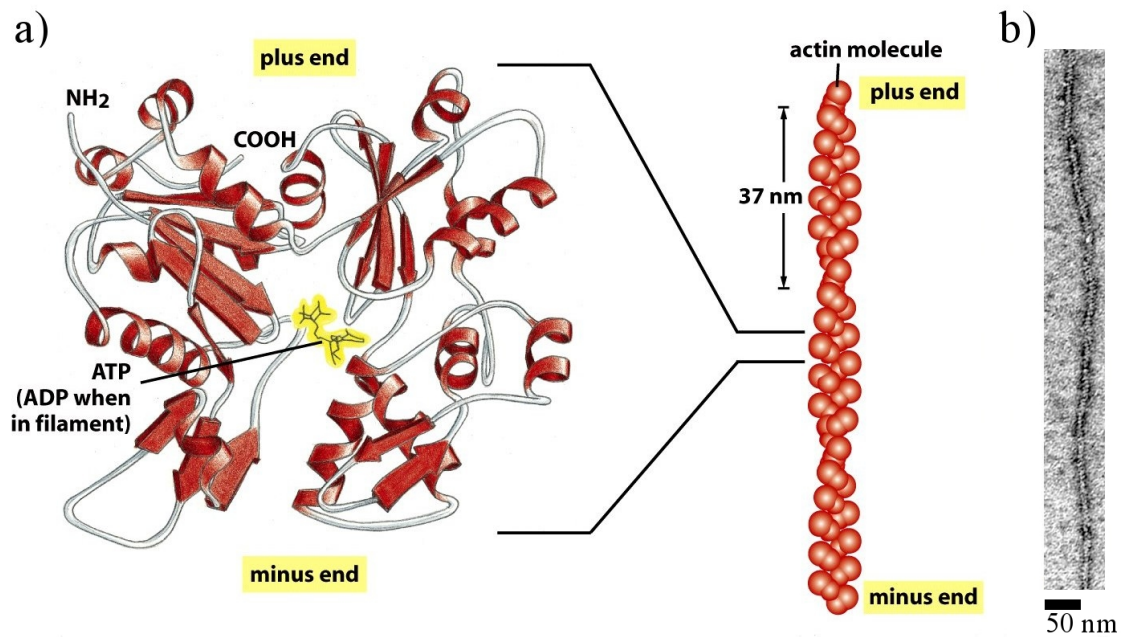
Figure 1.1: a) Structure of actin filaments. Schematic representation of an actin monomer. An ATP molecule is bound in the cleft between the two subparts of the protein (left). Two helical protofilaments form a twisted actin filament with a pitch of 37 nm (right) ©2008 from [27], 5th Edition by Alberts et al. Reproduced by permission of Garland Science/Taylor & Francis LLC. The regular structure of an actin filament can also be seen in electronmicrographs From [28]. ©Rockefeller University Press.

have an internal orientation and aggregate in a head-to-tail fashion into protofilaments. Actin filaments consist of two parallel protofilaments that are helically wound around each other with a pitch of 37nm, see Figure 1.1. The addition of a single subunit thus leads to a net length increment of 2.7nm. The more dynamic end is called the 'barbed end', while the other one is the 'pointed end'.

Actin monomers consist of two domains that form a deep cleft in which an adenosin-phosphate and a divalent cation can bind. The potential of actin monomers to polymerize depend sensitively on its binding factors. It polymerizes most readily if bound to Ca^{2+} and the energy rich adenosin-tri-phosphate (ATP), but can also polymerize in presence of Mg^{2+} and adenosin-di- or -mono-phosphates (ADP and AMP) [7].

Under physiological conditions, monomers are typically associated with Ca^{2+} and are either bound to ATP or ADP. The metabolism of living cells ensures that the ADP molecule

on G-actin is readily replaced by ATP which keeps the actin filament out of thermodynamic equilibrium. F-actin is a kinase which dephosphorylates the adenosine, thereby dissipating energy. The phosphate release of the nucleotide leads to conformational changes in the monomer and modifies its polymerization properties. When the third phosphate group (the γ- phosphate) of the ATP is hydrolyzed, it remains bound to the actin for some time before it is released into the cytosol (ADP-P_i). The affinity of an actin monomer to the filament depends on the binding state of the adenosine. Polymerisation rates could be determined experimentally for the three mentioned states [3, 4, 7, 29, 30]. Together with filament polarity, the energetically driven character of actin polymerization can lead to the simultaneous addition of monomers at one filament end and monomer loss at the other. This dynamical state of filaments is called 'treadmilling' and plays an important role in the present study.

The formation of new actin filaments is a highly concentration dependent process [7, 31]. Due to the helical structure and the two protofilaments, at least three monomers have to come together to form a new helical nucleus which is then able to further accumulate monomers. Since the intermediate states are highly unstable [31, 32] the rate of nucleus formation is very low, leading to a lag phase at early stages of polymerization [7, 27]. Once a nucleus is formed, the addition of further monomers occurs at a much higher rate. This behavior gave rise to the notion of a crystallization-like dynamics of filament formation [7]. *In vivo*, however, a large number of proteins facilitates and controls the formation of actin filaments.

Actin polymers have a persistence length of about 17 μm [33]. Since the persistence length is of the same order as typical cell sizes, actin filaments are called semi-flexible. In living cells, actin filaments form a multitude of different structures such as the cell cortex, filament bundles, or stress fibers. The actin cortex is a highly dynamic network of actin polymers underneath the plasma membrane in living cells. Since the membrane itself is very fragile, the cortex gives the cell its mechanical stability. It reorganizes constantly, allowing the cell to deform on short timescales. The actin cortex also gives the cell the ability to exert forces on its environment and to translocate on substrates [34].

Proteins like α-actinin cluster the filaments into parallel bundles, which are able to withstand tensile stress. In combination with molecular motor molecules of the myosin family, actin is observed to form stress fibers in which antiparallel bundles of actin are interconnected by myosin clusters. These fibers are able to exert forces to the entire cell and play an important role during embryonic development [35]. Alternating groups of actin bundles and myosin filaments also form sarcomeres, the force producing units in muscle cells. Actin filaments are thus a key element to the movement of all animal cells.

Actin is expressed in virtually all eurkaryotic cell types and its amino acid sequence is

highly conserved among species. Actin from yeast is to 90% identical to the human form. In procaryotes, the actin homologue MreB was found which is also able to polymerize into linear aggregates but is much less active [36]. However, the results on polymerization of MreB remain controversial [37]. Actin monomers and filaments interact with a large number of accessory proteins to perform their multiple tasks. This might be the reason for the high equivalence of actin sequences among species. Since every alteration might impair a multitude of interactions, it may lead to a breakdown of actin control and, as a consequence, mutations are rapidly eliminated.
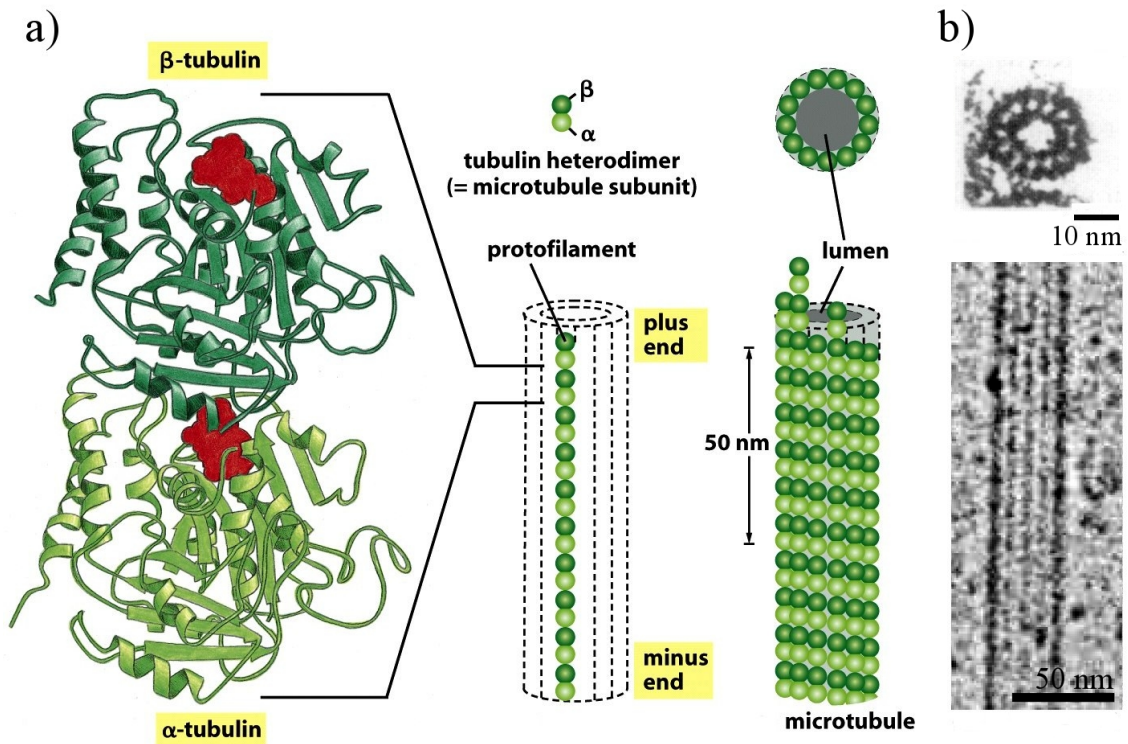
1.1.2 Microtubules

Tubulin is a 55 kDa large protein that is expressed in eukaryotic cells in three different isoforms, the α, β, and γ tubulin. α and β tubulin form heterodimers that polymerize into hollow tubes, the microtubuli [27]. These filaments are built from typically 13 straight protofilaments, each of which is a linear array of tubulin dimers that are arranged in a head-to-tail fashion, see Figure 1.2. The protofilaments in a microtubulus are not perfectly aligned but are shifted by 3/13 tubulin lengths. Thus, the microtubules have a seam at which a α-tubulin of one protofilament is adjacent to a β-tubulin molecule in the neighboring protofilament [1].

The outer diameter of a microtubulus is about 25 nm, while the individual tubulin subunits have a diameter of 6 nm. Due to their cylindrical structure, microtubuli have an extraordinary large persistence length of more than 1 mm [40, 41]. *In vivo*, microtubuli reach sizes up to 25 μm.

Microtubules are nucleated by γ-tubulin that concentrates at the microtubules organising center (MTOC) close to the cell nucleus. There, it forms rings on which α-β-tubulin dimers polymerize. The dynamic 'plus ends' of microtubuli extend into the cytosol exposing the β-tubulins of the protofilaments.

Similar to actin, each tubulin is able to bind a nucleotide. In contrast to actin, tubulin binds guanosin-di- phosphates (GDP) and -tri-phosphates (GTP). A GTP bound to the α-subunit is enclosed in a pocket between the two subunits of the dimer and is neither de-phosphorylated nor released. The nucleotide bound to the β- tubulin, on the other hand, is cleaved by the kinase activity of tubulin. The loss of the γ phosphate induces a conformational change in the tubulin dimer: GTP bound tubulin dimers form straight protofilaments that easily aggregate into microtubules, while the GDP-tubulin prefers a curved conformation storing mechanical strain energy in the tubular lattice. As long as a cap of GTP-tubulins protects the ends of the microtubulus, the mechanical tension cannot be released. If, by

Figure 1.2: Structure of microtubuli. a) Schematic representation of the tubulin dimer bound to two red GTP molecules. The heterodimers consist of an α- and a β-tubulin and assemble in a head-to-tail fashion into linear protofilaments. 13 protofilaments form the hollow microtubulus. ©2008 from [27], 5th Edition by Alberts et al. Reproduced by permission of Garland Science/Taylor & Francis LLC. b) Electronmicrographs show a microtubule from the side (bottom, From [38]. ©Rockefeller University Press.) and in a cross-section (top, Reprinted from [39] ©(1990), with permission from Elsevier.)
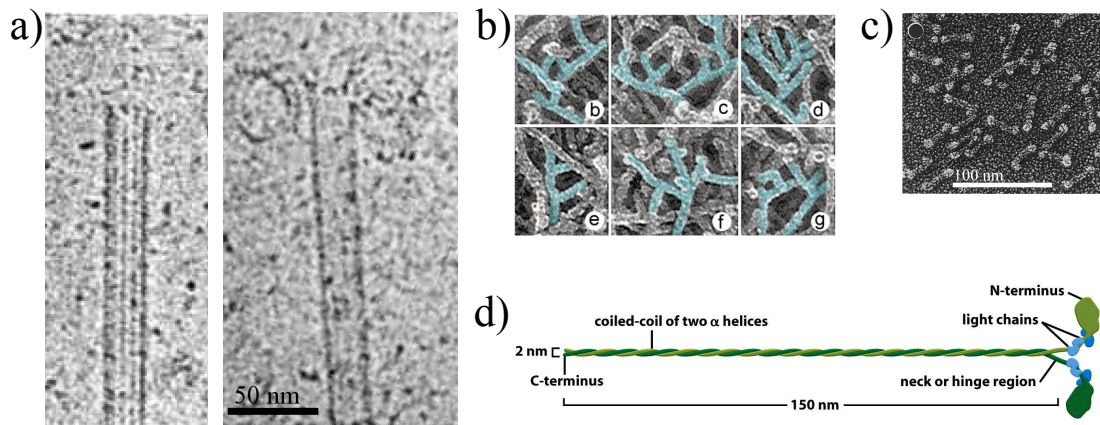
Figure 1.3: The shapes of selected accessory proteins. a) Electronmicrographs of stabilized (left) and depolymerizing (right) microtubules. The reeling of GDP-bound tubulin protofilaments is visible in the right image. From [38]. ©Rockefeller University Press. b) Different sections from an electron micrograph of the lamellipodium, an actin filled protrusion at the leading edge of migrating amoeboid cells. The branching of actin filaments is due to the nucleation of new filaments by the arp2/3 complex alongside existing filaments. From [45]. ©Rockefeller University Press. c) Electron micrograph of α-actinin molecules. The actin binding sites appear thicker than the linker domain. Reprinted from [46] ©1986 Wiley-Liss, Inc. d) A schematic representation of a myosin II motor. The heavy chain is colored in green, the light chains in blue. ©2008 from [27], 5th Edition by Alberts et al. Reproduced by permission of Garland Science/Taylor & Francis LLC.

stochastic fluctuations or because the filament grew against an obstacle, the GTP cap is lost and the curved protofilaments rip the microtubulus apart, see Figure 1.3 a). The process of rapid growth by GTP-tubulin followed by rapid disassembly of GDP rich microtubules that was found *in vivo* is called 'dynamic instability'. Even though microtubules were also observed to display treadmilling [5], there is strong evidence that the growth of microtubules is dominated by dynamic instabilities [6, 42–44].

Microtubules perform a number of vital tasks in living cells. During cell division, they form the mitotic spindle that is responsible for the segregation of the genetic material and its correct distribution to the daughter cells. They also serve as transport tracks for cellular cargo such as vesicles or mitochondria. In neurons, the tubulin structures span the whole axon which can reach sizes of meters. For example, vesicles filled with neurotransmitters are transported along the microtubules from the cell body to the synaptic cleft, where the transmitters are released upon stimulation of the nerve cell. If the transport of vesicles was dependent on diffusion, it would take years for the cargo to reach its destination [27].

Just as actin, the tubulins are evolutionarily very old proteins. They share genetic and

functional similarities with the procaryotic protein FtsZ which also polymerizes into filaments but only appears to be a single protofilament. Recently, tubulin related proteins, BtubA and BtubB, were found in bacteria. These proteins form microtubuli-like structures of 5 protofilaments [47] and are assumed to be derived from the same ancestral protein as tubulin.

For sake of completeness, a third type of biopolymer should be mentioned at this point as well. In eucaryotic cells, so called intermediate filaments can be found. These filaments are build of non-polar tetramers of 10 nm sized proteins. Intermediate filaments exist in a variety of types which share common genetic features. They play an important role in maintaining the structural integrity of the cell as they provide strong shear resistance, for example in the neurons of vertebrates. In contrast to actin and microtubules, however, they are neither polar nor active. Since they do not bind energy rich nucleotides, their polymerization dynamics differs fundamentally from the models discussed here and they are not considered in the remainder of this work [27, 48].

1.2 Accessory Proteins

The cell has a large number of regulatory proteins at its disposal to influence the dynamics and structure of the cytoskeletal filaments. Here, the accessory proteins that are most important in the context of the present work shall briefly be introduced. Their characteristic effects become relevant when experimental findings are discussed or when these effects are included in some of the analyzed models. These proteins can loosely be put into the following categories.

1.2.1 Sequestering Proteins

Profilin   is a small protein of 14-16 kDa weight which is expressed in most eucaryotic cell types. It binds actin monomers and fosters the replacement of an ADP by an ATP molecule. Profilin-actin dimers are able to bind to barbed ends of actin filaments but not to pointed ends. The reason is an overlap of the bound profilin molecule with the pointed end binding site of actin monomers. Polymerisation from profilin-actin at barbed ends proceeds at a slightly lower rate than from pure actin [49]. When the barbed end is bound by a protein called formin, profilin accelerates polymerization by up to a 20-fold [50]. Profilin bound actin monomers display a much lower tendency to nucleate spontaneously, but are easily nucleated by formins [51]. It was shown recently that profilin increases the rate of phosphate release

at the barbed ends of filaments [52].

β**-thymosin**   The extremely small 5 kDa β-thymosins are found in large quantities in the cell. They sequester the G-actin for almost all reactions. The binding affinity of β-thymosin to actin is, however, smaller than that of profilin. Thus, profilin can liberate the actin monomers from the large pool of β-thymosin bound monomers and can make them available for polymerization [53]. It is assumed that most of the cell's G-actin is bound to β-thymosin and is thus not available for immediate polymerization.

1.2.2 Nucleators

Formins   are a class of proteins that are associated with actin filament nucleation and elongation [54]. The amino-acid sequences of all formins contain two characteristic domains, the so-called formin-homology domains (FH1 and FH2). While the FH1 domain binds to proteins like profilin, the FH2 domain is required for the dimerization of formins. In the dimeric form, formins are able to nucleate new filaments. They remain bound to the filament's barbed end and progressively add actin monomers from profilin- actin. In absence of profilin, formins can switch from an 'open' to a 'closed' state. While monomer addition is possible in the open state, it is blocked in the closed state. The efficiency of polymerization varies among the different types of formin. The formin Cdc12 for example is mostly in the closed conformation and polymerizes filaments much slower than mDia1 that is known for its fast polymerization velocity [55].

Arp2/3   is a protein complex containing the two subunits, arp2 and arp3 that are closely related to actin. The complex is activated by nucleation promoting factors (NPFs) like WAVE/Scar complex or WASp (Wiskott-Aldrich-Syndrome protein). Arp2/3 binds to the side of an existing actin filament, the mother filament, and nucleates a new filament, the daughter filament. The pointed end of the daughter filament remains anchored in the arp2/3 complex while the barbed end accumulates monomers from the cytosol. The branches form a characteristic 70 degree angle with the mother filament, see Figure 1.3 b). In migrating cells, the arp2/3 complex nucleates filaments at the leading edge of the lamellipod and causes a large number of free barbed ends to push simultaneously against the cell membrane [56].

The stability of the arp2/3 complex seems to depend on the phosphorylation state of the monomer in the mother filament. The bond is most stable in the ATP- or ADP-P$_i$ bound actin state and is weakened by the dephosphorylation of the mother filament[57].

γ-**Tubulins** are microtubuli nucleating proteins. Besides α- and β-tubulin, which form the actual microtubules, they constitute a third tubulin isoform. γ-tubulin is mainly found at the microtubules organizing center (MTOC), where it forms ringlike structures. These structures mimic the plus end of microtubuli to which further α-β-tubulin dimers can add. From the MTOC, the plus ends of microtubules project outwards into the cytosol. The *de novo* formation of microtubuli essentially relies on the presence of γ-tubulins since the concentrations of α and β tubulin *in vivo* are much too low to efficiently nucleate microtubuli from a pure solution.

The γ-tubulin and the arp2/3 complex not only nucleate new filaments, they also inactivate the filament's minus or pointed end, respectively, and suppress monomer addition or removal. There are other proteins that are specialized to exclusively cap filament ends.

1.2.3 Capping Proteins

CapZ is a heterodimeric protein that binds to the barbed ends of actin filaments, where it prevents addition and removal of actin monomers. It consists of an α (36 kDa) and a β (32 kDa) subunit that have no similarity to actin itself. CapZ binds strongly to filament ends and influences the structure of the polymeric network already at low copy numbers, $K_D < 0.5\mathbf{n}M$ [58]. It is found for example in the Z-band of muscle cells, where it is responsible for the extraordinary stability of actin filaments in sarcomeres.

Tropomodulin binds to the pointed ends of actin filaments that are decorated with tropomyosin. Like capZ, it is found in sarcomeres, where it prevents the depolymerization of actin filaments. It was first isolated from red blood cells [59]. In presence of tropomyosin, it binds the pointed end of F-actin strongly preventing any addition or removal of monomers ($K_D < 1nM$). Without tropomyosin, it becomes a 'leaky' cap that hinders monomer addition and removal but does not block it completely ($K_D = 0.1 - 0.4\,\mu M$). It approximately doubles the critical concentration of the pointed end but has no influence on the barbed end polymerization of actin.

1.2.4 Cross-Linkers and Bundling Proteins

Cross-linkers and bundling proteins interconnect filaments. They have typically two binding sites for the filament and establish mechanically robust links between different filaments. Bundling proteins such as α-actinin, fimbrin, or fascin cluster filaments into tight parallel bundles. Gel-forming cross linkers like filamin favor crossings of filaments, thus generating gel-like networks. In this analysis, the effect of only one cross-linker will be of interest.

α-**Actinins** are single polypeptide chains consisting of a F-actin binding site and a linker region. α-actinin forms homodimers that cluster actin filaments into loosely packed parallel bundles. The linker connects the two subunits and acts as a spacer, keeping actin filaments 30 nm apart, see Figure 1.3 c). This allows the heads of myosin clusters to penetrate the filament bundle where they can interact with the F-actin. This arrangement is found particularly in sarcomeres where the acto-myosin interactions generate contraction forces. α-actinin is also found in the actin cortex and at focal contacts where the cell attaches to the substrate.

The affinity of α-actinin to actin filaments is given by an equilibrium constant of $K = 0.4 - 2.7 \, \mu M$ [60]. Binding is typically fast with rates of the order of $1 \, (s \, \mu M)^{-1}$. The release rates depend on the α-actinin isoform and were determined to range from $0.32 \, s^{-1}$ [61] to $5.2 \, s^{-1}$ [62].

1.2.5 Severing Proteins

Cofilin The actin depolymerizing factor (ADF) or cofilin is an abundant 15 kDa large protein that binds to G- and F-actin [63]. In cells, it is present at a 1:1 stoichiometry with actin monomers. It destabilizes the filament by un-twisting its helical structure, thereby destabilizing the actin- actin interactions. In concert with formin and profilin, it was found to increase the turnover rate of actin filaments *in vitro* by a factor of 25 [64]. In filaments, it binds with a higher affinity to ADP- than to ATP-bound subunits, suggesting that an increase in treadmilling velocity is responsible for the faster turnover.

Cofilin fosters the phosphate release of adjacent subunits in the filament lattice. Due to its ADP-actin specificity, it can form clusters along the filaments. Severing was observed to preferentially occur at the edges of such clusters [65]. The rate of filament severing is further increased by the proteins coronin and aip1.

Katanins are microtubule severing proteins. Katanins are heterodimers that aggregate into rings around the microtubule. They break the 13 longitudinal bonds in the microtubule under consumption of chemical energy via the hydrolysis of ATP. Katanins are localized at the centrosome where they are assumed to be responsible for microtubule release. The release of microtubules is an important step for the spindle formation prior to cell division. Free microtubules were observed to treadmill in the cytosol [5, 66].

1.2.6 Molecular Motors

Molecular motors are proteins which can move directionally along filaments. The movement is connected to the consumption of chemical energy. The function of motor stepping was explained by a brownian ratchet model that relies on the alternating forces the motor feels when cycling through an energy rich and an energy poor state [67]

Myosins are motor proteins that bind to actin filaments. Today, a large number of different myosin motors is known, all of them having a similar characteristic motor domain. Myosins typically move towards the barbed ends of actin filaments, but members of the myosin VI family are known to move towards the pointed ends [27]. The myosin II motor molecules are the force generating components in muscle cells. Each of these motors consists of two long proteins (heavy chains) and four small proteins (light chains). The heavy chains, for their part, consists of a motor head that binds to the actin filament and a long tail region that is responsible for heavy chain dimerization, see Figure 1.3. Myosin II aggregates into thick bipolar bundles that overlap with the actin bundles in sarcomers. When the motors move along the actin filaments, they contract the muscle. As already mentioned, myosins are kinases and their action is coupled to the hydrolysis of ATP molecules. An individual myosin motor can thereby exert forces up to 4 pN [68].

Kinesins are microtubule binding motors that are structurally similar to myosins. They are composed of two heavy chains and two light chains. The heavy chain contains a motor head region that binds to the micotubules and a long tail that fosters dimerisation of the heavy chains and binds to cell organelles. Kinesins typically move towards the microtubule plus end by 'walking' along a single protofilament in a hand-over-hand fashion [69]. Like for myosins, their movement is coupled to the hydrolysis of ATP.

Kinesins organize the transport of vesicles along microtubules and are involved in spindle formation during cell division. Some kinesins were observed to depolymerize microtubules, some of them in a length dependent manner [16]. The kinesins are a member of the kinesin superfamily that comprises ten different families of motor proteins. They all share the motor domain but otherwise vary widely in structure. Some of these kinesin related proteins are known to move towards the minus end of microtubules.

Dyneins also bind to microtubules but move, in contrast to most kinesins, towards the minus end. Together with kinesins they organize the transport of vesicles along the axons of neuronal cells by a 'tug-of-war' mechanism [70–72]. Dyneins play an important role during spindle formation where they are responsible for the formation of spindle poles and

the regulation of spindle length [73, 74]. In contrast to kinesins, dyneins rather stabilize microtubules [75] and evidence was provided that dyneins can also foster the nucleation of microtubules [76].

1.3 Models and Methods

1.3.1 Lattice Models and Stochastic Simulations

In this work, the length dynamics of filaments is studied with help of lattice models. In general, lattice models describe a system on a discrete and regularly arranged set of states. Here, filaments are represented by a one-dimensional lattice in which every lattice site represents a filament subunit. The values associated with the lattice sites represent the subunit state in the filament.

Such lattice models were successfully applied to investigate the dynamics of filament systems in the past, e.g. in [10, 14, 52, 77–81]. The length of the lattice can be fixed [77, 78, 81] or dynamic [10, 52, 79]. These models were formulated for single one-dimensional filaments [52, 77, 79, 81, 82] or several arrays representing interacting filaments [80, 83]. Lattice models for filament systems are in contrast to continuous models which can be applied when the system's behavior is analyzed on length-scales much larger than the constituent filaments [84–86].

The state of the filament is unequivocally given by the length and the sequence of subunit states of the lattice. Every change of the filament length or the state sequence is given by a constant transition rate. Hence, the evolution of the filament can be described by a Markov Chain. For such systems, a Master Equation can be given which describes the evolution of the system in terms of probabilities.

If every monomer can be in either of N states, a filament of length L is in one of N^L possible configurations. In the systems that are to be analyzed, filaments easily reach sizes of several hundred monomers. Even for $N = 2$, it exceeds the capacity of today's commercially available computers to store and process information about the probabilities of all possible microstates. Thus, to analyze the dynamics of such models, one has to resort to stochastic Monte-Carlo methods. In this approach, stochastic realizations of a single instance of the system are determined numerically. Relevant information is then extracted by averaging over an ensemble of such realizations.

The application of stochastic methods is no serious drawback of the presented approach since the major interest lies in characteristic properties of the system rather than the fate of individual microstates. Values of interest are for example the mean filament length or the

typical distribution of monomer states along the filament.
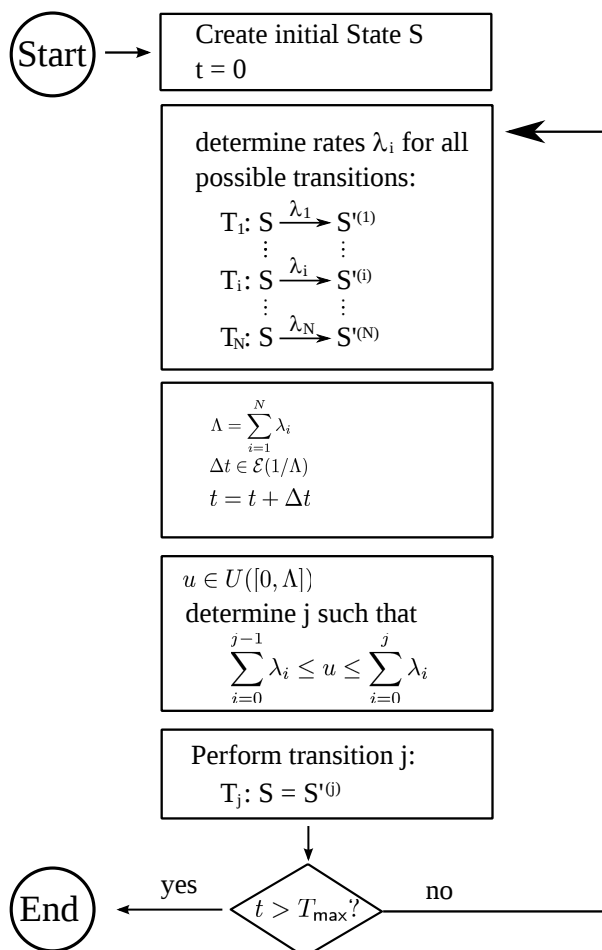
Figure 1.4: Flowchart of a simulation using the Gillespie scheme for well-mixed solutions [87]. $\mathcal{E}(x)$ denotes an exponential distribution of random numbers with average x, $\mathcal{U}([x_1, x_2])$ denotes a uniform distribution on the interval from x_1 to x_2.

In the simulations carried out for this work, the Gillespie scheme was used to update the filament's state [87]. It allows an exact and efficient determination of the system's stochastic evolution, keeping track of the elapsed time. It was first developed for the computation of the dynamics of well-mixed chemical reactions but is easily generalized to more complex situations if a Master Equation can be formulated. Figure 1.3.1 sketches the general idea of the Gillespie algorithm in a flowchart.

Note at this point that stochastic models have to be defined carefully when physical systems are described. To reach an equilibrium state, for example, the reaction rates have to be chosen such that detailed balance is fulfilled. Only then, the system complies with the physical condition of energy conservation. The filaments that are described within the present analysis are constantly driven out of thermodynamic equilibrium and rates are chosen to break detailed balance on purpose. From a physical point of view, it is still important to define the transitions rigorously which provide the energy to drive the system's dynamics.

1.3.2 Analytical Methods

When analytical calculations are carried out, the evolution of system parameters is formulated in the form of rate equations. Such equations connect the time derivative of a state's probability to the probability fluxes through state space. If transition rates only depend on the current state of the system but not on time or the system's history, the dynamics complies with the Markov Condition. The dynamics of the system then constitutes a Markov Chain and can be described by a Master Equation [88–90]. As mentioned above, such systems can be simulated by Monte Carlo methods using the Gillespie algorithm.

In the present work, the filament states as well as their transitions are defined such that they fulfill the Markov Condition. For all these systems, a Master Equation can be formulated but can not be computed in most of the discussed cases. In order to derive analytic expressions, two principal strategies are used: Under certain conditions, Master Equations allow an equivalent description by Fokker-Planck Equations. Therefore, the evolution of the system in the discrete state space is transformed into a partial differential equation in continuous parameters, which might allow a simpler solution. This transformation can be done systematically by the Ω expansion described by VanKampen [89]. The Fokker-Planck Equations are often valid approximations of the system's behavior, even if the conditions under which the exact equivalence is ensured are not met.

Alternatively, the dynamics of averaged values of interest can be formulated in the form of independent rate equations, thereby neglecting the stochastic behavior of the underlying microstates of the system. The formulation of such equations requires particular care and a qualitative understanding of the system's behavior. The results of such approximations are validated by comparison with numeric results.

Wherever appropriate, the random character of the system was considered by taking into account the distributions of the stochastic values. In many situations, however, considering the averages was sufficient to derive valuable expressions.

All analytic calculations are explained in detail to provide the reader with all necessary information to reproduce the results. Numerical results were obtained by implementation in C/C++ (stochastic simulations) or MATLAB™ [1] scripts (fitting and data processing). Symbolic calculations were verified with help of Mathematica™ [2].

---

[1]The MathWorks Inc., Version 7.13 (R2011b)
[2]Wolfram Research, Version 8.0

2 The Treadmilling Phenomenon

2.1 Experimental Background

Biopolymers like actin and microtubules are highly dynamic structures in living cells. They form networks that can reorganize rapidly, providing at a time stability and plasticity to the cell. Under physiological conditions, the growth of both polymer types consumes chemical energy in form of ATP or GTP molecules, respectively. These molecules bind to the monomers and are converted to ADP or GDP within the filament. The affinity of globular actin to an existing filament is higher if bound to ATP than if bound to ADP [7, 30]. After incorporation of an ATP-bound actin monomer into a filament, the rate of ATP-hydrolysis increases by a factor of 40,000 compared to an isolated monomer [91].

Actin filaments and microtubules are both structurally polar with one typically fast growing and the other slowly growing end. The fast ends are referred to as the barbed (actin) or the plus ends (MTs) while the slow ends are called the pointed (actin) or minus ends (MTs), respectively. Both filament types interact with a large variety of other proteins that determine the organization and the mechanical properties of the cytoskeleton. A number of these proteins interfere specifically with the assembly and disassembly of cytoskeletal filaments.

Due to their structural polarity and the dependence of monomer affinity on the nucleotide bound, the assembly and disassembly dynamics of actin filaments differs markedly from "passive" polymers, that is, polymers at equilibrium. One fascinating state of active filaments kept out of thermodynamic equilibrium is treadmilling, in which filaments grow at the one end and shrink at other, see Figure 2.1 for examples.

This mode of polymerization was predicted on theoretical grounds by Wegner in 1976[3], who explained how both ends of actin filaments can start polymerization at different monomer concentrations. In the following, treadmilling was observed for microtubules as well as for actin in living cells [5, 66, 93]. Panda et al. recorded explicitly the filament length distribution of treadmilling microtubules *in vitro* and found that they differ markedly from the exponentially decreasing length distributions of equilibrium polymers [7, 82].

The length of filaments has an important influence on the mechanical properties of the cytoskeleton, see for example Refs. [25, 94, 95]. In addition to the mechanical properties, the
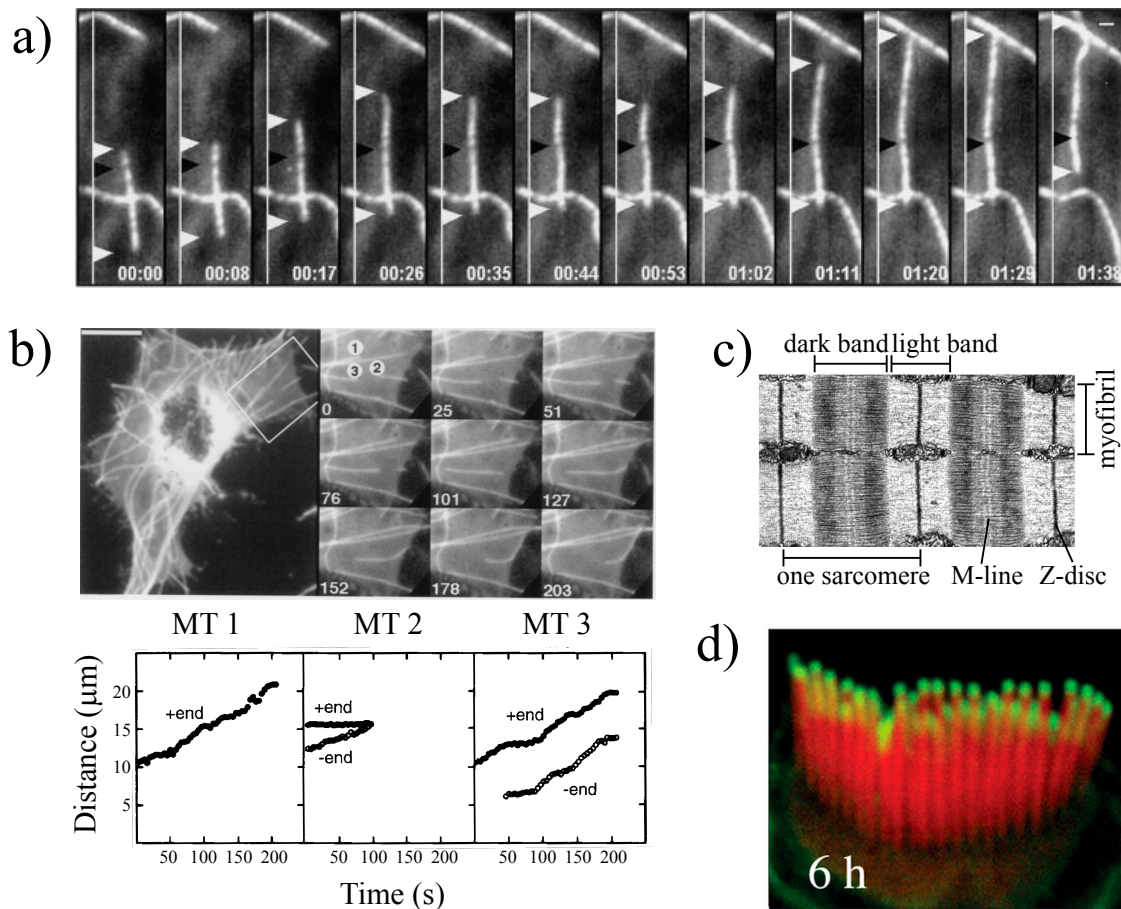
Figure 2.1: Examples of treadmilling filaments. a) Treadmilling microtubule in a living newt lung epithelial cell. From [66]. ©Rockefeller University Press. The filament seems to move from bottom to top while individual monomers remain at fixed positions, as can be confirmed by the dark arrowhead that marks a defect in the fluorescence along the microtubule. b) Images of microtubules within a fragment of a melanophore cell. The microtubule 3 that extends from the cell center detaches and moves towards the cell periphery where it disassembles. It preserves its length during its movement through the cytosol. From [5]. Reprinted with permission from AAAS. c) The sarcomeres of striated muscle cells illustrate how accurately the length of actin filaments is tuned. The light band region is mainly filled with parallel actin filaments, while the dark band consists of myosin filaments. In an even darker region inbetween, actin and myosin filaments overlap. Pointed ends of actin filaments in neighboring sarcomeres are connected to the Z-disc. From [92] ©American Physiological Society.d) Actin bundles in the stereocilia of the inner ear. Green filament parts were polymerized within the last 6 *h* prior to taking the image. Stereocilia length were reported to be constant during the experiment. The accumulation of green monomers at only one end of the filaments suggests that actin is treadmilling within stereocilia. From [93]. ©Rockefeller University Press.

filament lengths also determine directly the size of a number of cellular structures. Prominent examples are filopodia and stereocilia of inner hair cells [93, 96, 97] as well as sarcomeres of striated muscles [98], see Figure 2.1 c) and d). Importantly, in many of these structures most of the filaments have a similar length, such that the ensuing length distribution is unimodal.

A number of mechanisms for regulating cytoskeletal filament length have been investigated in the past. Most of these mechanisms are based on changes of the assembly and/or disassembly rates with filament length. Such changes could, for example, be due to mechanical interactions. Indeed, forces have been observed to affect the polymerization rate of actin filaments [99, 100]. Also the depolymerization rate is affected by mechanical stresses [101] and such effects may play an important role in determining the length of stereocilia [97]. Another way to affect filament assembly rates is through regulatory proteins. For example, capping proteins stabilize barbed ends of actin resulting in longer filaments [102]. The proteins formin or VASP, together with the actin-sequestering protein profilin, have the same effect since they increase the attachment rate of ATP-actin monomers to existing filaments [103].

As long as the regulation of filament assembly and disassembly occurs independently of the filament length, however, the length distribution will in general be exponential. Consequently, non-exponential distributions require regulation of the filament dynamics in a length-dependent manner. This is the case for actin filaments in sarcomeres, where the filament length is set by the protein nebulin through an unknown mechanism [98]. Effectively length dependent depolymerization rates have been demonstrated to act on microtubules through depolymerization induced by the motor protein Kin-8 (Kip3p) [16]. This motor moves directionally towards the plus end, where it induces tubulin removal. The Kin-8-density at the plus end depends on the microtuble length as the rate of motor attachment increases with the length, which ultimately results in an effectively length dependent depolymerization rate and thus to a non-exponential length distribution. In the case of treadmilling filaments, non-motile proteins triggering subunit removal at one end can form a gradient along a filament and thus induce a depolymerization rate that effectively increases with the filament length [14]. Similarly, severing proteins forming a gradient along a filament will generate a non-exponential length distribution [12, 13].

Due to their structural polarity, treadmilling actin filaments establish an intrinsic gradient: the probability of encountering an ATP molecule decreases with the distance from the barbed end [104]. The question is, whether this gradient can lead to a unimodal length distribution. To answer this question, a stochastic lattice model is introduced, similar to others used in studies of filament dynamics [8, 10, 80, 105–108].

The focus of this chapter is to understand under which conditions, linear active polymers show treadmilling. First, a short introduction to equilibrium polymers is given, summarizing

the recent understanding of polymer nucleation and polymerization. Then, active filaments will be analyzed using a two-state model and a random hydrolysis scheme. Stochastic simulations are used to determine the phase diagram and reveal, notably, a phase of unimodal length distribution. In addition, length distributions can be exponential or filaments grow without bound. Analytical calculations of the typical filament length in the unimodal phase and of the corresponding phase boundaries are presented. In the next step, the model is applied to the polymerization dynamics of actin. Since a detailed view on actin was established during the last years, the two-state model is extended to account for these additional insights. Finally, the effects of some accessory proteins on the polymerization dynamics of actin are analyzed within the framework of this model.

In the following the naming convention of microtubules will be adopted and the growing end is called the plus end to illustrate its typically growing character and the shrinking end is called the minus end. This is more intuitive than the names of barbed- and the pointed ends that are used for actin filaments. Nonetheless, the presented principles of filament polymerization can equally be applied to actin filaments as well as to microtubules.

2.2 A Short Introduction to Passive Equilibrium Polymers

Polymers are aggregates of identical subunits, the monomers. This definition of a polymer comprises a large variety of supramolecular structures ranging from chemical polymers in which small molecules are covalently bound to one another, through DNA as a chain of ribonucleinacids and linear protein aggregates like F-actin to viral capsides that form three-dimensional structures. The present analysis is limited to linear aggregates of proteins, which are called filaments in the following.

The aggregates are formed spontaneously in a solution by increasing the chemical free energy of the monomers. This can be the result of a change in pH, ionic strength, or the monomer concentration. Depending on the microscopic structure of the filaments, a nucleation step can precede the agglomeration or self-assembly of the polymers. After polymerization was initiated, the system tends to an equilibrium state described by the degree of polymerization and the filament length distribution. Equilibrium polymers are characterized by monomer addition and removal that satisfy detailed balance, i.e. monomers attach on average as fast as they detach.

The strength of bonds between monomers can differ largely. Many industrial polymers as those in rubber or plastics are linked covalently, resulting in very strong bonds. Such polymers can be able to resist very high temperatures. For example, Teflon™ coatings are stable up to temperatures of 349°C. The rates of spontaneous removal of the monomers from

the filaments are correspondingly small. The binding energy of C-C bonds such as in Teflon is approximately 348kJ/mol [109], leading to a very slow turnover of such filaments in equilibrium. The resulting relaxation times for these polymer solutions into the thermodynamic equilibrium are extremely long and a real equilibrium state will practically never be reached. Their filament length distribution remains 'frozen' [110].

In the case of biological polymers such as actin or microtubules, the bonds are formed by protein-protein interactions which rely on hydrogen-bonds and Van-der-Vaals interactions. The binding energy of actin can be estimated from the polymerization speed of actin against an external force *in vivo* to be ≈10-20 kJ/mol [7, 111]. Thus, the bonds break already at room temperature, rendering these polymers highly dynamic as compared to polymers with covalent bonds. Biopolymers can reach equilibrium at times accessible in experiments. Such dynamic polymers are often referred to as 'living polymers' where the word 'living' rather refers to the rapid and reversible adaption of the filament length to changes in the external conditions [24, 110, 112, 113] than to their appearance in living organisms.

Two important key figures of polymer solutions are the number average and the weight average filament length. The number average is taken relative to the overall number of filaments. Its value gives the average filament size, when it is drawn from the ensemble of all filaments present in the solution. Its formal definition reads

$$\langle L \rangle_n = \sum_{i=1}^{\infty} i \, \mathcal{P}(i),$$

where $\mathcal{P}(i)$ is the probability to find a filament of length i.

The weight average on the other hand considers the mass of the filaments. It answers the question of the average size of the filament in which a randomly chosen monomer is integrated. The weight average is defined as

$$\langle L \rangle_w = \sum_{i=1}^{\infty} i^2 \, \mathcal{P}(i).$$

The number and weight average length of polymer solution are thus the first and second moment of the filament length distribution $\mathcal{P}(i)$. If not indicated otherwise, the average filament length will denote the number average. The weight average then results by its definition from the average filament length and the variance of the length distribution.

The number and weight averages of the filament length play important roles in the determination of the viscous properties of polymer melts or solutions [25]. It was shown that the first and second moment of the length distribution can relax on very different timescales [110].

In the following, I will briefly discuss how passive polymers are formed, how they elongate, and how their filament length distribution equilibrates. The notion of co-polymerization is introduced and it will be explained how different interchangeable versions of monomers can lead to polymers that are constantly kept out of thermodynamic equilibrium.

2.2.1 Nucleation

The *de novo* formation of polymers can proceed in different ways. In general, for the initiation of polymerization, some sort of polymerization seed is needed, to which monomers from the solution can add. In some systems, like the polymerization of tropomyosin [114], every monomer has the potential to serve as a nucleator. In other systems, the number of nuclei is determined by a chemical reactant, e.g. in the case of Poly(α-methylstyrene) [112]. Biopolymers such as actin and microtubules can nucleate spontaneously or as a result of an enzymatic reaction. It was shown that formin or gelsolin are enzymes that foster nucleation of actin filaments. Microtubules grow on nuclei preformed by γ-tubulin rings at the cell center.

Consider a solution in which a chemical nucleator is present at fixed concentration n mixed with polymerizeable monomers of total concentration c_{tot}. Let c_{mon} denote the concentration of free monomers. It can be shown that the concentration of free monomers then follows from the condition

$$n \langle i \rangle = c_{tot} - c_{mon} \tag{2.1}$$

with $\langle i \rangle$ being the average length of a filament. The filament length follows from the equilibrium condition for the polymerization dynamics, see below.

For systems of linear filaments where every monomer can serve as a nucleation site, the description changes slightly [7]. Let the concentration of monomers and nucleation sites be c_1 and the addition rate $\nu_a = r_{on}c_1$. In equilibrium, it follows that

$$c_{tot} = c_1 / \left(1 - Kc_1\right)^2 \quad , \tag{2.2}$$

with equilibrium constant K for monomer binding. An example for such a polymerization scheme is the protein tropomyosin that forms aggregates *in vitro* [7, 114].

Actin, however, is an example for a polymer that displays a different polymerization dynamics. Equation (2.2) predicts a slowly saturating function of the monomer concentration c_1 as a function of c_{tot}, see Figure 2.2, a). When actin polymerization reaches the equilibrium state, it was observed that the concentration of free actin monomers abruptly levels off at a critical value, c_c, independently of the initial amount of monomers in the system. This
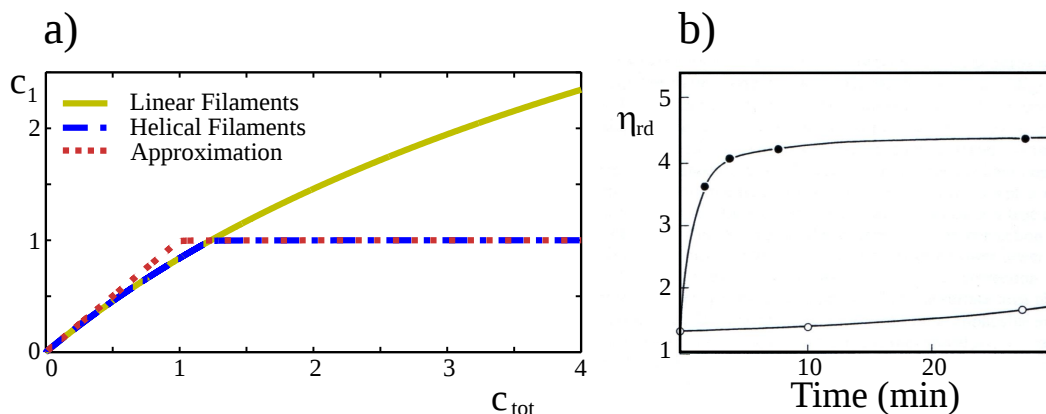
Figure 2.2: Nucleation and polymerization dynamics of actin *in vitro*. a) Equilibrium monomer concentration as a function of total monomer concentration for linear and helical filaments. Parameters are $K = 0.1 mol^{-1}$, $K_h = 1 mol^{-1}$, and $\kappa(K/K_h)^2 = 10^{-6}$. The solid yellow line indicates how monomer concentration increases if polymers are simple linear arrays. The dashed-dotted blue line is solution of Equation (2.3) and shows a sharp kink when the critical concentration of helical filaments is reached. The dashed red line gives the approximation by Equation (2.4). b) The accelerating effect of sonication on the equilibration timescale of actin polymerization. The degree of polymerization is measured by the viscosity of the solution, η_{rd} as a function of time after initiation of polymerization by salts. In one experiment, actin at a concentration of 2.8 mg/ml was polymerized in presence of 0.04 mM ADP ($\circ$). In the other, 1 ml of the solution of the previous experiment ($\circ$) was sonicated after it had reached equilibrium ($\bullet$) and polymerization was observed again. This figure was published in [7] ©Academic Press (1975) .

observation cannot be explained by a linear polymerization scheme as sketched above.

The rapid saturation of the monomer concentration can be explained by the helical structure of actin: Consider a filament that is able to form contacts to more than two neighbors. If the monomer forms lateral contacts to two other monomers in the filament, the minimal nucleus is a trimer, see Figure 2.3. In the parameter regime where filaments spontaneously polymerize, they minimize their free energy by forming as many contacts as possible. Then, the binding to a helical filament allows one monomer to form three contacts at a time, which is more favorable than to bind a linear filament where only one contact is possible. The binding constant K_h for binding a helical filament is thus larger than K for binding a linear filament. Let κ denote the equilibrium constant for the transition of a linear to a helical filament, then the total monomer concentration is connected to the concentration of free
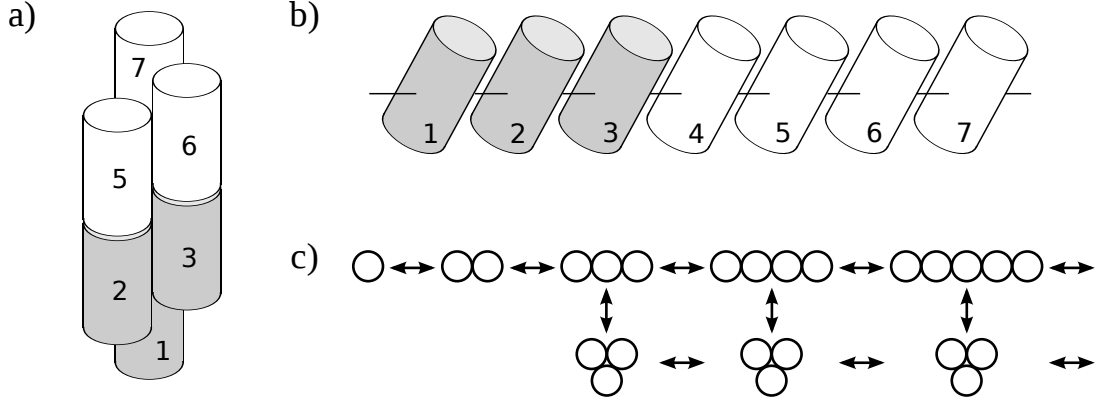
Figure 2.3: Schematic representation of the linear and helical conformation of a linear polymer. a) The helical structure of a filament made from three protofilaments. Monomer number 4 vanishes behind the other monomers; it forms contacts to other monomers instead of only to monomers 3 and 5 as in a linear configuration. b) The linear configuration of the same filament. c) Representation of the possible transitions of filament configurations. The polymers in the lower line have the same number of monomers than in the upper line but are in the helical configuration.

monomers by [7]

$$c_{\text{tot}} = \frac{c_{\text{mon}}}{(1 - Kc_{\text{mon}})^2} + \kappa \left(\frac{K}{K_h} \right) c_{\text{mon}} \left(\frac{1}{(1 - K_h c_{\text{mon}})^2} - 2K_h - 1 \right). \tag{2.3}$$

It follows immediately that the monomer concentration cannot exceed $c_c = K_h^{-1}$. For increasing amounts of c_{tot}, $1 - K_h c_{\text{mon}}$ tends to zero.

If the formation of a helical nucleus and addition of monomers to linear aggregates are energetically unfavorable as compared to the addition of monomers to a helical structure, one has $\kappa \left(K/K_h \right)^2 \ll 1$ and Equation (2.3) is approximated by

$$c_{\text{tot}} = c_{\text{mon}} + \kappa \left(\frac{K}{K_h} \right)^2 \frac{c_1}{(1 - K_h c_{\text{mon}})^2}. \tag{2.4}$$

Typical values for $\kappa(K/K_h)^2$ of helical filaments lie in the order of 10^{-8}. In particular, this is the case for actin where the nucleation rate at $5\mu M$ actin was estimated to be about $10^{-13} M/s$ [32].

Due to the low reaction rate, the nucleation of actin filaments is typically the time limiting step in the polymerization process. This finding is confirmed by experiments on sonicated actin solutions. Under sonication, long acin filaments break, the number of filaments in-

creases, and equilibrium is reached faster, see Figure 2.3, b).

I concentrate in the Chapters 2 and 3 on the case of a single filament in an unlimited reservoir of monomers. *A priori*, this seems to be an artificial situation for two resasons. Firstly, filaments can then in principle grow arbitrarily long without depleting the pool of monomers. These situations are treated as unphysical since they cannot be observed in living cells. The assumption of a constant monomer concentration, however, is not artificial itself since cells constantly replenish the monomer pool by production of the respective proteins. Still, the production of new proteins takes place on much longer timescales as the rapid reactions of the cytoskeleton. Secondly, filaments of length zero are not removed from the solution but rather persist as nuclei to which monomers can be added. Without considering the microscopic details, it is thus assumed that the number of filaments is already equilibrated in these situations. It will be shown later that this assumption is justified in the regime of regulated filament length since then filaments barely shrink to zero length.

2.2.2 polymerization

Once a polymer nucleus is formed, it exchanges monomers with the solution. In dilute solutions, the rate of monomer addition is limited by the diffusion of monomers to the polymer's ends. The polymerization rate ν_a then roughly scales linearly with the monomer concentration, $\nu_a = r_{on} c_{mon}$. The rate at which monomers detach from the polymer, ν_d, is independent of the monomer concentration in the surrounding solution and only depends on the binding energy of the tip monomers to the rest of the polymer, $\nu_d = k_{off}$.

Consider the situation of a fixed concentration n of nucleators. Let c_{mon} be the concentration of free monomers and c_i the number concentration of filaments with a nucleator that has bound a polymer of i subunits. The mass action law then gives for the stationary state

$$c_i = n \left(1 - \frac{\nu_a}{\nu_d} \right) \left(\frac{\nu_a}{\nu_d} \right)^i, \tag{2.5}$$

satisfying $\sum_{i=0}^{\infty} c_i = n$. The concentration of free monomers then follows from the condition

$$\sum_{i=0}^{\infty} i\, c_i = c_{tot} - c_{mon}. \tag{2.6}$$

The average filament length is then given by

$$\langle i \rangle = \frac{Kc_1}{1 - Kc_1} \tag{2.7}$$

with binding constant $K = k_{\text{off}}/r_{\text{on}}$. Together with Equation (2.6) or, equivalently, (2.1), the equilibrium state is fully determined.

In the case of linear polymers, this scheme slightly changes and for the concentration of filaments of length i, c_i follows

$$c_{\text{i}} = K^{-1} \left(Kc_1 \right)^i . \tag{2.8}$$

The concentration of monomers is then connected to the total concentration of subunits in the system by Equation (2.2), given above. For the average filament length follows

$$\langle i \rangle = \frac{1}{1 - Kc_1}. \tag{2.9}$$

For helical polymers, the number of nuclei depends in a non-linear fashion on the monomer concentration. Then, in equilibrium, the length distribution of helical filaments is given by

$$c_i = \kappa (K/K_h)^2 \, K_h^{-1} \left(K_h c_{\text{mon}} \right)^i, \tag{2.10}$$

using the notation introduced in the last paragraph. The average filament length then yields

$$\langle i \rangle = \frac{1}{1 - K_h c_{\text{mon}}}. \tag{2.11}$$

In all three cases, an exponential equilibrium length distribution is found. The only difference lies in the number of filaments which amounts to a different form of the respective normalization constants for the three distributions. The exponential character is a generic result of polymers of identical subunits and originates essentially from the linear increase of the free energy of such polymers.

The polymerization and depolymerization rates are usually not only a function of the monomer concentration but also depend on temperature, pH, ionic conditions and possibly other parameters [7, 115]. When polymerization is initialized by changing the external parameters or providing nucleation factors, the value of the critical concentration drops such that the monomer concentration becomes supercritical. The concentration then relaxes to the new critical concentration reaching a new equilibrium state. The number of filaments also converges to a new equilibrium value, that itself depends on the specific nucleation mechanism [82].

To summarize, the polymerization equilibrium is reached in several steps. After the nucleation, filaments first grow until the equilibrium monomer concentration is reached. Only then, on a longer timescale, monomers are redistributed among filaments until eventually the stationary length distribution is established [7, 110].

Note that the polymerization was assumed here to occur in a dilute solution, where the addition of monomers is diffusion limited and therefore linear in the concentration of monomers. In saturated solutions, however, the monomer addition can be rate limited and the elongation rate saturates at a maximum velocity. One would assume that, similar to enzymatic reactions, the addition rate follows a Michaelis-Menten dynamics,

$$\nu_a = \frac{\nu_a^\infty \, c_{\mathrm{mon}}}{K_{\mathrm{MM}} + c_{\mathrm{mon}}}, \tag{2.12}$$

with maximum binding rate ν_a^∞ and Michaelis-Menten constant K_{MM}. This might be of importance in living cells where monomer concentrations of several hundred μM were measured even though the critical concentration of actin under physiological conditions is rather in the range of a tenth of μM [1].

2.2.3 Polarity

So far, only unpolar polymers were considered, that have the same chemical properties at both ends. A large number of biological examples of polymers, such as single stranded DNA, peptide chains in proteins, and particularly actin and microtubules have a polar structure. Both ends of these filaments are chemically distinct, yielding different rates for subunit addition and removal.

Even though the chemical properties at both ends are different, the energy gain upon polymerization of a single subunit should be independent of whether it was added to one or the other end since the initial and the final state of the system are identical for both reaction ways. Let one filament end be called the 'plus'-, the other one the 'minus'-end with the corresponding addition and removal rates r_{on}^+, r_{on}^-, k_{off}^+, and k_{off}^-. Then, one has

$$\frac{r_{\mathrm{on}}^+ c}{k_{\mathrm{off}}^+} = \mathrm{e}^{(-\Delta G/k_B T)} = \frac{r_{\mathrm{on}}^- c}{k_{\mathrm{off}}^-} \quad , \tag{2.13}$$

with ΔG denoting the energy gain upon polymerization of a single subunit and c the monomer concentration.

Relation (2.13) has an important consequence for the critical monomer concentration c_c above which filaments start to grow. Since the polymerization velocity is a linear function

of the monomer concentration, the filament grows if $c > c_c = k_{\mathrm{off}}/r_{\mathrm{on}}$. As a consequence, the critical concentration of monomers is the same at both filament ends,

$$c_c^+ = c_c^- \quad . \tag{2.14}$$

Thus, at fixed monomer concentration, filaments show the same qualitative behavior, growth or shrinkage, at both ends. The rate constants for monomer addition or removal at both ends can then differ from the values at the other end only by the same factor θ. Without loss of generality, θ can be chosen such that $\theta > 1$ and by convention, the end with the faster dynamics is called the plus end,

$$r_{\mathrm{on}}^+ = \theta r_{\mathrm{on}}^- \tag{2.15}$$
$$k_{\mathrm{off}}^+ = \theta k_{\mathrm{off}}^- \quad . \tag{2.16}$$

The naming convention will become clear from the analysis below. The faster plus end is typically the end at which treadmilling filaments accumulate monomers, while monomers are mainly lost at the minus end.

2.2.4 Activity

Up to this point, our discussion was limited to the polymerization of identical subunits. One important result was the observation that such filaments have the same net behavior at both ends. Treadmilling dynamics, however, cannot be explained by such models. To understand the steady separation of polymerization and depolymerization to the two different ends of actin filaments and microtubules, a more detailed model has to be invoked.

As mentioned in chapter 1, actin and tubulin bind nucleotides of different degrees of phosphorylation. Strictly speaking, the resulting polymer is a co-polymer of the monomers in different states. It was found that the phosphorylation state of the monomers has an impact on the affinity of monomers to the filaments, leading to different critical concentrations of the respective monomer type. Addition and removal of each kind of monomer has thus to be treated separately.

Consider two types of monomers with different binding affinities to the filament. Let them, in allusion to the phosphorylation state of actin and tubulin, be denoted by indices 'T' and 'D'. With varying affinity to the polymer, their respective critical concentrations are different. If the binding energy solely depends on the internal state of the monomer, the free energy of the system is defined only by the number of T- and D-subunits in the solution and in the filamentous part. Their order or whether they were added to the plus or the minus

end has no influence on the energetic state of the system. The change in free energy upon polymerization of a monomer of a specific type is then the same regardless of the end it is added to. It follows

$$c_c^{T+} = c_c^{T-} = c_c^T \qquad \text{and} \qquad c_c^{D+} = c_c^{D-} = c_c^D. \qquad (2.17)$$

The monomer type with a higher affinity to the filament, the 'stable' species, has a lower critical monomer concentration than the 'unstable' species. Let the T-species denote the monomer type of higher filament affinity. The polymerization dynamics is then described by the theory of co-polymers [7, 116, 117]. Depending on whether the individual monomer concentrations are above or below the respective critical values, different compositions of the equilibrium polymers are to be expected. In equilibrium, however, the monomer concentrations can again never exceed their respective critical values.

If monomers can undergo transitions and switch from one state to the other, the situation changes fundamentally. A monomer with high binding affinity can be integrated into the filament where it switches to the state of low affinity, thereby dissipating energy. The energy consumption makes subunits cycle between the monomeric and polymeric state. Equilibrium is only reached when the switching rates are such that they account for the energy difference between both states. If monomers randomly undergo state changes, independent of the states of neighboring subunits, the conditions read

$$\frac{r_{\text{on}}^{\text{T+}}}{r_{\text{on}}^{\text{D+}}} = \frac{r_{\text{on}}^{\text{T-}}}{r_{\text{on}}^{\text{D-}}} \qquad (2.18)$$

and

$$\frac{\omega_{\text{TD}}^{\text{fil}}}{\omega_{\text{DT}}^{\text{fil}}} = \frac{r_{\text{on}}^{\text{D}\pm}}{r_{\text{on}}^{\text{T}\pm}} \frac{\omega_{\text{TD}}^{\text{mon}}}{\omega_{\text{DT}}^{\text{mon}}}, \qquad (2.19)$$

with $\omega_{\text{TD}}^{\text{fil}}$ ($\omega_{\text{DT}}^{\text{fil}}$) and $\omega_{\text{TD}}^{\text{mon}}$ ($\omega_{\text{DT}}^{\text{mon}}$) the rates of subunit state transitions from the T- (D-) to the D-(T-)state in the filamentous and monomeric form, respectively. These conditions reflect that equilibrium is only reached if the state transitions in the monomeric and polymeric part of the solution are equilibrated.

Since the center of mass of a treadmilling filament moves through the cytosol, it is obvious that treadmilling is an intrinsically non-equilibrium effect. It is only possible when the system is constantly kept out of thermodynamic equilibrium, for example by enriching the amount of stable subunits in the solution. An adequate model for treadmilling must therefore include different critical concentrations of at least two different monomer types. The monomer concentrations then have to be adjusted such that the plus end accumulates monomers

while they are lost at the minus end.

The individual rate constants for the addition and removal of actin subunits in all phosphorylation states have been measured *in vitro* [30]. Within the experimental errors, critical concentrations of the different monomer types are indeed independent of the filament end. The deviations could indeed be explained by the the next-neighbor interactions between the filament's subunits. However, the data suggests that these interactions only play a minor role for the attachment and detachment rates.

In the first part of the following analysis, I concentrate on the case that Equations (2.17) are fulfilled and show that the sheer out-of-equilibrium of monomer concentrations can already generate the treadmilling phenomenon. In the following, the system's behavior is studied, using experimentally determined parameters. I use the averaged parameters from the literature which do not exactly comply with Equations (2.17), but may effectively take the subunit interactions into account.

The analysis starts with a model in which two different states of the subunits are considered. It will be shown that this system already shows treadmilling dynamics. Moreover, a regime is found where the length of filaments is regulated resulting in unimodal length distributions instead of the exponential length distribution that are typical for equilibrium polymers. The phase boundaries as well as the average system length in the regime of unimodal filament length distributions are studied in detail. I will give approximations for the average treadmilling velocity as well as an expression of the length dependent depolymerization rate. From these expressions, the typical filament length will be inferred.

Then, the two state model is applied to the polymerization of actin filaments: First to the binding of α- actinin to actin filaments, identifying the two subunit states in the filament with subunits being bound or not to an α-actinin molecule. For this setup the filament length distribution was experimentally determined as a function of time. A second application of the two state model is based on a measurement of the molecular polymerization- and depolymerization rates of actin assuming two different monomer states within the filament. To match the more complex actin-system, the two state model is then extended step by step. It is complemented by a three-state scheme, end-induced phosphate release, and capping of filament tips. The action of profilin, formin, capping proteins, and an increased depolymerization are then considered in turn. In every step, the results of the model were compared with experimentally determined rate constants if possible. This allows us to determine the parameter regions in which unimodal length distributions can be expected.
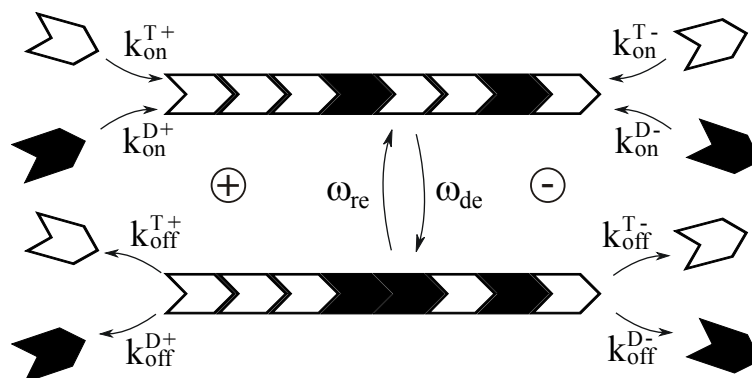
Figure 2.4: A sketch of the two state model. Subunits aggregate into linear arrays of a well defined orientation. White arrowheads stand for T-subunits (stable), while black arrowheads are D-subunits (unstable). Both types of subunits are added to and removed from both filament ends at constant rates. Within the filament, T-subunits are transformed into D-subunits at rate ω_{de} and back at rate ω_{re} within the filament. [23] ©AIP (2013)

2.3 Theoretical Aspects of Treadmilling And Active Polymer Dynamics

In this section, the polymerization dynamics of linear polymers out of thermodynamic equilibrium is investigated by means of a lattice-model, taking into account two different monomer states. The filament is represented as a linear array of variable length L with each site representing one filament subunit, see Fig. 2.4. Sites are indexed such that the site with $i = 1$ corresponds to the plus end, while the site with $i = L$ corresponds to the minus end. Each subunit of the array can be in either of two states, a stable and an unstable one, corresponding to the different phosphorylation state of actin or microtubules. Here, the stable state is associated with a nucleotide-tri-phopsphate bound subunit (the 'T'-state) and the unstable state with binding a nucleotide-di-phosphate (the 'D'-state). Subunits of both states are added to both filament ends at constant rates $k_{\mathrm{on}}^{\mathrm{T}+}$, $k_{\mathrm{on}}^{\mathrm{D}+}$, $k_{\mathrm{on}}^{\mathrm{T}-}$, and $k_{\mathrm{on}}^{\mathrm{D}-}$, respectively. The monomers at the filament tips are removed at rates depending on the subunit's state, $k_{\mathrm{off}}^{\mathrm{T}+}$, $k_{\mathrm{off}}^{\mathrm{D}+}$, $k_{\mathrm{off}}^{\mathrm{T}-}$, and $k_{\mathrm{off}}^{\mathrm{D}-}$.

Subunits within a filament switch between the different states. It is assumed that these events occur at fixed rates and are independent of the states of neighboring subunits. This is the so-called random hydrolysis model, which is supported by several lines of evidence. Early experimental evidence were reported in [118, 119]. Also recent experiments, in which a microfluidic device was used to track the depolymerization of individual actin filaments, strongly argue in favor of the random hydrolysis model [52]. Stable monomers in the filament

can switch spontaneously to the unstable state at rate ω_{de} and back at rate ω_{re}, see Fig. 2.4.

In the following, I concentrate on the steady state properties of the system. Thus, only the case of a fixed monomer concentration is considered. In a dilute solution, the addition rate of T-subunits at the plus end, for example, is a function of the monomer concentration of this type, $k_{\text{on}}^{\text{T}+} = r_{\text{on}}^{\text{T}+} c^T$, with $r_{\text{on}}^{\text{T}+}$ being the proportionality coefficient. This corresponds to experimental conditions in which either the state transitions of the monomeric subunits are much faster than the polymerization and the state dynamics within the filament, or in which a small number of filaments is immersed in a huge reservoir of monomers.

In the simulations, only one filament is considered at a time. When it shrinks to length zero, it is treated as an empty nucleation site to which free monomers can attach and form a new filament. This corresponds to neglecting fluctuations of the filament number in the stationary state. The general case of dynamic nucleation of filaments is treated in Chapter 4. Let me note here that the results do not alter qualitatively.

Stochastic simulations of filament assembly are performed following the Gillespie scheme [87]. The filament is represented as a linear array of variable length with entries '0' or '1', representing the state of the nucleotide ('T' or 'D') that is bound to the respective monomer in the filament. In each simulation step, first, the total rate of changes of the system's state, ω_{tot}, is determined as the sum of all possible transition rates. Then, the time increment until the next event is drawn from an exponential distribution with an average given by $1/\omega_{\text{tot}}$. I used the Mersenne twister as a random number generator [120] throughout all numerical analyses. A second random number is drawn from a uniform distribution to determine the microscopic transition that has occurred.

Simulations start with a filament of length zero. The system is then evolved for 10^6s simulated time to suppress any transients. The state of the system is sampled at intervals of length t_{samp}. The value of t_{samp} needs to be large enough to avoid correlations between two successive samples. If not indicated otherwise, a time-step of $t_{\text{samp}} = 5/\omega_{\text{PD}}$ was chosen, since ω_{PD} is usually the smallest non-zero rate that was used. The shown results were determined from an ensemble of at least 10^6 samples.

Under which conditions can the filament be expected to display treadmilling dynamics? First, the stable type of monomers has to polymerize into filaments, that is $k_{\text{on}}^{\text{T}+}/k_{\text{off}}^{\text{T}+} = k_{\text{on}}^{\text{D}+}/k_{\text{off}}^{\text{D}+} > 1$. At the same time, the unstable type is preferentially in the monomeric form, $k_{\text{on}}^{\text{D}+}/k_{\text{off}}^{\text{D}+} = k_{\text{on}}^{\text{D}-}/k_{\text{off}}^{\text{D}-} < 1$. Beyond that, the plus end needs to display a net polymerization, which can be ensured if free T-monomers are added more rapidly than the tip monomer switches to the D-state, $k_{\text{on}}^{\text{T}+} \gg \omega_{\text{de}}$. At the minus end, T-monomers have to polymerize much slower such that the switching to D-state occurs at a significant rate, $k_{\text{on}}^{\text{T}-} \lesssim \omega_{\text{de}}$. Only then, monomers can effectively be removed from the minus end. This reasoning already
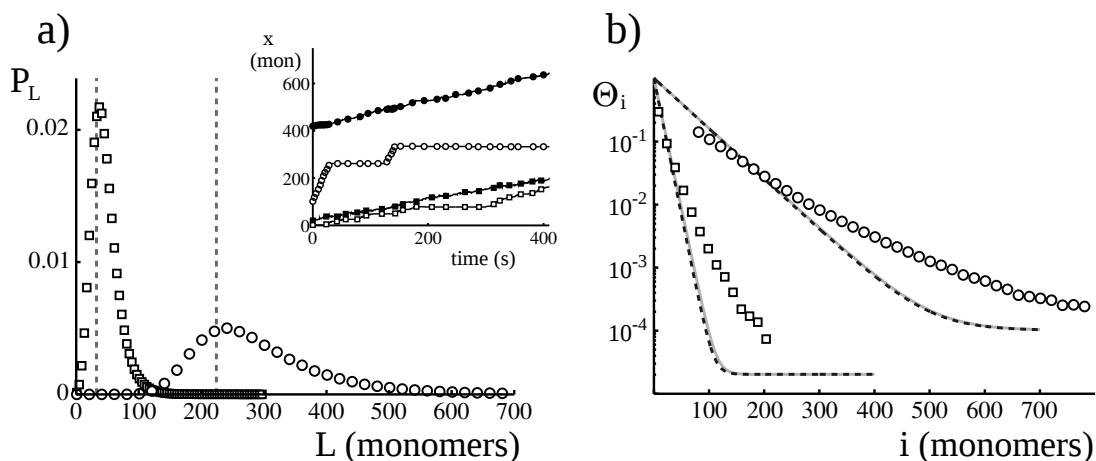
Figure 2.5: Examples for treadmilling filaments. a) Stationary filament length distributions with rates, taken from Table 2.1. For both parameter sets, unimodal filament length distributions are found. The dashed lines give the respective typical filament length L_{typ} as determined by Equation (2.50). The inset illustrates the treadmilling dynamics of the filaments. In both cases, the filaments elongate constantly at the plus end (closed symbols) while monomers are lost at the minus end (empty symbols), thereby moving through space. b) The local probability to find a T-subunit, Θ_i at position i along the filament. Symbols were obtained by averaging over all filaments having at least length i. The dashed line gives the gradient as determined from the delta-approximation, the solid line follows from the Poisson-approximation, see text. [23] ©AIP (2013)

suggests that the probability to find a T-monomer at the plus end should be larger than the probability to find one at the minus end.

Figure 2.5 a) presents two examples of simulations that resulted in constantly treadmilling filaments. The inset of the figure shows how plus and minus end of the filament steadily move into the direction of the plus end. The filament length distribution is clearly unimodal in both cases and therefore differs strongly from the exponential form of equilibrium polymers. In Figure 2.5 b), the distribution of T-monomers along the filament, Θ_i, is displayed, showing clearly that these monomers accumulate at the filament's plus end. This gradient generates a length-dependent depolymerization rate that is responsible for the unimodal length distribution of filaments.

According to the basic assumption that the attachment and detachment rates are essentially determined by the state of the monomer, the equilibrium constants were chosen to be

Rates	Figure 2.5 squares	Figure 2.5 circles	Figure 2.11	Ref. [29]	Figure 2.14 squares	Figure 2.14 circles
k_{on}^{T+}	1	0.8	$k_{off}^{T+} \cdot c^T$	$7.4 \cdot c^T$	0.962	1.036
k_{on}^{D+}	10^{-5}	10^{-5}	$4 \cdot 10^{-5} \cdot c^T$	$3.8 \cdot c^D$	0	0
k_{on}^{T-}	0.01	0.008	$0.01 \cdot k_{off}^{T+} \cdot c^T$	$0.56 \cdot c^T$	0.0728	0.0784
k_{on}^{D-}	$2 \cdot 10^{-5}$	$2 \cdot 10^{-5}$	$8 \cdot 10^{-5} \cdot c^T$	$0.16 \cdot c^D$	0	0
k_{off}^{T+}	0.5	0.25	*variable*	0.9	0.9	0.9
k_{off}^{D+}	0.5	2.5	40	1.5	1.5	1.5
k_{off}^{T-}	0.005	0.0025	$0.01 \cdot k_{off}^{T+}$	0.19	0.19	0.19
k_{off}^{D-}	1	5	80	0.26	0.26	0.26
ω_{de}	0.05	0.01	1	0.0068	0.0068	0.0068
ω_{re}	10^{-6}	10^{-6}	0	0	0	0
c^T			*variable*		$0.13 \mu M$	$0.14 \mu M$
c^D					$0 \mu M$	$0 \mu M$

Table 2.1: Values of the rate constants used for the two-state model in this section. The values in the first two columns are examples that comply with Equations (2.20) and (2.21). The rates in the third column were measured by Kuhn and Pollard for actin *in vitro* [29]. In these experiments, the ATP-G-actin concentrations remain free parameters of the model. The rate for ω_{de} was determined in an independent experiment [52], the rate ω_{re} was assigned. All rate constants are given in s^{-1}.

the same for both filament ends, that is,

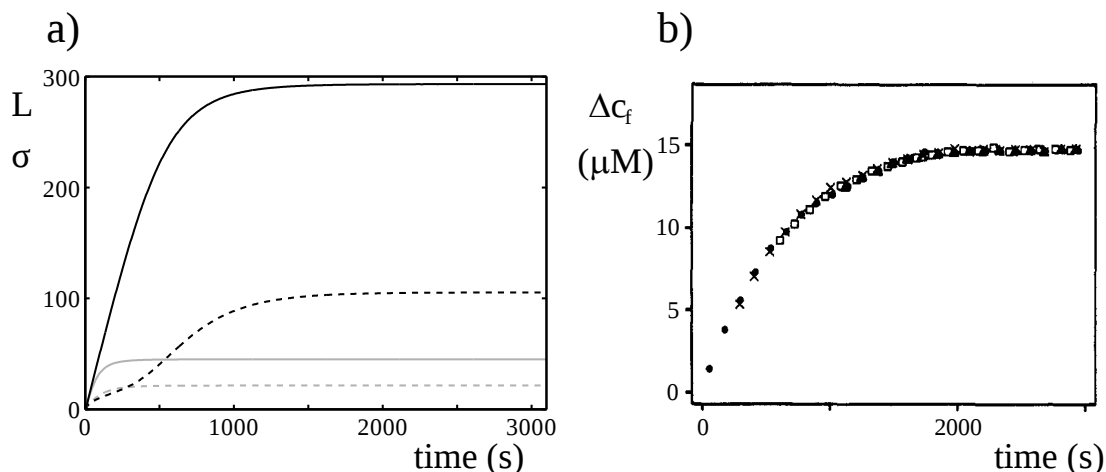$$\frac{k_{on}^{T+}}{k_{off}^{T+}} = \frac{k_{on}^{T-}}{k_{off}^{T-}} \tag{2.20}$$

and

$$\frac{k_{on}^{D+}}{k_{off}^{D+}} = \frac{k_{on}^{D-}}{k_{off}^{D-}} \quad . \tag{2.21}$$

Note that Equations (2.20) and (2.21) are equivalent to conditions (2.17). As a consequence, unimodal length distributions can emerge also in the absence of cooperative effects during monomer binding and/or unbinding.

Figure 2.6: The average filament length and the standard deviation of the distribution as a function of simulated time. a) Results of simulations with parameters are as in Figure 2.5. Solid lines represent the average filament length, the dashed lines the standard deviation of the distribution. The fact that the standard deviation is much smaller than the average length is an indicator of unimodal length distributions. b) The average degree of polymerization for various concentrations of ATP-actin nucleated by 4 μM polymeric ATP-actin. Δc_f is the increase of the concentration of polymeric actin. Initial concentrations of monomeric actin were 4 μM ($\triangle$), 8 μM ($\square$), 12 μM ($\times$), and 16 μM ($\bullet$). The starting points were arranged so that a superimposition of the curves were achieved. Subfigure b): Reprinted with permission from [121]. ©1986 American Chemical Society.

2.3.1 Relaxation of the Distribution's First and Second Moment

At this point let me briefly describe how the average and the standard deviation of the filament length distribution approache their stationary values. Figure 2.6 displays both values as a function of simulated time for the two parameter sets that were already used in Figure 2.5. Initially, the average filament length grows linearly with time and saturates when it approaches its stationary value. The standard deviation of the length distribution shows a more complex behavior. After an initial slow increase, it speeds up at intermediate times before it eventually saturates.

The time course of the average filament length is reminiscent of what was found for the polymerization of actin [121–123]. Note, however, that for Figure 2.6, the time average of a single isolated filament was recorded. It will be shown in Chapter 4, that the time course of polymerization remains qualitatively the same when an ensemble of filaments in a finite reservoir of monomers is considered.

The unimodal form of the distributions can already be appreciated by the observation that

in stationary state, the average filament length is much larger than the standard deviation σ of the distribution. For exponential distributions like the one given by Equation (2.5), one expects σ to be of the same order as $\langle L \rangle$, since

$$\sigma = \sqrt{\langle L \rangle \left(1 + \langle L \rangle\right)} \xrightarrow{\langle L \rangle \gg 1} \langle L \rangle. \tag{2.22}$$

In both cases, the distribution is reasonably close to the stationary state after $10/\omega_{\mathrm{de}}$. To avoid transients, it should therefore be appropriate to wait for 10^6 simulated seconds before taking samples even if the rate ω_{de} is as low as $10^{-4}s^{-1}$. In the following, only the steady state will be investigated.

2.3.2 Shape of the Distribution and Quality of Length Regulation

From a semi-log plot of the length distribution, it becomes obvious that the length distribution consists of a Gaussian and an exponential part, see Fig. 2.7, a). The shape can come about as the result of a convolution of a Gaussian with an exponential function. In fact, the distribution is well approximated by

$$\mathcal{P}(x) = \mathcal{N} e^{-x/\lambda} \int\limits_{-\infty}^{x} dx' e^{x'/\lambda - (x'-\mu)^2/2\sigma^2} \quad , \tag{2.23}$$

see Fig. 2.7 a). Here, $\mathcal{N}$ is a normalization constant such that $\int_0^\infty \mathcal{P}(x)dx = 1$.

Such a distribution emerges, for example, for the sum of two independent random variables with an exponential and a Gaussian distribution, respectively. Let $u \geq 0$ be a random variable with a probability density $\mathcal{P}_u(u) = e^{-u/\lambda}/\lambda$. Furthermore, let $v \in \mathbb{R}$ be a Gaussian random variable independent of u with distribution $\mathcal{P}_v(v) = e^{-(v-\mu)^2/2\sigma^2}/\sqrt{2\pi}\sigma$, where λ, μ, and σ being positive constants. Then, the probability distribution of the variable $x = u + v$ is given by the convolution of $\mathcal{P}_u$ and $\mathcal{P}_v$:

$$\mathcal{P}(x) = \frac{1}{\sqrt{2\pi}\sigma\lambda} \int\limits_{-\infty}^{\infty} dv \int\limits_{0}^{\infty} du \, e^{-u/\lambda} e^{-(v-\mu)^2/2\sigma^2} \delta(x - u - v)$$

$$= \frac{e^{-x/\lambda}}{\sqrt{2\pi}\sigma\lambda} \int\limits_{-\infty}^{x} dv \, e^{v/\lambda} \, e^{-(v-\mu)^2/2\sigma^2} \quad .$$

Note, that since x is identified with the filament length, this expression is only used for
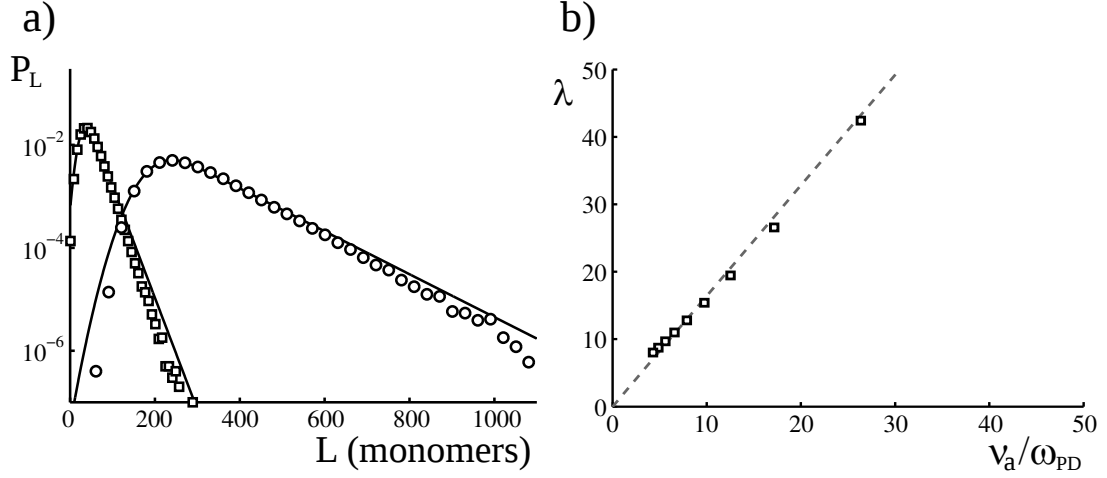
Figure 2.7: The shape of the filament length distributions. a) The filament length distribution as in Figure 2.5 in a semi-logarithmic plot. It is well fitted by a convolution of a gaussian with an exponential part (solid line). b) The fitting parameter λ as a function of typical length excursions before a phosphate release, $\langle \nu_a \rangle / \omega_{de}$. The dashed line is given by $\lambda = 1.64 \langle \nu_a \rangle / \omega_{de}$. Except for ω_{de}, the parameters are as for the circles in Figure 2.5. [23] ©AIP (2013)

$x \geq 0$.

These considerations suggest that the length distribution found numerically above results from two processes acting on different time-scales. All processes involved in the filament dynamics are *a priori* Poissonian. The fast processes among them essentially mix to the Gaussian part of the distribution, while there must be one slow process retaining its exponential characteristics. The slowest relevant processes are transitions between the T- and the D-state, such that λ is expected to be given essentially by the net gain in filament length during the waiting times between phosphate release at the minus end, $\langle \nu_a \rangle / \omega_{de}$. Numerical analysis confirms a strong correlation of λ with this expression, see Fig. 2.7 b). Consequently, for these parameters, whenever a T-subunit is present at the pointed end, it is in general first transformed to a D-subunit before it is eventually removed.

To gain further insight in treadmilling and unimodal filament length distributions, the two-state model is now analyzed in detail. First, the T-state gradient along the filament is determined as a function of the probability Θ_1 of having a T-subunit at the barbed end. Then the average growth rate is expressed in terms of Θ_1 from which Θ_1 can determined self-consistently. Finally, the probability of having a T-subunit at the pointed end is determined from which the average disassembly rate can be deduced. Having access to theses quantities, the typical filament length can be determined by equating the average assembly rate at the barbed end with the length-dependent average disassembly rate at the pointed end.

2.3.3 The Stability Gradient

For treadmilling filaments such as those introduced in Figure 2.5 a), the probability to find a subunit in the T-state is higher near the plus end than at the minus end, as expected, see Figure 2.5 b). In order to estimate how the density of T-subunits relaxes along the filament, a filament that elongates at the plus end with a constant velocity $\langle \nu_a \rangle$ is considered.

After integration into the filament, a monomer changes its state at rates ω_{de} and ω_{re}, respectively. The probability Θ_n of having a T-subunit at lattice site $n \geq 1$ can now be calculated, where $n = 1$ corresponds to the plus end. Recall that the subunits of a filament are assumed to be independent from each other. The probability $\mathcal{P}_T(t)$ to find a subunit in the T-state a time t after its incorporation into the filament thus evolves according to

$$\frac{d}{dt}\mathcal{P}_T = -\omega_{\mathrm{de}}\,\mathcal{P}_T + \omega_{\mathrm{re}}\left(1 - \mathcal{P}_T\right) \quad . \tag{2.24}$$

For a subunit incorporated at time $t = 0$, the initial condition is $\mathcal{P}_T(t = 0) = \Theta_1$. It follows

$$\mathcal{P}_T(t) = \frac{\omega_{\mathrm{re}}}{\omega_{\mathrm{de}} + \omega_{\mathrm{re}}} + \left(\Theta_1 - \frac{\omega_{\mathrm{re}}}{\omega_{\mathrm{de}} + \omega_{\mathrm{re}}}\right)\mathrm{e}^{-(\omega_{\mathrm{de}}+\omega_{\mathrm{re}})t} . \tag{2.25}$$

From the time-dependent probability for a single subunit, the gradient of T-monomers along the filament can be inferred. If $\langle \nu_a \rangle$ denotes the average rate of monomer addition at the plus end, the distance x of a monomer from the plus end at time t after incorporation can roughly be approximated by

$$x = \langle \nu_a \rangle t. \tag{2.26}$$

The probability to find a T-monomer at site n along the filament is thus given by

$$\Theta_n = \mathcal{P}_T((n-1)/\langle \nu_a \rangle). \tag{2.27}$$

From Equation (2.25) one obtains the characteristic length Λ of the exponential gradient,

$$\Lambda = \frac{\langle \nu_a \rangle}{\omega_{\mathrm{de}} + \omega_{\mathrm{re}}} \quad . \tag{2.28}$$

This approximation neglects all stochastic fluctuations in the polymerization of monomers and fluctuations by the state transitions. It will be shown below that assuming a Poissonian addition of monomers to the plus end indeed only changes the gradient of T-subunits marginally. Since the direct correlation of the subunit's age to its distance from the plus end by Equation (2.26) is easier to handle, it is used in the following analysis.

2.3.4 The Plus End

The next step is to determine the average attachment rate at the plus end. It is given by the sum of all attachment rates minus all detachment rates, that is,

$$\langle \nu_a \rangle = k_{\mathrm{on}}^{\mathrm{T+}} + k_{\mathrm{on}}^{\mathrm{D+}} - \Theta_1 k_{\mathrm{off}}^{\mathrm{T+}} - (1 - \Theta_1) k_{\mathrm{off}}^{\mathrm{D+}} \quad . \tag{2.29}$$

To determine the value of Θ_1 its time evolution is considered. Employing a mean-field ansatz to replace the joint probability of finding monomer 1 and 2 in the T-state by $\Theta_1 \Theta_2$, one finds

$$\frac{d}{dt}\Theta_1 = (k_{\mathrm{on}}^{\mathrm{T+}} + \omega_{\mathrm{re}})(1 - \Theta_1) + k_{\mathrm{off}}^{\mathrm{D+}}\Theta_2(1 - \Theta_1) - k_{\mathrm{off}}^{\mathrm{T+}}(1 - \Theta_2)\Theta_1 - (k_{\mathrm{on}}^{\mathrm{D+}} + \omega_{\mathrm{de}})\Theta_1 \quad . \tag{2.30}$$

The first term describes addition of a T-subunit to a D-subunit as well as the transformation of a D-subunit into a T-subunit at the plus end. The second term accounts for removal of a D-subunit from the plus end with the new plus end being a T-subunit. The remaining terms account for the corresponding processes that lead to a loss of a T-subunit at the plus end.

Using

$$\Theta_2 = (1 - e^{-1/\Lambda})\omega_{\mathrm{re}}/(\omega_{\mathrm{de}} + \omega_{\mathrm{re}}) + \Theta_1 e^{-1/\Lambda}, \tag{2.31}$$

see Equation (2.25), the steady state value of Θ_1 can be calculated from Equation (2.30). In the limit of large average subunit addition rate as compared to the rate of state changes, $\Lambda \gg 1$ and $\Theta_1 \approx \Theta_2$. In this case, one gets an explicit expression for Θ_1, namely

$$\Theta_1 = \frac{k_{\mathrm{on}}^{\mathrm{T+}} + \omega_{\mathrm{re}}}{k_{\mathrm{on}}^{\mathrm{T+}} + k_{\mathrm{on}}^{\mathrm{D+}} + \omega_{\mathrm{re}} + \omega_{\mathrm{de}}} \tag{2.32}$$

for $k_{\mathrm{off}}^{\mathrm{D+}} = k_{\mathrm{off}}^{\mathrm{T+}}$ and

$$\Theta_1 = \frac{1}{2}\left[1 - \frac{k_{\mathrm{on}}^{\mathrm{D+}} + k_{\mathrm{on}}^{\mathrm{T+}} + \omega_{\mathrm{re}} + \omega_{\mathrm{de}}}{k_{\mathrm{off}}^{\mathrm{D+}} - k_{\mathrm{off}}^{\mathrm{T+}}} \right.$$
$$\left. + \sqrt{1 + 2\frac{k_{\mathrm{on}}^{\mathrm{T+}} - k_{\mathrm{on}}^{\mathrm{D+}} + \omega_{\mathrm{re}} - \omega_{\mathrm{de}}}{k_{\mathrm{off}}^{\mathrm{D+}} - k_{\mathrm{off}}^{\mathrm{T+}}} + \frac{(k_{\mathrm{on}}^{\mathrm{T+}} + k_{\mathrm{on}}^{\mathrm{D+}} + \omega_{\mathrm{re}} + \omega_{\mathrm{de}})^2}{(k_{\mathrm{off}}^{\mathrm{D+}} - k_{\mathrm{off}}^{\mathrm{T+}})^2}}\right] \tag{2.33}$$

otherwise. By using Equations (2.28) and (2.29), one gets explicit expressions for $\langle \nu_a \rangle$ and Λ.

Figure 2.8 compares the position of the plus end for both examples presented in Figure 2.5 with the expected positions determined by Equations (2.29) and (2.33). In both cases, the analytic results give good estimates of the polymerization velocity. As expected, solving
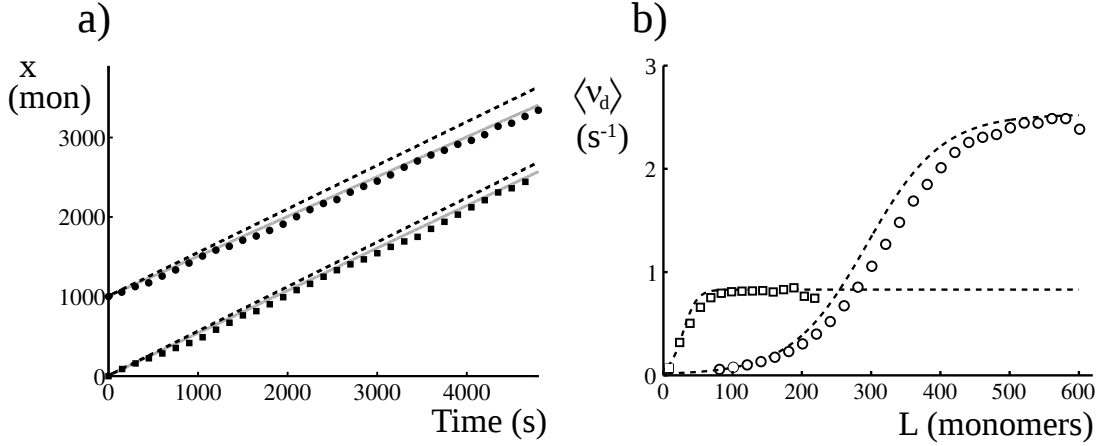
Figure 2.8: Comparison of treadmilling velocities to analytic predicitons. a) The position x of the plus end as a function of time. Symbols are results of stochastic simulations. The dashed black line shows the solution of Equations (2.29) and (2.33), the solid gray line also takes the state of the second monomer into account, see text. b) The average depolymerization rate as a function of the filament length for both distributions shown in Figure 2.5. Symbols represent the results of stochastic simulations. The dashed line follows from Equation (2.40), complemented by the effect of the cap of subunits that polymerize at the minus end. [23] ©AIP (2013)

Equations (2.28), (2.29), (2.30), and (2.31) simultaneously leads to a better approximation.

2.3.5 The Minus End

The calculation of the average detachment rate at the minus end is more involved than the average attachment rate at the plus end. To derive approximate expressions, first the detachment of monomers that have been added to the filament at the plus end is considered. In a second step, the contribution of monomers that have been incorporated at the minus end will be determined.

To calculate the average detachment rate at the minus end of monomers added to the filament at the plus end, the case $k_{\mathrm{on}}^{\mathrm{T}-} = k_{\mathrm{on}}^{\mathrm{D}-} = 0$ is analyzed. Similar to Equation (2.29), their average depolymerization rate $\hat{\nu}_d$ can be written as

$$\hat{\nu}_d = k_{\mathrm{off}}^{\mathrm{D}-} + T_-(L)\left(k_{\mathrm{off}}^{\mathrm{T}-} - k_{\mathrm{off}}^{\mathrm{D}-}\right) \tag{2.34}$$

with T_- being the probability to find a T-subunit at the minus end. In the stationary state, this value is given by [14]

$$\left[\omega_{\mathrm{de}} + k_{\mathrm{off}}^{\mathrm{T}-}(1 - \Theta_{L-1})\right] T_-(L) - \left[\omega_{\mathrm{re}} + k_{\mathrm{off}}^{\mathrm{D}-}\Theta_{L-1}\right](1 - T_-(L)) = 0 \quad . \tag{2.35}$$

This equation reflects that the probability of having a T-subunit at the minus end can change either by nucleotide exchange in the subunit at the tip or by its detachment. Using Equation (2.27) to determine Θ_{L-1}, this equation can be solved for T_-:

$$T_-(L) = \frac{\omega_{\mathrm{re}} + k_{\mathrm{off}}^{\mathrm{D}-}\,\Theta_{L-1}}{\omega_{\mathrm{re}} + \omega_{\mathrm{de}} + k_{\mathrm{off}}^{\mathrm{D}-}\,\Theta_{L-1} + k_{\mathrm{off}}^{\mathrm{T}-}\,(1 - \Theta_{L-1})} \quad . \tag{2.36}$$

Note, that the value of T_- is in general different from the value of Θ_L. This is clearly illustrated by considering the limit of $k_{\mathrm{off}}^{\mathrm{D}-} \to \infty$. In that case, $T_- = 1$ as any D-subunit reaching the minus end is instantly removed, while clearly $\Theta_L < 1$.

The same result can be obtained when considering the fate of the last monomer of the filament. Its state is given by

$$\frac{d}{dt}\begin{pmatrix} p_0 \\ p_1 \end{pmatrix} = \begin{pmatrix} -\omega_{\mathrm{de}} - k_{\mathrm{off}}^{\mathrm{T}-} & \omega_{\mathrm{re}} \\ \omega_{\mathrm{de}} & -\omega_{\mathrm{re}} - k_{\mathrm{off}}^{\mathrm{D}-} \end{pmatrix}\begin{pmatrix} p_0 \\ p_1 \end{pmatrix}, \tag{2.37}$$

with the probabilities $p_0(t)$ and $p_1(t)$ for the monomer to be in the stable or unstable state, respectively. Note that probability conservation for all times only holds if a probability $p_x(t)$ is introduced that accounts for the possibility that the monomer has been removed from the filament prior to time t. Then, $p_0(t) + p_1(t) + p_x(t) = 1$ for all t.

These probabilities are connected to the current filament length L via the initial conditions. The probabilities $p_0(0)$ and $p_1(0)$ are given by the probability to find a T-subunit at the second to last position in the filament at the moment, when the subunit at the tip is removed. The state of the second to last monomer is well approximated by $p_0(0) = \Theta_{L-1}$ and $p_1(0) = 1 - \Theta_{L-1}$.

The rate at which the monomer at the minus end detaches is then given by $-\partial_t(p_0(t) + p_1(t))$ and the average lifetime $\langle \tau \rangle$ of a monomer at the minus end can be determined by using

$$\langle \tau \rangle = \int_0^\infty dt\,(p_0(t) + p_1(t)) \quad . \tag{2.38}$$

The effective depolymerization velocity $\hat{\nu}_d$ then follows since it is nothing else than the inverse of the monomer's lifetime,

$$\hat{\nu}_d = \langle \tau \rangle^{-1} \quad . \tag{2.39}$$

An explicit expression for $\hat{\nu}_d(L)$ is easily derived,

$$\hat{\nu}_d(L) = \frac{(k_{\text{off}}^{\text{D}-} + \omega_{\text{re}})(k_{\text{off}}^{\text{T}-} + \omega_{\text{de}}) - \omega_{\text{de}}\,\omega_{\text{re}}}{\omega_{\text{de}} + \omega_{\text{re}} + \Theta_{L-1}k_{\text{off}}^{\text{D}-} + k_{\text{off}}^{\text{T}-}(1 - \Theta_{L-1})} \tag{2.40}$$

and the result agrees with Equation (2.34) when using Equation (2.36).

Consider now the case that subunits can also be added to the minus end. These subunits form a 'cap' with a distribution of nucleotide states that is distinct from the rest of the filament. The cap can be treated as a factor that transiently inhibits subunit removal at the minus end. If the probability that the minus end carries a cap is α, one obtains the average depolymerization rate $\langle \nu_d \rangle$ from Equation (2.40) by replacing the depolymerization rates $k_{\text{off}}^{\text{D}-}$ and $k_{\text{off}}^{\text{P}-}$ in the calulation above by $k_{\text{off}}^{\text{D}-}(1-\alpha)$ and $k_{\text{off}}^{\text{P}-}(1-\alpha)$, respectively. Such a cap appears at constant rate $k_{\text{on}}^{\text{P}-} + k_{\text{on}}^{\text{D}-}$.

In order to determine the probability α in the stationary state, the problem of filaments with one inert and one dynamic end which is growing and shrinking is considered, see Fig. 2.9 a). The assembly and disassembly rates of the cap are those at the minus end and the subunits can switch between the D- and the T-state at rates ω_{de} and ω_{re}, respectively, as before. The length dynamics of a cap is thus reminiscent of that of microtubuli growing form a nucleating site [107]. In contrast to the full filament system, I find here numerically that the effective subunit attachment and detachment rates are, on average, independent of the cap length. This implies that the length distribution $\mathcal{C}(L)$ is exponential such that $\mathcal{C}(L) = (1-\alpha)\,\alpha^L$.

Simulations of the cap dynamics indeed show that the length distributions $\mathcal{C}(L)$ are exponential, $\mathcal{C}(L) = (1-\alpha)\,\alpha^L$, see Figure 2.10 a). Here, $0 < \alpha < 1$ is the probability of finding a cap with length $L > 0$ and the average cap length $\langle L \rangle$ is obviously $\langle L \rangle = \alpha/(1-\alpha)$. Since the length distribution is exponential, the steady state should be described by effective rates of subunit addition and removal that are independent of the cap length. Consequently, the probability T_- that the tip monomer is in the T-state should be independent of the filament length, implying that the probability of finding a cap with a T-monomer at the tip is αT_-. Furthermore, it was observed in the simulations that the probability $T_{L,i}$ that monomer i of a cap of length L is in the T-state depends exponentially on i: $T_{L,i} = T_-\beta^{L-i}$ for some $0 < \beta < 1$ and $0 < i \leq L$.

Now consider the mean number N of T-monomers in the cap. By definition

$$N = \sum_{L=1}^{\infty} \mathcal{C}(L) \sum_{i=1}^{L} T_{L,i} = \frac{\alpha T_-}{1 - \alpha\beta} \quad . \tag{2.41}$$
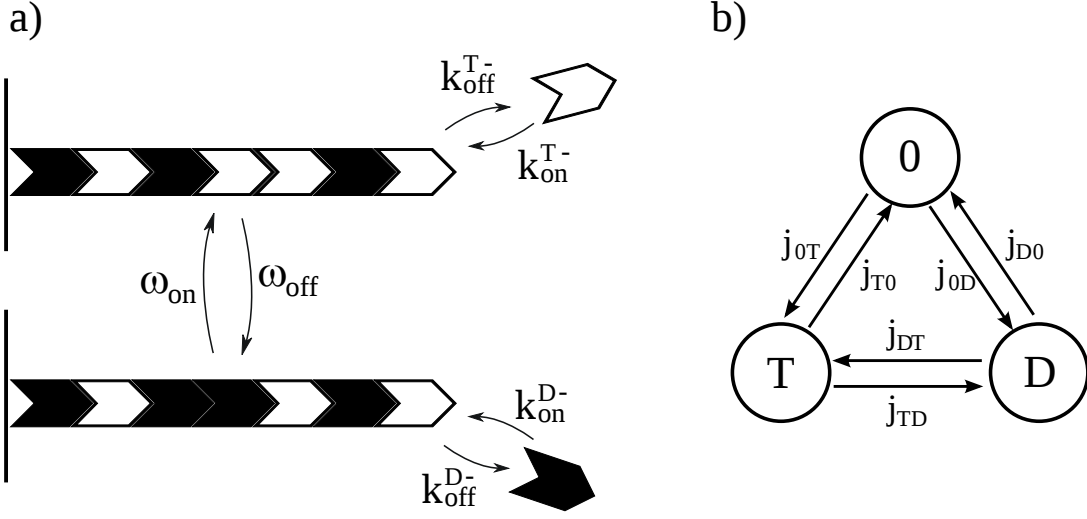
Figure 2.9: The monomer cap at the filament's minus end. a) A sketch of a filament cap with an inert end at the left and an active minus end at the right. Addition, removal, and transition rates are defined as for the two-state model, see Figure 2.4. [23] ©AIP (2013) b) A schematic representation of the definition of the fluxes between the three states of the cap introduced in the text.
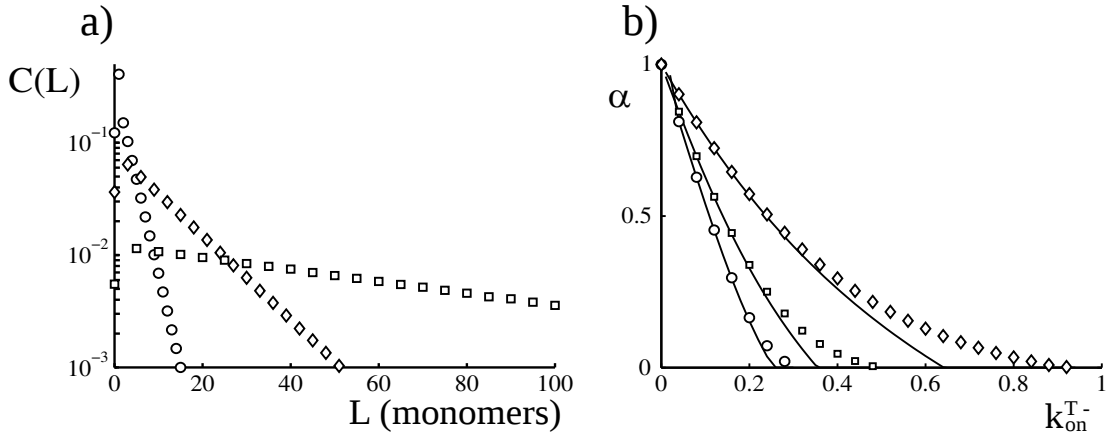
Figure 2.10: Comparison of analytic results and numerical calculations for the capping probability α. a) Three examples of the cap length distribution for $k_{on}^{T-} = 0.15$ (○), 0.22 (◇), and 0.25 (□). Other parameters are $k_{on}^{D-} = 0$, $k_{off}^{T-} = 0.2$, $k_{off}^{D-} = 1$, $\omega_{de} = 0.01$, and $\omega_{re} = 0$. b) The probability α of finding a cap at the filament's minus end as a function of k_{on}^{T-} for three different values of $\omega_{de} = 0.01$ (○), 0.05 (□), and 0.2 (◇). Other parameters $k_{off}^{T-} = 0.2$, $k_{off}^{D-} = 10$, $k_{on}^{D-} = 0$, and $\omega_{re} = 0$. Solid lines are the result of the analytic approximations, see text. [23] ©AIP (2013)

Balancing the binding rate of T-monomers with their unbinding rate, one finds

$$k_{\mathrm{on}}^{\mathrm{T}-} + \omega_{\mathrm{re}}(\langle L \rangle - N) = k_{\mathrm{off}}^{\mathrm{T}-} \alpha T_- + \omega_{\mathrm{de}} N \quad . \tag{2.42}$$

From these two expressions, N can be eliminated and one obtains

$$\alpha T_- = \frac{(1-\alpha)k_{\mathrm{on}}^{\mathrm{T}-} + \alpha \omega_{\mathrm{re}}}{(1-\alpha\beta)k_{\mathrm{off}}^{\mathrm{T}-} + \omega_{\mathrm{de}} + \omega_{\mathrm{re}}} \frac{1 - \alpha\beta}{1 - \alpha} \quad , \tag{2.43}$$

which can be seen as an expression for T_- in terms of α and β. To determine their values, consider the probabilities of a cap with a T- and with a D-monomer at the tip as well as of having no cap, see Figure 2.9. In steady state the probability fluxes into and out of one of these states must balance[1]. Let $j_{0\mathrm{T}}$ denote the probability flux from the no cap situation to one having a cap with a T-state tip and define the other fluxes analogously. Consequently,

$$j_{\mathrm{T}0} - j_{0\mathrm{T}} = j_{0\mathrm{D}} - j_{\mathrm{D}0} \tag{2.44}$$

and

$$j_{\mathrm{T}0} - j_{0\mathrm{T}} = j_{\mathrm{DT}} - j_{\mathrm{TD}} \quad . \tag{2.45}$$

Using

$$\begin{aligned}
j_{0\mathrm{T}} &= (1-\alpha)\, k_{\mathrm{on}}^{\mathrm{T}-} \\
j_{0\mathrm{D}} &= (1-\alpha)\, k_{\mathrm{on}}^{\mathrm{D}-} \\
j_{\mathrm{T}0} &= \alpha T_-(1-\alpha)k_{\mathrm{off}}^{\mathrm{T}-} \\
j_{\mathrm{D}0} &= \alpha(1 - T_-)(1-\alpha)k_{\mathrm{off}}^{\mathrm{D}-} \quad ,
\end{aligned}$$

from Equation (2.44) follows

$$\alpha T_- = \frac{k_{\mathrm{on}}^{\mathrm{D}-} + k_{\mathrm{on}}^{\mathrm{T}-} - \alpha k_{\mathrm{off}}^{\mathrm{D}-}}{k_{\mathrm{off}}^{\mathrm{T}-} - k_{\mathrm{off}}^{\mathrm{D}-}} \quad , \tag{2.46}$$

Replacing αT_- in Equation (2.43) by (2.46), it gives α as a function of β.

The missing condition determining the value of β can be obtained from Equation (2.45). The currents j_{DT} and j_{TD} involve the two-point correlation functions C_{TT} and C_{TD} of monomer $L - 1$ being in the T-state and the tip monomer being in the T- and D-state,

---

[1]In general, these fluxes will not vanish, though, because the system is out of equilibrium.

respectively. Explicitly

$$
\begin{aligned}
j_{\mathrm{TD}}(C_{\mathrm{TT}}) &= \alpha T_-(\omega_{\mathrm{de}} + k_{\mathrm{on}}^{\mathrm{D}-} + k_{\mathrm{off}}^{\mathrm{T}-}\alpha(1 - C_{\mathrm{TT}}/T_-)) \\
j_{\mathrm{DT}}(C_{\mathrm{TD}}) &= \alpha(1 - T_-)(\omega_{\mathrm{re}} + k_{\mathrm{on}}^{\mathrm{T}-} + k_{\mathrm{off}}^{\mathrm{D}-}\alpha C_{\mathrm{TD}}/(1 - T_-)) \quad .
\end{aligned}
$$

Normalization imposes

$$
C_{\mathrm{TT}} + C_{\mathrm{TD}} = \beta T_- \quad . \tag{2.47}
$$

The two-point correlation function can thus be expressed in terms of β, but still one more relation is needed to determine the value of β. One might be inclined to use a mean-field approximation and replace the two-point correlations by a product of probabilities as was done for the plus end. However, in the present case this is not appropriate since the rates ω_{de} and ω_{re} markedly affect the correlation. Instead, consider the ratio between the currents j_{TD} and j_{DT}. Replacing in the respective expression for these currents C_{TT}/T_- and $C_{\mathrm{TD}}/(1-T_-)$ by an averaged correlation ξ with

$$
\xi = \frac{k_{\mathrm{off}}^{\mathrm{D}-}C_{\mathrm{TD}} + k_{\mathrm{off}}^{\mathrm{P}-}C_{\mathrm{TT}}}{k_{\mathrm{off}}^{\mathrm{P}-}T_- + k_{\mathrm{off}}^{\mathrm{D}-}(1 - T_-)} \quad , \tag{2.48}
$$

Numerically, one finds that the value of $j_{\mathrm{TD}}/j_{\mathrm{DT}}$ does not change. This yields the last relation necessary to determine the values of β and thus α:

$$
\frac{j_{\mathrm{TD}}(C_{\mathrm{TT}})}{j_{\mathrm{DT}}(C_{\mathrm{TD}})} = \frac{j_{\mathrm{TD}}(\xi)}{j_{\mathrm{DT}}(\xi)} \quad . \tag{2.49}
$$

Thus, the six Equations (2.43), (2.45), (2.46), (2.47), (2.48), and (2.49) fully determine the system with the six unkowns α, β, T_-, c_{TT}, c_{TD}, and ξ. These equations can be solved simulataneously, thereby determining the fraction of time α a cap is present at the minus end. This calculation provides an excellent approximation for large values of α but decreases in quality when α is small, see Figure 2.10.

In Figure 2.8 b), the inverse of the average time a monomer spends at the pointed end is displayed, that is, the effective depolymerization rate, as a function of the filament length. The numerical results agree nicely with the length dependence that was derived analytically from the gradient of T-monomers, shown in Figure 2.5 b). As anticipated above, the rate increases with the filament length and thus leads to the unimodal length distribution.

2.3.6 Approximative Determination of the Typical Filament Length

Having access to analytic expressions describing the average net polymerization rate, the relaxation length of the T-state gradient along the filament, and the effective depolymerization rate at the minus end as a function of filament length, the typical filament length L_{typ} in the regime of unimodal length distributions can be calculated. In steady state the average polymerization rate $\langle \nu_a \rangle$ must equal the average depolymerization rate $\langle \nu_d \rangle(L)$, such that

$$\langle \nu_a \rangle = \langle \nu_d \rangle(L_{\text{typ}}) \quad . \tag{2.50}$$

Note that $\langle \nu_d \rangle$ monotonically increases with L, because $\langle \nu_d \rangle$ increases with decreasing Θ_L and Θ_L decreases with increasing L. If $\langle \nu_d \rangle(L = 0) < \langle \nu_a \rangle < \langle \nu_d \rangle(L = \infty)$, the above equation implicitly determines a finite typical length L_{typ}. If, however, $\langle \nu_d \rangle(L = 0) > \langle \nu_a \rangle$, then the filaments will disassemble faster than they grow, which will result in an exponential length distribution with typical length $L_{\text{typ}} = 0$. Also, if $\langle \nu_a \rangle > \langle \nu_d \rangle(L = \infty)$, then filaments will grow faster than they shrink and the typical filament length will diverge.

Note furthermore that the solution of Equation (2.50), L_{typ}, coincides with the most probable filament length, that is, the position of the maximum of the length distribution, as can be seen for the two examples shown in Figure 2.5 a). In the case of an exponential length distribution, the typical filament length is thus zero while the filaments have still a well-defined average length $\langle L \rangle > 0$.

In Figure 2.11a) a phase diagram in terms of the average filament length is shown as a function of the concentration c^T of free T-monomers and of the T-subunit detachment rate $k_{\text{off}}^{\text{T}+}$ at the barbed end. Here, it was assumed that the attachment rates, $k_{\text{on}}^{\text{T}+}$ and $k_{\text{on}}^{\text{T}-}$, of T-monomers at the plus and minus ends are proportional to c^T, which is true for dilute solutions. For low depolymerization speeds and low T-subunit concentrations, the filament length is exponentially distributed (blue region). For a higher polymerization rate, the average filament length grows and the distribution becomes unimodal. Further increase of the polymerization activity then leads to diverging filament lengths.

In comparison, Figure 2.11 b) displays the typical filament length derived from Equation (2.50) for the same parameters. The agreement between both plots shows the overall good agreement between stochastic and analytic results, given the number of approximations that were applied.
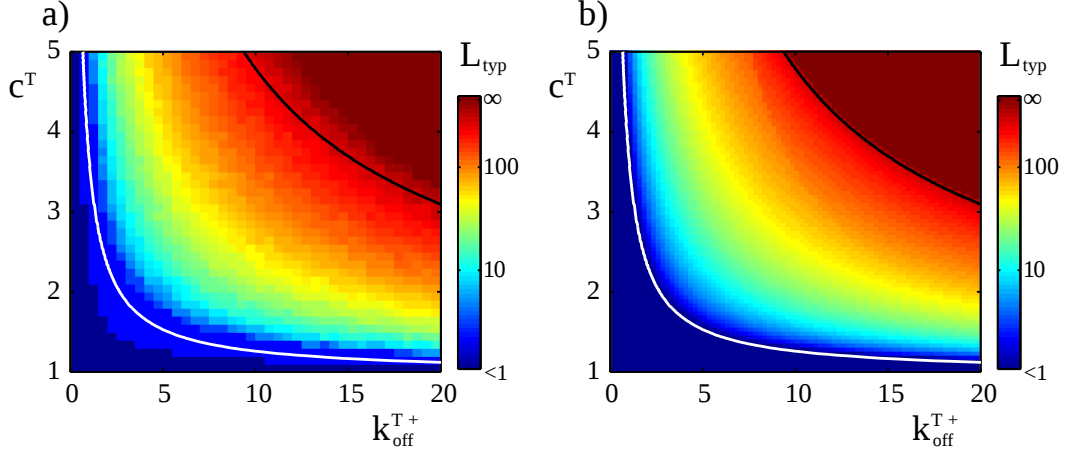
Figure 2.11: The typical filament length L_{typ} as a function of the T-subunit detachment rate $k_{\text{off}}^{\text{T}-}$ and T-monomer concentration c^T. a) Numerical results, b) Approximate typical length according to Equation (2.50). The value of the typical filament length is color coded, blue indicates exponential distributions, $L_{\text{typ}} = 0$, and red a diverging typical length. The white line indicates the approximate boundary between regions of exponential distributions and length regulation, the black line between length regulation and unbounded growth. Parameters are given in Table 2.1. Note that the rates are chosen such that Equations (2.20) and (2.21) hold for all parameters. [23] ©AIP (2013)

2.3.7 Age Distributions of Monomers And Applicability of Delta-Approximation

In the above section, the time a monomer has spend within the filament was directly linked to its distance from the plus end via the average polymerization velocity, see Equation (2.26). Thereby, the fluctuations that arise from the stochasticity of subunit addition were neglected. Let me comment here on why this approximation is applicable for the T-state gradient on the filament.
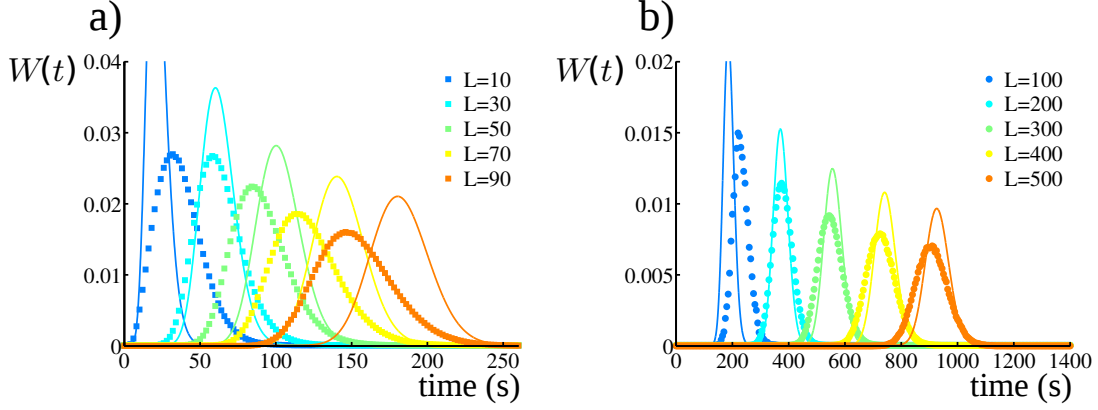
If polymerization occurs with a constant rate, ν_a, it can be described by a Poisson process. The number i of monomers polymerized within a fixed time t is thus a Poisson distributed stochastic variable,

$$\mathcal{P}oiss(i|\nu_a) = \frac{\nu_a^i}{i!}\,\mathrm{e}^{-\nu_a}.$$

Conversely, the age t of a monomer at a fixed distance i from the plus end is distributed following an Erlang-distribution,

$$\mathcal{E}rl(t|\nu_a, i) = \frac{\nu_a^i\, t^{i-1}}{(i-1)!}\,\mathrm{e}^{-\nu_a t} \qquad t \geq 0. \tag{2.51}$$

Figure 2.12: The distribution of monomer age for different filament length for both example parameter sets given in Table 2.1. Symbols represent stochastic results. The age of a monomer at the minus end was recorded immediately after the last monomer was removed. Only subunits that were integrated into the filament at the plus end were taken into account. The solid lines show the Erlang distribution to the parameters ν_a and L for comparison.

Figure 2.12 shows that the age distribution in the filament is indeed well approximated by the Erlang distribution. The deviation of the averages is due to the selective removal of occupied monomers whose appearance correlates with the age of the monomer [124]. Taking the stochasticity of polymerization into account by the Erlang distributed monomer age, the average state of a monomer is given by

$$
\hat{\Theta}_i = \int\limits_{0}^{\infty} dt \, \frac{\nu_a^i \, t^{i-1}}{(i-1)!} \, \mathrm{e}^{-\nu_a t} \, \mathcal{P}_{\mathrm{T}}(t)
$$

$$
= \frac{\omega_{\mathrm{re}}}{\omega_{\mathrm{de}} + \omega_{\mathrm{re}}} + \left(\Theta_1 - \frac{\omega_{\mathrm{re}}}{\omega_{\mathrm{de}} + \omega_{\mathrm{re}}} \right) \frac{\nu_a^i}{\left(\nu_a + \omega_{\mathrm{de}} + \omega_{\mathrm{re}} \right)^i}. \tag{2.52}
$$

The thus obtained T-state gradient is in the following called the 'Poisson-' or the 'Erlang-approximation'.

For the direct correlation (2.26) that was used above, the kernel of the integral in Equation (2.52), is the delta-distribution, $\delta\left(i - \nu_a t\right)$. Therefore, it is called in the present analysis the 'delta-approximation' of the T-state gradient. From Figure 2.5, it can be seen that the difference between the delta- and the Poisson- approximation is negligible. It can in general be expected that the approximation works well as long as $\omega_{\mathrm{de}} + \omega_{\mathrm{re}} \ll \nu_a$, since then

$$
\frac{\nu_a^i}{\left(\nu_a + \omega_{\mathrm{de}} + \omega_{\mathrm{re}} \right)^i} = \mathrm{e}^{-\ln\left(1 + (\omega_{\mathrm{de}} + \omega_{\mathrm{re}})/\nu_a \right) i} \approx \mathrm{e}^{-(\omega_{\mathrm{de}} + \omega_{\mathrm{re}}) i / \nu_a}.
$$

This is also exactly the limit in which long filaments are to be expected. Only if $\Lambda = \langle \nu_a \rangle / (\omega_{\mathrm{de}} + \omega_{\mathrm{re}}) \gg 1$, the gradient stretches over more than only a few monomers and the length dependency of the depolymerization rate varies slowly with filament length. Since the rate of phosphate release from actin monomers in filaments was determined to be much slower than the monomer removal rates, this assumption should be appropriate for the actin polymerization. In the following section, the potential of actin filaments to display intrinsic length regulation is investigated in more detail.

2.4 Application to Actin polymerization

After the two-state model was analysed on a theoretical basis, I now want to investigate the model's implications for experimental findings. The analysis concentrates on experiments that were performed on actin *in vitro*. In a first step, one of the few observed unimodal actin length distributions is studied. Then, the conditions under which unimodal filament length distributions are expected to occur are investigated. Step-by-step, the model is extended to take into account more details of actin polymerization. Eventually, it will become clear that the observation of unimodal filament length distributions is indeed difficult under *in vitro* conditions.

### 2.4.1 The Effect of α-Actinin on the Actin Length Distribution

In this section, the two-state model is applied to an experimental situation in which the cross-linking protein α-actinin was added to a solution of F-actin [14].

Biron and Moses obtained length distributions before and after adding α-actinin to an actin solution [125]. In addition, the solution contained ATP and gelsolin to control the number of actin filaments. The protein α-actinin is found in filopodia and lamellipodia [9, 126], where it acts to bundle actin filaments. A few minutes after adding α-actinin, the initially exponential distribution narrowed and became unimodal[2], see Figure 2.13. While short filaments tended to grow, long filaments shortened. Furthermore, the average filament length decreased, indicating a higher actin turnover rate and an overall destabilizing effect of α-actinin on the actin polymers.

The two-state model is applied to such a situation by identification of the stable state with an empty subunit, while unstable subunits are bound to an α-actinin molecule. Actin filaments are assumed to treadmill by constant addition of empty subunits at the plus end at a rate $k_{\mathrm{on}}^{\mathrm{T}+}$. Initially, subunits are lost at the minus end at rate $k_{\mathrm{off}}^{\mathrm{D}-} > k_{\mathrm{on}}^{\mathrm{T}+}$,

---

[2]Measurements were made on filaments outside bundles.
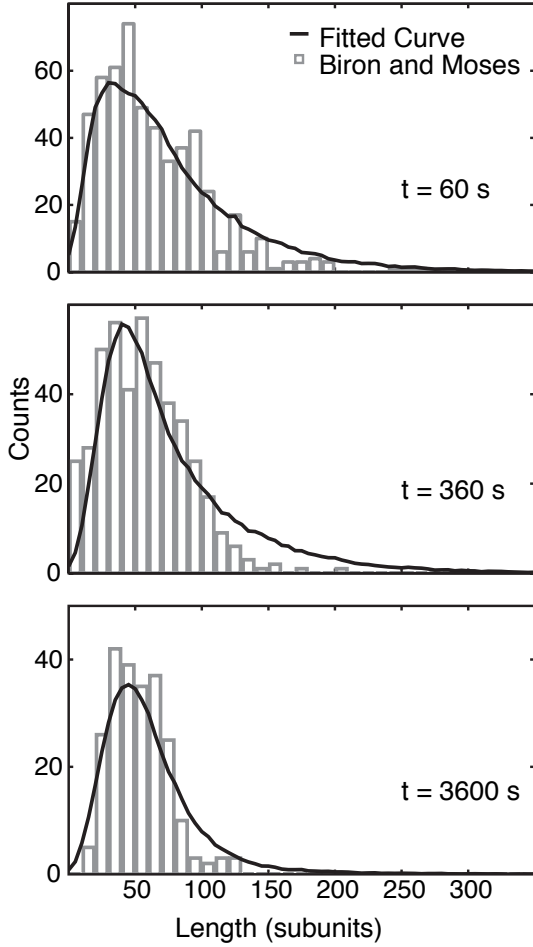
Figure 2.13: The filament length distribution as measured by Biron and Moses [125] at different times after the addition of α-actinin. The solid curve gives the corresponding distributions obtained from the presented model. Parameter values: $k_{\text{on}}^{\text{T+}} = 0.9s^{-1}$, $k_{\text{off}}^{\text{T-}} = 0.64s^{-1}$, $k_{\text{off}}^{\text{D-}} = 1s^{-1}$, $\omega_{\text{de}} = 0.04s^{-1}$, $\omega_{\text{re}} = 0.005s^{-1}$. [14] ©IOP (2009)

leading to a stationary exponential distribution of filament length. When α-actinin is added, the net depolymerization rate increases since α-actinin bound monomers are removed from the minus end at rate $k_{\text{off}}^{\text{D-}}$. Binding and unbinding of α-actinin to and from filament subunits occur at rates ω_{de} and ω_{re}, respectively. For the purpose of this investigation, the removal of subunits at the plus end as well as the addition of subunits at the minus end are neglected, $k_{\text{on}}^{\text{D+}} = k_{\text{off}}^{\text{T+}} = k_{\text{off}}^{\text{D+}} = 0$ and $k_{\text{on}}^{\text{T-}} = k_{\text{on}}^{\text{D-}} = 0$. Thus, $k_{\text{on}}^{\text{T+}}$, $k_{\text{off}}^{\text{T-}}$, and $k_{\text{off}}^{\text{D-}}$ must be considered effective rates. Figure 2.13 shows how the the evolution of the length distribution can be fitted by a single set of parameters for the so modified two-state model.

Usually, α-actinin is not thought to act as a length regulating protein, although some evidence exists, that it participates in the control of actin filament length in striated muscle [127]. Concerning the results of Biron and Moses, explanations have been proposed that rely on minimizing the equilibrium free energy of bundled polymers [128] or on the protective effect of bundles with respect to filament severing [129]. As shown in Figure 2.13, the distributions at different times can also be coherently explained by direct subunit destabilization through binding of α-actinin.

A few remarks on the parameter values that were used are in order. The polymerization velocity $\nu_a = 0.9s^{-1}$ is larger than expected. It corresponds to actin monomer concentrations at which no stationary treadmilling should be obervable, as will be shown below. The

increased density of monomers could, however, be the result of the assumed increase of the depolymerization rate induced by α-actinin. The binding and unbindig rate constants of α-actinin that were employed are somewhat small compared to values obtained from other experiments [130]. This discrepancy indicates that the suggested mechanism of α- actinin increasing the depolymerization rate at the minus end, might not be responsible for the observed changes in the length distribution and should be reconsidered. Notwithstanding, these results show that a mechanism effectively yielding a length dependent depolymerization rate is able to consistently describe the time evolution of the length distribution.

2.4.2 Actin Polymerization Assuming Two Monomer States

The two-state model is also easily applied to actin filaments, making the stability of monomers depend on the state of the bound nucleotide. The rates of subunit attachment and detachment as well as for nucleotide exchange on subunits have been measured in several experiments *in vitro*. The two-state model can now be used to infer the length distribution of actin filaments in such setups. Kuhn and Pollard determined the rates of subunit addition and removal at both filament ends for different phosphorylation states [29]. They measured polymerization and depolymerization velocities in independent assays. The data was fitted to a two- state model, taking into account a stable ATP/ADP-P$_i$ state and an unstable ADP-state of actin subunits in the polymer. The use of two monomer states is based on the observation that ATP bound monomers are more stable within the filament as compared to the ADP-P$_i$ bound monomers. The determined removal rates of the dephosphorylated actin subunits at the pointed end then differ significantly from the phosphorylated form. While ADP-actin depolymerizes at $0.26 s^{-1}$, ATP/ADP-P$_i$-actin is found to be removed from the minus end at $0.19 s^{-1}$ [29]. Since the rates at which monomers are added to the filament depend on the concentration of free subunits, c^T and c^D remain free parameters of the model.

It is still under debate at which rate the phosphate is released from actin filaments. Under the assumption of random hydrolysis, the measured dephosphorylation rates range from $\omega_{\text{de}} = 0.0026 \, s^{-1}$ [104] to $\omega_{\text{de}} = 0.0068 \, s^{-1}$ [52]. Both values are much smaller than the typical values for polymerization and depolymerization at which treadmilling is to be expected. To be able to compare the various results in this section, a phosphate release rate of $0.0068 \, s^{-1}$ is used throughout. Variations of ω_{de} in the experimentally determined range do not change the results qualitatively. The re-phosphorylation of actin- bound ADP, on the other hand, is negligible and is set to $\omega_{\text{re}} = 0$.

Figure 2.14 a) displays two filament length distributions that were found for different T-monomer concentrations in the solution. Using the parameters presented in Table 2.1, the
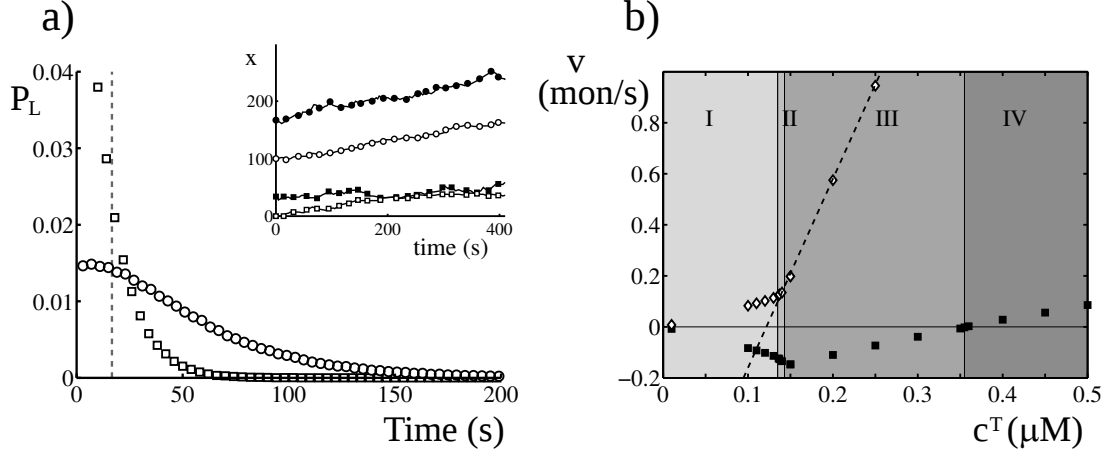
Figure 2.14: Stationary filament length distribution and treadmilling speed for the two-state model. a) Stationary filament length distributions of the two-state model with experimentally determined rates, taken from [29] and [52], see Table 2.1. One parameter set shows the results for $c^T = 0.12$, resulting in exponentially distributed lengths (squares), while the other one shows a peaked distribution for $c^T = 0.14 \mu M$ (circles). In both cases $c^D = 0$. b) Average monomer addition rate of plus (empty diamonds) and minus end (solid squares) as a function of ATP- actin monomer concentration c_T. Positive values indicate filament elongation, negative values monomer loss at the respective end. The dashed line is given by $v = k_{\mathrm{on}}^{\mathrm{T}+} c^T - k_{\mathrm{off}}^{\mathrm{T}+}$, the polymerization speed of a homogeneous filament of T-monomers.

simulations show that the filaments grow on average at the plus end and that they shrink at the minus end, see Figure 2.14 a) inset. When the free monomers in solution are assumed to always be in the T-state, the ensuing filament length distribution is exponential up to a monomer concentration of $c^T = 0.1375 \mu M$. Beyond that point, the distributions cease to be exponential but the average filament length still stays bounded. A shallow maximum in the distribution can be observed until filaments grow unrestrictedly at $c^T = 0.1425 \mu M$. Note that the range of free T-monomer concentrations compatible with filament length regulation becomes smaller if c^D increases. The treadmilling of filaments can be observed independently of the shape of the length distribution.

Let me note that the experimentally determined rates do not comply with conditions (2.20) and (2.21). The reason might lie in neglecting the differences between ATP and ADP-P_i bound monomers. I discuss below that the affinity of the phosphate to the monomer at the filament tip differs also from its affinity to bulk subunits. Neglecting this effect might also add to the experimental error. Both critical concentrations of the T-monomers ($c_c^{T+} = 0.12 \mu M$ and $c_c^{T-} = 0.34 \mu M$), however, are smaller than the critical concentrations of the D-monomers ($c_c^{D+} = 0.39 \mu M$ and $c_c^{D-} = 1.63 \mu M$), indicating that the state of the

monomer still dominates the addition and removal at the filament ends.

In Figure 2.14 b), the dependence of the polymerization velocity on the concentrations of free actin monomers in the buffer is explicitly accounted for. Positive values indicate monomer addition, negative ones monomer loss. By variation of the concentration of free T-subunits, four different regimes are found. In region I and II, filament length stays bounded, either with exponential (region I) or peaked distributions (region II). When the concentration c^T lies in region III, filaments treadmill, but depolymerization at the minus end is not able to fully compensate the polymerization at the plus end. In region IV, filaments grow at both ends.

In region I and II, the growth velocity at the plus and minus end have equal modulus but opposite sign: The same amount of monomers added to the plus end is removed at the minus end, showing that such filaments show a stationary treadmilling dynamics. The ensuing common velocity is called the treadmilling velocity.

Even though filaments show treadmilling in regions I-III, the interesting case of length regulation appears only in region II. As could already be seen in Figure 2.14 a), the distributions in region II are rather broad, such that fluctuations still dominate the average filament length.

The concentration range in which length regulation is possible under *in vitro* conditions is only $5nM$ wide and will hardly be visible in experiments. Already slight fluctuations in monomer concentration can lead to a qualitative change of the filaments' behavior. In the following, more detailed models are analyzed, particularly with regard to the quality and robustness of the mechanism of filament length regulation.

2.4.3 Actin Polymerization Assuming Three Monomer States

The analysis of the two-state model suggests that treadmilling of actin filaments should be observable *in vitro*. Due to the strong fluctuations, the possible intrinsic length regulation on the other hand will be much harder to detect. In this paragraph, the influence of a third monomer state on the length regulation mechanism is studied. As mentioned above, the ATP- as well as the ADP-P_i-bound actin are distinct states in the filament. The hydrolysis rate of the ATP molecules was experimentally determined to be $0.3s^{-1}$ [131]. Since this is comparable to typical monomer addition and removal rates of treadmilling filaments that were found for the two-state model, it can be expected that the hydrolysis also influences the filament dynamics. The two-state model introduced above is complemented by a third subunit state, the 'P-state'. All three subunit types have characteristic addition and removal rates. Transitions within the filament are only allowed from the T- to the P- and from the
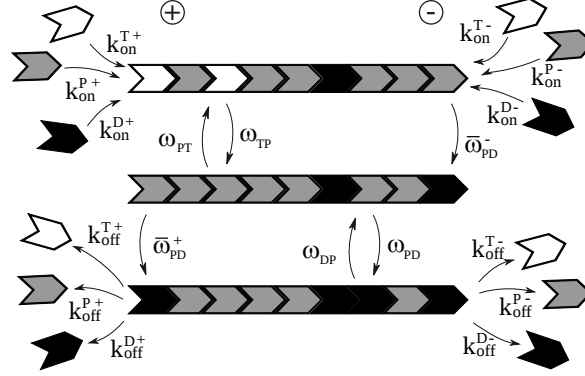
Figure 2.15: A sketch of the three-states model. Monomers of three types are added to and removed from the plus (left) and the minus end (right). White arrowheads stand for T-, gray arrowheads for P-, and black arrowheads for D-subunits. Within the filament, T-monomers are transformed into the P-state at rate ω_{TP} and back at rate ω_{PT}; monomers in the P-state turn into D-states at rate ω_{PD} and back at rate ω_{DP}. At filament ends, the transition of the P- to the D-state is faster and occurs at rate $\bar{\omega}_{\mathrm{PD}}^{+}$ or $\bar{\omega}_{\mathrm{PD}}^{-}$, respectively. The system is fully described by these 18 rates. [23] ©AIP (2013)

P- to the D-state, see Figure 2.15.

The generalization of the calculations in Section 2.3 is straightforward. Let $\mathcal{P}_T$, $\mathcal{P}_P$, and $\mathcal{P}_D$ be the time dependent probabilities for a monomer in the filament to be in the T-, the P-, or the D- state, respectively. Their dynamics is then given by

$$\frac{d}{dt}\begin{pmatrix} \mathcal{P}_T \\ \mathcal{P}_P \\ \mathcal{P}_D \end{pmatrix} = \begin{pmatrix} -\omega_{\mathrm{TP}} & \omega_{\mathrm{PT}} & 0 \\ \omega_{\mathrm{TP}} & -\omega_{\mathrm{PT}}-\omega_{\mathrm{PD}} & \omega_{\mathrm{DP}} \\ 0 & -\omega_{\mathrm{PD}} & -\omega_{\mathrm{DP}} \end{pmatrix}\begin{pmatrix} \mathcal{P}_T \\ \mathcal{P}_P \\ \mathcal{P}_D \end{pmatrix}. \tag{2.53}$$

The state distribution along the filament can be deduced using the delta-approximation to correlate the monomer's age and its position. The polymerization velocity follows from

$$\langle \nu_a \rangle = k_{\mathrm{on}}^{\mathrm{T+}} + k_{\mathrm{on}}^{\mathrm{P+}} + k_{\mathrm{on}}^{\mathrm{D+}} - \Theta_1 k_{\mathrm{off}}^{\mathrm{T+}} - \Delta_1 k_{\mathrm{off}}^{\mathrm{P+}} - \Pi_1 k_{\mathrm{off}}^{\mathrm{D+}}, \tag{2.54}$$

with Θ_i, Π_i, and Δ_i denoting the probability to have a T-, P-, or D-monomer at distance i from the plus end. To determine Θ_1, Δ_1, and Π_1 (and to determine an initial condition for

Equation (2.53)), Equation (2.30) has to be modified:

$$\frac{d}{dt}\Theta_1 = (k_{\text{on}}^{\text{T}+} + \omega_{\text{PT}})(\Delta_1 + \Pi_1) + k_{\text{off}}^{\text{D}+}\Delta_1\Theta_2 - k_{\text{off}}^{\text{T}+}\Theta_1(\Delta_2 + \Pi_2) - (k_{\text{on}}^{\text{D}+} + k_{\text{on}}^{\text{P}+} + \omega_{\text{TP}})\Theta_1$$

(2.55)

$$\frac{d}{dt}\Delta_1 = (k_{\text{on}}^{\text{D}+} + \omega_{\text{DP}})(\Theta_1 + \Pi_1) + k_{\text{off}}^{\text{T}+}\Theta_1\Delta_2 - k_{\text{off}}^{\text{D}+}\Delta_1(\Theta_2 + \Pi_2) - (k_{\text{on}}^{\text{T}+} + k_{\text{on}}^{\text{P}+} + \omega_{\text{TP}})\Delta_1.$$

(2.56)

Π_1 then follows from $\Theta_i + \Delta_i + \Pi_i = 1$ for all i. The average lifetime of a monomer at the minus end that was added to the plus end of the filament then follows from

$$\frac{d}{dt}\begin{pmatrix} p_0 \\ p_1 \\ p_2 \end{pmatrix} = \begin{pmatrix} -\omega_{\text{TP}} - k_{\text{off}}^{\text{T}-} & \omega_{\text{PT}} & 0 \\ \omega_{\text{TP}} & -\omega_{\text{PD}} - \omega_{\text{PT}} - k_{\text{off}}^{\text{P}-} & \omega_{\text{DP}} \\ 0 & \omega_{\text{PD}} & -\omega_{\text{DP}} - k_{\text{off}}^{\text{D}-} \end{pmatrix}\begin{pmatrix} p_0 \\ p_1 \\ p_2 \end{pmatrix}, \quad (2.57)$$

instead of Equation (2.37). The determination of the time a cap of minus end polymerized monomers is present is again much more involved. Here, we rely on an independent stochastic computation of the three-state version of the model sketched in Figure 2.9.

Assuming the monomers to be bound to either ATP, ADP-P$_i$, or ADP, Fujiwara and Pollard determined addition and removal rates of monomers in all three states [30]. Figure 2.16 a) shows two stationary filament length distributions for different concentrations of free T-subunits using the parameters of Fujiwara and Pollard listed in Table 2.2. For both parameter sets, filaments display treadmilling while only for one, filament length is regulated. Figure 2.16, b) displays the probabilities for having a T, P-, or D-states at position i in the filament. The amount of T-subunits drops rapidly with increasing distance from the plus end. At intermediate distances, the P-state dominates and drops slowly towards the minus end where the D-state monomers accumulate.

The numerically determined gradients only agree poorly with the values estimated from the analytic calculations. One reason might be the very low polymerization velocity of about 0.06 monomers per second. At such low addition rates, the fluctuations of filament length become important and it is not sufficient anymore to only take into account the states of the first two monomers at the plus end [10, 29, 132]. The numeric results suggest that the polymerization rate is twice the value estimated by the analytic approximation.

Similar to the case of the parameter set determined by Kuhn and Pollard, in Figure 2.17 the effective addition and removal velocities at plus and minus ends are shown as a function of the concentration of free T-subunits in solution. The same four phases of polymerization behavior can be observed as in the two-state model. The concentration range in which
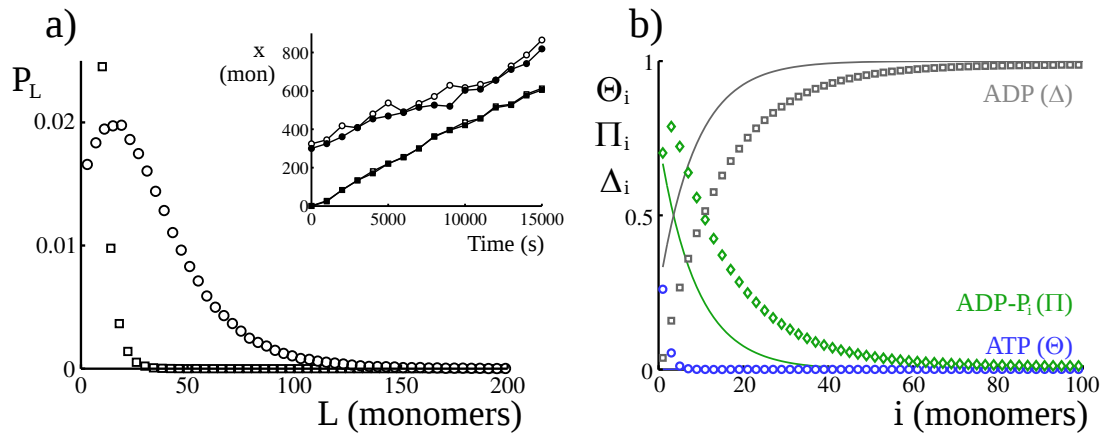
Figure 2.16: Stationary filament length distributions and state gradients in the three-states model. a) Two examples of stationary filament length distributions of the three-states model with rate constants from *in vitro* experiments, see Table 2.2. At $c^T = 0.04\mu M$, the filament length distribution is exponential (squares) but becomes peaked for $c^T = 0.055\mu M$ (circles). In both cases, filaments show treadmilling dynamics (inset). b) Gradients of the three monomer states along the filament for $c^T = 0.055\mu M$. Symbols are results of stochastic simulations, solid lines follow from Equation (2.53). For their calculation, the polymerization velocity was derived from simulations. The characteristic length of the simulated gradient deviates from analytic results roughly by a factor of 2.

Rates	Fig. 2.16 squares	Fig. 2.16 circles	Fig. 2.17	Fig. 2.18 a)	Fig. 2.18 b)	Fig. 2.19 circles	Fig. 2.19 diamonds	Fig. 2.19 squares
$k_{\mathrm{on}}^{\mathrm{T}+}$	0.464	0.638	$11.6^* \cdot c^T$	$11.6^* \cdot c^T$	$11.6^* \cdot c^T$	*variable*	*variable*	*variable*
$k_{\mathrm{on}}^{\mathrm{T}-}$	0.052	0.0715	$1.3^* \cdot c^T$	$1.3^* \cdot c^T$	$1.3^* \cdot c^T$	0.01	0.01	0.01
$k_{\mathrm{on}}^{\mathrm{P}+}$	0	0	$3.4^* \cdot c^P$	$3.4^* \cdot c^P$	$3.4^* \cdot c^P$	0	0	0
$k_{\mathrm{on}}^{\mathrm{P}-}$	0	0	$0.11^* \cdot c^P$	$0.11^* \cdot c^P$	$0.11^* \cdot c^P$	0	0	0
$k_{\mathrm{on}}^{\mathrm{D}+}$	0	0	$2.9^* \cdot c^D$	$2.9^* \cdot c^D$	$2.9^* \cdot c^D$	0	0	0
$k_{\mathrm{on}}^{\mathrm{D}-}$	0	0	$0.09^* \cdot c^D$	$0.09^* \cdot c^D$	$0.09^* \cdot c^D$	0	0	0
$k_{\mathrm{off}}^{\mathrm{T}+}$	1.4^*	1.4^*	1.4^*	1.4^*	1.4^*	1.5	1.5	1.5
$k_{\mathrm{off}}^{\mathrm{T}-}$	0.8^*	0.8^*	0.8^*	0.8^*	0.8^*	0	0	0
$k_{\mathrm{off}}^{\mathrm{P}+}$	$0.16^\dagger$	$0.16^\dagger$	$0.16^\dagger$	$0.16^\dagger$	$0.16^\dagger$	0.2	0.2	0.2
$k_{\mathrm{off}}^{\mathrm{P}-}$	0.02^*	0.02^*	0.02^*	0.02^*	0.02^*	0	0	0
$k_{\mathrm{off}}^{\mathrm{D}+}$	$5.8^\dagger$	$5.8^\dagger$	$5.8^\dagger$	$5.8^\dagger$	$5.8^\dagger$	5	5	5
$k_{\mathrm{off}}^{\mathrm{D}-}$	0.25^*	0.25^*	0.25^*	0.25^*	0.25^*	$10 \cdot k_{\mathrm{on}}^{\mathrm{T}+}$	$10 \cdot k_{\mathrm{on}}^{\mathrm{T}+}$	$10 \cdot k_{\mathrm{on}}^{\mathrm{T}+}$
ω_{TP}	$0.3^\S$	$0.3^\S$	$0.3^\S$	$0.3^\S$	$0.3^\S$	0.3	0.3	0.3
ω_{PD}	$0.0068^\dagger$	$0.0068^\dagger$	$0.0068^\dagger$	$0.0068^\dagger$	$0.0068^\dagger$	0.02	0.02	0.02
ω_{PT}	0	0	0	0	0	0	0	0
ω_{DP}	0	0	0	0	0	0	0	0
$\bar\omega_{\mathrm{PD}}^{-}$					18^*	0	0.1	2
$\bar\omega_{\mathrm{PD}}^{+}$				$1.8^\dagger$	$1.8^\dagger$	0	1	20
c^T	$0.04\mu M$	$0.55\mu M$	*variable*	*variable*	*variable*			
c^P	0	0	0	0	0			
c^D	0	0	0	0	0			

Table 2.2: Parameter values for polymerization and depolymerization of all three types of monomers to plus and minus end as determined by Fujiwara et al., complemented by the hydrolysis and phosphate release rate from independent measurements. The values labeled with $*$ are taken from [52], $\dagger$ are from [30], $\ddagger$ are from [133], and $\S$ are from [131]. All rate constants are given in s^{-1}, all concentrations in μM.
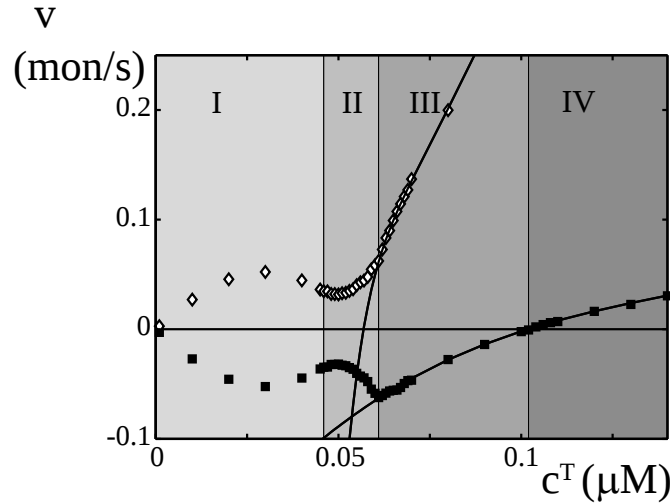
Figure 2.17: Polymerization velocities at both filament ends for the three-states model, employing the monomer addition and removal rates measured by Fujiwara et al.[30]. Symbols show the rates of plus (solid squares) and minus end (open diamonds) of the same filament. The solid lines reproduce the results of the model of Vavylonis et al. [10]. [23] ©AIP (2013)

filament length regulation is possible is again very small and extends from $0.047\mu M$ to $0.062\mu M$ of T-monomers in absence of free P- and D-monomers.

Note that in region I, a regime is found where the treadmilling velocity *decreases* with *increasing* monomer concentration. This behavior is a consequence of the fact that P-monomers have a lower removal rate than T-monomers. In region I, the treadmilling velocity is governed by the depolymerization rate since for exponential length distributions, the filament often consists only of a single monomer that can be removed either from the plus or the minus end. With increasing T-monomer concentration in solution, the average filament length and thus the average lifetime of a monomer within the filament increases. Thereby, also the chance that a T-monomer turns into a P-monomer increases. Since P-monomers are removed at a slower rate than T-monomers, the treadmilling velocity slows down.

For comparison, the velocities of isolated filament ends in a solution of T-subunits is drawn in the same plot. These curves reproduce the results of Vavylonis et al. [10], who investigated the growth dynamics of semi-infinite filaments of ADP-actin in a solution of free ATP-actin monomers. Besides the non- linear behavior of the velocity curves at $v^{\pm} = 0$, they found increasing length fluctuations at this point. It shows that in region III and IV, both filament ends decouple with independent net polymerization speeds. Their length dynamics is then exclusively determined by the addition and removal rates of monomers. The influence of the state gradient then vanishes.

Overall, the treadmilling velocities remain very low. The removal rate of D-monomers from the minus end of $0.25\,s^{-1}$ limits the maximum treadmilling velocity. In most cases, however, the real treadmilling velocity is even smaller since the minus end cannot release plus end polymerized monomers for a considerable amount of time. For the example shown in Figure 2.16, the capping time amounts to 74%, reducing the net monomer release rate to a quarter of the value it would have without monomer addition at the minus end.

2.4.4 Induced Switching at the Filament Ends

Before engaging into an analysis of the potential effects of accessory proteins on the filament length distribution, let me introduce another important property of actin filaments that was uncovered recently. Fujiwara and Pollard reported in 2007 that the inorganic phosphate has a low affinity to the filament ends [30] but were unable to determine the rate of phosphate release. Jégou et al. observed the growth and shrinkage of the plus end of the same filament as monomer concentration was lowered [52]. From these experiments, they were able to deduce the removal rates at the filament's plus end as well as the phosphate release rates at the tip and in the filament bulk. Jégou et al. established that the phosphate release of actin subunits at the filament's plus end is much faster than in the filament bulk.

Figure 2.18 shows how polymerization velocities change when end-induced phosphate release is included into the three-state model. In subplot a), only phosphate release at the plus end is implemented. It leads to an effect that one might call 'reverse treadmilling', since between $c^T = 0.124\mu M$ and $0.131\mu M$, monomers are *added* to the minus and *removed* from the plus end, see inset. Up to $c^T = 0.13\mu M$, filament length is exponentially distributed. Beyond this value, the dynamics of plus and minus end uncouple and filament length diverges.

If phosphate is released from the plus end at a higher rate than in the bulk, there is no fundamental reason, why it should not also have a higher release rate at the minus end. Indeed, Fujiwara and Pollard found that the affinity of the phosphate to the minus end is by a factor of 10 smaller as compared to the plus end. Figure 2.18 b) illustrates the effect of a plus end induced phosphate release rate $\bar{\omega}_{PD}^+ = 10\,\bar{\omega}_{PD}^-$. The region of reversed treadmilling vanishes but the region of filament length regulation does not reappear.

To understand the disappearance of length regulation, note that an ADP-actin molecule at the plus end is dephosphorylated in only $0.6\,s$. At a typical addition rate of 0.2 monomers/s, the monomer at the plus end forms the tip for about $5\,s$. Already after $3\,s$, the ATP bound to the monomer is hydrolyzed and $0.6s$ later, it is dephosphorylated. Consequently, if steady polymerization takes place at the plus end at such slow rates, almost all subunits are bound to an ADP molecule. Since no gradient can be established along the filament, the
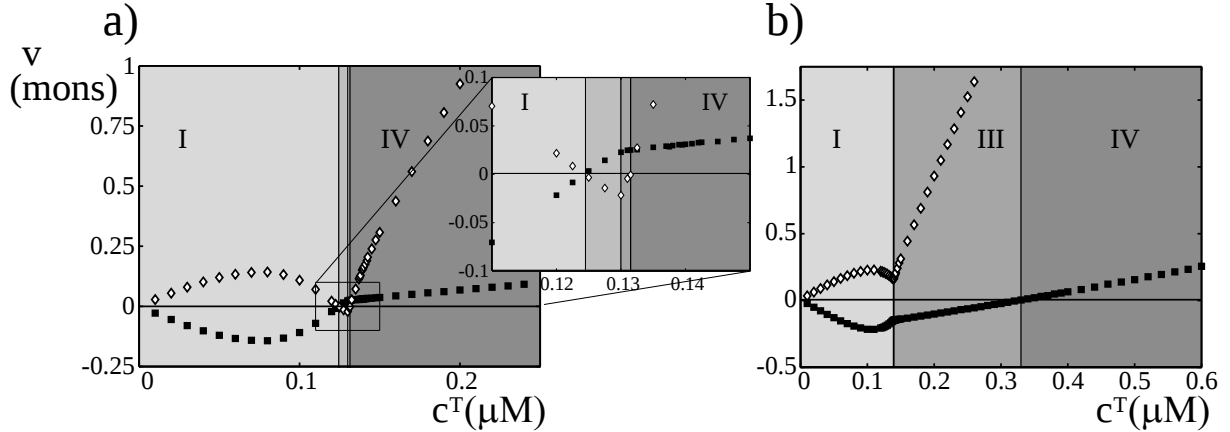
Figure 2.18: The assembly rates at the plus and minus ends as a function of T-actin monomer concentration in the three-states model including induced phosphate release at one or both ends. The end-induced phosphate release is implemented a) only at the plus end or b) at both ends. In both cases, the regime of length control vanishes. For induced phosphate release at the minus end only, actin filaments are expected to accumulate monomers at the minus end and loose them at the plus end for a small range of monomer concentrations, see inset. Parameters are given in Table 2.2. [23] ©AIP (2013)

depolymerization rate is not length-dependent and consequently length cannot be regulated.

Note the overall similarity between Figure 2.14 b) and 2.18 b). In both situations, filament length diverges for T-monomer concentrations above $\sim 0.13 \mu M$ and minus ends start growing at concentrations $c^T \approx 0.35 \mu M$. This suggests that the two-states system that Kuhn et al. investigated behaves similar to a three-states model with end-induced phosphate release.

The analytic expressions above are again easily generalized to account for end-induced phosphate release. If ω_{PD} is replaced by $\omega_{\mathrm{PD}} + \bar{\omega}_{PD}^+$ in Equation (2.56) and by $\omega_{\mathrm{PD}} + \bar{\omega}_{PD}^- (1 - \alpha)$ in Equation (2.57), approximations of the typical filament length can be derived, provided the treadmilling velocity is sufficiently high, see Figure 2.19 a).

In the case that unimodal length distributions are generated, induced phosphate release at the minus end reduces the length fluctuations, see Figure 2.19 b). As stated above, the exponential tail of distributions is dominated by the slow phosphate release of the ATP/ADP-P_i monomers at the minus end. Since phosphate release at the tips now occurs at an increased rate, the gradient and the length fluctuations decouple, potentially leading to long filaments and small fluctuations.

With the inclusion of fast phosphate release at filament ends, a microscopic model for the polymerization of actin filaments is established. The analysis of experimentally determined rates suggests that actin filaments in solution should display treadmilling dynamics. Even
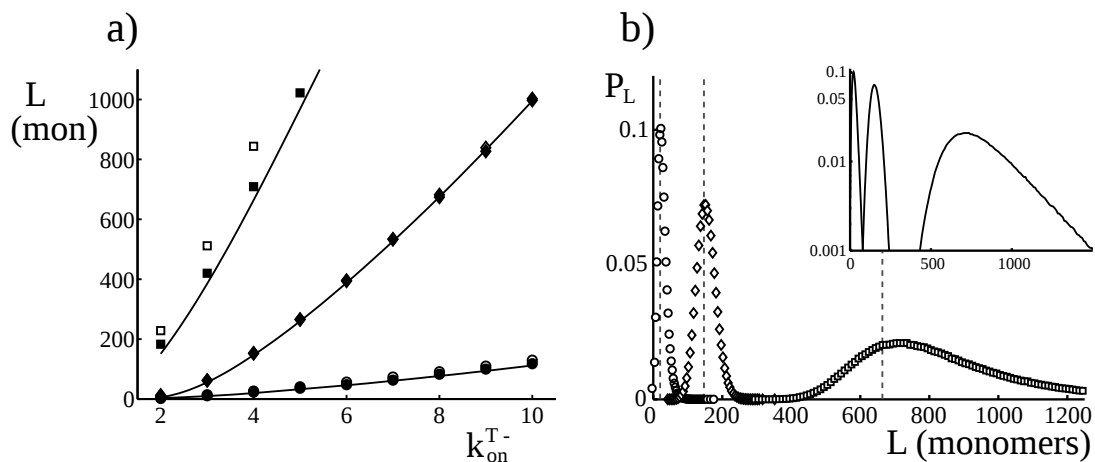
Figure 2.19: Average filament length and filament length distributions for the three-state model with induced phosphate release. a) Comparison of the typical filament length from stochastic (symbols) and analytic (lines) calculations. The average filament length is given by the open symbols, the maximum of the distribution by closed symbols. The analytic expressions agree nicely with the maximum of the distributions. Filament length is smaller with end- induced phosphate release ($\Diamond$ and $\circ$) than without ($\Box$). The asymmetry of the distribution can be deduced from the difference between average and maximum position of the distribution and is in general smaller when end-induced phosphate release is included. Parameters are listed in Table 2.2. b) Expamles of filament length regulation with and without induced phosphate release for $k_{on}^{T+} = 4\,s^{-1}$. Symbols are results of stochastic simulations. The dashed line gives the analytic estimate of the typical filament length, using stochastic results for α. Note that no exponential tail is visible if end- induced phosphate release is included, see inset. Other parameters are the same as for a).

though the same processes that lead to treadmilling provide a mechanism for the intrinsic regulation of filament length, it is not found for parameters that correspond to actin polymerization.

It is well known that in living cells, actin interacts with a number of proteins that have a strong impact its polymerization dynamics. In the remainder of this chapter, the influence of proteins such as profilin, formin, capping proteins, and depolymerizing factors like cofilin are analyzed with respect to the robustness and quality of length regulation.

2.4.5 The Effects of Profilin and Formin

Profilin is a small peptide (12-16kDa) that binds actin monomers. In contrast to the sequestering protein thymosin with which it competes, it only blocks monomer addition to the F-actin's plus ends but allows its growth at the minus ends. While profilin lowers the addition rate to the filament's plus end only slightly (from $11.6 s^{-1}\mu M^{-1}$ to $9 s^{-1}\mu M^{-1}$), it blocks addition to the minus end almost completely [55]. Jégou et al. found that the dephopsphorylation rates at the filament's plus end increases strongly with the amount of profilin in the solution[52].

Consider now a solution in which the actin is in binding equilibrium with profilin at various actin and profilin concentrations. Let c^T denote the concentration of free ATP-actin monomers, c^{Prof} the concentration of free profilin, and c^{dim} the concentration of the actin-profilin dimer. Then

$$c^{\mathrm{Prof}} = \frac{1}{2}\left(c_0^{\mathrm{Prof}} - c_0^T - K_S + \sqrt{(c_0^{\mathrm{Prof}} - c_0^T - K_S)^2 + 4\,K_S\,c^{\mathrm{Prof}}}\right) \qquad (2.58)$$

$$c^T = c_0^T/(1 + c^{\mathrm{Prof}}/K_S) \qquad (2.59)$$

$$c^{\mathrm{dim}} = c^{\mathrm{Prof}}\,c^T/K_S, \qquad (2.60)$$

with initial T-actin concentration c_0^T and profilin concentration c_0^{Prof}. Different values for the equilibrium constant of this reaction can be found in the literature. Experimental measurements give constants ranging from $0.1\mu M$ [9] through $0.4\mu M$ [134] to $2.1\mu M$ [52]. Here, I choose an intermediate value of $K_S = 0.6\mu M$. However, its effect on the phase diagram should be limited since profilin-actin only weakly modulates the addition rate of monomers at the plus end.

The polymerization rate is then given as $k_{\mathrm{on}}^{\mathrm{T+}} = 11.6\,c^T + 9\,c^{\mathrm{dim}}$. Profilin binds P-monomers at the plus end with equilibrium constant $K_P = 5.9\mu M$ and D-monomers with $K_D = 28.1\mu M$ [52]. Applying a Michaelis-Menten dynamics, the depolymerization rate constants read $k_{\mathrm{off}}^{\mathrm{P+}} = 0.16 + (4.7 - 0.16)\,c^{\mathrm{Prof}}/(K_P + c^{\mathrm{Prof}})$ and $k_{\mathrm{off}}^{\mathrm{D+}} = 5.8 + (51.6 - 5.8)\,c^{\mathrm{Prof}}/(K_D + c^{\mathrm{Prof}})$.
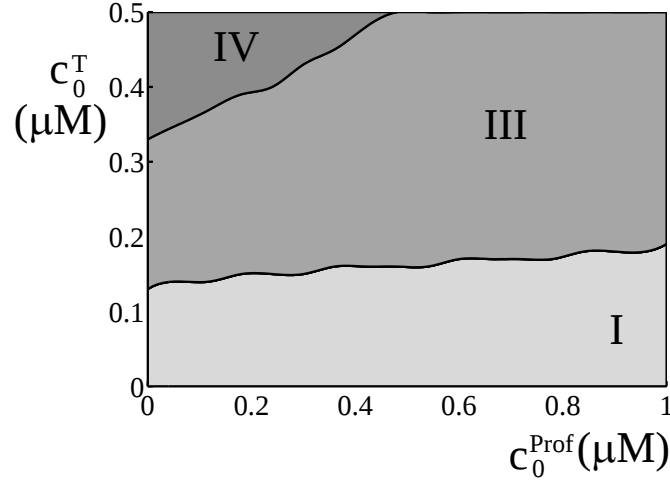
Figure 2.20: The phase diagram for the dynamics of an actin filament in contact to profilin under variation of initial T-monomer and profilin concentrations. The three-states model with induced dephopsphorylation at filament ends was used. No regime of filament length regulation (region II) is found.

The phosphate release occurs at a rate $\bar{\omega}_{PD}^+ = 1.8 + (6.1 - 1.8) * c^{\text{Prof}}/(K_P + c^{\text{Prof}})$.

Profilin binds to the face of the actin monomer that forms contact to the filament's minus end. The profilin- actin dimer can thus not contribute to monomer addition to the minus end [27, 51]. I assume that the removal rates at the minus ends are also not influenced by the presence of profilin. It was shown that profilin has no impact on the hydrolysis of ATP on filamentous actin [131]. Its small effect on the phosphate release was not significant at the experimental error and is completely neglected here. The resultant parameters are listed in Table 2.3.

Figure 2.20 shows that an increasing amount of profilin shifts the onset of filament growth at the minus end to higher initial actin concentration. This behavior was expected since only free T-sbunits can add to the minus end and c^T decreases with increasing c_0^{Prof} at constant c_0^T. However, in the regime of investigated concentrations, profilin alone doesn't appear to have any influence on the emergence of filament length regulation.

In vivo, profilin interacts strongly with a protein called formin. Formin is known to nucleate actin filaments and to stay bound to the filament's plus end while it elongates [135]. Various types of formin proteins were found that influence the polymerization speed to different extends. Some, such as Cdc12, tend to cap the filament, preventing further addition from T-monomers, while others, e.g. mDia1, barely interfere with T-monomer addition[49]. When combined with profilin, all formins increase the polymerization speed of filaments. The

Rates	Fig. 2.20	Fig. 2.21	Fig. 2.22 Top Row	Fig. 2.22 Bottom Row	Fig. 2.24 (Fig. 2.23)
k_{on}^{T+}	$11.6^* \, c^T + 9^{\ddagger} \, c^{dim}$	$40^{\ddagger} \cdot c^T$	$11.6^* \cdot c^T$	$11.6^* \cdot c^T$	$11.6^* \cdot c^T$
k_{on}^{T-}	0	0	$1.3^* \cdot c^T$	$1.3^* \cdot c^T$	$1.3^* \cdot c^T$
k_{on}^{P+}	0	0	$3.4^* \cdot c^P$	$3.4^* \cdot c^P$	$3.4^* \cdot c^P$
k_{on}^{P-}	0	0	$0.11^* \cdot c^P$	$0.11^* \cdot c^P$	$0.11^* \cdot c^P$
k_{on}^{D+}	0	0	$2.9^* \cdot c^D$	$2.9^* \cdot c^D$	$2.9^* \cdot c^D$
k_{on}^{D-}	0	0	$0.09^* \cdot c^D$	$0.09^* \cdot c^D$	$0.09^* \cdot c^D$
k_{off}^{T+}	1.4^*	1.4^*	1.4^*	1.4^*	1.4^*
k_{off}^{T-}	0.8^*	0.8^*	0.8^*	0.8^*	0.8^*
k_{off}^{P+}	$0.16^* + \dfrac{4.54^* \, c^{Prof}}{5.9^* + c^{Prof}}$	$4.7^{\dagger}$	$0.16^{\dagger}$	$0.16^{\dagger}$	$0.16^{\dagger}$
k_{off}^{P-}	0.02^*	0.02^*	0.02^*	0.02^*	0.02^*
k_{off}^{D+}	$5.8^* + \dfrac{45.8^* \, c^{Prof}}{28.1^* + c^{Prof}}$	51.6^*	$5.8^{\dagger}$	$5.8^{\dagger}$	$5.8^{\dagger}$
k_{off}^{D-}	0.25^*	0.25^*	0.25^*	0.25^*	*variable* (2.5, 5, 9.5)
ω_{TP}	$0.3^{\S}$	$0.3^{\S}$	$0.3^{\S}$	$0.3^{\S}$	$0.3^{\S}$
ω_{PD}	$0.0068^{\dagger}$	$0.0068^{\dagger}$	$0.0068^{\dagger}$	$0.0068^{\dagger}$	$0.0068^{\dagger}$
ω_{PT}	0	0	0	0	0
ω_{DP}	0	0	0	0	0
$\bar{\omega}_{PD}^{-}$	18^*	18^*	18^*	18^*	18^*
$\bar{\omega}_{PD}^{+}$	$1.8^* + \dfrac{4.3^* \, c^{Prof}}{5.9^* + c^{Prof}}$	6.1^*	$1.8^{\dagger}$	$1.8^{\dagger}$	$1.8^{\dagger}$
η^{+}			0, 0.1, 1, 10	0	
$\bar{\eta}^{+}$			$\eta^{+} \, \frac{1-\pi_{\eta}^{+}}{\pi_{\eta}^{+}}$	0	
η^{-}			0	0, 0.1, 1, 10	
$\bar{\eta}^{-}$			0	$\eta^{-} \, \frac{1-\pi_{\eta}^{-}}{\pi_{\eta}^{-}}$	
$\pi_{\eta}^{\pm}$			0.1, 0.5, 0.9	0.1, 0.5, 0.9	
c^T	*see text*		*variable*	*variable*	*variable* (0.15)
c^P	0		0	0	0
c^D	0		0	0	0
c^{Prof}	*see text*				
c^{dim}	*see text*				

Table 2.3: Parameter values for the simulations of actin in presence of accessory proteins. The values labeled with $*$ are taken from [52], $\dagger$ are from [30], $\ddagger$ are from [133], $\S$ are from [131], and $\ddagger$ are from [49]. Untagged rates are chosen. All rate constants are given in s^{-1}, all concentrations in μM.
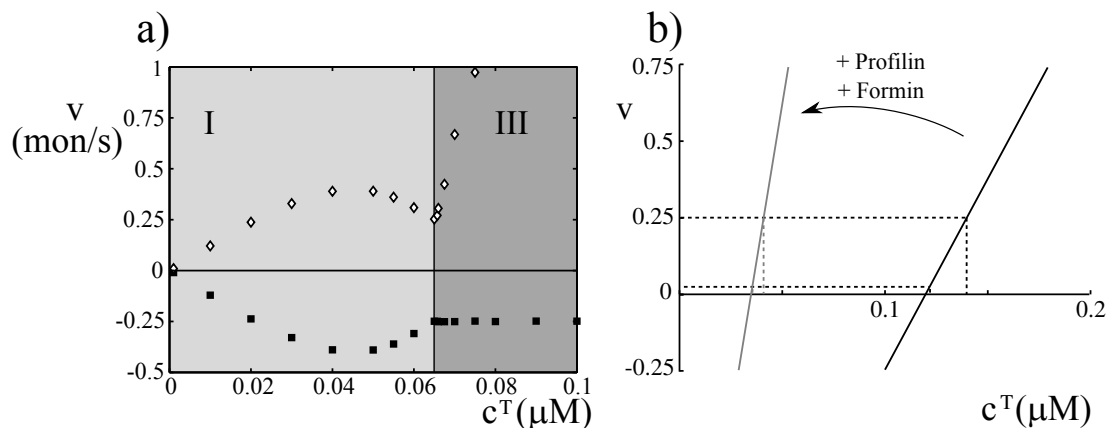
Figure 2.21: a) Actin growth velocities as a function of T-monomer concentration for a formin bound filament in a solution saturated with profilin. Rates are given in Table 2.3. b) Sketch of the polymerization velocity as a function of T-monomer concentration to illustrate steady state conditions.

formin mDia1 from mice was observed to polymerize at a rate of at least $k_{on}^{T+} = 47s^{-1}\mu m^{-1}$ for actin and profilin concentrations up to several μM [55].

In Figure 2.21 a), the simulated growth velocities of plus and minus end are shown as a function of T-actin monomer concentrations in a solution saturated with profilin. All actin monomers in solution are assumed to be bound to profilin. Consequently, no no cap is formed and $\alpha = 0$. The depolymerization of actin at the minus end then saturates at $k_{off}^{D-} = 0.25s^{-1}$. Again, filaments show treadmilling dynamics for low actin concentrations. For virtually all monomer concentrations that lead to a stationary system, filament length is exponentially distributed. The regime of length regulation is not found down to a precision of T-monomer concentrations of $\Delta c^T = 2.5 \cdot 10^{-4} \mu M$.

What is the reason for the disappearance of length regulation? To find a stationary state, the net polymerization rate needs to equal the depolymerization. The largest depolymerization rate at the minus end is given by $k_{off}^{D-} = 0.25s^{-1}$, which limits the possible net polymerization rate $\langle \nu_a \rangle$ to a value smaller than that. Particularly, $\langle \nu_a \rangle < k_{off}^{D-} < \omega_{TP}$, which means that monomer addition is so slow that T-subunits at the plus end are typically hydrolyzed before a new monomer can add. The fast phosphate release at the tip then leads to a disappearing of all gradients along the filament.

The scheme doesn't change essentially when formin is added to the system. Formin increases the efficiency of polymerization. In a situation without hydrolysis, the polymerization velocity as a function of monomer concentration would follow a straight line, see Figure 2.21 b). Formin increases its slope and shifts the zero to smaller concentrations. The increased

slope reduces the range of concentrations at which the system can be stationary but has no effect on the treadmilling velocity. As soon as polymerization is faster than $k_{\mathrm{off}}^{\mathrm{D}-}$, filament length diverges.

From these arguments, it can be concluded that increasing the polymerization velocity will not make length regulation more robust, nor does it improve its quality. In the next paragraph, the influence of capping proteins is analysed, which decreases addition and removal rates of monomers.

2.4.6 The Effect of Capping

Capping proteins such as capZ or tropomodulin can transiently bind to the ends of actin filaments and prevent further attachment or detachment of monomers. The average rates of filament growth and shrinkage are expected to decrease in presence of such proteins. Here, their effect is investigated within the framework of the three-states model. Filaments are capped at rates η^+ and η^- at the plus and minus end, respectively. Caps are removed from either side at rates $\bar{\eta}^+$ and $\bar{\eta}^-$. If a filament is capped, the end- induced phosphate release is assumed to be suppressed.

In well-mixed systems, the capping rate should scale linearly with the concentration of capping proteins. The release rate of caps depends on the interactions between filament and cap and it is thus specific to the isoform of the capping protein. The average time, a filament end is capped can thus be easily modulated by variation of the concentration of capping proteins in solution. The probability to find a cap at a particular end is then given by $\pi_\eta^\pm = \frac{\eta^\pm}{\eta^\pm + \bar{\eta}^\pm}$.

Instead of analyzing specific capping proteins at defined concentrations, the effect of capping is investigated systematically. In Figure 2.22, the growth rate of filaments with plus (top row) and minus end capping (bottom row) is shown. The average occupancy of the tip is fixed at 0.1 (left), 0.5 (middle), and 0.9 (right). It is clearly visible that the slopes for steady polymerization are reduced in proportion to $\pi_\eta^\pm$. The reaction kinetics of cap binding and unbinding has only little effect on the curves. A variation of $\eta^\pm$ by two orders of magnitude (between 0.1 and 10) leads to no significant variation.

The effect of capping on the polymerization rate can be taken into account when reformulating Equations (2.54) - (2.56) by multiplying all addition- and removal rates by a factor $1 - \pi_\eta^+ < 1$, the fraction of time that the filament tip is not capped. At the minus end, there is no conceptual difference between a cap formed by monomers that were added to the minus end and a capping protein. In the expressions for the depolymerization rate, the factor $1 - \alpha$ has then to be replaced by $(1 - \alpha)(1 - \pi_\eta^-)$ since for the removal of monomers
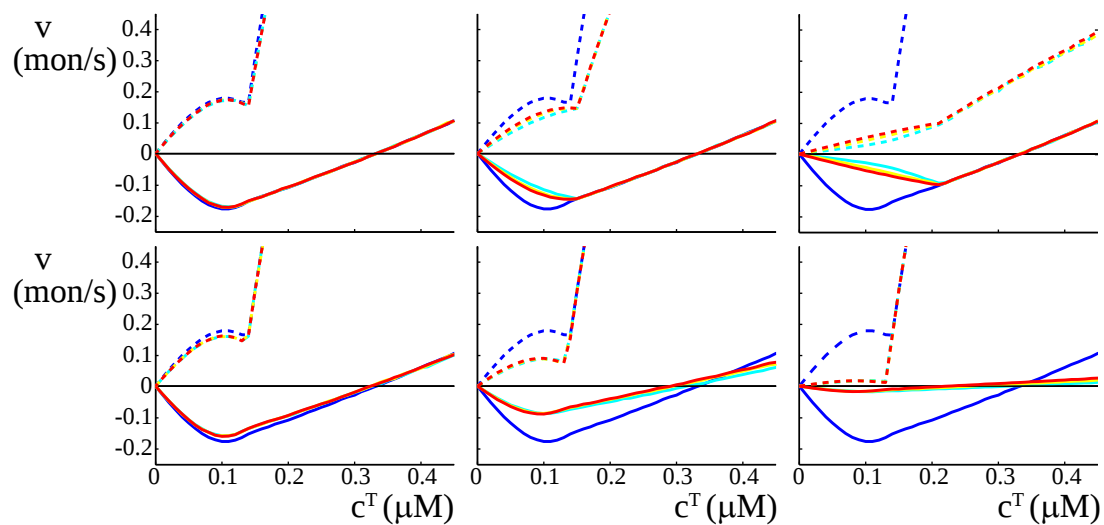
Figure 2.22: The effect of different capping ratios for the plus and minus ends. The top row shows numeric results for the polymerization velocities of plus and minus ends as a function of monomer concentration in presence of a plus end capping protein. The same is shown in the bottom row for a minus end capping protein. Rates were fixed such that the caps are capped for 10% (left), 50% (middle), or 90% (right) of the time. The capping rate is 0.1 s^{-1} (cyan), (yellow) 1 s^{-1}, or 10 s^{-1} (red). For comparison, the results in absence of a capping protein are shown in blue.

that were polymerized at the plus end, the minus end has to be void of minus end poly-merized monomers as well as of capping proteins. The value of α itself also depends on the capping dynamics. In its calculations, addition and removal rates have thus also be rescaled by $1 - \pi_\eta^-$.

Capping thus leads to an effective reduction of the averages of polymerization- and de-polymerization velocities. Since the capping and uncapping constitute an additional source for stochasticity in the system, one expects the fluctuations of filament length to increase systematically. The slower the binding of capping proteins at the filament end, the stronger the variations of filament length that are expected. The quality of length regulation would thus be impaired by slow capping.

To sum up, capping is not likely to increase the ability of actin filaments to autoregulate their length. It was shown here that under *in vitro* conditions, the capping of filament ends is not expected to have a substantial effect on the phase diagram of the system. Even strong capping did not let show a phase of length regulation. Slow capping, however, would be expected to rather suppress efficient length control due to an increase in length fluctuations.

2.4.7 Depolymerization by Cofilin

As was shown above, the turnover velocity of actin filaments *in vitro* is limited by the slow depolymerization rate of ADP-actin from the filament's minus ends. Carlier et al. [64] reported that ADF1 from *Arabidopsis thaliana* increases the turnover rate of actin. Based on various biochemical assays it was concluded that ADF1 targets filamentous ADP-actin with high specificity and enhances its removal rate from the filament by a factor of 25 as compared to ADF1-free ADP-actin subunits. It was claimed that the depolymerization occurs without breaking the filaments, although this finding remains controversial [136]. ATP-actin, in contrast, was found to poorly bind to ADF1. In the presence of ADF/Cofilin, treadmilling velocities of ≈ 2 subunits/s were measured [64].

More recent results indicate that cofilin severs filaments [65, 137] rather than remove monomers in a one-by-one manner. I want to embark on a more detailed model of the effect of cofilin later in chapter 4. Here, cofilin is assumed to specifically increase the rate at which ADP-monomers are removed from the filament at the minus end, as suggested in [64].

Figure 2.23 a) shows three filament length distributions for different values of $k_{\mathrm{off}}^{\mathrm{D}-}$ at $c^T = 0.25\,\mu M$. It clearly shows that unimodal filament length distributions reappear for elevated monomer concentration, if the depolymerization rate of D-monomers in the filament is selectively increased. In Figure 2.24, the effect of an elevated depolymerization rate on the phase diagram is investigated more systematically. Region II, in which filament
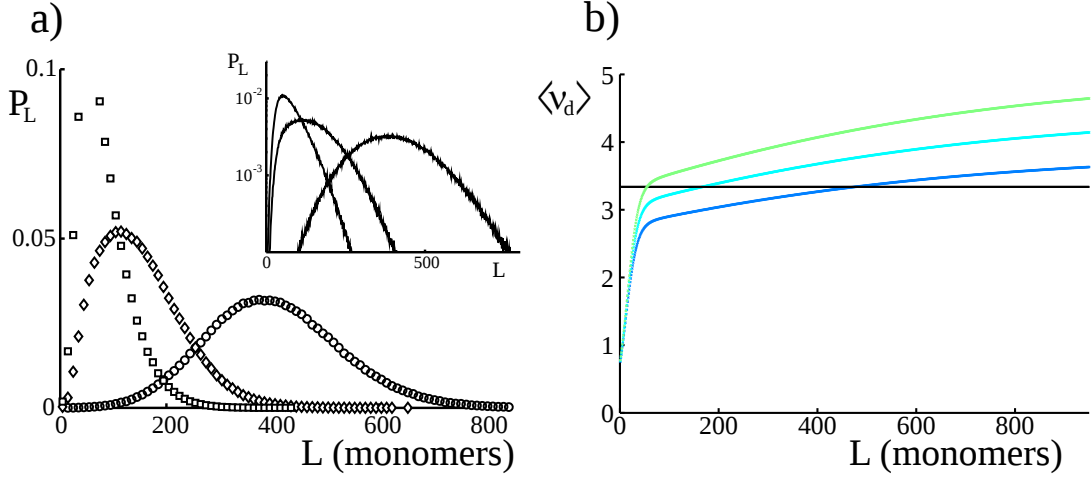
Figure 2.23: a) Examples of filament length distributions for $k_{\text{off}}^{\text{D}-} = 2.5s^{-1}$ ($\circ$), $5s^{-1}$ ($\Diamond$), and $9.5s^{-1}$ ($\Box$) at monomer concentration $0.25\mu M$. Inset: The same distributions in a semilog-arithmic representation. Length regulation is visible for all three parameter sets. The right flank of the distributions shows a fast drop. b) The effective length dependent depolymerization rates as a function of filament length for the three parameter sets in a). The blue curve corresponds to the circles, cyan to diamonds, and green to the quares in a). The presented curves were derived analytically. They equal the polymerization velocity (black line) at the position of the distribution's maximum. [23] ©AIP (2013)

length regulation is observed, appears for $k_{\text{off}}^{\text{D}-} \gtrsim 1$ and broadens henceforth for increasing depolymerization rates. The closer the parameters are to the boundary of region II to region III, the longer filaments get, preserving their peaked character, see Figure 2.23. The average length of roughly 400 monomers in the case of $k_{\text{off}}^{\text{D}-} = 2.5s^{-1}$ in this figure corresponds to a filament length of $1\mu m$, which is in the range of experimental findings.

The length dependent depolymerization rate that can be extracted from an analytic treatment of the system is shown in Figure 2.23 b) in comparison to the constant polymerization rate. The typical filament lengths that are deduced agree nicely to the simulation results. The sole increasing of depolymerization of D-monomers from minus ends can thus reestablish filament length regulation in the *in vitro* system. It will be shown in chapter 4 that this effect persists even when the monomer number is limited. The protein cofilin could provide this functionality. Experiments that record the filament length remain to be done.
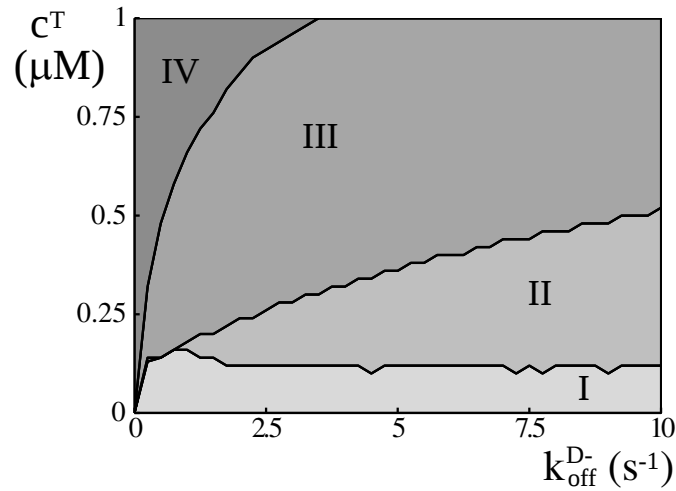
Figure 2.24: The phase diagram of actin length dynamics under variation of the depolymerization rate $k_{\text{off}}^{\text{D}-}$ and the T-monomer concentration. For low T-monomer concentrations, filament length is exponential independent of the monomer removal rate at the minus end. The regime of filament length control, region II, emerges if $k_{\text{off}}^{\text{D}-} \gtrsim 1$. The border between the regime in which filaments only grow at the plus end (region III) or at both ends (region IV) shifts rapidly to large concentrations when $k_{\text{off}}^{\text{D}-}$ rises. Figure 2.18 can be viewed as a vertical section at $k_{\text{off}}^{\text{D}-} = 0.25 s^{-1}$. [23] ©AIP (2013)

2.5 Summary and Further Considerations

In this chapter, I introduced a lattice model for the polymerization dynamics of active filaments. Using stochastic simulations and analytic derivations, I was able to show that filaments display the experimentally observed treadmilling dynamics. Moreover, a parameter regime was identified in which filaments are able to auto-regulate their length. It was found in particular that the energy balance of monomer addition that are given by Equations (2.20) and (2.21) are no principle limit neither for treadmilling nor for length regulation. A two-state model was sufficient to generate both effects.

I derived approximative expressions for key parameters of the system, such as the average polymerization speed, and the length-dependent depolymerization rate. From these values, the typical filament length in the case of unimodal length distributions could be deduced in a systematic way. As a part of the calculations, the typical cap length of minus end polymerized monomers was determined. To do so, a model for a filament with one inert end was invoked and analyzed. It may also serve as a model to describe the dynamic instability of microtubules.

The model was then applied to the polymerization dynamics of actin. I was able to

successfully fit the length distribution as a function of time for an actin system after addition of the actin-binding protein α- actinin [125]. Even though the resulting rates for the binding dynamics of α-actinin deviate from known literature values, the present analysis constitutes the first comprehensive fit of the evolution of the length distribution.

Based on the parameters determined by Kuhn and Pollard [29] for the polymerization of actin, the *in vitro* dynamics of filament length was analysed as a function of the concentration of ATP-actin monomers. Unimodal length distributions could indeed be observed but were limited to a narrow range of monomer concentrations. More recent experiments are interpreted in the frame of a three-state model [30] and indicate that phosphate release at filament ends is faster than in the bulk [30, 52]. For an accordingly extended version of the model, the regime of unimodal length distributions vanished when induced phosphate release was included. Even if the filament ends released phosphate at the same rate as subunits in the bulk, the monomer concentration needed to be fine-tuned to nanomolar precision for unimodal length distributions to appear. In the case that the monomer concentration could be controlled to such accuracy, the resulting average filament length would still be small. I conclude that it is unlikely that unimodal filament length distributions can be observed in the pure actin system.

In order to check if accessory proteins interacting with actin filaments could provide a means to establish length regulation, the effects of monomer sequestration by profilin, amplification of polymerization speed by formin, capping of filament ends, and increased depolymerization were investigated in turn. Modulation of polymerization speed at the plus end had no perceivable effect on the phase diagram. Equally, the suppression of monomer addition to the minus end or transiently capping could not generate unimodal filament length distributions. Only the increase of the removal rate of D-monomers from the minus end led to the emergence of a phase of length regulation. Filaments in this regime showed plausible lengths in a broad range of parameters.

One protein candidate for the amplification of monomer removal is the protein cofilin. Its precise effect is still under debate and a one-by-one monomer removal scheme as well as a severing effect were proposed and underpinned by experimental findings [64, 65]. In general, gradients along the filaments are expected to generate unimodal length distributions. This expectation is supported by results obtained for other effectively length-dependent processes. For example, severing proteins like cofilin [12, 13] or motor proteins like Kin-8 on fixed microtubules [16, 19, 86] can show a length-dependent distribution along filaments and thus induce unimodal distributions. Note that severing proteins have been shown to produce unimodal length distributions also in absence of gradients if the rate of severing increases with the filament length [138]. It would be interesting to see, how the interplay of different

such mechanisms influences the length distribution. Notably, one might expect that by adding active processes to the intrinsic ADP-P$_i$ gradient, for example, by using molecular motors, cells arrive at a tighter control of the filament length. One example of such models is analyzed in detail in the following chapter.

Another extension of the model could include more than three monomer states. Such a model could take into account further potential sub-states of actin [139] or binding of additional factors like cofilin to actin monomers. More states could also mimic a more complex binding situation of protein subunits within filaments. The generalization of the analytic results presented here to a multi-state model are straightforward and can be done in parallel to the transition from the two-state model to the three-state model. As long as the monomer states follow sequentially one after the other and the depolymerization rate grows monotonically when going through the individual states, the behavior of filament length is similar to what was presented here [124].

In the presented model, it was assumed that the rates of ATP-hydrolysis and of phosphate release in the filament bulk do not depend on the state of neighboring actin monomers, which is known as random hydrolysis. Alternatively, ATP-hydrolysis and ADP-P$_i$ phosphate release might be cooperative within actin filaments. One can construct a model in which the rates of hydrolysis and phosphate release depend on the states of the neighboring subunits in the filament lattice [140]. For low cooperativity, Equation (2.24) should have non-linear terms and the exponential gradients that were found for independent monomers, are expected to assume a sigmoidal shape. An extreme case of such a scenario is known as vectorial hydrolysis [141, 142]. In this case, hydrolysis or phosphate release only occur at the boundaries of homogenous regions on the filament. In contrast to the unimodal distributions found above, the filament length is in this case always exponentially distributed [105]. The experimental detection of unimodal length distributions in an *in vitro* assay would be a strong evidence for a random hydrolysis scheme. However, from the analysis presented here, one would expect such distributions only to occur if the release rate of ADP-bound monomers from the minus end can be enhanced. These experiments remain to be done.

3 The Effect of Depolymerizing Molecular Motors

Parts of the presented results were published in [20] and [22]. They were obtained in cooperation with Denis Johann, whose bachelor thesis I supervised as a part of my regular teaching duties in the doctoral program. He is to be credited in particular for the continuous formulation of the motor flux and the dynamics of the domain wall in the case $\gamma \to \infty$, $\bar{\omega} = 0$.

3.1 Molecular Motors as Filament Depolymerizers

In Chapter 2 evidence was supplied that the processes leading to the treadmilling dynamics implicitly provide a mechanism by which the length of cytoskeletal filaments could be regulated. The polymerization and depolymerization rates that were determined experimentally for actin, however, suggest that cells do not exploit this potential. One problem of the mechanism might be its susceptibility to fluctuations in the monomer concentration, which easily can lead to a breakdown of the regulation mechanism. Even in combination with the effects of known regulatory proteins, the quality of length regulation remains poor.

How would an ideal mechanism for filament length regulation look like? It would guarantee a maximal net polymerization velocity as long as the filament is smaller than the desired length and a maximal depolymerization, if the filament becomes longer than that, e.g. by fluctuations. In terms of a stability gradient that is to be established along a filament, a sudden change from stable to unstable monomers would be required. This transition needs to occur stably at a fixed distance from, say, the plus end of the filament.

One way to generate such a gradient would be to increase the next-neighbor interactions of monomer states within the filament. If dephosphorylation and hydrolysis depend on the states of the neighboring subunits, one expects non-linear terms in the equation that describes the development of the monomer states. On a treadmilling filament, the gradient along the filament should therefore show a more sudden transition than the exponential function found in the random hydrolysis model. Combined with measured rates for actin
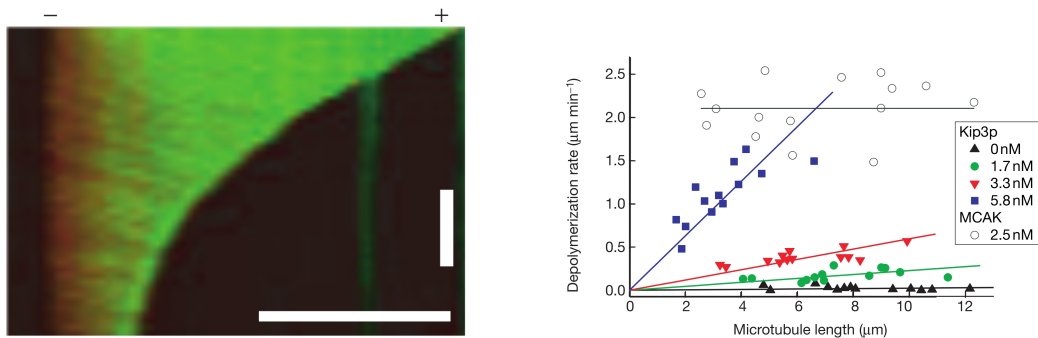
Figure 3.1: Left: A space-time plot of a fluorescently labeled microtubule in presence of the kinesin motor Kip3p. The microtubule is colored in red while motor molecules are labelled in green. Right: The depolymerization velocities of microtubules as in the left figure for different motor concentrations. As a comparison, the depolymerization velocity of the MTs in presence of the motor MCAK is shown that is moving in a diffusive manner on the lattice. Reprinted by permission from Macmillan Publishers Ltd: Nat. Cell Biol. [16], ©2006.

polymerization, however, the system is not expected to differ substantially from the model discussed in the previous chapter. In the limiting case of interactions dominating the internal switching, the vectorial hydrolysis model is recovered. This model, however, is not able to generate unimodal filament length distribution, as was shown in earlier studies [106]. Instead, I present an alternative mechanism of length regulation in this chapter that is based on the movement of molecular motors.

As detailed in the introduction, molecular motors are enzymes capable of moving directionally along actin filaments or microtubules by transforming chemical energy into mechanical work [1, 2]. The hydrolysis of ATP triggers conformational changes within their structure, giving rise to a stepwise movement along the polymeric lattice of the filament they are bound to, cf. [67, 143]. By cycling from an ATP to an ADP-bound state, they are kept out of thermodynamic equilibrium.

In cells, molecular motors are known to perform a number of vital tasks such as cargo transport or generation of mechanical stresses. In addition to these properties, some motors are known to remove subunits form the end of filaments [86, 144, 145]. Experimental and theoretical work suggests that motor molecules can lead to an effectively length dependent subunit removal rate [16–21], see Figure 3.1. As a consequence, cells might use them to regulate the length of cytoskeletal filaments.

Molecular motors have inspired a large class of driven diffusive systems that have been used to study fundamental properties of physical systems out of thermodynamic equilibrium. In this context, the Totally Asymmetric Simple Exclusion Process (TASEP) is probably the
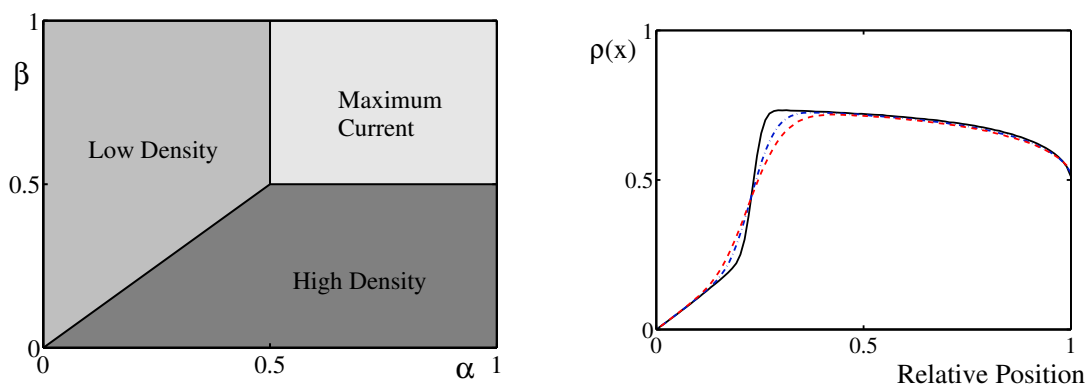
Figure 3.2: Left: The Phase diagram of the TASEP model with entering rate α at one end and leaving rate β at the other end. Particles directionally move on the lattice at rate 1, provided the target site is empty. In the original TASEP model, particles can only enter and leave the system at the boundaries. Right: An example of the coexistence phase in the Langmuir-TASEP model for different scaling parameters Ω. The average motor density ρ is draw as a function of the relative position $x = i/L$ with i the index of the site and L the system length. A low density regime to the left is separated from a high-density regime at the right by a domain wall or 'shock'. The particles move to the right. Parameters are system length $L = \Omega$, entering rate $\alpha = 0$, leaving rate $\beta = 0.5$, bulk attachment rate $\omega = \Omega^{-1}$, bulk detachment rate $\bar{\omega} = \omega/3$, hopping rate $\gamma = 1$. Scaling factor $\Omega = 100$ (dashed line), 200 (dash-dotted line), and 1000 (solid line).

best known system [146–149]. It consists of a linear lattice of fixed size and particles on the lattice sites. Particles can hop into one direction provided that the target site is not occupied. They enter the lattice at a constant rate at one end and leave it at the other. Depending on the rates of particle entering and leaving the system, different phases have been identified. If the rate at which particles enter the system, α is larger than the rate at which they leave, β, and $\beta < 0.5$, particles accumulate in the system. If, on the other hand, particles have a higher rate of leaving the lattice than of entering, the lattice is emptied and the system is in the low density phase. The maximum current regime is assumed if both rates are above 0.5 times the hopping rate. Then, the density of particles is dominated by their mobility on the lattice and not by the boundaries, see Figure 3.2.

This behavior has led to the notion of boundary-induced phase transitions [148–150], a phenomenon unknown for equilibrium systems. Since molecular motors in a biological context only have a finite binding affinity to a filament, the TASEP has been extended by attachment and detachment of particles anywhere along the lattice. The inclusion of Langmuir kinetics for the particles has lead to the discovery of stationary domain walls [77, 151], separating a phase of low and high particle density on the same lattice.

Some models have been introduced recently to study theoretically the interplay of molecular motors and length dynamics of cytoskeletal filaments. In spatially extended systems the organization of filaments into asters and waves was observed [85, 152, 153], filament networks were found to polarize [154, 155], and contractile bundles of filaments and motors were seen to be stabilized by filament assembly and disassembly [156]. The latter also leads to a suppression of motor jams [79, 83]. More recently lattice models have been introduced to study the effect of molecular motors on the filament length distribution [18, 20, 21, 157, 158].

Most of these models concentrate on the case of plus end directed motors [18, 19, 21]. In contrast, I will study in this chapter a model that is motivated by the effect of the minus-end directed motor molecules such as Kar3p and KLP10A with microtubules. In vitro experiments with Kar3p have shown that it increases the depolymerization rate of the minus-ends of treadmilling microtubules [159, 160]. Experiments on the fruit fly *Drosophila melanogaster* suggest that KLP10A influences the length of mitotic spindles by increasing depolymerization [161]. Independent experiments suggest that microtubules are treadmilling within the spindle [162].

In this chapter, I will introduce and study a lattice model for treadmilling filaments to which molecular motors can attach. Motors bound to the filament's minus-end can induce the removal of subunits, while empty subunits are constantly added to the lattice at the the plus end. The limited motor capacity of a monomer will lead to motor jams in the system that eventually can generate a domain wall at a fixed distance from the plus end.

I start by introducing the model and show that the length distribution in steady-state can be unimodal. The investigation of the motor distribution on a filament with stabilized minus-end will provide a basis for the determination of estimates of the average filament length. In some limiting cases, exact expressions for the whole filament length distributions can be derived. I will generalize these results and show under which conditions they reproduce the numerical findings. Finally, I will show that filament length regulation becomes more efficient when the motor activity increases but levels off as soon as motors move essentially at the speed of filament elongation.

3.2 A Stochastic Driven Lattice-Gas Model for Motors on Filaments

Consider a single isolated filament in a solution of filament subunits and motor molecules at fixed concentrations. The filament is represented by a dynamic lattice of identical subunits. Empty lattice sites are added at one end, the plus end, at a constant rate α and are removed
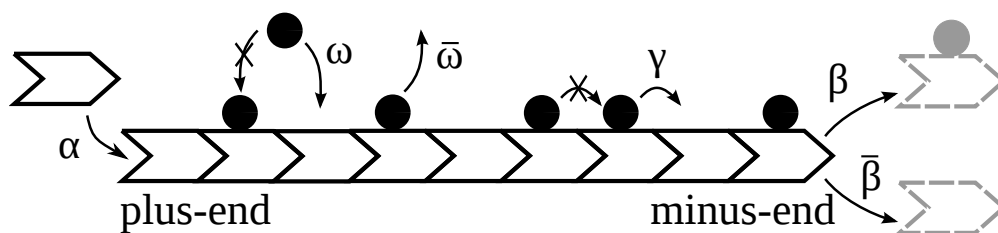
Figure 3.3: Schematic representation of the filament in contact to motor molecules. The filament is a lattice of dynamic length. Motors are represented as particles that occupy the sites. At the plus end sites are added at rate α. At the opposing end, the minus-end, empty (occupied) sites are removed at rate β ($\bar{\beta}$). Particles attach to empty sites at rate ω and detach from the lattice at rate $\bar{\omega}$. Particles hop to adjacent free sites in direction of the shrinking end at rate γ, provided that the destination subunit is empty. [20] ©APS (2012)

at the opposite end, the minus-end, at rate $\bar{\beta}$. If the lattice only consists of a single subunit, no more monomers are removed. At this point, the microscopic origin of the treadmilling dynamics is neglected and the reader is referred to Chapter 2 for details.

Particles attach to empty subunits all along the filament at constant rate ω and leave the lattice at rate $\bar{\omega}$. When the subunit at the minus-end is occupied by a particle, it is removed at a rate β. In contrast to the model discussed in Chapter 2, particles can now hop towards the minus-end at rate γ, provided that the target site is empty, see Figure 3.3. From now on all rates are scaled by the rate of site addition α.

In Figure 3.4 a,b,c), three different types of filament behavior are shown. Filaments either regularly shrink back to zero length (a), establish a finite stationary filament length (b), or grow without bounds, depending on the system's parameters. In the first case, a stationary filament length distribution is monotonically decreasing (d) but in general not exponential. In the third case, the filament length distribution doesn't reach a stationary state but rather grows at a finite constant velocity. In between these two extremes, there is a phase in which the stationary filament length distribution assumes a unimodal form (e). The filament length fluctuates then around a well defined typical filament length. The case of unimodal length distributions is of special interest for the present analysis since it represents a form of filament length regulation. In the following, the unimodal distributions are characterized by their average, their maximum, and their standard deviation.

The filament's behavior can easily be understood qualitatively: Since newly added monomers are empty and the filament accumulates motors as it grows, the monomer removal rate depends inherently on the filament's length. The removal rate can vary at most between the removal rates for empty and occupied subunits, $\bar{\beta}$ and β. Short filaments will have a depolymerization rate close to $\bar{\beta}$, while the depolymerization on long filaments will never exceed
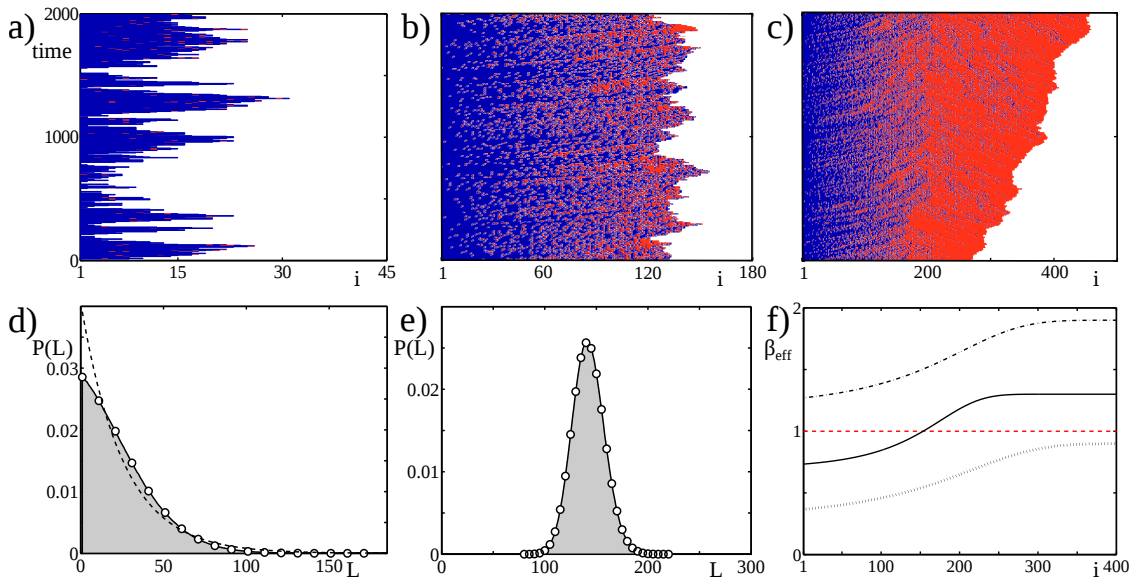
Figure 3.4: Motor dependent length dynamics of treadmilling filaments. The kymographs represent the stochastic evolution of the system with blue sites being empty while red sites are occupied. The plus end is always located at $i = 1$. a, d) Monotonically decreasing length distribution; dashed line: exponential distribution with the same average as a comparison, b,e) unimodal length distribution, c) diverging system size. f) Illustration of the effectively length-dependent depolymerization rate for the three cases. Parameters are a,d) $\beta = 1.1$, $\bar{\beta} = 1.01$, $\omega = 0.01$, $\bar{\omega} = 0.002$, and $\gamma = 2$, b,e) $\beta = 10$, $\bar{\beta} = 0$, $\omega = 0.01$, $\bar{\omega} = 0.002$, and $\gamma = 2$, c) $\beta = 0.8$, $\bar{\beta} = 0$, $\omega = 0.01$, $\bar{\omega} = 0.002$, and $\gamma = 2$. [22] ©APS (2012)

β. When it is assumed that $\bar{\beta} < \beta$, the effective depolymerization rate is a monotonically increasing function of filament length, $\beta_{\text{eff}}(L)$, see Figure 3.4 f). If the depolymerization is smaller than the polymerization, $\beta_{\text{eff}} < 1$ for all L, the filament will always grow. If, on the other hand, $\beta_{\text{eff}}(L)$ is larger than the polymerization for all L, the most probable filament length is zero and only fluctuations lead to a transient finite filament length. The ensuing length distribution is then monotonically decreasing. Unimodal filament length distributions emerge when $\beta_{\text{eff}}(1) < 1$ and $\lim L \to \infty \beta_{\text{eff}} > 1$. This can only be the case if $\bar{\beta} < 1$ and $\beta > 1$. In such a situation, short filaments have a tendency to grow since on average more monomers are added than are removed. Long filaments, on the other hand, will shrink because the depolymerization rate increases with length. The typical filament length will then be somewhat close to the length L where $\beta_{\text{eff}}(L) = 1$ is fulfilled.

Even though these meanfield arguments provide a good intuition for the system's behavior, it fails quantitatively. If the steady-state length distribution P_{L} is known, an effective depolymerization rate $\beta_{\text{eff}}(L)$ can always be determined such that the distribution is reproduced. Explicitly,

$$\beta_{\text{eff}}(L) = \frac{P_{\text{L}-1}}{P_{\text{L}}}. \tag{3.1}$$

However, it is not evident how to derive the functional form of $\beta_{\text{eff}}(L)$ *a priori*. It will become clear below that care is needed to derive good estimates for the average length and the amplitude of fluctuations.

Note that for a vanishing hopping rate, $\gamma = 0$, a simplified version of the two-state model discussed in Chapter 2 is recovered. It was already found that the filament length distribution is unimodal under certain conditions. The potential to regulate the filament length for the two-state model was limited, though. However, with an increasing hopping rate γ, the average filament length decreases and the fluctuations are reduced, see Figure 3.5. The main goals of the following analysis will be to systematically determine the limits of the mechanism and the quality of length regulation under action of depolymerizing motor molecules.

The system can be formally described by the probability π_i of site i to be occupied by the following Master-equation:

$$\dot{\pi}_i = \omega(1 - \pi_i) - \bar{\omega}\pi_i + \gamma\pi_{i-1,\bar{i}} - \gamma\pi_{i,\overline{i+1}} + \alpha\pi_{i-1} - \alpha\pi_i \tag{3.2}$$
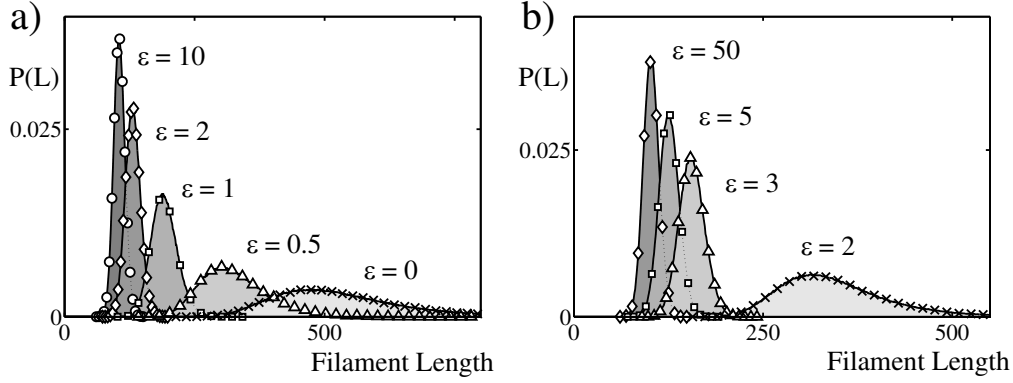
Figure 3.5: Unimodal system size distributions for various values of γ with $\bar{\omega} = 0$ (a) and $\bar{\omega} = 0.01$ (b). The length distributions considerably sharpen when the motor activity increases. Other parameter values are $\bar{\beta} = 0$, $\beta = 10$, and $\omega = 0.01$. [22] ©APS (2012)

for $i = 2, \ldots, L - 1$ and

$$\dot{\pi}_1 = \omega(1 - \pi_1) - \bar{\omega}\pi_1 - \gamma\pi_{1,\bar{2}} - \alpha\pi_1 \tag{3.3}$$

$$\dot{\pi}_L = \omega(1 - \pi_L) - \bar{\omega}\pi_L + \gamma\pi_{L-1,\overline{L}} + \alpha\pi_{L-1} - \alpha\pi_L, \tag{3.4}$$

where the plus end is always the site at $i = 1$ and where $\pi_{i,\overline{i+1}}$ denotes the probability that site i is occupied and that site $i + 1$ is empty. The dynamics of the filament length can accordingly described by

$$\dot{L} = \alpha - \beta\pi_L - \bar{\beta}(1 - \pi_L). \tag{3.5}$$

The difficulty is now to determine π_L correctly, taking into account the correlations induced by particle interactions and the history of the filament tip. I start the analysis with the discussion of the semi-infinite system.

3.3 The Motor Gradient on a Semi-Infinite Lattice

In a first step, let me analyse the profile of motors on a semi-infinite filament with only a plus end. Empty filament subunits are constantly added at this end while motors keep moving away from it. Let n_i be the occupation number of site i with $n_i = 0$ for an empty and $n_i = 1$ for an occupied site. In Figure 3.6, the average occupation number $\rho_i = \langle n_i \rangle \equiv \pi_i$ is shown for different values of the hopping rate γ and different particle detachment rates $\bar{\omega}$. As the motors accumulate, the density asymptotically approaches the equilibrium density
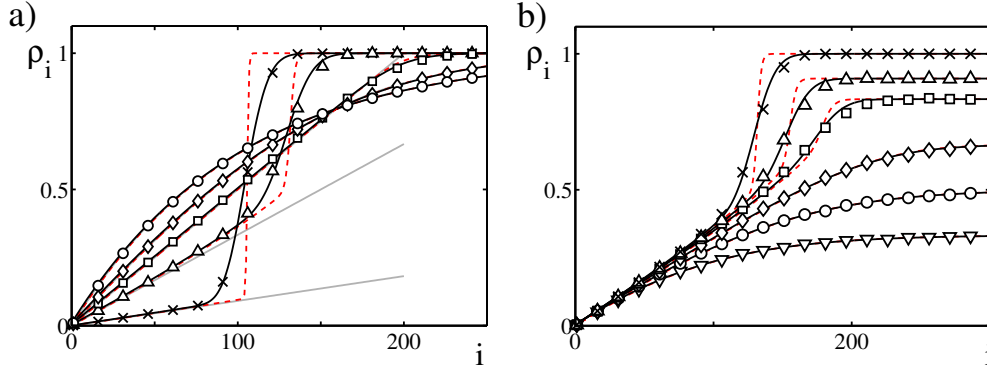
Figure 3.6: The average motor density along a semi-infinite filament. a) Motor density for different values of the hopping rate γ: $\gamma = 0$ ($\circ$), 0.5 ($\diamond$), 1 ($\square$), 2 ($\triangle$), 10 ($\times$). Furthermore, $\omega = 0.01$ and $\bar{\omega} = 0$, such that $\gamma_c = 1$. b) Motor density for different values of the detachment rate $\bar{\omega}$: $\bar{\omega} = 0$ ($\times$), 0.001 ($\triangle$), 0.002 ($\square$), 0.005 ($\diamond$), 0.01 ($\circ$), 0.02 ($\triangledown$). In addition, $\omega = 0.01$ and $\gamma = 2$, such that $\gamma < \gamma_c$ for the first three values of $\bar{\omega}$ and $\gamma < \gamma_c$ for the last three. Symbols are results of numeric simulations, red dashed lines are solutions of Equations (3.6) and (3.7), and solid black lines solutions of Equation (3.17). The solid gray lines are linear approximations of the motor density for $\gamma \leq 1$ given by $\omega x/(1 + \gamma)$, where x is the distance from the plus end, see text. [22] ©APS (2012)

$\rho_\infty = \frac{\omega}{\omega + \bar{\omega}}$. At the plus end, a stationary cap of low motor density is established and the probability to find a motor increases monotonically with the distance to the plus end, see Figure 3.6.

In the motor density gradients of Figure 3.6, two qualitatively distinct types of gradients can be distinguished: When the stepping rate or the asymptotic motor density is low, the density smoothly increases towards its asymptotic value. If, on the other hand, the stepping rate is high and the motor affinity to the filament is strong, a region of a sudden increase in the motor density, a 'shock', emerges. This 'shock' separates a region of high density ($\rho = \rho_\infty$) at large distance from the end from a region of low motor density close to the plus end, similar to the domain wall that could be observed in the Langmuir-TASEP model. While the average motor concentration beyond the shock is constant, it increases almost linearly with distance from the plus end in the low density region.

To calculate the average occupation profile in steady state, a mean-field approximation can be made, leading to $\langle n_i n_{i+1} \rangle = \langle n_i \rangle \langle n_{i+1} \rangle$. For the TASEP, the phase diagram obtained from the mean-field approximation equals the exact phase diagram [148, 150]. In Figure 3.7, the correlation term $\langle n_i n_{i+1} \rangle$ is shown as a function of the average site occupation $\langle n_i \rangle$ for different values of γ and $\bar{\omega}$. The mean-field approximation is numerically found to be exact as long as $\gamma < 1$ (Figure 3.7, a). The function becomes increasingly linear as γ
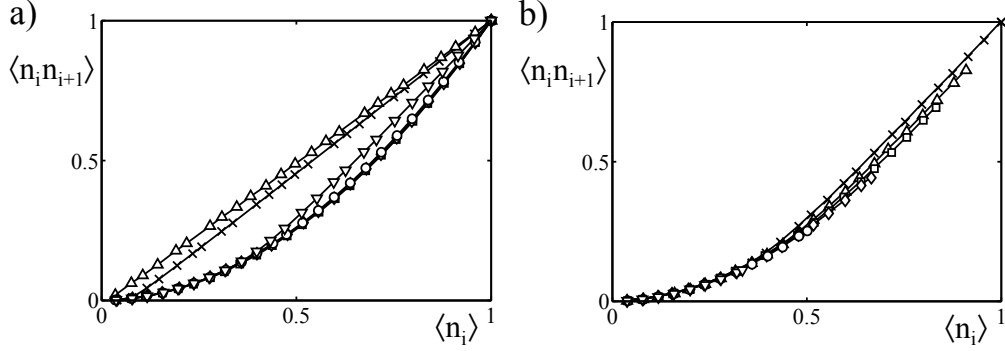
Figure 3.7: Two-point density correlation $\langle n_i n_{i+1} \rangle$ as a function of the mean occupation number $\langle n_i \rangle$. a) The quadratic dependency turns linear when $\gamma > 1$. Parameter values are $\omega = 0.01$, $\bar{\omega} = 0$, and $\gamma = 0$ ($\times$), $0.5(\triangle)$, 1 ($\square$), 2 ($\Diamond$), 10 ($\circ$), 50 ($\triangledown$). b) The detachment rate $\bar{\omega}$ has a negligible influence on the two-point correlation function. Note that beyond $\langle n \rangle = \rho_\infty$, no data points are available. Parameter values are $\gamma=2$, $\omega = 0.01$, and $\bar{\omega} = 0$ ($\times$), 0.001 ($\triangle$), 0.002 ($\square$), 0.005 ($\Diamond$), 0.01 ($\circ$), 0.02 ($\triangledown$). Data points were collected at values closest to an equidistant distribution in the interval $0 \ldots 1$. The solid lines are guides to the eye. [22] ©APS (2012)

increases. Variations in the motor release rate has under these conditions almost no effect (see Figure 3.7, b).

Using the mean-field expression, the term $\pi_{i,\overline{i+1}}$ in the Master-equation (3.2) and (3.3) turns into $\rho_i^{\mathrm{mf}}(1 - \rho_{i+1}^{\mathrm{mf}})$. In this form it can be used to calculate the time evolution of the mean-field density ρ_i^{mf}. Explicitly, it is given by

$$\dot{\rho}_i^{\mathrm{mf}} = \omega(1 - \rho_i^{\mathrm{mf}}) - \bar{\omega}\rho_i^{\mathrm{mf}} + j_{i-1} - j_i \tag{3.6}$$

for $i > 1$ and

$$\dot{\rho}_1^{\mathrm{mf}} = \omega(1 - \rho_1^{\mathrm{mf}}) - \bar{\omega}\rho_1^{\mathrm{mf}} - j_1. \tag{3.7}$$

Here, the particle current j_i from site i to site $i + 1$ is given by

$$j_i = \gamma\rho_i^{\mathrm{mf}}(1 - \rho_{i+1}^{\mathrm{mf}}) + \rho_i^{\mathrm{mf}} \tag{3.8}$$

for $i = 1, \ldots$ The first term accounts for particle hopping while the second term describes the addition of subunits since the site at $i = 1$ is always associated with the plus end. To calculate the stationary motor density, we can either integrate this equation into the stationary state or solve the stationary mean-field equations (3.6) and (3.7) recursively by noting that for $\dot{\rho}_i^{\mathrm{mf}} = 0$ ($i \leq 1$), ρ_i^{mf} can be expressed in terms of ρ_1^{mf} for $i > 1$. The value

of ρ_1^{mf} is determined by the condition that the net flux of motors to the filament needs to equal the stationary motor flux at infinite distance from the plus end:

$$\sum_{i=1}^{\infty} \left[\omega(1 - \rho_i^{\mathrm{mf}}) - \bar{\omega}\rho_i^{\mathrm{mf}} \right] = \gamma\rho_\infty(1 - \rho_\infty) + \rho_\infty. \tag{3.9}$$

It reflects that the total net rate of particle attachment must equal the net particle flux out of the system.

Note, however, that the discrete mean-field Equations (3.6) and (3.7) yield excellent results for both types of gradients, the smooth increase and the shock, even though the quadratic dependence of the correlation function on the motor density is only expected to work for low hopping rates γ.

A deeper insight into the limit of the phase of a smooth gradient can be gained when the continuum limit of the discrete Equations (3.6) and (3.7) is considered. Taking ρ_i^{mf} as a function $\rho(x)$ of a continuous parameter x and expanding $\rho_{i\pm1}^{\mathrm{mf}}$ into a Taylor-series up to first order in x, $\rho_{i\pm1} \simeq \rho(x) \pm d\rho(x)/dx$, one finds

$$\partial_t\rho = \omega(1 - \rho) - \bar{\omega}\rho - \gamma\partial_x\rho(1 - \rho) - \partial_x\rho \tag{3.10}$$

with boundary condition $\rho(x = 0) = 0$. In the steady state, this leads to

$$\frac{d\rho}{dx} = \frac{\omega(1 - \rho) - \bar{\omega}\rho}{1 + \gamma(1 - 2\rho)}. \tag{3.11}$$

Integration yields an implicit solution of the gradient,

$$x = \frac{2\gamma\rho}{\omega + \bar{\omega}} - \frac{\gamma(\bar{\omega} - \omega) + (\bar{\omega} + \omega)}{(\omega + \bar{\omega})^2} \ln\left(1 - \frac{\rho}{\rho_\infty}\right) \quad, \tag{3.12}$$

that is indistinguishable from the solution of Equations (3.6) and (3.7) for the smooth gradients but differs considerably when a shock appears. A shock corresponds to a steep increase in the gradient, that is a large value of the first derivative of ρ. In Equation (3.11), one readily sees that the gradient diverges as $\rho_c = (1 + \gamma)/2\gamma$. A shock is thus expected when the equilibrium density ρ_∞ exceeds ρ_c, $\rho_\infty > \rho_c$. This condition can be expressed in terms of a critical hopping rate γ_c with

$$\gamma_c = 1 + \frac{2\bar{\omega}}{\omega - \bar{\omega}} \quad, \tag{3.13}$$
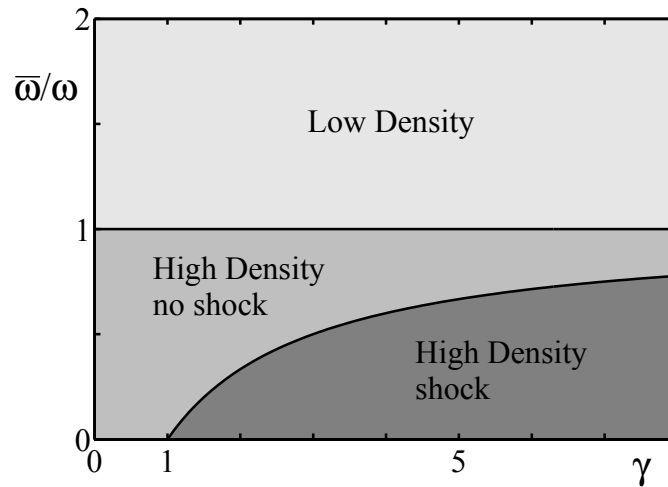
Figure 3.8: Phase diagram for a semi-infinite lattice as a function of the particle hopping rate γ and the ratio $\bar{\omega}/\omega$ of the particle detachment and attachment rates. In the low density phase $\rho_\infty = \omega/(\omega + \bar{\omega}) < 1/2$. In the high density phase $\rho_\infty > 1/2$ and the particle distribution is continuous. In the mixed phase, the particle density displays a shock. [22] ©APS (2012)

such that a shock exists for $\gamma > \gamma_c$. This result is consistent with numerical findings, see Figure 3.6.

Note, that γ_c diverges for $\bar{\omega} = \omega$. It is therefore appropriate to divide the parameter space into three different regimes, see Figure 3.8. For low release rates $\bar{\omega} < \omega$, the equilibrium motor density $\rho_\infty = \frac{\omega}{\omega + \bar{\omega}}$ is larger than $1/2$ and depending on the stepping rate γ a shock in the density gradient can emerge. The high density phase is thus subdivided in a region where the gradient has a smooth shape and a second region, in which shocks can form. The low density phase is defined by a large release rate, $\bar{\omega} > \omega$. In this phase, a shock cannot exist since the maximum motor density is lower than $1/2$. This is similar to the behavior of the TASEP with Langmuir kinetics, where a stationary density $\rho_\infty > 1/2$ is a necessary condition for the emergence of shocks [151].

In the shock region, it was already mentioned that the motor gradient is approximatively linear. To determine the slope of the density increase, one can exploit the fact that in the limit of small densities, the both types of gradients obey a similar dynamics. Linearizing expression (3.12) for small ρ, one gets $\rho(x) = \frac{\omega}{1+\gamma}x$, which is in excellent agreement with numerical findings, see Figure 3.6. Note that this expression is independent of the motor release rate $\bar{\omega}$, as can also be seen in Figure 3.6, b).

To fully characterize the shock, its position x_s remains to be determined. It can be derived by exploiting the flux-balance condition. The sum in Equation (3.9) turns into an integral

with respect to x and the condition for x_s yields

$$\int_0^\infty \left[\omega(1 - \rho(x)) - \bar{\omega}\rho(x)\right] dx = \int_0^{x_s} \left[\omega(1 - \rho(x)) - \bar{\omega}\rho(x)\right] dx \qquad (3.14)$$

$$= \gamma\rho_\infty(1 - \rho_\infty) + \rho_\infty \quad , \qquad (3.15)$$

where x_s denotes the shock position. Approximating the density for $x < x_s$ by the linear profile given above, it follows

$$x_s = \frac{1 + \gamma}{\omega + \bar{\omega}} \left(1 - \sqrt{1 - 2\frac{\bar{\omega}\gamma}{(1 + \gamma)(\omega + \bar{\omega})} - \frac{2}{1 + \gamma}}\right). \qquad (3.16)$$

Consistently with Equation (3.13), this expression implies that the shock position is defined only for $\gamma > \gamma_c$.

The motor density in the case of shock formation can be described by a linear profile with slope $\omega/(1+\gamma)$ up to a position x_s. Beyond this point, the density jumps to the equilibrium value ρ_∞. Before this section is closed, I'd like to comment on the origin of the discrepancy between the sharp shock that follows from Equations (3.6) and (3.7) and the numerically determined gradients.

An improved description of the average occupation profile in the case of shock formation is obtained, if the fluctuations in the process of site addition at the plus end are accounted for. Indeed, the time T having passed since site i has been incorporated into the system is a stochastic variable. Let $\langle n_i \rangle_T$ denote the average occupation number of site i at a time T after it has been added to the system. Then one can write $\rho_i = \int_0^\infty dT \langle n_i \rangle_T p_i(T)$, where $p_i(T)$ is the probability that site i has been incorporated a time T ago. As site addition is a Poisson process, the corresponding probability distribution of times T is given by $p_i(T) = T^{i-1}e^{-T}/(i-1)!$. If site addition occurred regularly at $T = 0, 1, \ldots$, then one would expect that $\langle n_i \rangle_T = \sum_{j=1}^\infty \rho_j^{\text{mf}}\delta_{jT}$, where δ_{jk} denotes the Kronecker-delta. Inserting this expression into the formula for ρ_i, the expression reads

$$\rho_i = \sum_{j=1}^\infty \rho_j^{\text{mf}}p_i(j) \quad . \qquad (3.17)$$

The motor profile obtained in this way is in remarkably good agreement with the simulation results, see Figure 3.6.

I have shown that using Equations (3.6) and (3.7), the motor gradient on semi- infinite filaments can be described to a satisfying degree. Moreover, it was found that if the motor

density can reach values above $1/2$, a motor jam (a discontinuity in the gradient) can emerge along the filament. Its position can then be determined using a coarse-grained version of the constituting Equations (3.6) and (3.7). Having analyzed the motor distribution on a semi-infinite filament thus far, the case of a finite filament with two ends can be considered.

3.4 Filaments With Two Ends

Now, let us return to the original model of a filament with a growing plus and a shrinking minus-end. As discussed above and in parallel to the model analyzed in Chapter 2, three different types of filament dynamics are observed: unbounded filament growth without a stationary state and stationary distributions that are either unimodal or monotonically decreasing. In a first step, the conditions under which the filament length diverges are studied. Then the analysis focuses on the case of filaments of finite length to investigate the stationary filament length distributions.

Before detailed calculations are invoked, some fundamental limits of the model shall be considered. Be reminded that the analysis is limited to the case of destabilizing motor proteins, which means that $\bar{\beta} < \beta$. For the sake of simplicity, $\bar{\beta} = 0$ in the remainder of this chapter unless stated otherwise.

It is clear that filaments will always grow if $\beta < 1$ since depolymerization never could compensate polymerization. Let β_c denote the depolymerisation rate that is required to limit net filament growth. In general, β_c will be a function of all other parameters but already, one can state that $\beta_c > 1$ for all values of γ, ω, $\bar{\omega}$, and $\bar{\beta}$.

Already at this point, it can be noted that $\beta_c \equiv 1$ for $\bar{\omega} = 0$, $\omega > 0$, and $\gamma > 0$. The reason is that the equilibrium motor density is $\rho_\infty = 1$ in this case. Thus, on long filaments, the depolymerization rate approaches β. For every value of $\beta > 1$, there will be a finite length at which depolymerization becomes faster than polymerization. If filament length stays bounded for all values of $\beta > 1$ then, by definition, $\beta_c \equiv 1$.

Figure 3.9 shows how β_c varies with $\bar{\omega}$ for different values of γ but fixed ω. As just mentioned, one observes that all curves converge to 1 for $\bar{\omega} \to 0$. The value of β_c increases as $\bar{\omega}$ increases and diverges at some finite value $\bar{\omega}_c$. Beyond that threshold, even for an instantaneous removal of occupied monomers the filament length diverges. It is inferred from this plot that $\bar{\omega}_c$ is a monotonically increasing function of γ for fixed ω.

In the following I present a series of arguments and calculations that allow an approximation of β_c for arbitrary values for the hopping rate γ. To this end, note that β_c is, in general, determined by the condition $\langle \tau \rangle = 1$, where $\langle \tau \rangle$ is the average lifetime of the site $i = L$ analogously to the function $\langle \tau \rangle$ that was introduced in Chapter 2. As above, $p_0(t)$ and $p_1(t)$
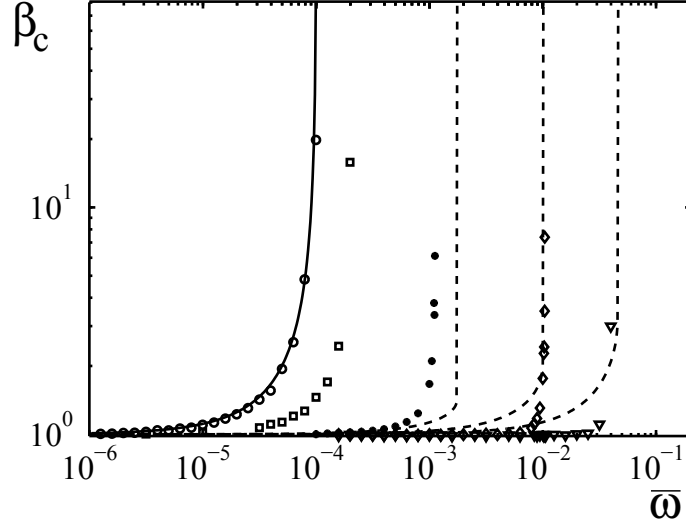
Figure 3.9: The critical value β_c separating bounded from unbounded system growth as a function of $\bar{\omega}$. The solid line is given by Equation (3.24) and the dashed lines by Equation (3.20). For $\bar{\omega} \to 0$, the critical value β_c approaches 1 independently of γ. Other parameter values are $\omega = 0.01$, $\bar{\beta} = 0$, and $\gamma = 0$ (○), 0.5 (□), 1 (●), 2 (◊), and 5 (▽). Note the logarithmic scales on both axes. [22] ©APS (2012)

shall denote the probabilities that the site $i = L$ is, respectively, empty or occupied at time t after this site became the minus-end. Then, $\langle \tau \rangle$ can be determined using Equation (2.38) when the time dependency of the values of p_0 and p_1 is known.

The time evolution of p_0 and p_1 follows a modified version of Equation (2.37):

$$\frac{\partial}{\partial \tau} \begin{pmatrix} p_0 \\ p_1 \end{pmatrix} = \begin{pmatrix} -\omega - \gamma c_{10} & \bar{\omega} \\ \omega + \gamma c_{10} & -\bar{\omega} - \beta \end{pmatrix} \begin{pmatrix} p_0 \\ p_1 \end{pmatrix} \quad . \tag{3.18}$$

The equation is complemented by the initial conditions $p_0(0) = 1 - c_{11}$ and $p_1(0) = c_{11}$. Here, c_{10} denotes the joint probability, that site $i = L - 1$ is occupied and site $i = L$ is empty, while c_{11} is the joint probability for both sites being occupied. This initial condition holds, because just prior to site removal the last and penultimate site were occupied, if site $i = L$ is occupied at $t = 0$. The steady state values of c_{11} and c_{10} are estimated and these values are used to solve the above equation for $p_0(t)$ and $p_1(t)$.

Numerically, it was found that $c_{10} = \rho_\infty$ as long as $\beta < \beta_c$. For estimating c_{11}, the relation

$$\rho_{L-1} = \rho_L c_{11} + (1 - \rho_L) c_{10} \tag{3.19}$$

can be exploited, where ρ_i denotes the average occupation of site i in steady state. For very long systems, the density ρ_i approaches the value ρ_∞ with increasing i and then elongates from this value towards the minus-end. Consequently, the value of ρ_{L-1} is between the values ρ_∞ and ρ_L. For simplicity and in absence of an accurate expression for ρ_{L-1}, the density at the second to last monomer is in the follwing approximated by $\rho_{L-1} = (\rho_L + \rho_\infty)/2$. Finally, the value of ρ_L obeys $\rho_L\beta = 1$ as long as $\beta \leq \beta_c$.

Taken together, one finds that β_c is approximatively given as the solution of the quadratic equation

$$\beta_c^2 \rho_\infty/2 - \beta_c \left(\omega + (\gamma + 1)\rho_\infty - 1/2\right) + \omega + \bar\omega + \gamma\rho_\infty = 0. \tag{3.20}$$

Note that this equation has only solutions for $\gamma > 1$. In the special case $\gamma = 0$, an exact expression for β_c can be derived from the results of Chapter 2. I give the explicit solution to this case below.

In Figure 3.9, the dashed lines give the results of Equation (3.20). The quality is satisfactory and at last gives a reasonable estimate of the critical value $\bar\omega_c$ at which β_c diverges for all values of $\gamma \geq 1$ that were checked, see Figure 3.9. For the case $\gamma = 0$, however, the theoretical solutions exactly reproduce the numeric results. Note furthermore, that the above mentioned relations are only valid in the case of constantly growing filaments and cannot in general be used to infer the average system size for $\beta < \beta_c$.

3.4.1 The Limit of Immobile Binding Factors

The situation of resting motor molecules is identical to the two-state model that was analyzed in Chapter 2 with a constant monomer addition rate $k_{\text{on}}^{(e)+} \equiv \alpha \equiv 1$ at the plus end and removal rates $k_{\text{off}}^{(e)-} \equiv \bar\beta$, and $k_{\text{off}}^{(o)-} \equiv \beta$ at the minus-end. All other rates in the two-state model are to be set to 0. In this section, only the main results of the two-state model are summarized. For detailed calculations, the reader is referred to Chapter 2.

For immobile motors, the occupation states of neighboring subunits in the filament become independent of one another. The gradient of motor density thus becomes exponential,

$$\rho(x) = \frac{\omega}{\omega + \bar\omega} \left(1 - e^{(-(\omega+\bar\omega)\,x)}\right), \tag{3.21}$$

where x denotes the distance from the filament's plus end in the continuum limit. The same result is obtained by setting $\gamma = 0$ in expression (3.12).

Under which conditions, can one expect filament length regulation? Consider the average lifetime of a monomer at the minus-end, $\langle\tau\rangle$. The dynamics of the last monomer that

has become the filament's tip on a filament of length L at time $t = 0$ is determined by Equation (2.37). The independence of neighboring subunits now allows to use $p_0(0) = 1 - \rho(L)$ and $p_1(0) = \rho(L)$ as initial conditions. From Equation (2.38) for the lifetime of a monomer it can be inferred

$$\langle \tau \rangle = \frac{\omega + \bar{\omega} + \beta + (\bar{\beta} - \beta)\rho(L)}{\omega\beta + \bar{\omega}\bar{\beta} + \beta\bar{\beta}}. \tag{3.22}$$

In this formulation, $\langle \tau \rangle$ is primarily a function of the motor density ρ, which, in turn, is a function of the filament length. The condition for a stationary filament length, $\langle \tau \rangle = 1$, can thus be formulated as a condition for ρ_c, the motor density at which polymerization is exactly balanced by depolymerization,

$$\rho_c := \rho(L_{\text{typ}}) \overset{!}{=} \frac{\beta + \omega + \bar{\omega} - \beta\bar{\beta} - \omega\beta - \bar{\omega}\bar{\beta}}{\beta - \bar{\beta}}. \tag{3.23}$$

Only if ρ assumes the value of ρ_c anywhere along the filament, a stationary unimodal length distribution can form.

Since $\rho(L)$ is a monotonically increasing function, that varies between 0 and $\omega/(\omega + \bar{\omega})$, one can use Equation (3.23) to determine the boundaries of the regime of length regulation. The filament length is expected to diverge if $\langle \tau \rangle > 1$ for arbitrary filament lengths. This is the case if ρ doesn't reach ρ_c anywhere along the filament, i.e. if $\rho_\infty < \rho_c$. From this condition, it can be inferred that

$$\beta_c = \frac{(\omega + \bar{\omega})^2 + \bar{\beta}(\omega + \bar{\omega}(\omega + \bar{\omega}))}{\omega(\omega + \bar{\omega}) - \bar{\omega} + \bar{\beta}(\omega + \bar{\omega})}. \tag{3.24}$$

This relation exactly reproduces the the numerical results for β_c that are presented in figure 3.9.

Equation (3.23) can also be used to derive a condition for the appearance of monotonically decreasing filament length distributions. In analogy to what was said, this is the case if $\rho(L) > \rho_c$ for all values of L. Since the motor gradient grows from 0 at the plus end, independently of the other parameters, the distribution becomes monotonically decreasing if $\rho_c < 0$. Let me note at this point that such a behavior is only possible if $\bar{\beta} > 0$.

Since the exact dependence of ρ on L is known, Equations (3.22) or 3.23 can be used to derive an explicit form of the typical filament length,

$$L_{\text{typ}} = \frac{-1}{\omega + \bar{\omega}}\log\left(1 - \rho_c/\rho_\infty\right), \tag{3.25}$$
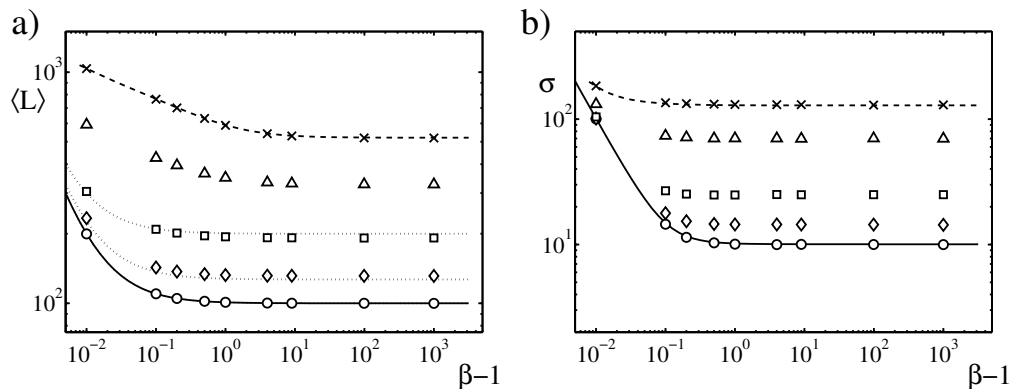
Figure 3.10: Mean values and variances of the steady state system size distributions. Symbols are from stochastic simulations, dashed lines follow from the analysis in Section 3.4.1, solid lines from the analysis in Section 3.4.3, and dotted lines represent the values of Equation (3.32) Parameters are $\omega = 0.01$ and $\gamma = 0$ ($\times$), 0.5 ($\triangle$), 1 ($\square$), 2 ($\diamond$), 10^5 ($\circ$). In all cases $\bar{\omega} = 0$ and $\bar{\beta} = 0$. [22] ©APS (2012)

which coincides well with the maximum of the length distribution as was shown above. Figure 3.10 also shows the quantitative agreement of analytic and numeric results.

A drawback of this approach lies in the fact that it doesn't provide a way to estimate the fluctuations of filament length about its typical value. To account for the fluctuations, I now consider the probabilities $p_0(L, \ell, \tau)$ and $p_1(L, \ell, \tau)$ for the site at the minus-end of the system, $i = L$, to be empty or occupied, respectively. These quantities depend on the actual filament length L as well as on the length ℓ the filament had when the site first reached the minus-end and on the time τ that has passed since this moment. Together with the probability $p_x(L, \ell, \tau)$ that the monomer was removed from the filament prior to time τ, one has again $p_0 + p_1 + p_x = 1$. The quantities $p_0(t)$ and $p_1(t)$ can again be derived from Equation (2.37), with initial conditions $p_0(0) = 1 - \rho(\ell - 1)$ and $p_1(0) = \rho(\ell - 1)$. Thus, the rate at which the minus-end site is removed at time τ after it has become the minus end can be determined by $\partial_\tau p_x$.

The average steady state removal rate $\beta_{\ell,L}$ of a site from a filament of length L that had become the minus-end when the system had length ℓ then reads

$$\beta_{\ell,L} = \int d\tau \left(\partial_\tau p_x(L, \ell, \tau) \right) \frac{\tau^{L-\ell}}{(L-\ell)!} e^{-\tau}. \tag{3.26}$$

In this expression, a Poissonian distribution was used to relate the time τ that has passed since the respective site has become the minus end to the length increase $L - \ell$ of the system through addition of sites at the plus end. The expression for the current in steady state is

then given by

$$j_L = P_L - \sum_{\ell=1}^{L+1} \beta_{\ell,L+1} P_\ell = 0 \quad . \tag{3.27}$$

Note, that this expression for the current is only valid in steady state. Otherwise the probabilities P_ℓ, $\ell = 1, \ldots, L+1$ would need to be taken at different time points and the calculation of the rate $\beta_{\ell,L}$ would involve an integration of the system's history. The steady state length distribution is obtained by solving Equation (3.27) numerically. As shown in Figure 3.10, the distribution now agrees well with the one obtained from simulations.

With these considerations, the complex time-dependent non-Markovian problem of filament dynamics was transformed into a non-local random walk. The analysis can be extend even more by calculating a recursion relation for the length dependent hopping rate a *classic* random walk would need to have to produce the same stationary distribution. Integrating Equation (3.26) and reformulating Equation (3.27), the position dependent rate $\beta_{\text{eff}}(L)$ can be given by [1]

$$\beta_{\text{eff}}(1) \quad = \quad \frac{\beta_{1,1}}{(1 - \beta_{0,1})} \tag{3.28}$$

$$\beta_{\text{eff}}(L+1) \quad = \quad \frac{\beta_{L+1,L+1}}{1 - \sum_{\ell=1}^{L-1} \beta_{\ell,L+1} \left(\prod_{i=1}^{L-\ell} \beta_{\text{eff}}(\ell+i) \right)} \quad . \tag{3.29}$$

3.4.2 Flux Balance to Access the Average Filament Length

For finite motor hopping rates, $\gamma > 0$, the states of neighboring subunits start to correlate. To account for these correlations, the correlation functions c_{11} and c_{01} have to be introduced as was already mentioned in the paragraph on the critical depolymerization rate β_c. Unfortunately, a-priori no information on these functions is available. Instead, in the stationary state, a flux-balance condition can be exploited. It reflects that the net flux of motors to the filament has to be compensated by a net flux from the filament. In the continuum limit, the flux-balance condition, as it is called henceforth, takes the form

$$j(L) - j(0) = \int_0^L dx \ (\omega(1 - \rho(x)) - \bar{\omega}\rho(x), \tag{3.30}$$

where L is the system length, j the motor current, and ρ the particle density profile in steady state. Since sites added to the system are empty, $j(0) = 0$. For $\bar{\beta} = 0$ and in steady

---

[1]The result is easily derived from Equation (3.27) when the ansatz $\mathcal{P}_L = \mathcal{P}_{L-1}/\beta_{\text{eff}}(L)$ is used.

state, the effective rate of site removal at the minus-end equals the flux of particles out of the system. At the same time it is equal to the rate of site addition. Hence, $j(L) = 1$. Since the density profiles differ markedly between the high and the low density phase, both cases shall be treated in turn. Be reminded that the analysis is limited to the case $\bar{\beta} = 0$.

The Low Density Phase, $\bar{\omega} > \omega$

The two-point correlation function $\langle n_i n_{i+1} \rangle$ depends quadratically on $\langle n_i \rangle$ as was shown in Figure 3.7 such that the particle current is given by the corresponding mean-field expression, $j = \rho + \gamma\rho(1-\rho)$. From $j(L) = 1$, it follows that in steady state $\rho(L) = 1/\gamma$. Equation (3.12) then leads to

$$L = \frac{2}{\omega + \bar{\omega}} - \frac{\gamma(\bar{\omega} - \omega) + \omega + \bar{\omega}}{(\bar{\omega} + \omega)^2} \ln\left(1 - \frac{\bar{\omega} + \omega}{\gamma\omega}\right). \tag{3.31}$$

A comparison to numerical results shows that this expression approximates the average system length well as long as $\gamma \gtrsim 2$, see Figure 3.11. The breakdown of relation (3.31) for $\gamma < 2$ was expected, because in that case $\rho(L) = 1/\gamma > 1/2$, which is outside the low density phase and the two-point correlations start to deviate from their mean-field values, see Figure 3.7.

**The High Density Phase, $\bar{\omega} < \omega$**

In the high density phase, the particle profile is prone to form a shock and the mean-field approximation for the current breaks down. Note, that if a shock emerges on the filament, the average site removal rate becomes independent of L when $L > x_s$. Consequently, the average system size in the high-density regime must lie below the shock position x_s. In this case, the right hand side of Equation (3.30) can be used to estimate the average system size L. For $x < x_s$, the particle density profile can be approximated by a linear gradient $\rho_{\text{lin}}(x) = \omega x/(1+\gamma)$, see Sect. 3.3. Replacing ρ by ρ_{lin} in Equation (3.30), the integral yields

$$L^2 - \frac{2(1+\gamma)}{\omega + \bar{\omega}} L + \frac{2(1+\gamma)}{\omega(\omega + \bar{\omega})} = 0. \tag{3.32}$$

As expected, this estimate of the system size agrees well with the values obtained from simulations for $\gamma \gtrsim 2$, see Figures 3.11 and 3.12. Remarkably, for sufficiently large values of γ the above estimate agrees rather well with the result obtained in the low density regime. In both cases, one finds $L = \omega^{-1}$ for $\gamma \to \infty$. Note, however, that solutions $0 \le L < \infty$ of Equation (3.32) only exist for $\gamma > 1 + 2\bar{\omega}/\omega$.
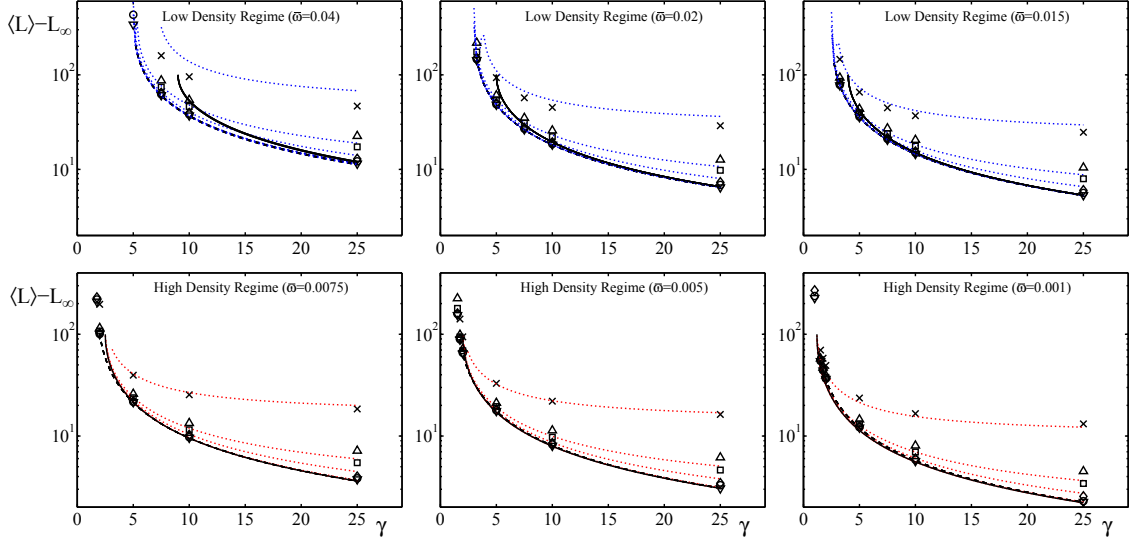
Figure 3.11: Average system sizes as a function of the hopping rate γ. Top row: $\bar{\omega} > \omega$ (low density regime), bottom row: $\bar{\omega} < \omega$ (high density regime). Symbols were obtained from stochastic simulations, dashed lines are given by Equation (3.31) and full lines by Equation (3.32). Blue dotted lines in the top row and red dotted lines in the bottom row show the average filament length if the correction terms from Equation (3.36) and Equation (3.35), respectively, are taken into account. Parameter values are $\omega = 0.01$, $\bar{\beta} = 0$, $\beta = 1.1$ ($\times$), 1.5 ($\triangle$), 2 ($\square$), 5 ($\diamond$), 10 ($\circ$), and 100 ($\triangledown$). Values of $\bar{\omega}$ are indicated in the panels. $L_\infty = \omega^{-1}$ is the system size in the limit $\gamma \to \infty$.
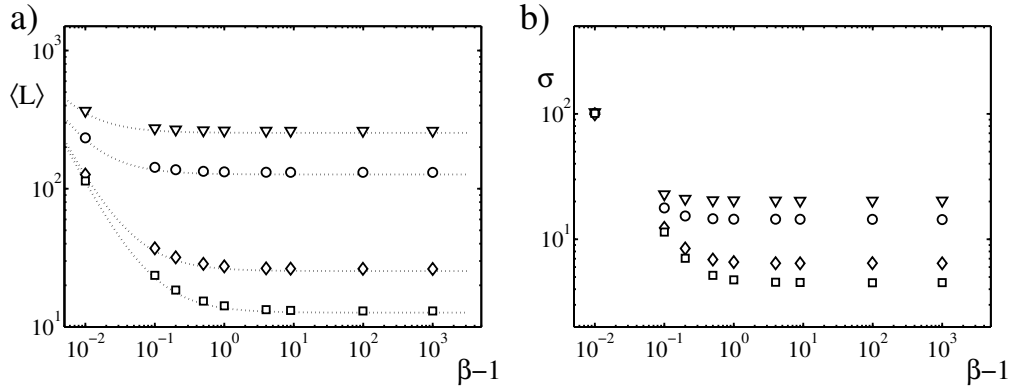
Figure 3.12: Mean values and variances of the steady state system size distributions. Symbols are from stochastic simulations, dotted lines are given by Equation (3.32). Parameters are $\gamma = 2$ and $\omega = 0.005$ ($\triangledown$), 0.01 ($\circ$), 0.05 ($\diamond$), 0.1 ($\square$). In all cases $\bar{\omega} = 0$ and $\bar{\beta} = 0$. [22] ©APS (2012)

Correction Terms

Analytic and numeric solutions for the average filament size agree well for fast monomer depolymerization rates. For smaller values of β, however, the quality of the approximation decreases. Nonetheless, expressions for the error can be estimated. I present here a derivation of correction factors that are based on heuristic arguments rather than rigorous derivations. The improvement is therefore expected to be mainly qualitative.

Let me start with considerations of the high density phase. A fully occupied lattice that gains monomers at rate 1 and looses them at rate $\beta \gtrsim 1$ has a finite average length. The dynamics of such a lattice can be described by a Random Walk with drift $v = 1 - \beta < 0$. The fluctuations in lattice length lead to a length distribution $\propto (1/\beta)^L$. The resulting average filament length amounts to $\langle L \rangle_{\mathrm{cap}} = 1/(\beta - 1)$.

Note furthermore that in steady state, the average motor density at the minus-end of a stationary filament has to be $\langle \rho(L) \rangle = 1/\beta$ to balance polymerization. If $\beta \gtrsim 1$, the motor density close to the minus-end approaches 1 and motors easily jam in this region. For some time, the lattice is then fully occupied, resulting in a constant depolymerization rate β. Following to what was said above, fluctuations then lead to a cap of length $1/(\beta - 1)$. If β is only marginally larger than 1, the size of these fluctuations can become very large and their effect on the total length distribution cannot be neglected anymore. Adding this term to the average filament length does not account for all deviations between numeric and analytic results.

If $1/\beta = \langle \rho(L) \rangle > \rho_\infty = \omega/(\omega + \bar{\omega})$, there is an additional loss of motors in the jamming region. Since the typical length of the jam region is given by $1/(\beta - 1)$ and the time scale of motor exchange is $\omega + \bar{\omega}$, the additional loss of monomers can be estimated to be approximatively

$$j_{\mathrm{jam}} = (\omega + \bar{\omega}) \, \langle L \rangle_{\mathrm{cap}} \left(\langle \rho(L) \rangle - \rho_\infty \right). \tag{3.33}$$

This additional motor current off the filament has to be balanced by motor transport into the cap region. The flux balance condition then gains an additional contribution and the left hand side of (3.30) then reads

$$j(L) - j(0) + j_{\mathrm{jam}} = 1 + \frac{\omega + \bar{\omega}}{\beta - 1} \left(\frac{1}{\beta} - \frac{\omega}{\omega + \bar{\omega}} \right). \tag{3.34}$$

Using the high density approximation, the average filament length L_{corr} is solution of

$$L_{\mathrm{corr}}^2 - \frac{2(1 + \gamma)}{\omega + \bar{\omega}} L_{\mathrm{corr}} + \frac{2(1 + \gamma)}{\omega(\omega + \bar{\omega})} \left(1 + \frac{\omega + \bar{\omega}}{\beta - 1} \left(\frac{1}{\beta} - \frac{\omega}{\omega + \bar{\omega}} \right) \right) = 0. \tag{3.35}$$

From Figure 3.11, it is found that the correction terms are in surprisingly good agreement with numerical results. I want to conclude with the remark that both correction terms rapidly vanish when $\beta \gg 1$.

The same correction terms can also be used to derive an approximation in the low density case. The average filament length is then given by

$$L = \frac{2}{\omega + \bar{\omega}} - \frac{\gamma(\bar{\omega} - \omega) + \omega + \bar{\omega}}{(\bar{\omega} + \omega)^2} \ln\left(1 - \frac{\rho_{\text{corr}}}{\rho_\infty}\right). \tag{3.36}$$

with $\rho_{\text{corr}} = \frac{1}{2\gamma}\left(\gamma + 1 - \sqrt{(\gamma - 1)^2 - 4\gamma\,j_{\text{cap}}}\right)$ and $j_{\text{cap}} = \frac{\omega + \bar{\omega}}{\beta - 1}\left(\frac{1}{\beta} - \frac{\omega}{\omega + \bar{\omega}}\right)$. Figures 3.10, 3.12, and 3.11 show that the corrections capture the deviations in the low density case qualitatively, but are less quantitative than in the high density case.

3.4.3 The Limit of Infinitely Fast Molecular Motors

In the limit of infinite motor hopping rate, $\gamma \to \infty$, again analytic expressions for the average filament length and the fluctuations can be deduced. The form of the particle distribution is known at any time in this case: the system is divided into a region of length M starting at site $i = 1$ that is void of particles and a region of length $N = L - M$ extending to the minus-end in which every site is occupied. This form allows an exact mapping of the length dynamics onto a two-dimensional Random Walk. For $M > 0$ and $N > 0$, the probability $P_{M,N}$ evolves according to

$$
\begin{aligned}
\dot{P}_{M,N} = {}& P_{M-1,N} - P_{M,N} + \beta\left(P_{M,N+1} - P_{M,N}\right) \\
& + \omega\left((M+1)P_{M+1,N-1} - MP_{M,N}\right) \\
& + \bar{\omega}\left((N+1)P_{M-1,N+1} - NP_{M,N}\right)
\end{aligned}
\tag{3.37}
$$

while

$$\dot{P}_{M,0} = P_{M-1,0} - P_{M,0} + \beta P_{M,1} - \omega M P_{M,0} + \bar{\omega}P_{M-1,1} + \bar{\beta}\left(P_{M+1,0} - P_{M,0}\right) \quad \text{for} \quad M > 1 \tag{3.38}$$

$$\dot{P}_{0,N} = -P_{0,N} + \beta\left(P_{0,N+1} - P_{0,N}\right) + \omega P_{1,N-1} - \bar{\omega}N P_{0,N} \quad \text{for} \quad N > 1 \tag{3.39}$$

and

$$\dot{P}_{1,0} = -P_{1,0} + \beta P_{1,1} - \omega P_{1,0} + \bar{\omega} P_{0,1} \tag{3.40}$$

$$\dot{P}_{0,1} = -P_{0,1} + \beta P_{0,2} + \omega P_{1,0} - \bar{\omega} P_{0,1} \tag{3.41}$$

$$P_{0,0} = 0. \tag{3.42}$$

To analyze this two-dimensional random walk, the marginal distributions $P_M^{\mathrm{I}} = \sum_{N=0}^{\infty} P_{M,N}$ and $P_N^{\mathrm{II}} = \sum_{M=0}^{\infty} P_{M,N}$ are studied. Using a mean-field approximation to write $\sum_{N=0}^{\infty} N P_{M,N} = \langle N \rangle P_M^{\mathrm{I}}$ and $\sum_{M=0}^{\infty} M P_{M,N} = \langle M \rangle P_N^{\mathrm{II}}$ from Equations (3.37)-(3.42) dynamic equations for the marginal distributions can be derived. Here, $\langle M \rangle$ and $\langle N \rangle$ denote the expectation values of M and N, respectively, that is, $\langle M \rangle = \sum_{M=0}^{\infty} M P_M^{\mathrm{I}}$ and $\langle N \rangle = \sum_{N=0}^{\infty} N P_N^{\mathrm{II}}$ Explicitly,

$$\dot{P}_M^{\mathrm{I}} = j_M^{\mathrm{I}} - j_{M+1}^{\mathrm{I}} \tag{3.43}$$

$$\dot{P}_N^{\mathrm{II}} = j_N^{\mathrm{II}} - j_{N+1}^{\mathrm{II}} \tag{3.44}$$

with

$$j_M^{\mathrm{I}} = P_{M-1}^{\mathrm{I}} - \omega M P_M^{\mathrm{I}} + \bar{\omega} \langle N \rangle P_{M-1}^{\mathrm{I}} - \bar{\beta} P_0^{\mathrm{II}} P_M^{\mathrm{I}} \tag{3.45}$$

$$j_N^{\mathrm{II}} = -\beta P_N^{\mathrm{II}} + \omega \langle M \rangle P_{N-1}^{\mathrm{II}} - \bar{\omega} N P_N^{\mathrm{II}} \tag{3.46}$$

and no-flux boundary conditions $j_0^{\mathrm{I}} = 0$ and $j_0^{\mathrm{II}} = 0$, respectively. Equation (3.44) thus uncouples from Equation (3.43) and can be analyzed independently. Using P_0^{II} as an input to Equation (3.43), the dynamics of the marginal distributions can be solved in turn. Their respective solutions in stationary state can be given in the form

$$P_M^{\mathrm{I}} = \left(\prod_{m=1}^{M} \frac{(1 + \bar{\omega} \langle N \rangle)}{\bar{\beta} P_0^{\mathrm{II}} + m\omega} \right) P_0^{\mathrm{I}} \tag{3.47}$$

$$P_N^{\mathrm{II}} = \left(\prod_{n=1}^{N} \frac{\omega \langle M \rangle}{\beta + \bar{\omega} n} \right) P_0^{\mathrm{II}}, \tag{3.48}$$

where the values P_0^{I} and P_0^{II} are determined from normalization of the marginal distributions. For the special case $\bar{\beta} = 0$, the dynamic equations for the marginal distributions separate completely and the expression for P_M^{I} simplifies to

$$P_M^{\mathrm{I}} = \frac{(1 + \bar{\omega} \langle N \rangle)^M}{M! \omega^M} P_0^{\mathrm{I}}. \tag{3.49}$$

These results can now be used to solve Equations (3.43) and (3.44) self-consistently. While the general result is rather cumbersome and not very revealing, it takes a simple form in the case $\bar{\omega} = 0$. Explicitly, $P_M^I = \frac{\omega^{-M}}{M!}e^{\left(-\frac{1}{\omega}\right)}$ and $P_N^{II} = (\beta - 1)\beta^{-N+1}$. Hence, the mean system size and the corresponding variance are given by

$$\langle L \rangle_\infty = \langle M \rangle + \langle N \rangle = \frac{1}{\omega} + \frac{1}{\beta - 1} \tag{3.50}$$

and

$$\sigma_\infty^2 = \frac{1}{\omega} + \frac{\beta^2}{(\beta - 1)^2}, \tag{3.51}$$

respectively. Comparison of these results with numerical simulations shows a good agreement, see Figure 3.11.

This result can be connected to the result of the flux-balance analysis of the high density case presented in Sect. 3.4.2. In that analysis, the system length was obtained by considering only the region in front of the shock. In the above discussion it was shown that the region behind the shock contributes $1/(\beta - 1)$ to the average system length. Adding this term to the average length obtained from Equation (3.32), an excellent agreement with simulation results is found, see Figure 3.10. Note, that this argument holds in a strict sense only in the case $\bar{\omega} = 0$ since otherwise, the density behind the shock is smaller than 1. A generalization leads to the correction terms discussed above.

Beyond the Flux-Balance Condition

For the case $\gamma = \infty$, an expression not only for the average but also for the fluctuations of filament length could be derived. One might expect that this description also holds in an approximative way for large but finite values of γ. To estimate the position dynamics of the shock, assume that it performs a biased random walk with hopping rates that depend on the position. The shock moves to the right, whenever a monomer is added to the plus end, thus the stepping rate of the walker to the right is 1. The effective hopping rate to the left is given by the quotient of the motor current to the site i = M, $\gamma\rho(M-1)(1-\rho(M))$ and the shock height $1 - \rho(M)$. The the motor distribution in the partially occupied domain is approximated by a linear profile and we use ρ_{lin}. Again, a mean-field assumption is applied and the two domains are considered to be independent of each other. In first order in $1/\gamma$ one finds a correction term for L_∞ and σ_∞ of $1/(\gamma\omega)$. Assuming that correlations between

the two regions are of the same order, one finds for $\bar{\omega} = 0$ [20]

$$\langle L \rangle = \langle L \rangle_\infty + \frac{1}{\gamma \omega} \tag{3.52}$$

and

$$\sigma^2 = \sigma_\infty^2 + \frac{2}{\gamma \omega} \quad . \tag{3.53}$$

Interestingly, the results generalize to the case of $\bar{\omega} > 0$ if the hopping rate γ is sufficiently large, as can be seen in Figures 3.14 and 3.13. The arguments used above hold best if a pronounced shock is established, that is, if γ is large and $\bar{\omega}$ is small. It can be concluded that the shock dynamics dominates the length of the system in these cases. Note that the scheme that was employed here to determine the average filament length differs fundamentally from the flux-balance condition that was used above. While the flux-balance-condition integrates over the whole filament, the movement of the shock is derived from a local condition on the motor density.

The flux-balance-condition usually determines the filament length with higher accuracy as compared to the shock position, but it does not provide an expression for the width of the distribution. The dynamics of the shock position on the other hand describes the fluctuations of filament length for large γ with satisfying precision.

3.5 Results

3.5.1 The Phase Diagram

At this point of the analysis, the phase diagram of the system for $\bar{\beta} = 0$ can be drawn. Let me recall that, in semi-infinite systems with $\beta = 0$, the average particle density increases monotonically and approaches asymptotically the value $\rho_\infty = \omega/(\omega + \bar{\omega})$. This suggests the existence of a situation in which filaments grow without limits. Such a behavior was expressed by a critical particle-induced site removal rate β_c which was defined such that the system size diverges for $\beta < \beta_c$. A rough approximation can be given by $\beta_c \rho_\infty = 1$. While this estimate gives a lower limit for β_c in the case $\gamma = 0$, this is no longer true for finite hopping rates $\gamma > 0$, see Figure 3.9. The deviations simply reflect that particles can pile up towards the minus-end as discussed above. Looking at the graph, one finds that β_c increases monotonically with an increasing particle detachment rate $\bar{\omega}$ and decreases monotonically with increasing values of γ.
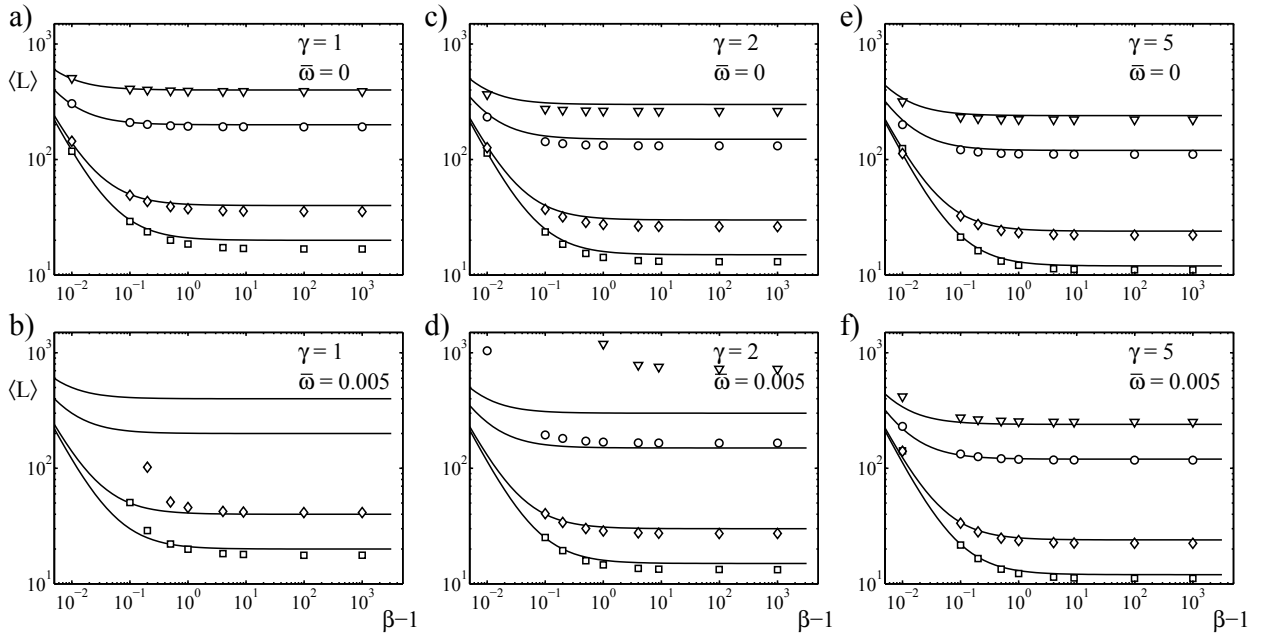
Figure 3.13: The average system length as a function of $\beta - 1$. Rates for γ and $\bar{\omega}$ are indicated for every graph. Symbols represent the numerical results for $\omega = 0.1$ ($\square$), 0.05 ($\diamond$), 0.01 ($\circ$), and 0.005 ($\triangledown$). Solid lines represent the approximation by Equation (3.53), values of ω decrease from 0.1 (lower line) to 0.005 (upper line). Data in Figure b) was already shown in Figure 3.12,a) when compared to the results of the high-density approximation.
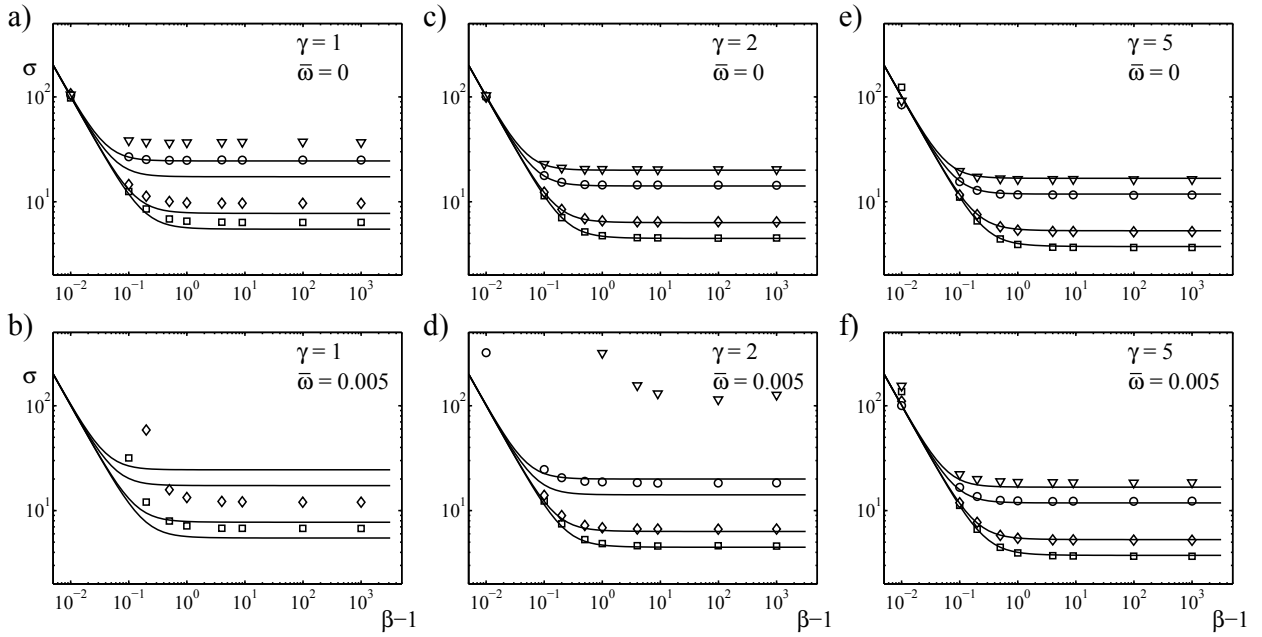
Figure 3.14: The standard deviation of the stationary length distribution as a function of $\beta - 1$. Rates for γ and $\bar{\omega}$ are indicated for every graph. Symbols represent the numerical results for $\omega = 0.1$ ($\square$), 0.05 ($\diamond$), 0.01 ($\circ$), and 0.005 ($\triangledown$). Solid lines represent the approximation by Equation (3.53), values of ω decrease from 0.1 (lower line) to 0.005 (upper line). Data in Figure b) was already shown in Figure 3.12,b) without an analytic expression.
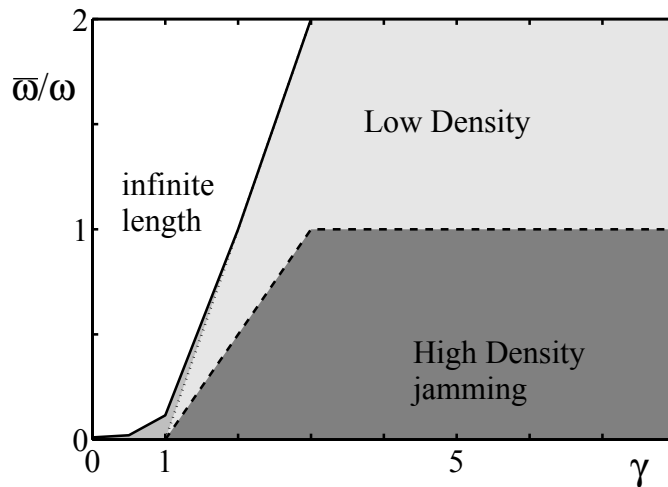
Figure 3.15: Phase diagram as a function of γ and $\bar{\omega}/\omega$ in the limit $\beta \to \infty$ and for $\bar{\beta} = 0$. The solid line is the result of stochastic simulations, the dashed line is given by $\bar{\omega}/\omega = \gamma - 1$, see text. The dotted lines mark the domain of applicability of Equation (3.32) for the average system length. Note, that for $\gamma = 0$ the system size diverges for $\bar{\omega} \geq \bar{\omega}_c = \omega^2/(1-\omega) > 0$. [22] ©APS (2012)

In the case $\gamma = 0$, the explicit expression for L_{typ}, Equation (3.25), can be used to estimate β_c. These values for β_c agree very well with our numerical results, see Figure 3.9. In the opposite limit $\gamma \to \infty$, one deduces from the expression for $\langle L \rangle_\infty$ that in this case $\beta_c = 1$.

For values $0 < \gamma < \infty$, no analytic expression for the average system length is available which takes into account the dependence of the average length on the depolymerization rate. Still, the value of β_c can be estimated without an explicit expression, see Section 3.4. While the numeric values differ for $\gamma > 0$ from the expression given in Equation (3.20), it still gives a reasonable estimate of the critical value $\bar{\omega}_c$ at which β_c diverges for all values of $\gamma \geq 1$ that were examined, see Figure 3.9.

In Figure 3.15, the phase diagram is displayed as a function of γ and $\bar{\omega}/\omega$ in the limit $\beta \to \infty$. One finds that the region of diverging system length persists even in this limiting case, which can be explained by the existence of a critical ω_c above which the equilibrium motor density is not high enough to restrict filament growth. However, the phase diagram hardly changes for values of β down to approximately $3/2$.

The results of the flux-balance analysis can be used to determine the boundary between the phases of finite and diverging system size. For $\bar{\omega} > \omega$, one obtains from Equation (3.31) in the limit $L \to \infty$ that $\bar{\omega}/\omega = \gamma - 1$. This exactly gives the numerical result for $\bar{\omega} > \omega$ and continues to be a good approximation of the phase boundary in the high motor density

regime. For $\bar{\omega} < \omega$, the solution of Equation (3.32) for the average system size exists only for $\bar{\omega}/\omega < (1 + \gamma)/2 - 1$. Remarkably, in the region $\bar{\omega} < \omega$ violating this condition, the average system length is well approximated by Equation (3.31), see also Figure 3.11.

3.5.2 Quality of Length Regulation

In a biological context, a cell might want to tightly control the length of filaments. That is, the width σ of the length distribution should be small compared to the average length $\langle L \rangle$. To discuss this property, I define the relative width or the quality Q of system size regulation as $Q = \sigma/\langle L \rangle$. For an exponential distribution $Q = 1$, while unimodal distributions have $Q < 1$. In Figure 3.16, Q is presented as a function of the particle-induced depolymerization rate β and the particle hopping rate γ. Independently of the particle detachment rate $\bar{\omega}$, it can be seen that the average system size is better defined with increasing γ, except in a small region at $\beta \gtrsim 1$. The value of Q saturates when γ is of the same order as the rate of system growth at the plus end. For $\bar{\beta} = 0$ and $\bar{\omega} = 0$, the saturating value can be obtained by using the results of Sect. 3.4.3 and is given by $Q_\infty = \sqrt{\omega(1 + \omega)}$.

This expression suggests that in the limit $\gamma \to \infty$ and $\beta \to \infty$, the length distribution is maximally peaked when $\omega \approx 0$. To understand this behavior, note, that with increasing length of the system, the number of possible processes leading to subunit removal increases as the attachment of a motor to any site along the system will result in immediate site removal at the minus end. In steady state, the average site removal rate equals 1, such that the mean filament length behaves as $\sim \omega^{-1}$. The law of large numbers then implies that the distribution of removal events has a variance of ω^{-1}. The relative width Q_∞ of the distribution consequently goes to 0 when $\omega \to 0$.

To see why Q increases as $\beta \to 1$, let us note that this limit is similar to the limit $\gamma \to \infty$. Indeed, since sites are removed from the minus-end at a very slow rate, there exists again a region with $\rho \approx \rho_\infty$. As I discussed in Section 3.4.3 filament length in this region is exponentially distributed with mean (and thus variance) $1/(\beta - 1)$. The other region should have a size of order $1/\omega$ and its variance is $1/\omega$, see Section 3.4.3. Thus, $Q = \sqrt{\omega(\omega + (\beta - 1)^2)}/(\omega + \beta - 1)$, which approaches 1 as $\beta \to 1$.

3.6 Summary and Further Considerations

Motivated by experiments on microtubules, a driven lattice gas model for the length dynamics of treadmilling filaments in presence of molecular motors was analyzed in this chapter. It included a finite binding affinity of molecular motors and a motor induced site removal
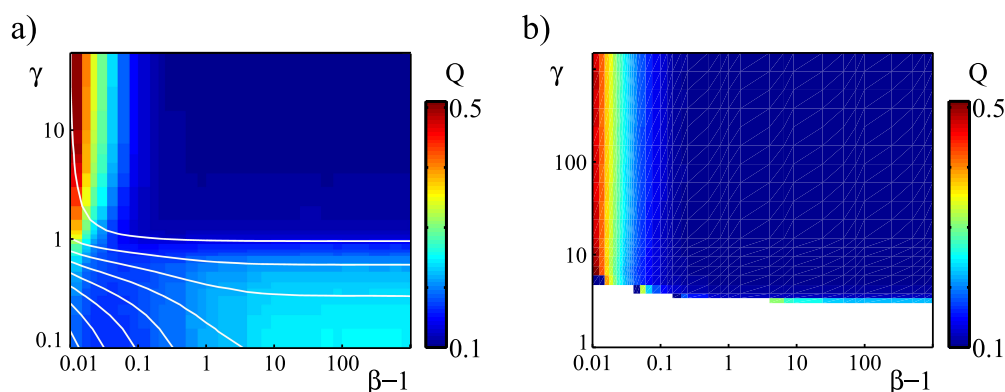
Figure 3.16: The quality $Q = \sigma/\langle L \rangle$ of size regulation as a function of the particle-induced site removal rate β and the particle hopping rate γ for $\omega = 0.01$ and a) $\bar{\omega} = 0$ and b) $\bar{\omega} = 0.02$. White lines connect points of equal filament length. [22] ©APS (2012)

at the minus-end. Two phases were found, one of bounded and one of unbounded growth, respectively. Critical values for the rate of motor-induced site removal and the detachment rate of motors were identified that separate both phases. In the limits $\gamma = 0$ and $\gamma \to \infty$, random walks could be introduced that accurately describe the corresponding steady state size distributions.

As was shown, mean-field arguments for the correlation of motor density gave a very good understanding of the behavior of semi-infinite systems. The deduced expression for the motor density gradient along filaments could explain the behavior of the full system qualitatively. Invoking another mean-field argument to turn this gradient into a length dependent depolymerization rate showed substantial differences between analytic and numeric results, in parallel to what was discussed for the two-states model in Chapter 2.

The case of vanishing hopping rate, $\gamma = 0$, was reduced to a special case of the two-states model that was discussed in Chapter 2. In this form, it could be analyzed in depth and expressions for the mean and variance of the stationary filament length distribution could be derived. The complex, time dependent and non-Markovian jump process that could be defined for the dynamics of the filament length was thus mapped to a classic random walker in an external potential.

For the general case of $0 < \gamma < \infty$, two different descriptions of filament length dynamics were invoked. One relies on a flux-balance condition, exploiting that the net flux of motors to the filament is a function of filament length. The other generalized the case of infinite motor speed, $\gamma \to \infty$, based on the observation that the filament length dynamics is dominated by the position of a shock on the filament. While the first approach gives good approximations of the filament length for most parameters, the second provided also an approximation for

length fluctuations in the parameter regime where shocks are expected to form.

In Figure 3.11 it was shown that an educated guess for the influence of the depolymerization rate β gave a correction to the results of the flux-balance condition that agrees surprisingly well with the average system size in the limit of large γ. Based on heuristic arguments and numerical investigations, correction terms could also be obtained for $0 < \gamma < \infty$ and $\bar{\omega} > 0$ [20]. Beyond the flux-balance condition, the results in the case $\gamma \to \infty$ could be generalized to finite values of the particle hopping rate and a good estimate of the length distribution's variance [20] was obtained. It will be challenging to give sound derivations of these results.

Having access to these approximations, the phase diagram of the filament system could be specified. Besides a region of unbounded growth, three distinct types of behavior could be identified. In the low density regime, motors are not expected to form a shock and the flux balance condition employing a smooth motor gradient along the filament gives a good approximation of the average filament length. In the high density regime, motors are prone to shock formation and the system size follows the shock dynamics on the lattice. However, both descriptions fail to explain the regime of low motor speed ($\gamma < 1$) and high motor binding affinity ($\bar{\omega} \ll \omega$). There, filament length is restricted by motor accumulation rather than motor movement, similar to the two-states model discussed in Chapter 2. Fluctuations have an important influence on the filament length in this regime.

The quality of filament length regulation was quantified by a dimensionless number $Q = \sigma/\langle L \rangle$. Interestingly, this value proved to be robust to variations in parameters if the motor hopping rate is larger than 1 and the depolymerization rate of occupied subunits $\beta \gtrsim 1.1$. For rates beyond these limits, Q does not substantially deviate from its saturation value $Q_{\infty} = \sqrt{\omega(1+\omega)}$ for large γ and β. Since ω can be assumed to be proportional to the motor concentration *in vivo*, this might be relevant for microtubule length regulation in living cells.

The results of these calculations can be tested in experiments. Treadmilling microtubules have been exposed to the minus-end directed motor Kar3p that increases the rate of subunit removal [159, 160]. To measure the length distribution of an individual microtubule, one could employ a microfluidic device that on one hand traps the filament and on the other hand allows one to control the concentration of cytosolic motors and tubulin subunits. To this purpose a cross-flow geometry similar to the one used in Ref. [163] to study fluctuations of actin filaments could be used.

A finding of possible biological relevance is the robustness of the quality of size regulation to changes in the particle-induced site removal rate or the particle hopping rate. It shows that a cell would not need to fine tune motor properties in order to achieve the filament

length distribution with the smallest dispersion. This could be used, for example, during early stages of development of the fruit fly *D. melanogaster*, when the embryo still consists of one cell with many nuclei, the syncytium. During mitosis, the size of the spindle separating the chromosome cannot be bounded by a cell membrane and has to be internally regulated through the length of the constituting microtubules. Since it was shown that the average system length is essentially set by the motor attachment rate, the embryo could regulate the spindle size by changing the concentration of motors in the cytosol.

4 Actin Dynamics in the Cell Cortex

Experiments reported in this section were carried out by Marco Fritzsche at the London Center for Nanotechnology (LCN), London, UK.

4.1 Introduction to the Cell Cortex

In this chapter, I investigate different models describing the dynamics of actin polymers within a living cell. In eucaryotic cells, filamentous actin forms a dense network underneath the membrane. The so-called actin cortex is tethered to the cell membrane by specialized proteins. It has a depth of $100 - 500 \, nm$ and its density drops rapidly with distance from the cell membrane [1]. The membrane itself is composed of a double layer of lipids and proteins [27]. Since the lipid membrane is rather fragile and its size is many times the surface of the cortex, it is the cortex that defines the shape of the cell and balances the external forces. The control of its dynamics and its mechanical properties is thus of vital importance for the cell.

Below, experimental results from experiments on cervical HeLa and Melanoma M2 cells are presented. These cells have a typical volume of $1 - 5 \cdot 10^3 \, \mu m^3$. At the surface of both cell types, an effect called 'blebbing' can be observed. In this process, parts of the membrane detach from the cortex and forms bubbles or blebbs that are filled with cytosol but do not possess a proper cortex. Subsequently, the cortex is regrown under the membrane and the tension that builds up in the intact cortex retracts the blebb [164]. Blebbing cells therefore constitute a model system to study the formation of the actin cortex *in vivo*. Here, however, I concentrate on the stationary properties of filament systems. Experiments presented here were thus carried out in stationary parts of the actin cortex

Note that actin and many accessory proteins are small molecules that diffuse rapidly within the cytosol. The diffusion constant for such proteins can be estimated to be of the order of $D \approx 50 \, \mu m^2/s$ or larger *in vitro* [1, 165]. In living cells, the diffusion of molecules is obstructed but actin monomers were still measured to move with $D = 25 \, \mu m^2/s$ *in vivo* [61] and are found throughout the whole cell. Filamentous actin is much less mobile since it is rapidly cross-linked in the cortex, thus fixing the positions of monomers. Filaments can still

translocate due to their treadmilling. In a living cell, roughly half of the actin is monomeric and half of it is bound in the cell cortex [27]. F-actin forms a dense network with a meshsize of about 100-200 nm [166], see Figure 4.1 for examples.

The main question of this chapter is how the principles of active polymerization that were studied in the previous chapters lead to the homeostatic cortex of living cells. In a first step, the nucleation of filaments in a finite volume is investigated by stochastic lattice models as introduced above. It will be shown that the results of Chapter 2 remain qualitatively correct when the monomer number is limited and the filament number is dynamic. Then, experimental findings are presented suggesting that cortex turnover occurs on two different timescales. Analytical calculations illustrate the experiment's capacity to unravel microscopic details of the polymerization process. Finally, I numerically analyze three microscopic scenarios providing molecular scenarios compatible with experimental findings.

In the remainder of this chapter, it is assumed that monomers show rapid diffusion in the investigated volume and no spatial gradients of monomer concentration is established. Furthermore, mechanical properties of the filaments are not considered. In particular, no forces or interactions between filaments are taken into account. Filaments are mobile only by treadmilling through the cytosol.

4.2 A Finite Size Model

First, the dynamics of an ensemble of filaments will be investigated by means of stochastic simulations. The polymerization and depolymerization occurs in the same way as described for the two- and three-states models discussed in Chapter 2. Filament subunits exist in either of two or three different states with characteristic polymerization- and depolymerization rates. In contrast to the above analysis, the rates of monomer addition are not constant but depend on the concentration of available monomers in the solution. In this chapter, the case of a linear dependency is considered, $k_{on} = r_{on} c$. The results do not qualitatively change if a non-linear dependency of the monomer addition rate is assumed, for example in the form of a Michaelis-Menten dynamics. In the following, two situations are considered: First, the evolution of a system with a fixed number of filaments is investigated. Then the *de novo* nucleation and disappearance of filaments is considered.
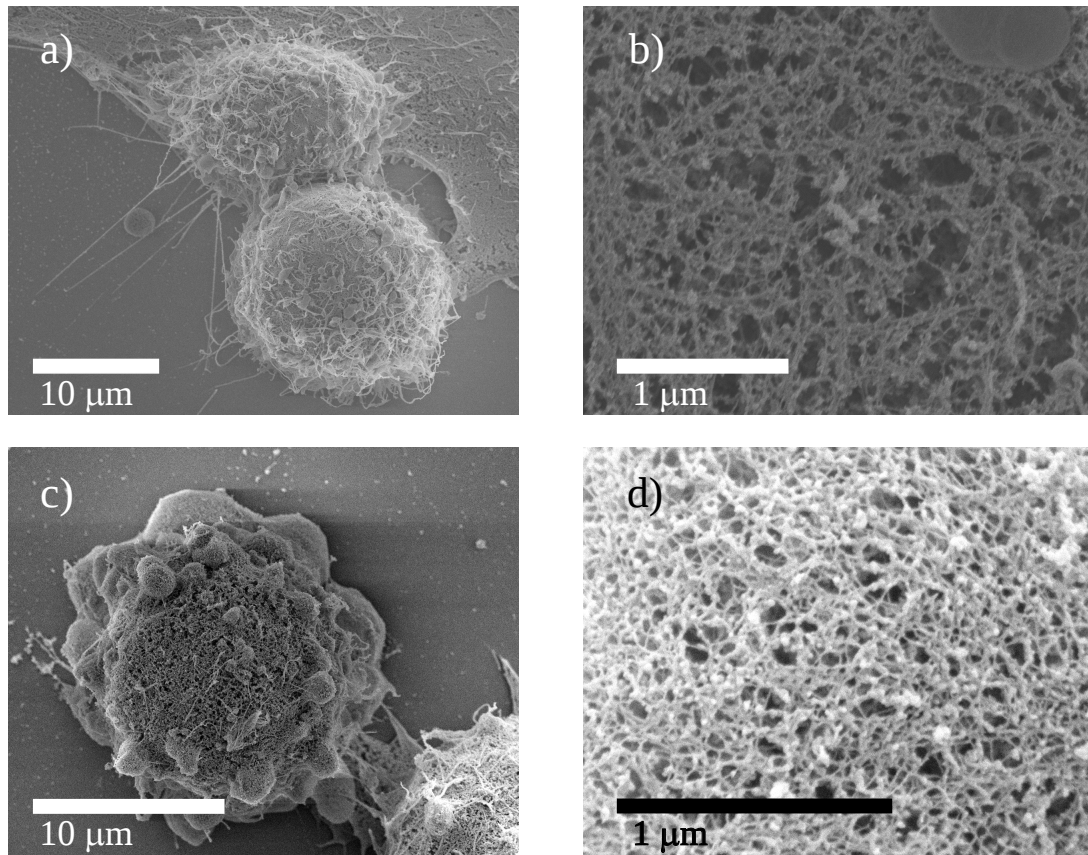
Figure 4.1: Electron micrographs of the cell cortex of HeLa (top row) and melanoma M2 (bottom row) cells. The cortex of the cells was fixed by treatment with glutaraldehyd and the membrane was dissolved prior to image acquisition. a) The entire cortices of two Hela cells. b) A magnified view on the mesh of the actin filaments. The disruption of the filaments might be due to the treatment of the cells. c) The cortex of a single melanoma M2 cell in an overview. The small spherical structures are blebbs with regrowing actin cortex. d) A magnification of the structure of the cell cortex outside a blebb. (Images were provided by M.Fritzsche.)

4.2.1 A Finite Reservoir of Monomers and a Constant Number of Filaments

In the following, an ensemble of filaments sharing a common pool of monomers is considered. The overall number of monomers in the system is fixed. It is assumed that the solution is well-mixed such that the monomer concentration is homogeneous. Hence, all filaments polymerize at the same velocity. As in the analysis presented in Chapter 2, all monomers are assumed to be in the T-state. This corresponds to a rapid exchange of ADP by ATP on the actin monomers in the living cell which could be provided by additional proteins such as profilin.

Simulations are carried out for a volume of $1\mu m^3$. Hence, a concentration of $1\mu M$ corresponds to

$$1\mu M = 10^{-21}\frac{\text{mol}}{\mu m^3} \approx 600\mu m^{-3} \quad .$$

Consider now a situation in which the number of nuclei is fixed to $N_{\text{fil}} = 1000\mu m^{-3} \approx 1.66\mu M$. Figure 4.2 shows the mean and the standard deviation of the filament length distribution as well as the monomer concentration as a function of time.

In all three cases, the initial monomer concentration determined the stationary filament length. The average length as well as the monomer concentration relax on a much shorter timescale to their stationary values than the second moment of the distribution. Note the logarithmic scale on the time axis. The average filament length and the monomer concentration are connected via Equation (2.1).

For the example parameters from Chapter 2 (see Figure 2.5) and for the rates of Kuhn et al. [29] (left and center columns), the standard deviation of the distribution does not reach the value of the average length, indicating a unimodal filament length distribution as was found for a single filament. The first parameter set (left) shows an increase in the monomer concentration on the time scale of $\sim 100s$, which corresponds to the timescale on which subunits in the filament turn from the ATP- to the ADP- bound state. So the monomer concentration after 10s is close to the value of a pure ATP-monomer system. When monomers are in the D-state, they are readily released from the filament tip and replenish the monomer pool again. After roughly 100s, the monomer concentration has reached its steady state. The increase in monomer concentration is also present in the case of the Kuhn parameters (center) but less pronounced and barely visible in the fluctuations. For the three state model with end-induced phosphate release, the average and the standard deviation of the stationary length distribution are very close, indicating that the corresponding length distribution is again exponential.
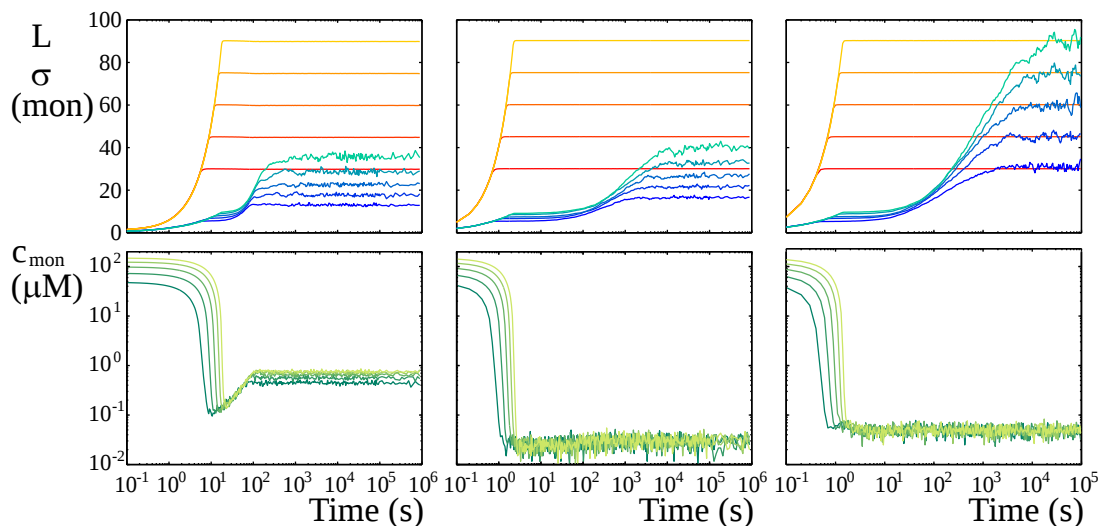
Figure 4.2: Top row: Average filament length and the distribution's standard deviation as a function of time. Bottom row: The monomer concentration as a function of time. Three different parameter sets are used: For the left column, rates were used that correspond to the two state model in Figure 2.5 (squares). The data for the center column was generated using the rates that correspond to the experimentally determined rates of Kuhn and Pollard for the two-states model. The right column shows the results when the rates were applied that were found by Fujiwara et al. and Jégou et al. for the three-states model. The initial monomer concentration increases with decreasing color saturation from $c_0^T = 50\,\mu M$ (dark colors) through $75\,\mu M$, $100\,\mu M$, $125\,\mu M$ to $150\,\mu M$ (light colors). The average filament length assumes its stationary value much earlier than the width of the distribution. The monomer concentration reaches its stationary value on the timescale of phosphate release. Rates are given in Table 4.1.

	Fig. 4.2 left	Fig. 4.2 center	Fig. 4.2 right	Fig. 4.3 left	Fig. 4.3 center	Fig. 4.3 right	Fig. 4.2.2 squares	Fig. 4.2.2 circles	Fig. 4.2.2 triangles
$r_{\mathrm{on}}^{\mathrm{T}+}$	1	7.4	11.6	1	7.4	11.6	1	7.4	11.6
$r_{\mathrm{on}}^{\mathrm{T}-}$	0.01	0.56	1.3	0.01	0.56	1.3	0.01	0.56	1.3
$r_{\mathrm{on}}^{\mathrm{P}+}$	10^{-5}	3.8	3.4	10^{-5}	3.8	3.4	10^{-5}	3.8	3.4
$r_{\mathrm{on}}^{\mathrm{P}-}$	$2\cdot10^{-5}$	0.16	0.11	$2\cdot10^{-5}$	0.16	0.11	$2\cdot10^{-5}$	0.16	0.11
$r_{\mathrm{on}}^{\mathrm{D}+}$			2.9	0	0	2.9	0	0	2.9
$r_{\mathrm{on}}^{\mathrm{D}-}$			0.09	0	0	0.09	0	0	0.09
$k_{\mathrm{off}}^{\mathrm{T}+}$	0.5	0.9	1.4	0.5	0.9	1.4	0.5	0.9	1.4
$k_{\mathrm{off}}^{\mathrm{T}-}$	0.005	0.19	0.8	0.005	0.19	0.8	0.005	0.19	0.8
$k_{\mathrm{off}}^{\mathrm{P}+}$	0.5	1.5	0.2	0.5	1.5	0.2	0.5	1.5	0.2
$k_{\mathrm{off}}^{\mathrm{P}-}$	1	0.26	0.02	1	0.26	0.02	1	0.26	0.02
$k_{\mathrm{off}}^{\mathrm{D}+}$			5.8	0	0	5.8	0	0	5.8
$k_{\mathrm{off}}^{\mathrm{D}-}$			0.24	0	0	0.24	0	0	0.24
ω_{TP}	0.05	0.0068	0.3	0.05	0.0068	0.3	0.05	0.0068	0.3
ω_{PD}			0.0068	0	0	0.0068	0	0	0.0068
$\bar{\omega}_{\mathrm{PD}}^{+}$			1.8	0	0	1.8	0	0	1.8
$\bar{\omega}_{\mathrm{PD}}^{-}$			18	0	0	18	0	0	18
N_{fil}	1000	1000	1000						
ν				10^6	10^6	10^6	var	var	var
n_{min}				3	3	3	3	3	3
V	2	2	2	1	1	1	1	1	1
T	10^6	10^6	10^5	10^5	10^5	10^5	10^4	10^4	10^4
c_0^T	50 - 150	50 - 150	50 - 150	50 - 150	50 - 150	50 - 150	100	100	100

Table 4.1: Table of parameter sets used in the first section. When a two-states model was employed, the P-state was assumed to be the unstable subunit state and the D-state was omitted. All rates r are given in units of $(s\,\mu M)^{-1}$, all rates k, ω and ν are given in s^{-1}. Simulation volume V is measured in μm^3, maximum simulation time T in s. All concentrations are given in μM. The constant number of filaments, N_{fil}, and the minimal nucleus size, n_{min}, are given as integer values, see text.

Interestingly, in all three cases the stationary monomer concentration seems to be largely independent of the initial amount of monomers present in the simulated volume. The average filament length, on the other hand side, is directly proportional to the total monomer number. The presented calculations show that the stationary monomer concentration is mainly determined by the addition- and removal rates of the monomers, while the average filament length follows from the number of filaments. Since the active nature of polymerization plays only a minor role in the determination of the stationary monomer concentration, this result could be expected from the discussion in Section 2.2. However, fixing the number of monomers in a solution does not obstruct the emergence of peaked filament length distributions and length control.

4.2.2 Spontaneous Nucleation

Consider now the situation in which filaments are formed spontaneously out of $n_{\min} = 3$ subunits. The rate of spontaneous filament creation can then be assumed to have the functional form $k_{\mathrm{nucl}} = \nu \, c_{\mathrm{mon}}^3$ with a nucleation rate constant ν and the monomer concentration c_{mon} [7]. From Figure 4.2, it follows that in the investigated parameter regime, the stationary monomer concentrations are rather low. If filaments are not created by filament fragmentation, the value of ν in units of $s^{-1}\mu M^{-3}$ must be large to lead to a significant number of filaments.

Figure 4.3 displays the average filament length and the number of filaments as a function of time for the same polymerization parameters that as are used in Figure 4.2. Qualitatively, the stationary length distributions are the same in both situations. However, for the presented parameters, filaments are rather short.

The average filament length now relaxes to its stationary value on the same time scale as the standard deviation of the distribution and the filament number. Filaments are removed from the ensemble whenever a subunit is removed from a filament of minimal size, $n_{\min}$ and is thus proportional to the probability to find a filament of minimal size, $\mathcal{P}_{n_{\min}}$. Thus, the rate of filament disappearance increases with increasing width of the distribution. The number of filaments becomes stationary only after the width of the distribution is stationary. Since the average length depends directly on the filament number in solution, it relaxes on the same time scale.

In Figure 4.4, the properties of stationary ensembles of the three systems are shown under variation of the nucleation rate constant ν. As expected, the number of filaments increases with increasing nucleation rate. At the same time, the average filament length and the amount of free monomers decreases. Given that the rate of nucleation is varied by 5 orders
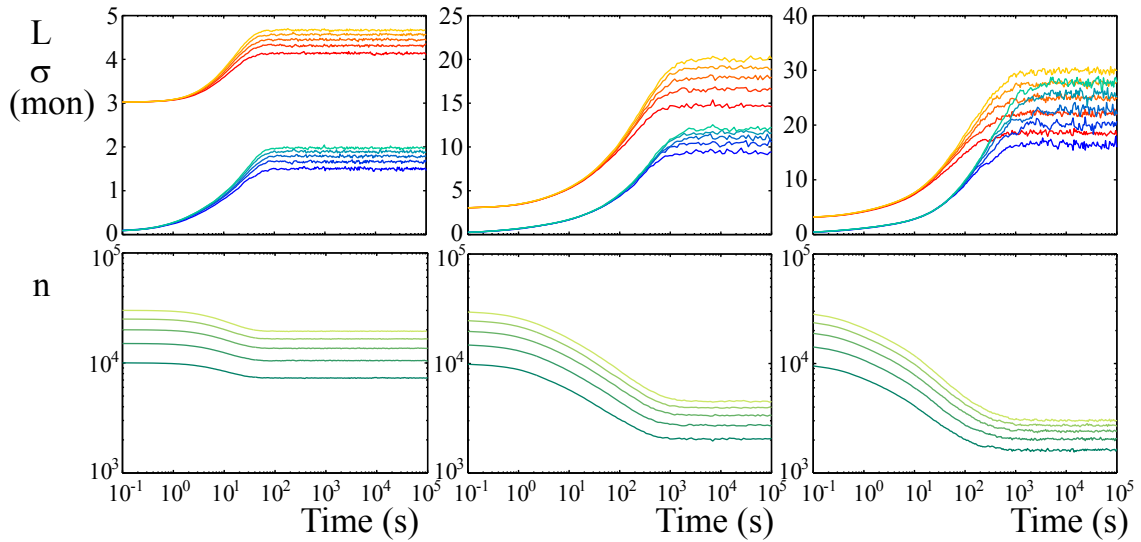
Figure 4.3: The dynamics of the polymers with spontaneous nucleation. a) The average filament length and the distribution's standard deviation as a function of simulated time. b) The number of filaments as a function of time. Average filament length relaxes on the same time scale as the length distribution's standard deviation and the filament number. Parameters of polymerization and depolymerization are as in Figure 4.2; rates are summarized in Table 4.1.

of magnitude, it can be deduced that its effect on the stationary states of the systems is limited. For very fast nucleation, all systems tend to the same state in which basically all monomers exist within filaments of the minimum size of three subunits.

The stationary number of filaments is also a function of the filament length distribution. Filament ensembles with exponentially distributed lengths have a higher rate of filament removal than systems with unimodal length of the same average. In the stationary state, the nucleation rate needs to be higher to generate the same number of filaments. This behavior can be observed for the three state model. The respective curves in Figure 4.2.2 shows the fastest decrease of filament number with decreasing nucleation rate. Note that for low ν, the average length reaches a size of 600 monomers while it retains its exponential shape.

Let me note that the spontaneous nucleation itself does not destroy the unimodal character of the length distributions found in Section 2.4.7. If the removal rate of D-monomers from the minus end is enhanced, actin filaments can still be expected to show unimodal length distributions. Figure 4.4 summarizes the steady state properties of the filament ensemble employing the modified actin polymerization rates that were used to generate Figure 2.23. For small nucleation rates, the average filament length is much larger than the length distribution's standard deviation, see Figure 4.4 d) for examples.
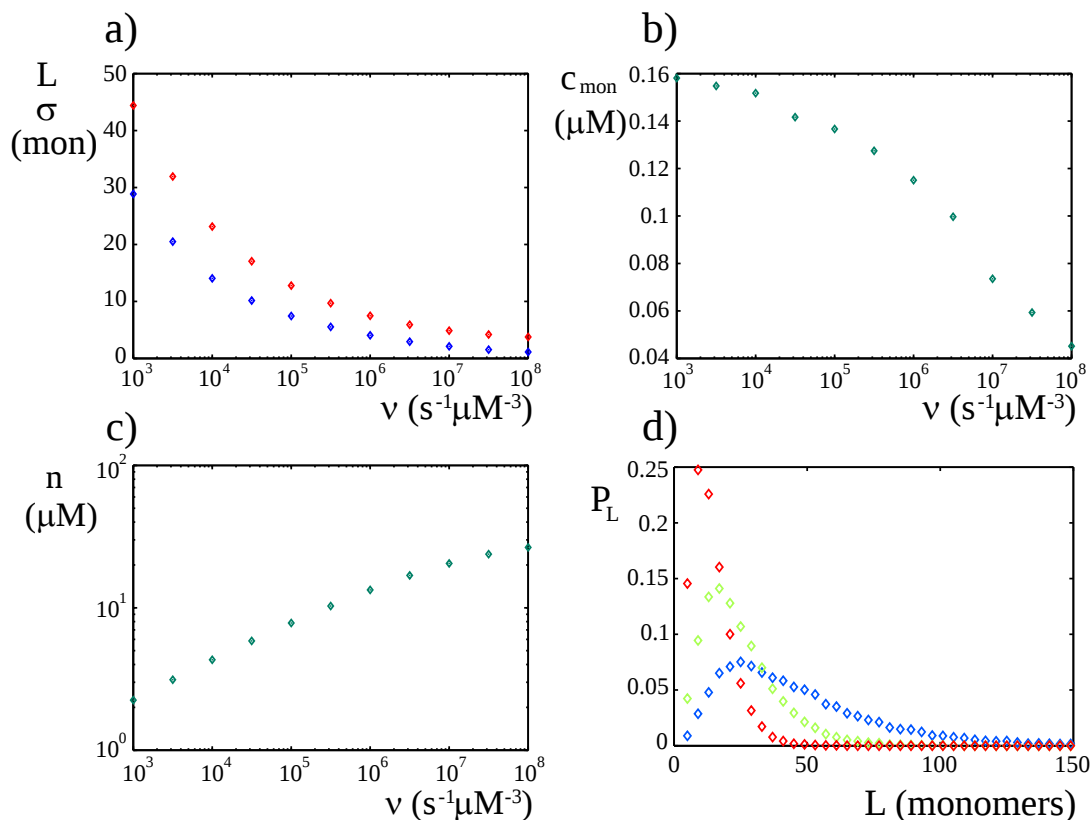
Figure 4.4: The characteristics of the stationary actin system with $k_{\text{off}}^{\text{D}-} = 2.5\,s^{-1}$ and spontaneous nucleation. a) Average filament length (red) and the distributions standard deviation (blue) as a function of the nucleation rate. b) The stationary monomer concentration. c) The number concentration of filaments in the stationary ensemble. d) Three examples of the length distribution for $\nu = 10^3$ (blue), $\nu = 10^4$ (light green), and $\nu = 10^5$ (red). Values were obtained by averaging over 10 samples of the whole distribution. Except for $k_{\text{off}}^{\text{D}-}$, all parameters were chosen as for the triangles in Figure 4.2.2.

a)

b)

c)
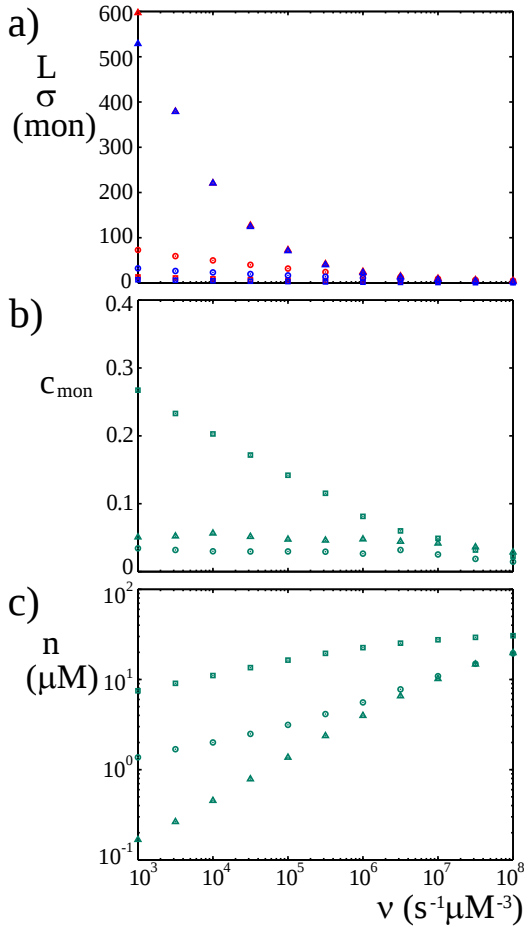
Figure 4.5: Properties of a stationary ensemble with spontaneous nucleation as a function of nucleation rate ν. a) Average filament length and standard deviation of the distribution for the three parameter sets from Figure 4.3, artificial parameters ($\square$), Kuhn parameters ($\circ$), and Fujiwara parameters ($\triangle$). b) The monomer concentration as a functin of the nucleation rate. c) The number concentration of filaments.

It was shown that the ability of actin monomers to spontaneously form a filament nucleus is very low. The concentration of actin filaments in a solution of $5M$ of monomers was estimated to be of the order of $10^{-15}M$ [32]. Thus, it must be concluded that if filament length is exponentially distributed, their number in stationary state is extremely low. Then, only very few polymers accomodate all available monomers. Such a behavior was indeed found for actin solutions that were let polymerize without sonication. Over time, the number of filaments decreased but their size grew [167].

In living cells, however, the number of filaments is very large, see for example the images of the cell cortex in Figure 4.1. Since the cells cannot safely rely on external forces to sever the filaments, it must resort to the action of nucleation promoting factors. A number of such proteins are known, for example formins, hem-1, or the arp2/3 complex [27, 168]. These proteins typically nucleate new filaments and stay bound to the filament end for some time. Formin for example stays bound to the barbed end of actin filaments where it facilitates the further addition of monomers. Together with the actin sequestering protein profilin it increases the polymerization speed by up to a 100-fold [49]. The arp2/3 complex on the other hand, binds to the sides of existing filaments and nucleates branches [169] connecting the pointed end of the new filament to the existing cortex. The arp2/3 also plays an essential role in the protrusion of the lamellipodia of migrating amoeboid cells [103]. Hem-1 is part of the Scar/WAVE complex that also con-

tains the proteins arp2 and arp3. It is activated at the cell membrane, leading to a localized enrichment of actin [168]. There is evidence that actin removes hem-1 from the membrane, leading to nucleation waves in the cell cortex [168, 170]. For cells, nucleating proteins are a simple lever to regulate the rate of filament formation.

In the next section, bleaching and photoactivation experiments are introduced. The dynamics of recovery or loss of fluorescence, respectively, can provide information about the organization of the cell cortex. Different hypotheses about the structure of filaments and their polymerization dynamics can then be tested with the help of stochastic simulations.

4.3 Bleaching and Activation Experiments

The dynamics of actin in the cortex can be investigated by Fluorescence Recovery After Photobleaching (FRAP) or Fluorescence Recovery After Photobleaching (FLAP) experiments. In these experiments, actin monomers are labeled with a fluorescent dye that can either be bleached or activated by a focused laser beam of a specific wavelength. In the FRAP setup, the recovery of fluorescence is recorded as a function of time after an initial bleaching of the dye. In a FLAP experiment, in contrast, the dye is initally activated and its loss within the activation zone is recorded.

In a bleaching experiment, for example, the initially dark region recovers its fluorescence as unbleached proteins from the cytosol diffuse and grow into the bleached spot, see Figure 4.6. For linear aggregates such as the actin filaments, the rates of fluorescence accumulation ω_a or loss ω_d are not equal to the rates at which monomers are added to and removed from the filaments, k_{on} and k_{off}. Since monomer exchange only occurs at the filament ends, it takes longer to replace a monomer in a long than in a short filament. In principle, it should therefore be possible to extract information on the filament length from the recovery curves of bleaching experiments.

If the cortex is in stationary state at the observed spot, the fluorescence gain that is recorded in a bleaching experiment must equal the fluorescence loss in the corresponding photoactivation experiment. The overall amount of actin in the region of interest, however, is constant. Thus, both types of experiments should give the exact same results and can be used interchangeably.

Besides FRAP and FLAP experiments, the investigation of fluorescent speckles can provide useful insight into the dynamics of the cortex. Speckles appear if the expression amplitude of labeled proteins is very low as compared to the amount of endogenous proteins in the cell. Then, only a small number of bright proteins is found in an ensemble of dark ones. In the microscope images, they appear as 'speckles' that can be tracked. Instead of probing the
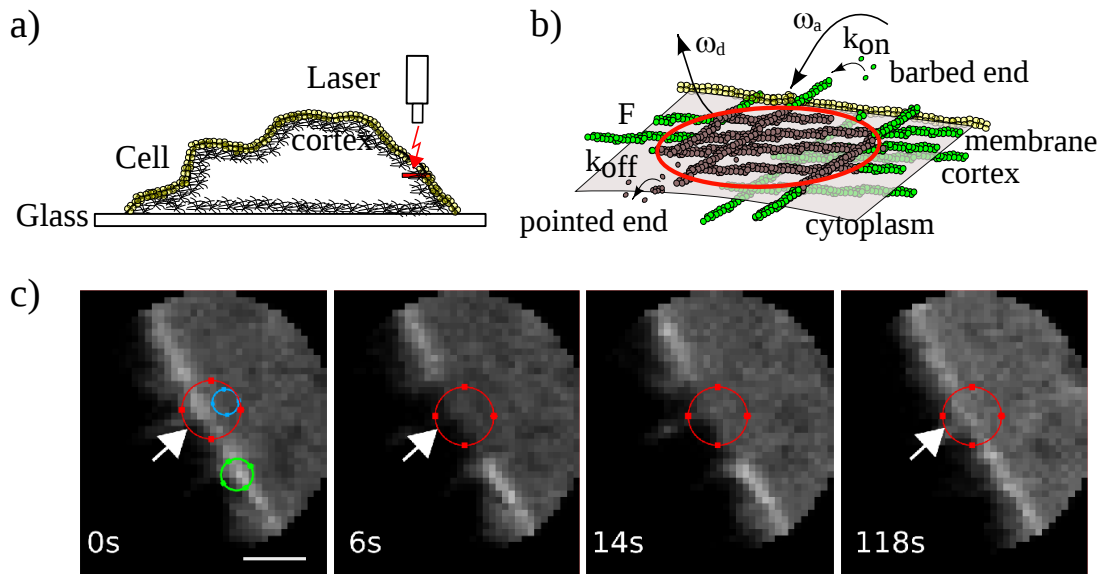
Figure 4.6: Illustration of bleaching experiments of the cortex of a living cell. a) A focused laser beam bleaches the fluorescent dye tethered to the actin monomers, leaving a dark spot in the bright cortex. b) Fluorescence recovers as bright monomers from the cytosol replace the bleached ones in the dark region. The rates of fluorescence exchange in the bleached spot, ω_a and ω_d differ from the effective rates of monomer addition and removal, k_{on} and k_{off} since monomers are only exchanged at filament ends. c) Snapshots of a FRAP experiment on cortical actin in a HeLa cell. The region in the red circle is bleached between time $t = 0\,s$ and $t = 1\,s$. Fluorescence slowly recovers with time. The region within the blue circle was used to determine the diffusion correction, the fluorescence in the region of the green circle was used to determine the loss of fluorescence due to imaging. The scale bar represents $1\,\mu m$. (Illustrations and Figures from [61], modified ©M. Fritzsche 2012)
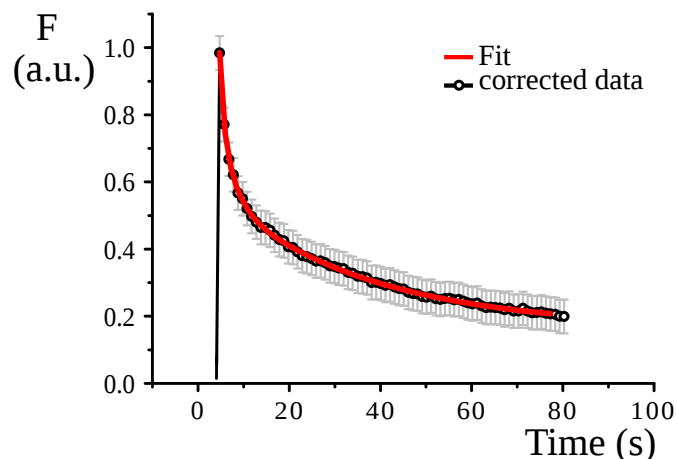
Figure 4.7: The fluorescence loss after Photobleaching in the actin cortex in M2 cells. Symbols give the fluorescence signal after the corrections for monomer diffusion and general loss of fluorescence by the imaging were applied. The signal can be fitted by a superposition of two exponential functions (solid red line). (Figure from [61], modified.)

whole ensemble at once, the fate of an individual protein can be observed.

4.3.1 Experimental Findings

FRAP and FLAP experiments were carried out on human Melanoma M2 cells [61]. The actin monomers were labeled with either green fluorescent protein (GFP) for FRAP- or with a combination of red fluorescent protein (RFP) and a photoactivatable (PA-GFP) for FLAP experiments. After the genetic manipulation that was needed for the labeling, the cells proliferated as usual and displayed normal phenotypes.

As predicted, bleaching and photoactivation experiments showed the same behavior. In both cases, the signal relaxed on different characteristic scales. The relaxation on a sub-second timescale could be attributed to the diffusion of free monomers into the region of interest and was subtracted from the curves. In order to extract the effect of the cortex turnover, a correction was applied that accounted for the general loss of fluorescence during the recording procedure. After that, recovery and dilution curves, respectively, showed a relaxation of the fluorescence signal on two different timescales, see Figure 4.7. One rapid process on the timescale of a second accounted for roughly 2/3 of the fluorescence and another slow process relaxed the remaining 1/3 of fluorescence on a timescale of about 25 seconds.

The fluorescence signals could be fitted with high accuracy by a superposition of two

exponentials. In the case of a FLAP experiment, it takes the form

$$F(t) = A_1 \, \mathrm{e}^{-\tau_1 \, t} + A_2 \, \mathrm{e}^{-\tau_2 \, t} \quad .$$

For FLAP- and FRAP curves on wild-type M2 cells, the characteristic rates for the best fit were $\tau_1 = 1.4 \, s^{-1}$ and $\tau_2 = 0.04 \, s^{-1}$. A fraction of $A_1/(A_1 + A_2) = 68\%$ of the fluorescence decayed on the rapid scale while the remaining 32% disappeared on the slower scale. The two distinct timescales suggest that two subpopulations of actin filaments are present in the cortex with monomer residence times that differ by a factor of 35.

Further investigations by mass spectrometry could show that a specific protein of the formin class, diaph1, is present in the actin cortex of M2 cells [171]. This protein is the human analog to the mouse protein mDia1 [172] that was already mentioned in Chapter 2. To get a closer view on the nucleation, speckle experiments on this formin were done. The speckles were either localized spots or blurred smears. Only the spots were considered since they can be attributed to formins that were bound to the membrane, the actin filaments, or both. Smears, on the other hand, were assumed to correspond to freely diffusing formins and are not considered in the following analysis.

In two different setups, full length diaph1 (FL-diaph1) and a constitutively active diaph1 (CA-diaph1) lacking its autoinhibitory domain were analyzed. In both cases, the whole population of speckles could be subdivided into a group of immobile and mobile formins. Mobile formin speckles moved directionally at a speed of roughly 300 nm/s which corresponds to a polymerization rate of about 100 monomers / s [61], see Table 4.2. Assuming a polymerization rate of diaph1 of about 45 $\mathrm{mon}(s\,\mu M)^{-1}$ that was reported for *in vitro* experiments [55], a concentration of 2.2 μM of polymerizable actin can be deduced.

Full-length diaph1 needs to bind the membrane protein RhoA to become activated by the signaling molecules PIP2. Only then it can nucleate and elongate actin filaments [173]. These speckles moved on average for 9 s before they disappeared. The distribution of lifetimes was exponential, suggesting that formin release is a spontaneous process described by a single detachment rate. CA-diaph1 was already released after 5.8 s from the barbed end. This protein is always able to nucleate and elongate actin filaments [174]. Since the polymerization velocities of both formins were similar, it can be concluded that the activation step is negligible for the polymerization dynamics. The results are summarized in Table 4.2.

The same type of experiment was carried out for actin speckles. Also there, mobile and immobile speckles were found. Analysis of the abundance of mobile and immobile speckles upon treatment with different drugs suggest that mobile actin speckles are monomers within filaments that are bound to immobile formins [61]. The movement is then caused by formin

		M2			HeLa		
FL-formin							
	immobile lifetime	2.7		*s*			
	mobile lifetime	8.9		*s*			
	mobile velocity	95	± 58	*mon/s*			
CA-formin							
	immobile lifetime	2.7		*s*	4.3		*s*
	mobile lifetime	5.8		*s*	9.3		*s*
	mobile velocity	102	± 51	*mon/s*	118	± 50	*mon/s*
actin							
	immobile lifetime	2.2		*s*	6.2		*s*
	mobile lifetime	6.8		*s*	7.7		*s*
	mobile velocity	92	± 10	*mon/s*	107	± 50	*mon/s*

Table 4.2: Results of the speckle experiments on formin and actin.

pushing filaments through the cytosol. The lifetime of mobile actin speckles was determined to be 6.8 *s* in M2 and 7.7 *s* in HeLa cells, see Table 4.2.

These experiments led to the idea that formin proteins localize at the membrane by binding to the membrane protein RhoA, where they are activated by PIP2. Active formins nucleate new actin filaments to which they add monomers at a speed of 100 *mon/s*, thereby pushing the filament at a comparable speed. Formins can then either detach from the membrane or from the filament. If it detaches from the membrane, it gets mobile while monomers in the bound filament become immobile. As soon as a formin detaches from the actin filaments, polymerization proceeds at a reduced velocity. Doubly detached formins are available for another cycle of binding and nucleation [61].

4.3.2 Three Modes of Monomer Exchange

Before I engage into detailed simulations of the polymerization dynamics of the cell cortex, let me briefly analyze what can be learned from FRAP- and FLAP-experiments about the organization and dynamics of the actin network. The fluorescence signal in FLAP or FRAP-experiments probes the residence times of, respectively, bleached or photo-activated monomers in an filament ensemble. In linear filaments, the residence time of monomers is a function of their relative distance to the filament's ends, hence, the filament length.
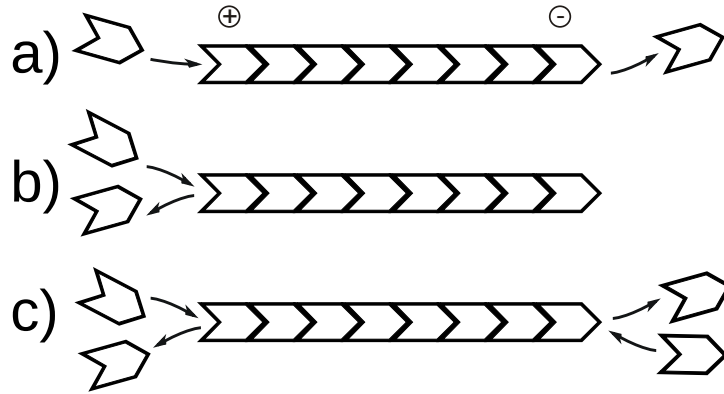
Figure 4.8: Illustration of the three filament assembly situations analyzed in this section. a) monomers are added to the filament at the plus end and are removed from the minus end at fixed rates. b) one filament end is inert while monomer exchange occurs only at the opposite end. c) monomer exchange occurs at both filament ends at fixed rates.

Moreover it depends on the microscopic mechanism of monomer addition and removal and on the rate of subunit exchange at the ends. In the remainder of this section, I investigate the residence times of monomers in three different types of filaments. The different modes of polymerization are depicted in Figure 4.8.

The situation corresponds to a FLAP-Experiment assuming photo-activation of the whole ensemble at time $t = 0$. The photo-activated monomers are lost one after the other and whenever a new monomer is added to the filament, it doesn't show up in the FLAP-signal.

For all three cases, first, the probability is calculated that a monomer is still part of the filament at a time t after photo-activation when it was initially at position x in a filament of length L, $\mathcal{P}(t; x, L)$. Then, the fluorescence of the whole filament decays as

$$f(t; L) = L - \sum_{x=0}^{L-1} (1 - \mathcal{P}(t; x, L)) \quad . \tag{4.1}$$

Note that indexing starts at $x = 0$.

Assuming a filament length distribution $C(L)$, the ensemble average of the fluorescence signal will be

$$F(t) = \sum_{L=0}^{\infty} \mathcal{C}(L) f(t; L) \quad . \tag{4.2}$$

Here, $\mathcal{C}(L)$ is assumed to be exponential. As was pointed out in Chapter 2, such filament

length distributions are found in equilibrated polymers or if depolymerization of monomers is always faster than polymerization. The treadmilling dynamics that is depicted in Figure 4.8 a) is a result of an active polymerization process and can also have a unimodal form. Since it was shown above that actin filaments are unlikely to have unimodal length distributions, this case is not investigated in detail. For the further analysis, scheme b) and c) are assumed to be passive such that exponential length distribution will emerge generically. For arbitrary rates, filaments in case c) could also show active treadmilling. If the treadmilling rate is of the order of the addition and removal rates, however, the results of case a) can be applied, using effective rates.

Treadmilling

In the case of a treadmilling filament, a single monomer at position x can only leave the filament if $L - x + 1$ monomers depolymerize from the minus end. As depolymerization occurs at a constant rate k_{off}, the probability for the removal of the monomer in a time interval between t and $t + dt$ follows a Poissonian law,

$$p(t; x, L)\, \mathrm{d}t = \frac{(k_{\text{off}}\, t)^{L-x}}{(L-x)!}\, \mathrm{e}^{-k_{\text{off}}\, t}\, k_{\text{off}}\, \mathrm{d}t \quad . \tag{4.3}$$

The probability for the monomer still to be integrated in the filament and still to contribute to the fluorescence signal at time t is deduced to be

$$\mathcal{P}(t; x, L) = 1 - \int_0^t p(t'; x, L)\, \mathrm{d}t' = \frac{\Gamma(L - x + 1, k_{\text{off}}\, t)}{(L-x)!} \quad , \tag{4.4}$$

where $\Gamma(z, a) = \int_a^\infty t^{z-1}\, \mathrm{e}^{(-t)}\, \mathrm{d}t$ is the incomplete Γ-function. The fluorescence signal of a filament of length L is then given by

$$f(t; L) = \frac{(k_{\text{off}}\, t)^{L+2}}{(L+1)!}\, \mathrm{e}^{-k_{\text{off}}\, t} + \frac{L + 1 - k_{\text{off}}\, t}{(L+1)!}\, \Gamma(L + 2, k_{\text{off}}\, t) \quad . \tag{4.5}$$

A stationary length distribution is only reached when $k_{\text{off}} > k_{\text{on}}$. The length distribution in an ensemble is then $\mathcal{C}(L) = \frac{k_{\text{off}} - k_{\text{on}}}{k_{\text{off}}} \left(\frac{k_{\text{on}}}{k_{\text{off}}} \right)^L$. After a straightforward calculation, one arrives at the simple result

$$F(t) = \frac{k_{\text{off}}}{k_{\text{off}} - k_{\text{on}}}\, \mathrm{e}^{-(k_{\text{off}} - k_{\text{on}})\, t} \tag{4.6}$$
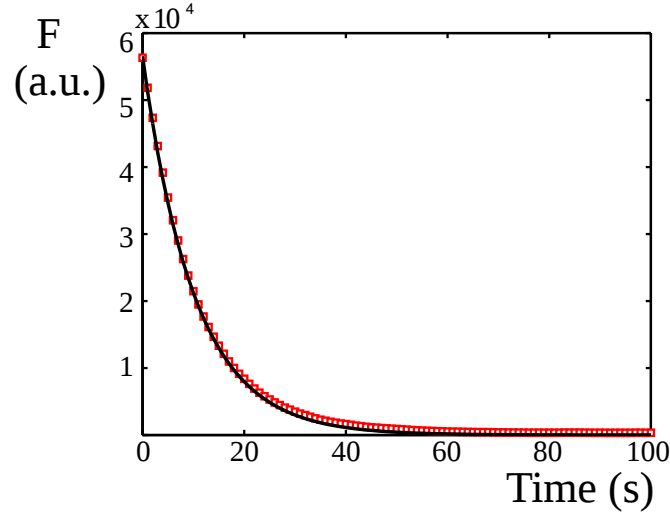
Figure 4.9: The FLAP Signal as a function of time for an ensemble of purely treadmilling filaments, i.e. monomers are attached at the plus end at rate $k_{\text{on}} = 0.18s^{-1}\mu M^{-1} c = 0.452s^{-1}$ and are removed from the minus end at rate $k_{\text{off}} = 0.55\text{s}^{-1}$. The ensemble consisted of 10^4 filaments and 10^7 monomers. Symbols are the results of stochastic simulations, the black line follows from the analytical treatment, see text. The deviations of both curves at long times is due to the finite amount of activated monomers in the simulation. The fluorescence signal saturates at the ratio of total activated monomers to total monomer number, which has a finite value. In the calculation, an infinite reservoir of dark monomers was assumed, thus the analytical fluorescence signal drops asymptotically to zero.

for the fluorescence signal of the whole ensemble. In Figure 4.9, the result of a stochastic simulation and the analytical result are compared for parameters $k_{\text{on}} = 0.452s^{-1}$ and $k_{\text{off}} = 0.55s^{-1}$ for an ensemble of $N = 10^4$ filaments. The average filament length then amounts to $\langle L \rangle = 5.6$ monomers. Numerical and analytical results show excellent agreement. The fluorescence signal of a treadmilling filament thus relaxes exponentially with a single characteristic rate $\tau = k_{\text{off}} - k_{\text{on}}$.

One-sided Activity

Now, the case is considered in which monomers are only exchanged at one filament end. They are added to the filament at rate k_{on} and removed at rate k_{off}, where again $k_{\text{on}} < k_{\text{off}}$. The filament tip then performs a biased Random Walk in the discrete length-space. To be removed from the filament, a monomer at distance m from the active tip has to wait until the tip has traveled this distance m into the filament bulk. The lifetime distribution can then

be formulated as the first-passage-time problem of a biased Random Walk, starting at $t = 0$ at position m, when the absorbing boundary is located at the origin. The Master-Equation of the full problem then reads

$$\frac{d}{dt}p_n^{(m)}(t) = -(k_{\text{on}} + k_{\text{off}})\, p_n + k_{\text{on}}\, p_{n-1} + k_{\text{off}}\, p_{n+1} \tag{4.7}$$

$$\frac{d}{dt}p_0^{(m)}(t) = -(k_{\text{on}} + k_{\text{off}})\, p_0 + k_{\text{off}}\, p_1, \tag{4.8}$$

with

$$p_n^{(m)}(t = 0) = \delta_{n\,m},$$

where $p_n^{(m)}(t)$ denotes the probability that at time t, a cap of n monomers separates the monomer in question from the tip of the filament, when initially the cap consisted of m monomers. If the filament length is given by L, the probability that a monomer at distance $L - x$ from the tip survives until time t is given by

$$\mathcal{P}(t; x, L) = 1 - \sum_{n=0}^{\infty} p_n^{(L-x)}(t).$$

The Master-Equation (4.8) and (4.8) can be solved analytically by recursion. However, one is faced with a result involving a number of non-trivial sums which seemingly have no closed form. To simplify things, I use the Fokker-Planck approximation, that yields [90]

$$p(x', t) = \frac{1}{\sqrt{4\pi D t}} \left(e^{-(x'-x-vt)^2/(4Dt)} - e^{-vx/D}\, e^{-(x'+x-vt)^2/(4Dt)} \right) \tag{4.9}$$

for the probability $p(x', t)$ for a biased Random Walk with drift $v = k_{\text{on}} - k_{\text{off}} < 0$ and diffusion coefficient $D = (k_{\text{on}} + k_{\text{off}})/2$ to be at position x' when initially it was at x. One then has

$$\mathcal{P}(t; x, L) = \int_0^{\infty} \mathrm{d}x'\, p(x', t) = \frac{1}{2}\left(1 - e^{-vx/D}\left[1 + \mathrm{erf}\left(\frac{vt - x}{2\sqrt{Dt}}\right)\right] + \mathrm{erf}\left(\frac{vt + x}{2\sqrt{Dt}}\right)\right).$$

The fluorescence signal of an individual filament of length L is then given by the rather

lengthy expression

$$
\begin{aligned}
f(t; L) &= \int_0^L \mathrm{d}x\, \mathcal{P}(t; x, L) \\
&= \frac{L}{2} + \frac{D}{2\,v}\left[\mathrm{e}^{-vL/D} - 1\right] + \sqrt{\frac{Dt}{\pi}}\left[\mathrm{e}^{-(vt+L)^2/(4Dt)} - \mathrm{e}^{-(vt)^2/(4Dt)}\right] \\
&\quad - \left[\frac{vt}{2} + \frac{D}{v}\right]\mathrm{Erf}\left(\frac{vt}{2\sqrt{Dt}}\right) + \left[\frac{vt+L}{2} + \frac{D}{2v}\right]\mathrm{Erf}\left(\frac{vt+L}{2\sqrt{Dt}}\right) \\
&\quad + \frac{D}{2v}\,\mathrm{e}^{-vL/D}\,\mathrm{Erf}\left(\frac{vt-L}{2\sqrt{Dt}}\right) \quad.
\end{aligned}
$$

Here, the Error-Function $\mathrm{Erf}(x) = \frac{2}{\sqrt{\pi}}\int_0^x \mathrm{e}^{-t^2}\,\mathrm{d}t$ was used. An exponential length distribution of filaments is assumed, which, in the Fokker-Planck limit, has the form

$$
\mathcal{C}(L) = -\frac{v}{D}\exp\left(\frac{vL}{D}\right)\ .
$$

Note again that in the whole calculation the drift velocity is negative, $v < 0$. One finds

$$
F(t) = \int_0^\infty \mathrm{d}L\,\mathcal{C}(L)\,f(t; L) = -\left(\frac{D}{v} + \frac{vt}{2}\right)\left(1 + \mathrm{Erf}\left(\frac{vt}{2\sqrt{Dt}}\right)\right) - \sqrt{\frac{Dt}{\pi}}\,\mathrm{e}^{-v^2 t/4D}.
$$

In Figure 4.10 a), it is shown that this result reproduces the FLAP-curve in stochastic simulations. Note that no kind of fitting was used. Figure 4.10 b) shows the same system but with an infinite reservoir of unlabeled monomers. The difference is only visible in the semilogarithmic plot, where the fluorescence drops to zero in accordance with the analytic predictions.

Summarizing, for the single sided polymerization and depolymerization, one finds a decay process with an exponential and a non-exponential part. This is in contrast to the tread-milling case, where the loss of fluorescence occurred by a simple exponential decay. The difference is no artifact of the application of the Fokker-Planck Equation as it appears also in the simulation results, see Figure 4.10. Instead, it is an intrinsic feature of the single sided addition and removal of monomers.

I want to note furthermore that the characteristic timescale of the exponential part in both, treadmilling and single sided activity, is qualitatively different: the timescale in the first case is linear in the drift velocity $v = k_{\mathrm{on}} - k_{\mathrm{off}}$, while in the second it is proportional
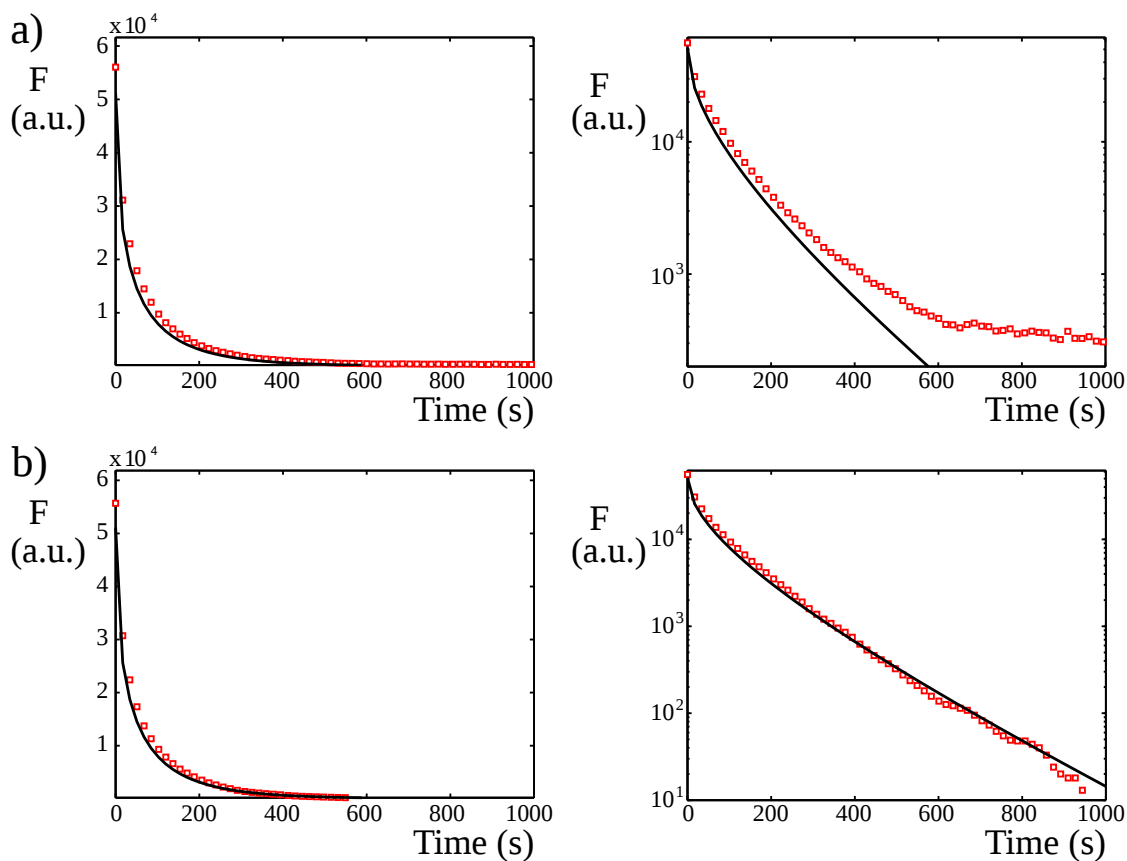
Figure 4.10: Fluorescence signal of an ensemble of filaments that have only one active end. Here, $k_{\mathrm{on}} = 0.18 \, c_{\mathrm{mon}} = 0.452 s^{-1}$, $k_{\mathrm{off}} = 0.55 s^{-1}$, $N = 10^7$ monomers interact with 10^4 filaments, resulting in $\langle L \rangle \approx 5.6$. a) A fraction of $56000/10^7$ monomers in the ensemble gets permanently labeled, the signal asymptotically reaches $56000^2/10^7 \approx 300$ monomers. The analytic result on the other hand tends to zero by definition. b) In this setup, all monomers loose their color as soon as they detach from the filament, newly added monomers are always dark. No fitting was employed, the only approximation lies in the application of the Fokker-Planck Equation.

to v^2.

Equilibrium Monomer Exchange at Both Filament Ends

In the third and last case, the subunit exchange occurs at both ends of filaments. The rates for addition and removal are denoted by k_{on}^+, k_{off}^+, k_{on}^-, and k_{off}^-, respectively. In the equilibrium case, the rates obey

$$\frac{k_{off}^+}{k_{on}^+} = \frac{k_{off}^-}{k_{on}^-}, \tag{4.10}$$

that is $k_{off}^+ = \theta\, k_{off}^-$ and $k_{on}^+ = \theta\, k_{on}^-$ with θ fixed. Explicitly, $v^+ = \theta\, v^-$ and $D^+ = \theta\, D^-$, which leads to

$$\frac{v^+}{D^+} = \frac{v^-}{D^-}.$$

Since both filament ends are independent of one another, the probability $\mathcal{P}(t; x, L)$ that both filaments have not yet reached a given monomer in the filament is the product of the probabilities that neither the one nor the other has done so at a given timepoint t. Thus,

$$\mathcal{P}(t; x, L) = \mathcal{P}^+(t; x, L) \cdot \mathcal{P}^-(t; L - x, L), \tag{4.11}$$

where $\mathcal{P}^\pm(t; x, L)$ are the expressions for $\mathcal{P}(t; x, L)$ in the case of single sided activity with the respective $v^\pm$ and $D^\pm$ [1]. As before, indexing of monomers starts at the plus end.

The integration over x leads to an integral of the form $\int_a^b \mathrm{d}s\, \mathrm{e}^{-s^2} \mathrm{erf}(\alpha + \beta\, s)$, which has no closed form. Therefore, the integral $\int_0^\infty \mathrm{d}L\, \mathcal{C}(L) \int_0^L dx\, \mathcal{P}^+(t; x, L)\, \mathcal{P}^-(t; L - x, L)$ is solved numerically in the following.

Again, the numerical and the analytical curves are in good agreement, see Figure 4.11. From the logarithmic plot, it can be inferred that for short times, the decay is again not purely exponential. I hypothesize that the decay for long times has a characteristic time scale of the order of $(v^+)^2 + (v^-)^2$.

Conclusions

Let me briefly summarize the results of the analytic treatment of fluorescence recovery at this point. Three modes of filament assembly were investigated: treadmilling filaments and

---

[1] One can think of it as a Random Walk in the plane, where one axis gives the distance of the monomer to the plus and the other the distance to the minus end. At the x- and the y-axis, absorbing boundaries are applied and the RW starts at $t = 0$ at $x + y = L$.
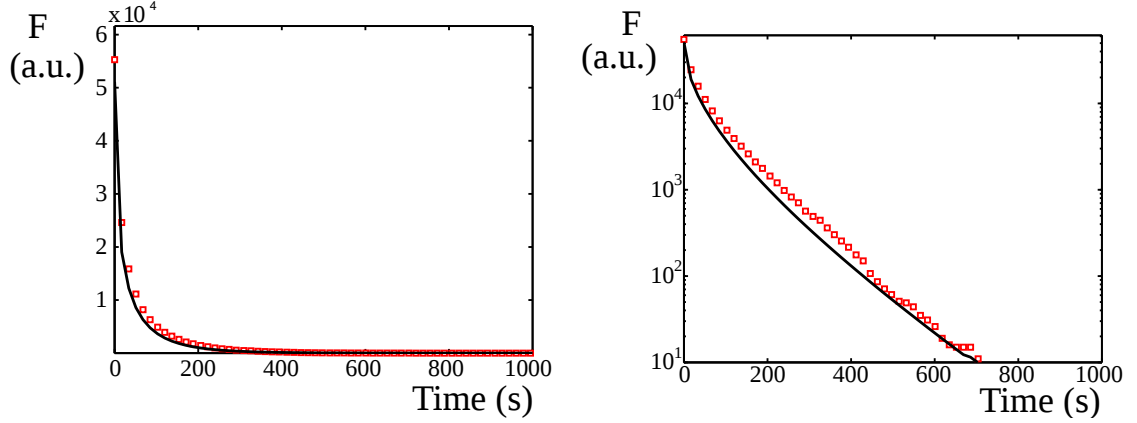
Figure 4.11: Fluorescence signal of an ensemble of filaments with monomer exchange at both ends. Here, $k_{on}^+ = 0.18\,c_{ss} = 0.452s^{-1}$, $k_{off}^+ = 0.55s^{-1}$, $k_{on}^- = 0.0.036\,c_{ss} = 0.0904s^{-1}$, $k_{off}^- = 0.11s^{-1}$, $N = 10^7$ monomers interacted with 10^4 filaments, resulting in $\langle L \rangle \approx 5.6$, as before. Here, the monomers loose their color as soon as they detach from the filament, newly added monomers are always dark. No fitting was employed, the only approximation lies in the application of the Fokker-Planck Equation.

equilibrium monomer exchange at one or both filament ends. For all three cases, analytic expressions for the fluorescence signal for an exponential filament length distribution were derived.

The fluorescence of a purely treadmilling filament ensemble drops exponentially at a rate, which is given by the length drift velocity $v = k_{on} - k_{off} < 0$. In contrast, equilibrium polymerization at one or both filament ends is dominated by fluctuations and their fluorescence decays on long time scales with a rate proportional to v^2. If the condition of equilibrium polymerization is released, the treadmilling state a) is a limiting case of the general scheme of double-sided activity, c). Hence, the fluorescence signal should converge to the same shape in the appropriate limit. If filaments of the type c) effectively display a treadmilling behavior, one would expect furthermore that the fluorescence signal drops as e^{-vt} rather than $e^{-v^2 t}$ for large t. This should hold true as soon as the drift dominates the fluctuations in length dynamics.

The models for one-sided and double sided activity give rise to a rapid non-exponential decay of the fluorescence signal on short times. The effect is visible in both, the simulation results and the analytical description. It is thus intrinsic to the mechanism of filament renewal. Can this non-exponential rapid drop account for the first of the two time scales observed in experiments? Two arguments are opposed to such a view: First, the drop has no

exponential characteristics and the ensuing curve can not be fitted by a simple superposition of two exponential decays. Second, the amount of fluorescence that recovers on each of the two scales would be fixed by the addition and removal rates. A modification of polymerization or depolymerization would then always affect the amplitudes and timescales of both processes simultaneously. A specific manipulation of one of the two scales as reported in experiments would not be possible [61].

In addition to these arguments, it appears implausible that active filaments like actin rely on a passive mode of monomer renewal *in vivo*. Since the analysis in Chapter 2 revealed that the addition and removal rates of actin are such that treadmilling is found for all monomer concentrations, it can safely be assumed that actin filaments are also in the treadmilling state *in vivo*.

In addition to the presented calculations, the analysis of other modes of active filament renewal remains to be done. In particular, the filament length distribution of active polymers doesn't need to be exponential as was pointed out in Chapter 2. Unimodal distributions with a strongly localized length could lead to non-exponential recovery curves. In the treadmilling case, one would expect a linear decrease in fluorescence as long as filaments are not fully renewed and a sudden drop in the signal when the dark part of the filament reaches the filament length of all filaments at the same time. Other modes of filament recovery could also include models for dynamic instability, vectorial hydrolysis, and fragmentation of filaments. Further theoretical analyses suggest that activity of a filament system increases the turnover rates rather generally [175].

4.4 Two Timescales in Cortex Simulations

In the last part of this chapter, I present stochastic calculations that reproduce the two distinct timescales that were found in FRAP and FLAP experiments on the actin cortex of melanoma M2 and HeLa cells. Three different scenarios are introduced and discussed.

4.4.1 The Simulation Algorithm in Detail

To simulate the cortex, stochastic simulations were used similar to those introduced above. In the present simulations, the state of the cortex is given by the number of free monomers and the ensemble of all filaments, including the internal states of all constituting monomers. The overall number of monomers that are either free or bound in filaments is held constant throughout the simulation. Their number is given by N_{tot}. Diffusion of free monomers is assumed to be very fast such that the concentration of free monomers is homogeneous in the

simulated volume.

Filaments are represented as linear arrays of monomers, each of which has an internal state that corresponds to a monomer bound to an ATP, ADP-P_i, ADP, or a cofilin molecule. Moreover, a color, bright or dark, is assigned to every monomer within the filaments. By convention, all monomers that are integrated into the filament are bright. When the cortex is bleached, the color of all filamentous subunits is set to dark. To further simplify the simulation, it is assumed that all free monomers are in the ATP-bound form.

In all presented simulations, a fixed number of formin molecules, N_{form}, is included into the simulation as nucleation factors. Free formins nucleate new filaments from a free monomer at rate ν_{form}. As long as a formin is attached to the filament it nucleated, it adds new monomers at a rate $k_{on}^{\mathrm{form}} c_{\mathrm{mon}}$, with c_{mon} being the monomer concentration. The formin is released from the barbed end at rate f_{off}. When released, the formins undergo another cycle of filament nucleation and monomer addition.

Free barbed and pointed ends exchange monomers with the cytosol as described for the two- or three states model in Chapter 2. Monomers in the solution are all assumed to be equivalent. Addition rates are chosen such that this state corresponds to the profilin bound form of ATP-actin. Empty and formin bound barbed ends thus perceive the same monomer concentration.

In these simulations, filament ends can also be inactivated by capping. The number of capping proteins in the simulated volume is fixed to N_{cap}^{+} and N_{cap}^{-}, for the barbed and pointed end capping proteins, respectively.

As mentioned above, subunits within the filament can also bind the severing protein cofilin. Since cofilin has a much higher binding affinity to ADP-actin than to ATP- or ADP-P_i-actin [136, 176], its binding is treated as a fourth subunit state. Transitions from the D-state to the cofilin bound state occur at fixed rate ω_{DC}. This corresponds to fixing the concentration of cofilins rather than their number. Cofilin bound subunits are the sites at which filaments can be severed. Two alternative models for the severing of filaments are detailed below.

Besides formin, a second nucleating protein, arp2/3, is introduced in the simulations. Arp2/3 is a complex of several proteins that bind to the side of existing actin filaments. Its nucleation rate *in vivo* is thus coupled to the presence of filamentous actin. In the simulations, it is implemented as a pointed end capping protein that is able to nucleate new filaments. All free arp2/3 molecules nucleate filaments at rate ν_{arp}. They detach from the respective filament at rate a_{off}. As long as an arp2/3 binds the minus end of a filament, no monomers can detach.

From the initial state without any filaments, the system is evolved into the stationary state

following the above polymerization dynamics. After a time of the order of $T > 10^3 \, s$, the system is bleached. At this moment, the color of all monomers in filaments is set to dark. Monomers that polymerized after that moment are bright again. During the subsequent recording of the FRAP-signal, the number of bright monomers within the filamentous part is determined as a function of time. The FLAP-signal is then given by the number of dark monomers in the filaments.

Before the simulation results are presented, I will provide estimates for some of the parameters in the system.

4.4.2 Model and Analytic Estimates

As pointed out above, in HeLa and melanoma M2 cells, the traveling speed of mobile formin speckles correspond to a polymerization rate of roughly 100 monomers per second. Under the assumption that monomers are bound to profilin, the concentration of polymerizable actin monomers in solution must be close to $2.2 \, \mu M$. It is known from independent experiments that profilin-actin polymerizes at barbed ends at a rate of about 9 monomers $(s \, \mu M)^{-1}$ [55] wich amounts in the present case to 22.5 monomers/s.

To establish a stationary cortex at these T-monomer concentrations, the net depolymerization per filament has to lie between 22.5 and 100 monomers/s. Both values lie far above the monomer removal rate of $k_{\text{off}}^{\text{D}-} = 0.25 \, s^{-1}$ that was reported for bare actin *in vitro* [30]. On the other hand, it was shown that addition of formin and cofilin to the *in vitro* solution increased the turnover velocity of actin polymerization by a factor of 25 [64] to 150 [177, 178]. The ensuing depolymerization rate reaches the right order but it can be assumed that the action of coronin and aip1 further speeds up the turnover *in vivo* [137, 179].

For treadmilling filaments, the net depolymerization speed can be estimated from the lifetime measurements of actin speckles. Consider a filament that is nucleated by a formin. On average, this filament will grow at its barbed end for $\langle t \rangle = 10 \, s$ at a velocity of $\langle \nu_a^{\text{form}} \rangle = 100 \, \text{mon}/s$ until the formin detaches. After that, polymerization proceeds with $22.5 \, \text{mon}/s$. Let me assume that depolymerization takes place at a constant velocity during the whole lifetime of the filament. Since speckles are integrated at random times, the average lifetime $\langle T \rangle$ of a monomer in such a filament can be given as a function of the average depolymerization rate $\langle \nu_d \rangle$,

$$\langle T \rangle = \frac{\langle \nu_a^{\text{form}} \rangle - \langle \nu_d \rangle}{2 \langle \nu_d \rangle} \langle t \rangle, \tag{4.12}$$

where $\langle t \rangle$ is the average lifetime of a formin at the barbed end [2]. Note that this expression

---

[2]Consider for this calculation for example the cumulative amount of seconds that all monomers stay bound

only depends on the polymerization rate of formin bound filaments, $\langle \nu_a^{\text{form}} \rangle$, but not on the growth rate of empty filament ends. Equivalently,

$$\langle \nu_d \rangle = \frac{\langle \nu_a^{\text{from}} \rangle \langle t \rangle}{\langle t \rangle + 2 \langle T \rangle}. \tag{4.13}$$

For an average lifetime of mobile actin speckles $\langle T \rangle = 7\,s$ and $\langle t \rangle$, the depolymerization is estimated to be $42\ s^{-1}$.

Based on these estimates, the emergence of the two timescales in FLAP and FRAP experiment is now studied numerically. Three different scenarios are presented in the following, all of which are able to recreate the qualitative behavior of actin cortex. They are based on, respectively, filament capping, severing, and the existence of two distinct filament nucleators. The parameters for the example curves are adjusted such that in a local neighborhood of the parameters, they fit the experimentally determined results best. However, the presented values are not necessarily the best fits in the whole parameter space.

4.4.3 The Effects of Capping Proteins

Consider first the capping of filaments. The slow recovery timescale can be the result of the inactivation of filaments by capping proteins while the free filaments recover their fluorescence rapidly. Capping proteins for the barbed (plus) and pointed (minus) ends are added to the simulation at fixed numbers N_{cap}^+ and N_{cap}^-. Filament ends are capped by free cappers at rates η_{cap}^+ and η_{cap}^- at the barbed and pointed ends, respectively. Cappers detach from the filament ends at rates η_{uncap}^+ and η_{uncap}^- or when the filament is completely disassembled.

Simulations of the cortex indeed show two timescales, see Figure 4.12. For the parameter set listed in Table 4.3, roughly 2/3 of the fluorescence is lost with rate $\tau_1 = 0.26\ s^{-1}$. The remaining fluorescence vanishes with characteristic rate $\tau_2 = 0.03\ s^{-1}$. The length distribution that can be extracted from the simulations is exponential with an average of 160 monomers.

The capping of filaments is thus in principle capable of explaining the two recovery rates that were found in experiments. However, with polymerization and de-polymerization rates as estimated above, the turnover of the fast part of the fluorescence signal is still almost an order of magnitude slower than expected. The recovery half-time of about $4s$ is compatible with the monomer release of filaments of a size of 160 subunits by depolymerization at a speed of $40\,mon/s$. A faster recovery is thus only obtained for higher depolymerization rates or shorter filaments, respectively. The fact that the monomer concentration in the solution does not reach the value that was expected from the speckling experiments is also in favor

---

in the filament. It is easily determined as an area in the space-time plot.
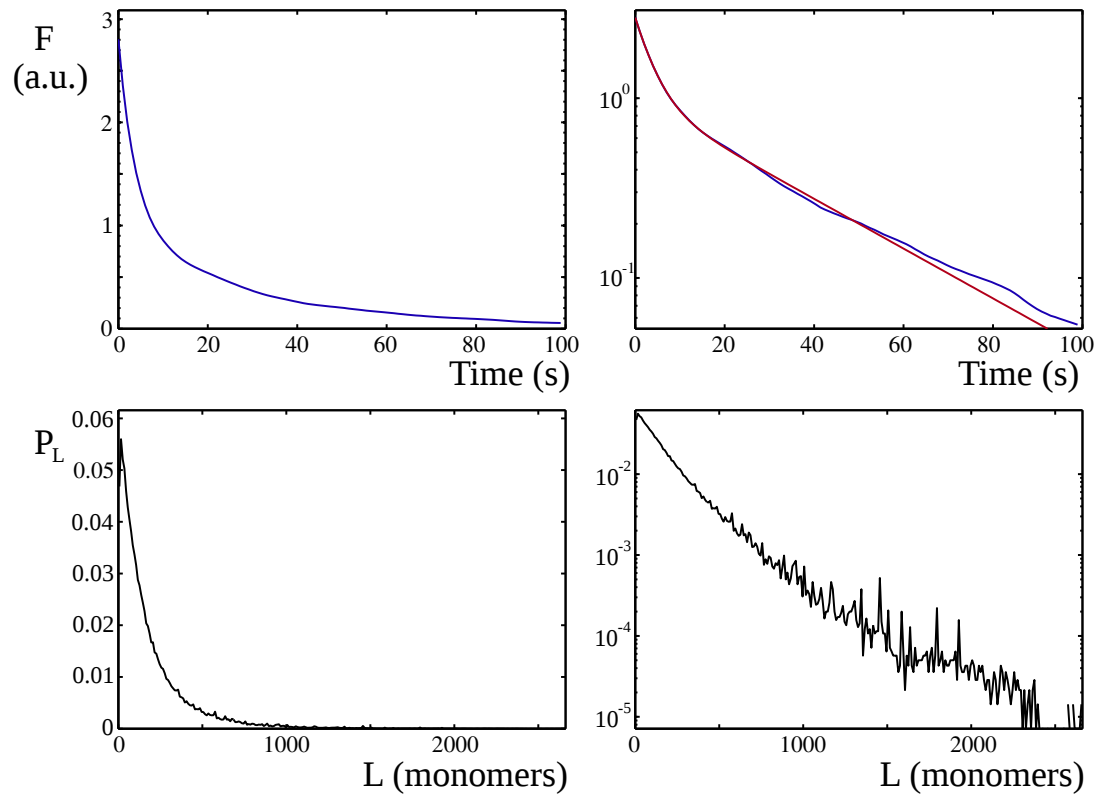
Figure 4.12: FLAP signal and filament length distribution extracted from simulations with capping of filament ends. The fluorescence decays on two exponential scales. Aproximately 2/3 of the fluorescence is lost by the fast relaxation (top). Filament length is exponentially distributed (bottom).

Parameter	Units	Figure 4.12	Figure 4.13	Figure 4.14	Figure 4.15
N_{tot}		301000	1806000	1806000	301000
$k_{\text{on}}^{\text{T}+}$	$(s\,\mu M)^{-1}$	9	9	9	9
$k_{\text{on}}^{\text{T}-}$	$(s\,\mu M)^{-1}$		0	0	
$k_{\text{on}}^{\text{P}+}$	$(s\,\mu M)^{-1}$		0	0	
$k_{\text{on}}^{\text{P}-}$	$(s\,\mu M)^{-1}$		0	0	
$k_{\text{on}}^{\text{D}+}$	$(s\,\mu M)^{-1}$		0	0	
$k_{\text{on}}^{\text{D}-}$	$(s\,\mu M)^{-1}$		0	0	
$k_{\text{off}}^{\text{T}+}$	s^{-1}		0	0	
$k_{\text{off}}^{\text{T}-}$	s^{-1}	40	24	24	24
$k_{\text{off}}^{\text{P}+}$	s^{-1}		0	0	
$k_{\text{off}}^{\text{P}-}$	s^{-1}		24	24	
$k_{\text{off}}^{\text{D}+}$	s^{-1}		0	0	
$k_{\text{off}}^{\text{D}-}$	s^{-1}		24	24	
$k_{\text{off}}^{\text{C}+}$	s^{-1}		0	0	
$k_{\text{off}}^{\text{C}-}$	s^{-1}		24	24	
ω_{TP}	s^{-1}	0	0.1	0.1	0
ω_{PD}	s^{-1}		0.05	0.05	
ω_{DC}	s^{-1}		0.05	0.05	
N_{form}		602	15	15	15
$k_{\text{on}}^{\text{form}}$	$(s\,\mu M)^{-1}$	40	40	40	40
f_{off}	s^{-1}	0.2	0.2	0.2	0.1
ν_{form}	$s^{-1}\,\mu M^{-2}$	100	100	100	100
N_{cap}^{+}		151			
η_{cap}^{+}	$s^{-1}\,\mu M^{-2}$	100			
η_{uncap}^{+}	s^{-1}	0.04			
N_{cap}^{-}		151			
η_{cap}^{-}	$s^{-1}\,\mu M^{-2}$	100			
η_{uncap}^{-}	s^{-1}	0.04			
$\sigma_{\text{cof}}^{\text{var}}$	s^{-1}		0.14		
L_{frag}	monomers			5	
$\sigma_{\text{cof}}^{\text{fixed}}$	s^{-1}			2	
N_{arp}					451
a_{off}	s^{-1}				2
ν_{arp}	$s^{-1}\,\mu M^{-2}$				100
T_{bleach}	s	1000	600	3000	4000
V	μm^{3}	10	50	50	50
$c_{\text{mon}}^{\text{ss}}$	μM	1.7	2.65	2.65	2.1
$A_1/(A_1+A_2)$		0.65	0.82	0.93	0.19
τ_1	s	0.26	0.14	0.45	1.87
$A_2/(A_1+A_2)$		0.35	0.18	0.07	0.81
τ_2	s	0.03	0.04	0.1	0.04
N_{fil}		1400	6000	16000	2800

Table 4.3: Rate constants and results for different models of the cell cortex.

of a higher depolymerization velocity.

The slow recovery rate is close to the value of filament uncapping, suggesting that the slow monomer exchange is directly influenced by the release rate of capping proteins. The ensemble of actin filaments could therefore be divided into two subpopulations: filaments with free or capped ends. The free filaments are responsible for the fast and capped filaments for the slow recovery.

4.4.4 Severing of Filaments

Two filament subpopulations that turn over on distinct timescales can also be the result of filament severing. The second model for the actin cortex is based on the idea that the filaments in both populations have different average length. Hence, monomers have different average lifetimes despite of identical filament removal rates.

Filaments that are nucleated by formin accumulate many monomers within a short time. The removal of subunits occurs by two different processes, depolymerization of individual monomers and severing of small filament pieces. The fragments that are chopped off the mother filament form a second pool of filaments. If the average size of these fragments is small, this pool should display a rapid turnover.

In a first attempt, the cortex dynamics is modeled by filaments that consists of subunits in one of 4 different states, corresponding to being bound to ATP, ADP-P_i, ADP, or ADP-cofilin. Monomers are integrated into the lattice in the T-state and sequentially change into the P-, D-, and C-state at rates ω_{TP}, ω_{PD}, and ω_{DC}, respectively. Monomers in the C-state trigger the severing of the filament that occurs at rate $\sigma_{\mathrm{cof}}^{\mathrm{var}}$. The fragment has now a free barbed end and can polymerize monomers. The nucleation of filaments is mediated by formins, as before.

The result of such a simulation is shown in Figure 4.13. See Table 4.3 for the reaction rates. In the dilution curves, indeed, two timescales can be distinguished. However, the characteristic times only differ by a factor of 13 instead of 35 as found in experiments. The filament length distribution is peaked, displaying a maximum at a length of roughly 200 monomers. In the semilogarithmic plot, it becomes apparent that the distribution consists of two parts. The majority of filaments has a peaked distribution while a second population is responsible for the exponential tail of the distribution.

Simulation results proved to be very sensitive to changes in the parameters. Slight changes in the severing rate already disturb the contrast of the characteristic timescales or let them collapse. The stationary monomer concentration can easily be modulated by manipulaton of the depolymerization rate. A concentration of $2.65 \, \mu M$ is reached for example when all
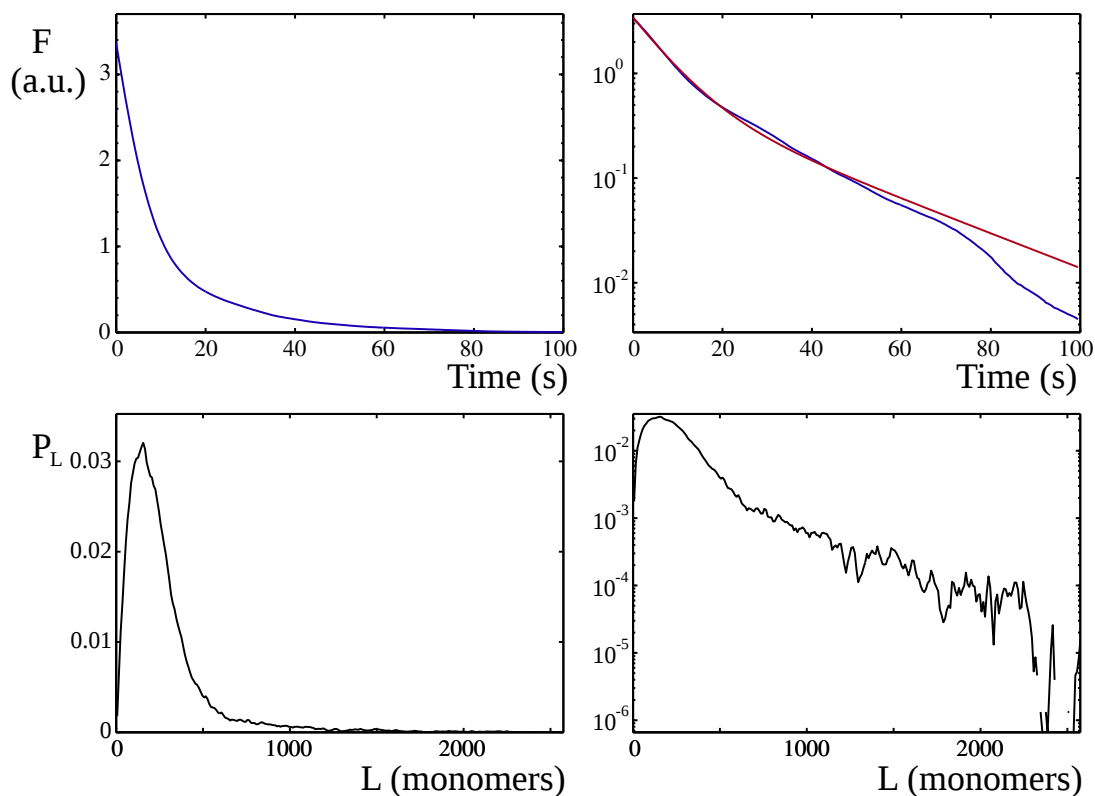
Figure 4.13: FLAP signal and filament length distribution extracted from simulations with spontaneous severing by cofilin. Top: The fluorescence signal as a function of time (left: linear scale, right: semilogarithmic scale). Simulation results are given by the blue curve, the fit by a superposition of two exponentials given by the red line. Bottom: The filament length distribution derived from simulations (left: linear scale, right: semilogarithmic scale).

depolymerization rates are all set to $24\,s^{-1}$.

While the slow timescale $\tau_2 = 0.04\,s$ in the fluorescence recovery is rather close to the experimentally determined values, the first timescale, $\tau_1 = 0.14\,s$ is much too slow as compared to experiments. One reason might be that the fragments that were chopped off had an average size of 120 monomers that is comparable to the size of the respective mother filaments of 160 monomers.

To overcome this difficulty, the scheme of filament dissection is modified. In the following, the size of the fragment that is to be cut from a filament was fixed to L_{frag}. Each filament that is larger than that has the same probability $\sigma_{\text{cof}}^{\text{fixed}}$ to loose a fragment, provided that there is a C-state monomer in the range of $L_{frag} \pm 2$ from the pointed end. This way, the size of fragments in the rapidly recovering pool can be controled. Setting L_{frag} to sufficiently
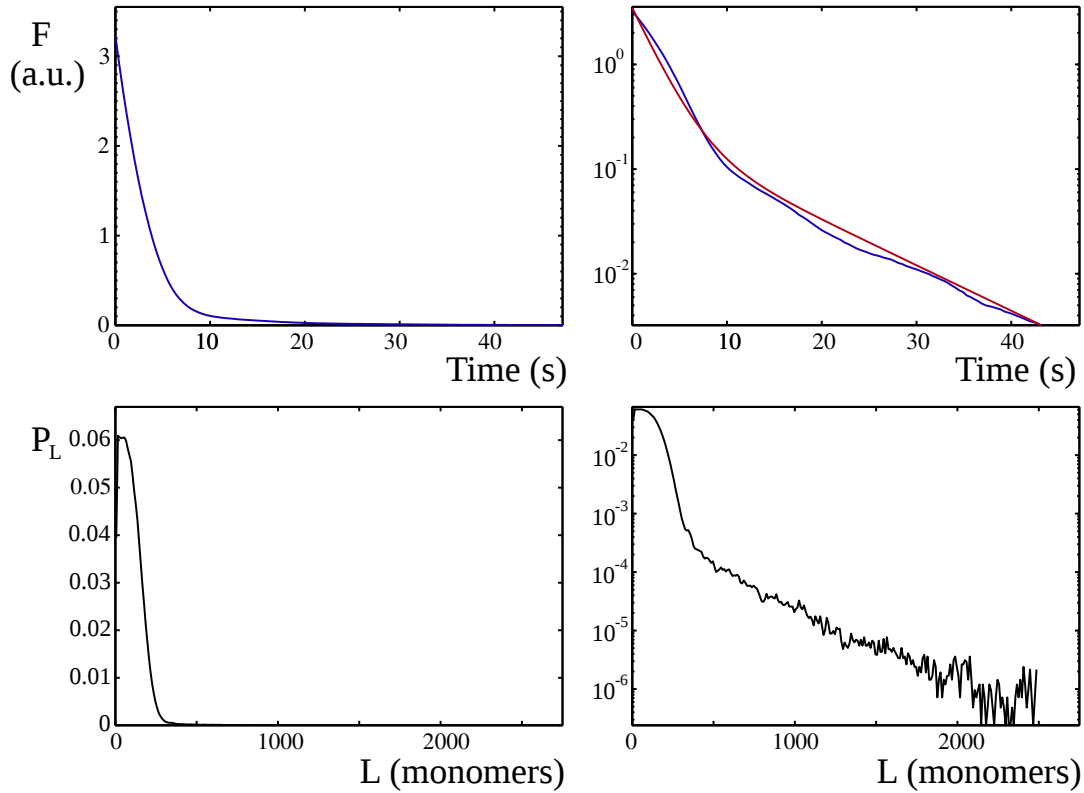
Figure 4.14: FLAP signal and filament length distribution extracted from simulations with severing of fragments of fixed size. Top: The fluorescence signal as a function of time (left: linear scale, right: semilogarithmic scale). Simulation results are given by the blue curve, the fit by a superposition of two exponentials given by the red line. Bottom: The filament length distribution derived from simulations (left: linear scale, right: semilogarithmic scale).

small values is expected to increase the turnover rate of the first pool of filaments.

For L_{frag} as small as 5 monomers, however, only a limited effect on the found timescales could be observed, see Figure 4.14. The first characteristic rate $\tau_1 = 0.45\,s^{-1}$ is only by a factor of 4 faster than the second recovery rate, $\tau_2 = 0.1\,s^{-1}$. The resulting filament length distribution is dominated by a huge pool of tiny fragments that peak around a very small typical length. Only in the semilogarithmic plot, a second population of long filaments becomes visible. Consequently, 93% of the fluorescence recovers on the fast timescale, which is in striking contrast to experimentally determined values.

As a result, the severing of filaments can only qualitatively explain the appearance of two time scales in the fluorescence recovery experiments. The analysis here was limited to two very simple ways of filament severing. It is known that the mechanism by which cofilin

severs actin is much more complicated than the presented models. In contrast to what was assumed here, cofilin was found to bind preferentially but not exclusively to ADP-bound actin subunits of filaments [103, 180]. When bound, it increases the dephosphorylation rate of adjacent actin monomers, thereby fostering the binding of more cofilin in the neighborhood of the already bound molecule [176]. The capability of cofilin to form clusters in this way was neglected here. Moreover, cofilin was found to foster severing at the edges of such clusters [65]. Additionally proteins like coronin and aip1 increase the efficiency of filament severing. Including these effects into the described model, however, did not qualitatively alter the simulation results. Both of the discussed scenarios are able to account qualitatively for the two timescales in FLAP experiments by the action of a severing protein such as cofilin.

4.4.5 Nucleation by Arp2/3

Another way to generate two distinct populations of actin filaments is by the action of a second nucleating protein. When cells were treated with CK666, the number of mobile actin speckles was significantly reduced [61]. The CK666 molecule is known to impair the function of the arp2/3 complex which nucleates new filaments as branches of existing filaments [27, 181]. It remains bound to the pointed end of the new filament and blocks further addition or removal of monomers. From the effect of CK666, it can be concluded that arp2/3 is active in the actin cortex.

The situation was simulated by combining the nucleation of a filament with the capping of its pointed end. A finite number N_{arp} of pointed end nucleators is present in the solution. Free nucleators form new filaments at a rate $\nu_{\mathrm{arp}} \cdot c^{\mathrm{fil}} \cdot \langle L \rangle$, with c^{fil} being the number concentration of actin filaments and $\langle L \rangle$ their average length. Arp2/3 nucleators are removed from the filament's pointed end at rate a_{off}.

Figure 4.15 shows the results of such a simulation. For the given parameter set, both nucleators almost instantaneously form a new filament once they are released. The dependence of the arp2/3 complex on the amount of filaments is thus negligible. The simulated FLAP curve is indeed similar to the one found in experiments. The initial fluorescence drops to half its value on the timescale of less than a second, $\tau_1 = 1.87 \, s^{-1}$. This drop is followed by a slower decrease of fluorescence on a much slower timescale, $\tau_2 = 0.04 \, s^{-1}$. The corresponding filament length distribution shows two exponential subpopulations of average length of about 15 and 550 monomers, respectively.

The implementation of the action of a second nucleator protein produced two relaxation rates that differed by a factor of about 45, which is even more than observed in experiments.
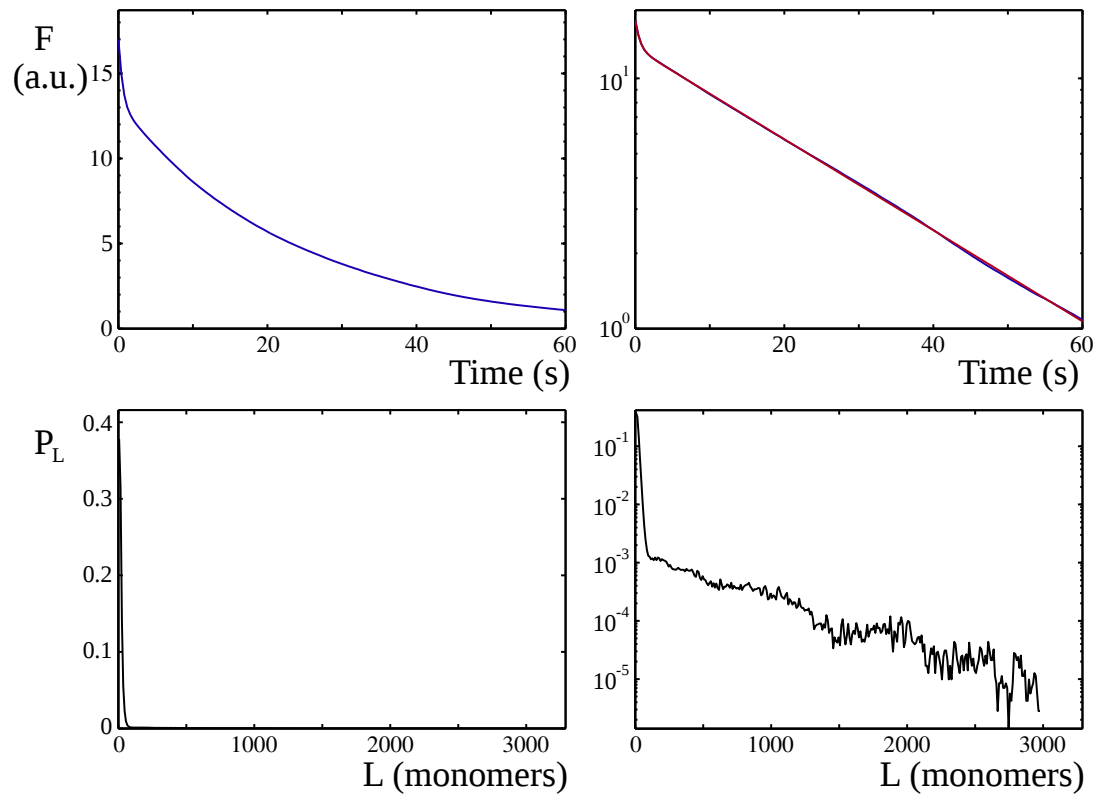
Figure 4.15: FLAP signal and filament length distribution extracted from simulations with nucleation by arp2/3. Top: The fluorescence signal as a function of time (left: linear scale, right: semilogarithmic scale). Simulation results are given by the blue curve, the fit by a superposition of two exponentials given by the red line. Bottom: The filament length distribution derived from simulations (left: linear scale, right: semilogarithmic scale).

The reason might lie in the strict independence of the average filament length in both subpopulations. The average length of arp2/3 nucleated filaments can be tuned by the arp2/3 detachment rate independently of all other parameters. In contrast to the models involving filament severing, the fluorescence decay is visibly exponential. Hence, the nucleation by arp2/3 is the model with the highest potential to fit the experimental results.

4.5 Summary and Further Considerations

In this chapter, the polymerization of active filaments in a finite volume was investigated by stochastic simulations. In the first part, it could be shown that the limited amount of available monomers does not alter the results of Chapter 2 qualitatively. Also, employing a dynamic nucleation of filaments does not impair the possibility of length control of active polymers. The average filament length, however, depends systematically on the number of filaments and the concentration of free monomers that are present in the solution. For polymerization parameters of actin, only an exponentially distributed filament length was found.

In the second part, experiments on the cortex of living cells were presented which can help to understand the details of actin polymerization *in vivo*. FLAP- or FRAP experiments on melanoma M2 cells revealed that the actin cortex is rebuilt on two distinct timescales. So far, the microscopic basis of the observed behavior is unknown. Speckle experiments on individual formin molecules revealed the polymerization velocity of formin bound filaments from which the monomer concentration could be derived. The average lifetime of mobile actin speckles could be used to estimate the average depolymerization velocity on filaments.

To explore the capacity of FLAP and FRAP experiments to elucidate the polymerization of actin, the residence time of actin monomers within filaments was determined analytically for three different scenarios. The results were validated by numerical calculations based on stochastic simulations of filament ensembles. The renewal of monomers in treadmilling filaments was found to be substantially faster than in equilibrium polymers. In the former case, the characteristic rate is proportional to the treadmilling velocity, while it is essentially given by the square of the (small) drift parameter in the latter.

Finally, more complex simulations were established in order to reproduce the experimentally determined fluorescence recovery or decay curves. Three different scenarios were analyzed that were all able to qualitatively match the cortex turnover behavior. In the first model, the slow release rate of capping molecules led to the appearance of a second, slower recovery. Subsequently, a model was analyzed in which severing produced a pool of very short fragments that rapidly exchanged their fluorescence. The two timescales thus emerge

from two filament population of distinct average length. The third model relied on an alternative nucleation mechanism to generate a second filament population. It was inspired by the action of the arp2/3 complex that was shown to be active in the cell cortex. Since the third model was the only one that could generate recovery times that differ by more than an order of magnitude, it seems to be the most plausible explanation for experimental results.

It proved difficult to exactly reproduce experimental results in all of the three situations. Compared to the physical situation in a living cell, the models are indeed highly simplified. The estimated parameters give thus only a coarse idea of the effective rates of the respective processes. Without further knowledge about the microscopic details of protein interactions in the actin cortex, the presented models remain of qualitative interest. Nonetheless, they provide useful insights into the potential organization of actin filaments *in vivo*.

To learn more about the dynamics of the actin cortex, the filament system's reaction to the modification of individual parameters can be studied in the future. Experimentally, this can for example be done by the genetic manipulation of expression levels of individual proteins. Simulations of the three described scenarios can then help to validate or rule out the underlying microscopic models.

5 Concluding Remarks

5.1 Summary

The regulation of the cytoskeletal filaments is of vital importance for the living cell. During evolution, a multitude of proteins and regulatory factors developed and were shaped to perform their specific part in the orchestra of cellular homeostasis. Only piece by piece, the complex network of protein interactions that are necessary for the proliferation of living organisms is uncovered.

In this work, the length dynamics of active polar filaments was investigated on theoretical grounds. Biopolymers like actin and microtubules are generic examples for such filaments. They polymerize under dissipation of chemical energy and are constantly kept out of thermodynamic equilibrium within living cells. Activity and polarity lead to a rich dynamic behavior that is regulated by the cell through accessory proteins. One peculiar property of these filaments is their ability to treadmill, that is to accumulate monomers at one end while they loose monomers at the other end.

The treadmilling phenomenon was analyzed here with help of numeric simulations of lattice gas models and stochastic jump processes. I was able to explain the treadmilling dynamics with a lattice model taking into account two different types of subunits that can switch states at random. I could show that the same properties that lead to filament treadmilling are also able to produce unimodal filament length distributions. Just as the treadmilling itself, the regulation of filament length is an inherently non-equilibrium property of these filaments. In equilibrium, however, only exponentially distributed filaments can be found.

The only energy source for treadmilling in this model was the artificially increased chemical potential of stable subunits in solution. Since it was assumed that subunits within the filament lattice do not interact, addition and removal rates of both states had to satisfy detailed balance independently. Let me note that these conditions do not constitute a fundamental limit to treadmilling or length regulation.

The regime in which unimodal filament length distributions are found, is a subset of parameters that lead to the treadmilling dynamics. A detailed analysis showed that the length dependent depolymerization rate is due to an inhomogeneous distribution of states

along the filament. The growing 'plus end' of the filament accumulates stable monomers which concentrate at this end of the filament. At the opposite end, the 'minus end', subunit addition is so slow that subunits switch to the unstable state before they are integrated in the filament lattice. Being in the unstable state, they are readily removed from the filament which on average looses subunits at the minus-end. By treadmilling, the conversion of stable to unstable subunits over time is translated into spatial information along the filament. Treadmilling is thus a prerequisite to length regulation.

I could derive approximate expressions for the net subunit accumulation rate at the plus end as well as for the characteristic length at which the concentration of stable subunits relaxes along the filament with distance to the plus end. Using this gradient as an input for the average lifetime of a monomer at the minus end, an expression for the length dependent depolymerization rate was formulated. It included the calculation of the probability that release depolymerization was blocked by subunits that were added to the minus end. They formed a transient cap of exponentially distributed length, which could be determined by an independent calculation. At this point, an approximation of the typical filament length at which length dependent depolymerization balances polymerisation was derived and validated by numerical simulations of the filament system.

The two-states model was successfully applied by fitting the evolution of the filament length distribution in a solution of F-actin and the actin binding protein α-actinin. To gain further insight into the polymerization of actin filaments, I used experimentally determined rates for actin monomer addition and removal that were determined *in vitro*. Using the two-states model, unimodal length distributions could only be found in a small range of actin monomer concentrations. At lower concentrations, the filaments were exponentially distributed, for larger concentrations, the filament length diverged. To account for recent experimental results, the model was extended by accounting for a third subunit state and an increased transition rate at the filament's ends. Including both effects in the simulations by rates measured for actin polymerization suppressed filament length regulation for all monomer concentrations. In accordance to experimental findings, length was exponentially distributed in all stationary situations.

After that, I investigated the influence of selected regulatory proteins on the filament length dynamics. Profilin suppresses the subunit addition to the minus end and increases in combination with formin the polymerization at plus ends, but neither the effect of profilin alone nor when combined with formin resulted in a reappearance of unimodal length distributions. The addition of capping proteins slowed the polymerization filaments ends but had little or no effect on the phase diagram. Only the addition of cofilin that fosters the removal of unstable subunits at the minus end could generate clearly peaked filament length

distributions. I conclude that pure actin displays exponential filament length distribution as a result of the low depolymerization rate of its dephosphorylated form. Consequently, unimodal length distributions should be observed *in vitro* only when a depolymerizing factor like cofilin is added. Since such molecules are known to be present in living cells, no clear statement on the filament length distribution *in vivo* can be derived from these results.

In the third chapter, the effect of destabilizing molecular motors on active filaments was investigated. A driven lattice-gas model was invoked to study the distribution of motor particles along the filament and how they influence the length dynamics of the system. In this model, molecular motors were assumed to bind alongside a filament on which they can slide. Here, I focused on the case that the filament was constantly adding monomers at the plus end while motors moved towards the minus end. At the tip of the minus end, they increased the rate at which the subunits were removed along with the binding motor. On the filament, motor movement was only allowed if the destination site of the lattice was empty, thereby introducing steric interactions between motors.

Particle interactions led to the formation of traffic jams or density shocks. The motor distribution was analyzed on a semi-infinite lattice consisting of a plus end and arbitrarily many lattice sites that extend into the direction of the minus end. It was found that for sufficiently large motor binding and stepping rates, a sharp domain wall emerges that separates a region of low motor density from a region of saturated density on the same lattice. In the low density region, the occupation probability increases linearly with distance to the plus end. In this case, the shock position was inferred from a flux-balance condition. If, on the other hand, motors are too slow or leave the lattice easily, a smooth gradient of motor density is observed.

In the full system, the formation of shocks had a strong influence on the length of the filament. For large hopping and monomer removal rates, it was found that the system size is dominated by the shock position on a corresponding semi-infinite lattice. Analytic expressions could be derived for the mean and variance of the filament length distribution in the case of infinitely fast motor movement. Interestingly, these expressions remained approximatively valid for large but finite values of the hopping rate.

The opposite case of immobile motors could be reduced to a special case of the two-states model that was introduced for the polymerisation of actin. In the simplified form, it allowed a mapping to a random walk in a potential, which in turn allowed to calculate the full filament length distribution.

At intermediate values of the motor hopping rate, two different strategies were used to quantify the system's size. If the motor speed is low, the flux-balance condition can be used to access the average filament length. If, conversely, the speed is high, the case of infinitely

fast motor hopping gives good approximations for the average filament length. The latter also provides expressions for length fluctuations. A simple correction term could be added by hand that accounts for large parts of the deviations for all tested parameters.

The results of the analytic treatment of the system could be condensed into a phase diagram that distinguishes between four different regimes. For low motor speed and low binding affinities, filament length will diverge. If motor speed is high, however, filament length will be bounded and be either dominated by the shock position (high binding affinity) or by the flux-balance condition (low binding affinity). For extremely high binding affinities, filament length stays bounded even for small or vanishing motor hopping rate. In this regime, system size is determined by the motor density rather than the motor movement.

A property of particular biological relevance is the robustness of the quality of length control of the motor- filament system. It was shown that for hopping rates slightly larger than the polymerization speed, the relative spread of the filament length distribution is essentially given by the motor binding rate and remains mostly independent of the other parameters.

In the last part of the present study, the situation of the cell cortex was investigated. In contrast to the analyses in Chapters 2 and 3 an ensemble of filaments was considered and the finite amount of filament subunits as well as a dynamic number of filaments were accounted for. In order to support the validity of assumptions made in Chapter 2, calculations were carried out using equivalent parameter sets in a finite volume. The results stayed qualitatively identical. It was found that filament length and monomer number relax rapidly to their stationary values while filament number and higher moments of the length distribution take substantially longer. To a certain degree, the stationary monomer concentration, that was fixed in Chapter 2, can be tuned by the nucleation rate of filaments.

Since the residence time of subunits in linear aggregates depends on the aggregate size, the turnover rate of the actin cortex can provide useful information on the length of cortical filaments. Therefore, fluorescence recovery after photo-bleaching (FRAP) and fluorescence loss after photo-activation (FLAP) experiments were analyzed. Analytical calculations for three selected polymerization schemes corroborated the potential of such experiments to provide information about the polymerization dynamics *in vivo*.

FRAP and FLAP experiments showed that the cortex in human M2 cells turns over on two distinct timescales, suggesting two different populations of filaments within the cortex. Experiments on actin and formin speckles, in which the movement of individual proteins could be tracked, provided estimates for the monomer concentration in the cell and the release rate of formin. To recreate the behavior found in experiments, three different simulations were established, based on filament capping, filament severing, and filament nucleation.

All three simulations could in principle account for the two observed timescales. Since the presence of the nucleating protein arp2/3 in the cortex was confirmed by additional experiments and experimental and numerical results in this case agreed best, it is most probable that the two timescales correspond to turnover of formin and arp2/3 nucleated filaments, respectively. These preliminary conclusions must be tested by further experiments.

5.2 Outlook

The presented work might serve as the starting point for a variety of future investigations on active filamentous systems.

This analysis was based on lattice models to describe the length dynamics of active polar filaments. These models are of particular interest for the understanding of biological systems since they allow a straightforward implementation of microscopic processes and can be evaluated by stochastic means. These properties make them to versatile and efficient tools for the further investigation of complex biological systems such as the cell cortex.

On a microscopic level, the interactions between the individual subunits in actin and microtubuli are largely unknown. Differences in binding energies of monomers to both filament ends provide evidence for the existence of mutual influence. Molecular dynamic simulations can help to understand some aspects but are limited by available computing capacity and short simulation times. Long protein arrays such as actin filaments and microtubules are still beyond the reach of these types of simulations. Taking into account effective interactions between filamentous subunits in lattice models could, however, lead to predictions on larger scales which could then be verified in experiments. The mean filament length and the dynamics of length fluctuations could in particular be targets of such investigations. A thorough analysis of the effect of next neighbor interactions in the filament would be needed to understand the effect of nucleotide hydrolysis on the filament beyond the extremes of random and vectorial hydrolysis. The mechanism of cooperative cofilin binding could then be investigated along the same lines.

The method is not limited to investigations of filament length but can easily be extended to account for spatial gradients, positional information, and molecular interactions. The polarization of amoeboid cells upon external stimuli could be, for example, a promising system to be studied within the framework of stochastic spatial lattice models.

On the grounds of the presented results, microscopic models for the polymerization of cellular cortex can be established and predictions tested in experiments. The three schemes presented in Chapter 4 might not be the only candidates compatible with experimental findings. Only further experiments and their systematic reproduction in simulations can

give information on the dominating interactions. The search for the microscopic origin of the different turnover dynamics has just begun.

So far, only the stationary cortex was considered. The architecture of the presented simulations, however, also permit the analysis of a *de novo* formin cortex, e.g. in a blebb. The early stages of cortex formation can help to understand the robust formation and self-organization of cellular structures.

Finally, the question concerning the filament length distribution of actin and microtubuli *in vivo* is still far from being answered. Many regulatory interactions between filaments and accessory proteins were uncovered in recent years but it still remains unclear how their activities combine to create the variety of structures that are observed in cells.

List of Figures

List of Tables

Dank

Bibliography

[1] D Bray. *Cell movements: From Molecules to Motility*. Garland, New York, 2nd edition, 2001.

[2] J Howard. *Mechanics of Motor Proteins and the Cytoskeleton*. Sinauer Associates, Sunderland, 2001.

[3] A Wegner. Head to tail polymerization of actin. *J Mol Biol*, pages 139–150, 1976.

[4] T D Pollard and J A Cooper. Actin and actin-binding proteins. A critical evaluation of mechanisms and functions. *Ann Rev Biochem*, 55:987–1035, January 1986.

[5] V I Rodionov and G G Borisy. Microtubule treadmilling in vivo. *Science*, 215(1997):215–218, January 1997.

[6] T Mitchison and M Kirschner. Microtubule assembly nucleated by isolated centrosomes. *Nature*, 312:232–237, 1984.

[7] F Oosawa and S Asakura. *Thermodynamics of the polymerization of Protein*. Academic Press, New York, 1975.

[8] T L Hill. Introductory analysis of the GTP-cap phase-change kinetics at the endof a microtubule. *PNAS*, 81:6728–6732, 1984.

[9] T D Pollard, L Blanchoin, and R D Mullins. Molecular Mechanisms Controlling Actin Filament Dynamics in Nonmuscle Cells. *Signals*, 29:545–576, November 2000.

[10] D Vavylonis, Q Yang, and B O'Shaughnessy. Actin polymerization kinetics, cap structure, and fluctuations. *PNAS*, 102(24):8543–8548, June 2005.

[11] B Bugyi and M-F Carlier. Control of actin filament treadmilling in cell motility. *Ann Rev of Biophys*, 39:449–70, June 2010.

[12] L Edelstein-Keshet and G B Ermentrout. A model for actin-filament length distribution in a lamellipod. *J Math Biol*, 43(4):325–355, 2001.

[13] J Roland, J Berro, A Michelot, L Blanchoin, and J-L Martiel. Stochastic severing of actin filaments by actin depolymerizing factor/cofilin controls the emergence of a steady dynamical regime. *Biophys J*, 94(6):2082–94, March 2008.

[14] C Erlenkämper and K Kruse. Uncorrelated changes of subunit stability can generate length-dependent disassembly of treadmilling filaments. *Phys Biol*, 6(4):046016, January 2009.

[15] F J Brooks and A E Carlsson. Actin polymerization overshoots induced by plus-end capping. *Phys Biol*, 7(1):16008, January 2010.

[16] V Varga, J Helenius, K Tanaka, A A Hyman, T U Tanaka, and J Howard. Yeast kinesin-8 depolymerizes microtubules in a length-dependent manner. *Nature Cell Biol*, 8(9):957–962, September 2006.

[17] V Varga, C Leduc, V Bormuth, S Diez, and J Howard. Kinesin-8 motors act cooperatively to mediate length-dependent microtubule depolymerization. *Cell*, 138(6):1174–83, September 2009.

[18] L E Hough, A Schwabe, M A Glaser, J R McIntosh, and M D Betterton. Microtubule depolymerization by the Kinesin-8 motor Kip3p: a mathematical model. *Biophys J*, 96(8):3050–64, April 2009.

[19] L Reese, A Melbinger, and E Frey. Crowding of molecular motors determines microtubule depolymerization. *Biophys J*, 101(9):2190–200, November 2011.

[20] D Johann, C Erlenkämper, and K Kruse. Length Regulation of Active Biopolymers by Molecular Motors. *Phys Rev Lett*, 108(25):258103, June 2012.

[21] An Melbinger, L Reese, and E Frey. Microtubule Length Regulation by Molecular Motors. *Phys Rev Lett*, 108(25), June 2012.

[22] C Erlenkämper, D Johann, and K Kruse. Impact of motor molecules on the dynamics of treadmilling filaments. *Phys Rev E*, 86:051906, 2012.

[23] C Erlenkämper and K Kruse. Treadmilling and length distributions of active polar filaments. *J Chem Phys*, 139(16):164907, October 2013.

[24] S C Greer Physical Chemistry of Equilibrium Polymerization. *J Phys Chem B*, 102(28):5413–5422, July 1998.

[25] M Doi and S F Edwards. *The theory of polymer dynamics*. Clarendon Press - Oxford, Oxford, 1988.

[26] P G de Gennes. Reptation of a Polymer Chain in the Presence of Fixed Obstacles. *J Chem Phys*, 55(2):572, July 1971.

[27] B Alberts, A Johnson, J Lewis, M Raff, K Roberts, and P Walter. *Molecular Biology of The Cell*. Garland Science, New York, 5th edition, 2008.

[28] R D Mullins, W F Stafford, and T D Pollard. Structure, subunit topology, and actin-binding activity of the Arp2/3 complex from Acanthamoeba. *J Cell Biol*, 136(2):331–43, January 1997.

[29] J R Kuhn and T D Pollard. Real-time measurements of actin filament polymerization by total internal reflection fluorescence microscopy. *Biophys J*, 88(2):1387–1402, February 2005.

[30] I Fujiwara, D Vavylonis, and T D Pollard. Polymerization kinetics of ADP- and ADP-Pi-actin determined by fluorescence microscopy. *PNAS*, 104(21):8827–32, May 2007.

[31] L S Tobacman and E D Korn. The kinetics of actin nucleation and polymerization. *J Biol Chem*, 258(5):3207–14, March 1983.

[32] D Sept and J A McCammon. Thermodynamics and kinetics of actin filament nucleation. *Biophys J*, 81(2):667–674, August 2001.

[33] A Ott, M Magnasco, A Simon, and A Libchaber. Measurement of the persistence length of polymerized actin using fluorescence microscopy. *Phys Rev E*, 48(3):1642–1645, 1993.

[34] D Pantaloni. Mechanism of Actin-Based Motility. *Science*, 292(5521):1502–1506, May 2001.

[35] A J Hayes, M Benjamin, and J R Ralphs. Role of actin stress fibres in the development of the intervertebral disc: cytoskeletal control of extracellular matrix assembly. *Dev Dyn*, 215(3):179–89, July 1999.

[36] R Carballido-López. The bacterial actin-like cytoskeleton. *Microbiol Mol Biol Rev*, 70(4):888–909, December 2006.

[37] J Domínguez-Escobar, A Chastanet, A H Crevenna, V Fromion, R Wedlich-Söldner, and R Carballido-López. Processive movement of MreB-associated cell wall biosynthetic complexes in bacteria. *Science*, 333(6039):225–8, July 2011.

[38] E M Mandelkow, E Mandelkow, and R A Milligan. Microtubule dynamics and microtubule caps: a time-resolved cryo-electron microscopy study. *J Cell Biol*, 114(5):977–91, September 1991.

[39] RH Wade, D Chrétien, and D Job. Characterization of microtubule protofilament numbers: how does the surface lattice accommodate? *J Mol Biol*, pages 775–786, 1990.

[40] J van Mameren, K C Vermeulen, F Gittes, and C F Schmidt. Leveraging single protein polymers to measure flexural rigidity. *J Phys Chem B*, 113(12):3837–44, March 2009.

[41] F Pampaloni, G Lattanzi, A Jonás, T Surrey, E Frey, and E-L Florin. Thermal fluctuations of grafted microtubules provide evidence of a length-dependent persistence length. *PNAS*, 103(27):10248–10253, July 2006.

[42] H Flyvbjerg, T E Holy, and S Leibler. Microtubule dynamics: Caps, catastrophes, and coupled hydrolysis. *Phys Rev E*, 54(5):5538–5560, November 1996.

[43] A Desai and T J Mitchison. Microtubule polymerization dynamics. *Ann Rev Cell Dev Biol*, 13(1):83–117, 1997.

[44] P Fanara, S Turner, R Busch, S Killion, M Awada, H Turner, A Mahsut, K L LaPrade, J M Stark, and M K Hellerstein. In Vivo Measurement of Microtubule Dynamics Using Stable Isotope Labeling with Heavy Water Effect of Taxanes. *J Biol Chem*, 279(48):49940–49947, 2004.

[45] T M Svitkina and G G Borisy. Arp2/3 complex and actin depolymerizing factor/cofilin in dendritic organization and treadmilling of actin filament array in lamellipodia. *J Cell Biol*, 145(5):1009–26, May 1999.

[46] T D Pollard, P C-H Tseng, D L Rimm, D P Bichell, R C Williams, J Sinard, and M Sato Characterization of alphaâactinin from Acanthamoeba. *Cell Mot Cytoskeleton*, 6(6):649–661, 1986.

[47] M Pilhofer, M S Ladinsky, A W McDowall, G Petroni, and G J Jensen. Microtubules in bacteria: Ancient tubulins build a five-protofilament homolog of the eukaryotic cytoskeleton. *PLoS Biol*, 9(12):e1001213, December 2011.

[48] B T Helfand, L Chang, and R D Goldman. Intermediate filaments are dynamic and motile elements of cellular architecture. *J Cell Science*, 117(Pt 2):133–41, January 2004.

[49] D R Kovar. Molecular details of formin-mediated actin assembly. *Curr Op Cell Biol*, 18(1):11–7, February 2006.

[50] S Romero, C Le Clainche, D Didry, C Egile, D Pantaloni, and M-F Carlier. Formin is a processive motor that requires profilin to accelerate actin assembly and associated ATP hydrolysis. *Cell*, 119(3):419–29, October 2004.

[51] J A Theriot and T J Mitchison. The Three Faces of Profilin. *Cell*, 75:835–838, 1993.

[52] A Jégou, T Niedermayer, J Orbán, D Didry, R Lipowsky, M-F Carlier, and G Romet-Lemonne. Individual actin filaments in a microfluidic flow reveal the mechanism of ATP hydrolysis and give insight into the properties of profilin. *PLoS Biol*, 9(9):e1001161, September 2011.

[53] D Pantaloni and M-F Carlier. How profilin promotes actin filament assembly in the presence of thymosin beta 4. *Cell*, 75(5):1007–14, December 1993.

[54] D Pruyne, M Evangelista, C Yang, E Bi, S Zigmond, A Bretscher, and C Boone. Role of formins in actin assembly: nucleation and barbed-end association. *Science*, 297(5581):612–5, July 2002.

[55] D R Kovar, E S Harris, R Mahaffy, H N Higgs, and T D Pollard. Control of the assembly of ATP- and ADP-actin by formins and profilin. *Cell*, 124(2):423–35, January 2006.

[56] G G Borisy and T M Svitkina. Actin machinery: pushing the envelope. *Curr Op Cell Biol*, 12(1):104–12, February 2000.

[57] P Dalhaimer, T D Pollard, and B J Nolen. Nucleotide-mediated conformational changes of monomeric actin and Arp3 studied by molecular dynamics simulations. *J Mol Biol*, 376(1):166–83, February 2008.

[58] J E Caldwell, S G Heiss, V Mermall, and J A Cooper. Effects of CapZ, an actin capping protein of muscle, on the polymerization of actin. *Biochemistry*, 28(21):8506–14, October 1989.

[59] A Weber. Tropomodulin caps the pointed ends of actin filaments. *J Cell Biol*, 127(6):1627–1635, December 1994.

Bibliography

[60] R K Meyer and U Aebi. Bundling of actin filaments by alpha-actinin depends on its molecular length. *J Cell Biol*, 110(6):2013–2024, June 1990.

[61] Marco Fritzsche. *Homeostasis of the cellular actin cortex and its filament length-distribution.* Phd thesis, University College London, 2012.

[62] D H Wachsstock, W H Schwarz, and T D Pollard. Cross-linker dynamics determine the mechanical properties of actin gels. *Biophys J*, 66(3):801–809, March 1994.

[63] A A Fedorov, P Lappalainen, E V Fedorov, D G Drubin, and S C Almo. Structure determination of yeast cofilin. *Nature Struct Biol*, 4(5):366–369, 1997.

[64] M-F Carlier, V Laurent, J Santolini, R Melki, D Didry, G X Xia, Y Hong, N H Chua, and D Pantaloni. Actin depolymerizing factor (ADF/cofilin) enhances the rate of filament turnover: implication in actin-based motility. *J Cell Biol*, 136(6):1307–22, March 1997.

[65] C Suarez, J Roland, R Boujemaa-Paterski, H Kang, B R McCullough, A-C Reymann, C Guérin, J-L Martiel, E M De la Cruz, and L Blanchoin. Cofilin tunes the nucleotide state of actin filaments and severs at bare and decorated segment boundaries. *Curr Biol*, 21(10):862–8, May 2011.

[66] C M Waterman-Storer and E D Salmon. Actomyosin-based Retrograde Flow of Microtubules in the Lamella of Migrating Epithelial Cells Influences Microtubule Dynamic Instability and Turnover and Is Associated with Microtubule Breakage and Treadmilling. *J Cell Biol*, 139(2):417–434, October 1997.

[67] F Jülicher, A Ajdari, and J Prost. Modeling molecular motors. *Rev Mod Phys*, 69(4):1269–1281, 1997.

[68] J T Finer, R M Simmons, and J A Spudich. Single myosin molecule mechanics: piconewton forces and nanometre steps. *Nature*, 368:113–119, March 1994.

[69] A Yildiz, M Tomishige, R D Vale, and P R Selvin. Kinesin walks hand-over-hand. *Science*, 303(5658):676–8, January 2004.

[70] A D Pilling, D Horiuchi, C M Lively, and W M Saxton. Kinesin-1 and Dynein are the primary motors for fast transport of mitochondria in Drosophila motor axons. *Mol Biol Cell*, 17(4):2057–2068, April 2006.

[71] C Kural, H Kim, S Syed, G Goshima, V I Gelfand, and P R Selvin. Kinesin and dynein move a peroxisome in vivo: a tug-of-war or coordinated movement? *Science*, 308(5727):1469–72, June 2005.

[72] M J I Müller, S Klumpp, and R Lipowsky. Tug-of-war as a cooperative mechanism for bidirectional cargo transport by molecular motors. *PNAS*, 105(12):4609–4614, March 2008.

[73] J Gaetz and T M Kapoor. Dynein/dynactin regulate metaphase spindle length by targeting depolymerizing activities to spindle poles. *J Cell Biol*, 166(4):465–71, August 2004.

[74] R Heald, R Tournebize, A Habermann, E Karsenti, and A Hyman. Spindle Assembly in *Xenopus* Egg Extracts: Respective Roles of Centrosomes and Microtubule Self-Organization. *J Cell Biol*, 138(3):615–628, August 1997.

[75] S Ohba, K Kamata, and T Miki-Noumura. Stabilization of microtubules by dynein-binding in vitro. Stability of microtubule-dynein complex. *Biochim Biophys Acta - General Subjects*, 1158(3):323–332, November 1993.

[76] V Malikov, A Kashina, and V Rodionov. Cytoplasmic dynein nucleates microtubules to organize them into radial arrays in vivo. *Mol Biol Cell*, 15(June):2742–2749, 2004.

[77] M Evans, R Juhász, and L Santen. Shock formation in an exclusion process with creation and annihilation. *Phys Rev E*, 68(2):1–8, August 2003.

[78] M Ebbinghaus and L Santen. A model for bidirectional traffic of cytoskeletal motors. *J Stat Mech*, 2009(03):P03030, March 2009.

[79] K E P Sugden and M R Evans. A dynamically extending exclusion process. *J Stat Mech*, 2007(11):P11013–P11013, November 2007.

[80] E B Stukalin and A B Kolomeisky. Simple growth models of rigid multifilament biopolymers. *J Chem Phys*, 121(2):1097–1104, July 2004.

[81] A Parmeggiani, T Franosch, and E Frey. Totally asymmetric simple exclusion process with Langmuir kinetics. *Phys Rev E*, 70(4):1–20, October 2004.

[82] B O'Shaughnessy and D Vavylonis. The Ultrasensitivity of Living Polymers. *Phys Rev Lett*, 90(11):1–4, March 2003.

Bibliography

[83] M Ebbinghaus, C Appert-Rolland, and L Santen. Bidirectional transport on a dynamic lattice. *Phys Rev E*, 82(4):1–4, October 2010.

[84] K Kruse, A Zumdieck, and F Jülicher. Continuum theory of contractile fibres. *EPL*, 716, 2007.

[85] K Doubrovinski and K Kruse. Self-Organization of Treadmilling Filaments. *Phys Rev Lett*, 99(22):1–4, November 2007.

[86] G A Klein. *Theoretical Aspects of Motor Protein Induced Filament Depolymerisation*. PhD thesis, TU Dresden, 2005.

[87] D Gillespie. A general method for numerically simulating the stochastic time evolution of coupled chemical reactions. *J Comuputational Phys*, 22(4):403–434, December 1976.

[88] C W Gardiner. *Handbook of Stochastic Methods*. Springer, 2nd edition, 1985.

[89] N G VanKampen. *Stochastic Processes in Physics and Chemistry*. North Holland, 3rd edition, 2007.

[90] S Redner. *A guide to first-passage processes*. Cambridge University Press, Cambridge, 2001.

[91] M A Rould, Q Wan, P B Joel, S Lowey, and K M Trybus. Crystal structures of expressed non-polymerizable monomeric actin in the ADP and ATP states. *J Biol Chem*, 281(42):31909–31919, October 2006.

[92] J Zhang, M L Bang, and D S Gokhin. Syncoilin is required for generating maximum isometric stress in skeletal muscle but dispensable for muscle cytoarchitecture. *Am J Physiol Cell Pysiol*, 0613:1175–1182, 2008.

[93] A K Rzadzinska, M E Schneider, C Davies, G P Riordan, and B Kachar. An actin molecular treadmill and myosins maintain stereocilia functional architecture and self-renewal. *J Cell Biol*, 164(6):887–97, March 2004.

[94] P A Janmey, J Peetermans, K S Zaner, T P Stossel, and T Tanaka. Structure and mobility of actin filaments as measured by quasielastic light scattering, viscometry, and electron microscopy. *J Biol Chem*, 261(18):8357, June 1986.

[95] C Storm, J J Pastore, F C MacKintosh, T C Lubensky, and P A Janmey. Nonlinear elasticity in biological gels. *Nature*, 435(7039):191–194, 2005.

[96] H W Lin, M E Schneider, and B Kachar. When size matters: the dynamic regulation of stereocilia lengths. *Curr Op Cell Biol*, 17(1):55–61, February 2005.

[97] J Prost, C Barbetta, and J-F Joanny. Dynamical control of the shape and size of stereocilia and microvilli. *Biophys J*, 93(4):1124–1133, August 2007.

[98] R S Littlefield and V M Fowler. Thin filament length regulation in striated muscle sarcomeres: pointed-end dynamics go beyond a nebulin ruler. *Seminars in cell & developmental biology*, 19(6):511–519, December 2008.

[99] M Dogterom. Measurement of the Force-Velocity Relation for Growing Microtubules. *Science*, 278(5339):856–860, October 1997.

[100] M J Footer, J W J Kerssemakers, J A Theriot, and M Dogterom. Direct measurement of force generation by actin filament polymerization using an optical trap. *PNAS*, 104(7):2181–6, February 2007.

[101] J Plastino, I Lelidis, J Prost, and C Sykes. The effect of diffusion, depolymerization and nucleation promoting factors on actin gel growth. *Europ Biophys J*, 33(4):310–320, July 2004.

[102] J Xu, J F Casella, and T D Pollard. Effect of Capping Protein , CapZ , on the Length of Actin Filaments and Mechanical Properties of Actin Filament Networks. *Cell Mot Cytoskeleton*, 81(September 1998):73–81, 1999.

[103] T D Pollard and G G Borisy. Cellular motility driven by assembly and disassembly of actin filaments. *Cell*, 112(4):453–465, February 2003.

[104] M Bindschadler, E Osborn, C Deweyjr, and J Mcgrath. A Mechanistic Model of the Actin Cycle. *Biophys J*, 86(5):2720–2739, May 2004.

[105] P Ranjith, D Lacoste, K Mallick, and J-F Joanny. Nonequilibrium self-assembly of a filament coupled to ATP/GTP hydrolysis. *Biophys J*, 96(6):2146–59, March 2009.

[106] P Ranjith, K Mallick, J-F Joanny, and D Lacoste. Role of ATP-hydrolysis in the dynamics of a single actin filament. *Biophys J*, 98(8):1418–27, April 2010.

[107] M Dogterom and S Leibler. Physical aspects of the growth and regulation of microtubule structures. *Phys Rev Lett*, 70(9):1347–1350, March 1993.

Bibliography

[108] M Ebbinghaus and L Santen. Theoretical modeling of aging effects in microtubule dynamics. *Biophys J*, 100(4):832–838, March 2011.

[109] M Bonnet. *Kunststoffe in der Ingenieuranwendung.* Vieweg+Teubner, Heidelberg, 2009.

[110] B O'Shaughnessy and D Vavylonis. Dynamics of Living Polymers. *Europ Phys J E*, 12:481–496, 2003.

[111] A G O Mogilner. Force Generation by Cellular Polymers. In Alberto Ciferri, editor, *Supramoecular Polymers*, chapter 22, pages 741–752. CRC Press, 2nd editio edition, 2005.

[112] S C Greer. Reversible polymerizations and aggregations. *Ann Rev Phys Chem*, 53:173–200, January 2002.

[113] J Dudowicz, K F Freed, and J F Douglas. Lattice model of living polymerization. I. Basic thermodynamic properties. *J Chem Phys*, 111(15):7116, October 1999.

[114] T Ooi, K Mihashi, and H Kobayashi. On the polymerization of tropomyosin. *Archives Biochem Biophys*, 98(1):1–11, July 1962.

[115] J Xu, W H Schwarz, J A Käs, T P Stossel, and P A Janmey. Mechanical properties of actin filament networks depend on preparation, polymerization conditions, and storage of actin monomers. *Biophys J*, 74(May):2731–2740, 1998.

[116] P C Painter and M M Coleman. *Fundamentals of Polymer Science: An Introductory Text.* CRC Press, 2nd edition, 1997.

[117] F R Mayo and F M Lewis. Copolymerization. I. A Basis for Comparing the Behavior of Monomers in Copolymerization; The Copolymerization of Styrene and Methyl Methacrylate. *J Am Chem Soc*, 66(9):1594–1601, 1944.

[118] T Ohm and A Wegner. Mechanism of ATP hydrolysis by polymeric actin. *Biochim Biophys Acta -Protein Structure and Molecular Enzymology*, 1208(1):8–14, September 1994.

[119] U Pieper and A Wegner. The end of a polymerizing actin filament contains numerous ATP-subunit segments that are disconnected by ADP-subunits resulting from ATP hydrolysis. *Biochemistry*, 35(14):4396–402, April 1996.

[120] M Matsumoto and T Nishimura. Mersenne twister: a 623-dimensionally equidistributed uniform pseudo-random number generator. *ACM Trans Model Comput Simul*, 8(1):3–30, January 1998.

[121] T Keiser, A Schiller, and A Wegner. Nonlinear increase of elongation rate of actin filaments with actin monomer concentration. *Biochemistry*, 25(17):4899–906, August 1986.

[122] E D Korn, M F Carlier, and D Pantaloni. Actin polymerization and ATP hydrolysis. *Science*, 238(4827):638–644, 1987.

[123] A A Halavatyi, P V Nazarov, S Medves, M van Troys, C Ampe, M Yatskou, and E Friederich. An integrative simulation model linking major biochemical reactions of actin-polymerization to structural properties of actin filaments. *Biophys Chem*, 140(1-3):24–34, March 2009.

[124] C Erlenkämper. *Stochastische Beschreibungen dynamischer Biopolymere.* Diploma thesis, TU Dresden, 2008.

[125] D Biron and E Moses. The Effect of α-Actinin on the Length Distribution of F-Actin. *Biophys J*, 86(5):3284–3290, May 2004.

[126] C Le Clainche and M-F Carlier. Regulation of actin assembly associated with protrusion and adhesion in cell migration. *Physiol Rev*, 88(2):489–513, April 2008.

[127] R Littlefield and V A Fowler. Defining actin filament length in striated muscle: rulers and caps or dynamic stability? *Ann Rev Cell Dev Biol*, 14:487–525, January 1998.

[128] D Biron, E Moses, I Borukhov, and S A Safran. Inter-filament attractions narrow the length distribution of actin filaments. *EPL*, 73(3):464–470, February 2006.

[129] N S Gov. Theory of the length distribution of tread-milling actin filaments inside bundles. *EPL*, 77(March):1–6, March 2007.

[130] A Spiros and L Edelstein-Keshet. Testing a model for the dynamics of actin structures with biological parameter values. *Bull Math Biol*, 60(2):275–305, March 1998.

[131] L Blanchoin and T D Pollard. Hydrolysis of ATP by polymerized actin depends on the bound divalent cation but not profilin. *Biochemistry*, 41(2):597–602, January 2002.

Bibliography

[132] I Fujiwara, S Takahashi, H Tadakuma, T Funatsu, and S Ishiwata. Microscopic analysis of polymerization dynamics with individual actin filaments. *Nature Cell Biol*, 4(9):666–673, September 2002.

[133] R Melki, S Fievez, and M-F Carlier. Continuous monitoring of Pi release following nucleotide hydrolysis in actin or tubulin assembly using 2-amino-6-mercapto-7-methylpurine ribonucleoside and purine-nucleoside phosphorylase as an enzyme-linked assay. *Biochemistry*, 35(37):12038–12045, September 1996.

[134] H J Kinosian, L A Selden, L C Gershman, and J E Estes. Actin filament barbed end elongation with nonmuscle MgATP-actin and MgADP-actin in the presence of profilin. *Biochemistry*, 41(21):6734–43, May 2002.

[135] N Watanabe and C Higashida. Formins: processive cappers of growing actin filaments. *Exp Cell Res*, 301(1):16–22, November 2004.

[136] E Andrianantoandro and T D Pollard. Mechanism of actin filament turnover by severing and nucleation at different concentrations of ADF/cofilin. *Mol Cell*, 24(1):13–23, October 2006.

[137] H Y Kueh, G T Charras, T J Mitchison, and W M Brieher. Actin disassembly by cofilin, coronin, and Aip1 occurs in bursts and is inhibited by barbed-end cappers. *J Cell Biol*, 182(2):341–353, July 2008.

[138] G B Ermentrout and L Edelstein-Keshet. Models for the length distributions of actin filaments: II. Polymerization and fragmentation by gelsolin acting together. *Bull Math Biol*, 60(3):477–503, May 1998.

[139] C Combeau and M-F Carlier. Probing the mechanism of ATP hydrolysis on F-actin using vanadate and the structural analogs of phosphate BeF-3 and A1F-4. *The J Biol Chem*, 263(33):17429–36, November 1988.

[140] X Li, J Kierfeld, and R Lipowsky. Actin Polymerization and Depolymerization Coupled to Cooperative Hydrolysis. *Phys Rev Lett*, 103(4):1–4, July 2009.

[141] M-F Carlier, D Pantaloni, and E D Korn. The mechanisms of ATP hydrolysis accompanying the polymerization of Mg-actin and Ca-actin. *J Biol Chem*, 262(7):3052–3059, 1987.

[142] D Pantaloni, T L Hill, M-F Carlier, and E D Korn. A model for actin polymerization and the kinetic effects of ATP hydrolysis. *PNAS*, 82(21):7207–7211, November 1985.

[143] K Svoboda and S M Block. Force and velocity measured for single kinesin molecules. *Cell*, 77(5):773–84, June 1994.

[144] L Wordeman. Microtubule-depolymerizing kinesins. *Curr Op Cell Biol*, 17(1):82–8, February 2005.

[145] J Howard and A A Hyman. Microtubule polymerases and depolymerases. *Curr Op Cell Biol*, 19(1):31–35, February 2007.

[146] C T MacDonald, J H Gibbs, and A C Pipkin. Kinetics of Biopolymerization on Nucleic Acid Templates. *Biopolymers*, 6:1–25, 1968.

[147] B Derrida, E Domany, and D Mukamel. An exact solution of a one-dimensional asymmetric exclusion model with open boundaries. *J Stat Phys*, 69(3-4):667–687, November 1992.

[148] G Schütz and E Domany. Phase Transitions in an Exactly Soluble One-Dimensional Exclusion Process. *J STat Phys*, 72(1-2):277–296, 1993.

[149] B Derrida, M R Evans, V Hakim, and V Pasquier. Exact solution of a 1D asymmetric exclusion model using a matrix formulation. *J Physics A: Mathematical and General*, 26(7):1493–1517, April 1993.

[150] J Krug. Boundary-induced phase transitions in driven diffusive systems. *Phys Rev Lett*, 1991.

[151] A Parmeggiani, T Franosch, and E Frey. Phase Coexistence in Driven One-Dimensional Transport. *Phys Rev Lett*, 90(8):1–4, February 2003.

[152] E N Cytrynbaum, V Rodionov, and A Mogilner. Computational model of dynein-dependent self-organization of microtubule asters. *J Cell Science*, 117(Pt 8):1381–97, March 2004.

[153] K Doubrovinski and K Kruse. Cell Motility Resulting from Spontaneous Polymerization Waves. *Phys Rev Lett*, 107(25), December 2011.

[154] R Hawkins, O Bénichou, M Piel, and R Voituriez. Rebuilding cytoskeleton roads: Active-transport-induced polarization of cells. *Phys Rev E*, 80(4), October 2009.

[155] P Greulich and L Santen. Boundary-induced orientation of dynamic filament networks and vesicle agglomerations. *Phys Rev E*, 84(6):1–4, December 2011.

Bibliography

[156] P Guthardt Torres, K Doubrovinski, and K Kruse. Filament turnover stabilizes contractile cytoskeletal structures. *EPL*, 91(6):68003, September 2010.

[157] B S Govindan, M Gopalakrishnan, and D Chowdhury. Length control of microtubules by depolymerizing motor proteins. *EPL*, 83(4):40006, August 2008.

[158] C Leduc, K Padberg-Gehle, V Varga, D Helbing, S Diez, and J Howard. Molecular crowding creates traffic jams of kinesin motors on microtubules. *PNAS*, 109(16):6100–5, April 2012.

[159] S A Endow, S J Kang, L L Satterwhite, M D Rose, V P Skeen, and E D Salmon. Yeast Kar3 is a minus-end mircotubule motor protein that destabilizes microtubules preferentially at the minus ends. *EMBO J*, 13(11):2708–2713, 1994.

[160] S A Endow. Microtubule motors in spindle and chromosome motility. *Europ J Biochem*, 262(1):12–18, May 1999.

[161] G C Rogers, S L Rogers, T A Schwimmer, S C Ems-McClung, C E Walczak, R D Vale, J M Scholey, and D J Sharp. Two mitotic kinesins cooperate to drive sister chromatid separation during anaphase. *Nature*, 427(6972):364–70, January 2004.

[162] T J Mitchison. Polewards Microtubule Flux in the Mitotic Spindle :. 109(August):637–652, 1989.

[163] V Kantsler and R Goldstein. Fluctuations, Dynamics, and the Stretch-Coil Transition of Single Actin Filaments in Extensional Flows. *Phys Rev Lett*, 108(3), January 2012.

[164] G T Charras, C-K Hu, M Coughlin, and T J Mitchison. Reassembly of contractile actin cortex in cell blebs. *J Cell Biol*, 175(3):477–490, November 2006.

[165] C Montague, K W Rhee, and F D Carlson. Measurement of the translational diffusion constant of G-actin by photon correlation spectroscopy. *J Muscle Res Cell Mot*, 4(1):95–101, February 1983.

[166] F C MacKintosh and P A Janmey. Actin gels. *Current Opinion in Solid State and Materials Science*, 2(3):350–357, January 1997.

[167] T Piekenbrock and E Sackmann. Quasielastic light scattering study of thermal excitations of F-actin solutions and of growth kinetics of actin filaments. *Biopolymers*, 32(11):1471–89, November 1992.

[168] O D Weiner, W A Marganski, L F Wu, and S J Altschuler. An actin-based wave generator organizes cell motility. *PLoS Biol*, 5(9), 2007.

[169] D M Veltman and R H Insall. WASP family proteins: their evolution and its physiological implications. *Mol Biol Cell*, 21(16):2880–2893, August 2010.

[170] K Doubrovinski and K Kruse. Cytoskeletal waves in the absence of molecular motors. *EPL*, 83(1):18003, July 2008.

[171] M Bovellan, Y Romeo, M Biro, M Fritzsche, A Boden, D Moulding, R Thorogate, A Jégou, A Thrasher, G Romet-Lemonne, E Paluch, P P Roux, and G T Charras. Diaph1 and the Arp2/3 complex act together to form the submembranous actin cortex. *Nature Cell Biol*, in revisio, 2012.

[172] M A Chesarone, A G DuPage, and B L Goode. Unleashing formins to remodel the actin and microtubule cytoskeletons. *Nature Rev. Mol Cell Biol*, 11(1):62–74, January 2010.

[173] R Rose, M Weyand, M Lammers, T Ishizaki, M R Ahmadian, and A Wittinghofer. Structural and mechanistic insights into the interaction between Rho and mammalian Dia. *Nature*, 435(7041):513–8, May 2005.

[174] N Watanabe, T Kato, A Fujita, T Ishizaki, and S Narumiya. Cooperation between mDia1 and ROCK in Rho-induced actin reorganization. *Nature Cell Biol*, 1(3):136–43, July 1999.

[175] D Swanson and N S Wingreen. Active Biopolymers Confer Fast Reorganization Kinetics. *Phys Rev Lett*, 107(21):218103, November 2011.

[176] L Blanchoin and T D Pollard. Mechanism of interaction of Acanthamoeba actophorin (ADF/Cofilin) with actin filaments. *J Biol Chem*, 274(22):15538–46, May 1999.

[177] A Michelot, J Berro, C Guérin, R Boujemaa-Paterski, C J Staiger, J-L Martiel, and L Blanchoin. Actin-filament stochastic dynamics mediated by ADF/cofilin. *Curr Biol*, 17(10):825–33, May 2007.

[178] H Chen, B W Bernstein, and J R Bamburg. Regulating actin-filament dynamics in vivo. *Trends Biochem Sciences*, 25(1):19–23, January 2000.

Bibliography

[179] W M Brieher, H Y Kueh, B A Ballif, and T J Mitchison. Rapid actin monomer-insensitive depolymerization of Listeria actin comet tails by cofilin, coronin, and Aip1. *J Cell Biol*, 175(2):315–24, October 2006.

[180] S K Maciver, H G Zot, and T D Pollard. Characterization of actin filament severing by actophorin from Acanthamoeba castellanii. *J Cell Biol*, 115(6):1611–20, December 1991.

[181] B J Nolen, N Tomasevic, A Russell, D W Pierce, Z Jia, C D McCormick, J Hartman, R Sakowicz, and T D Pollard. Characterization of two classes of small molecule inhibitors of Arp2/3 complex. *Nature*, 460(7258):1031–1034, August 2009.